Quantum Emission from Hexagonal Boron Nitride

A thesis submitted for the degree of Doctor of Philosophy at

University of Technology Sydney

Faculty of Science

School of Mathematical and Physical Sciences

Author

Trong Toan TRAN

Supervisors

Prof. Igor AHARONOVICH

Prof. Milos TOTH

Assoc. Prof. Charlene LOBO

April 2018

Certificate of Original Authorship

I, Trong Toan Tran, certify that the work in this dissertation entitled, “Quantum emission from Hexagonal Boron Nitride”, has not previously been submitted for a degree nor has it been submitted as part of requirements for a degree except as fully acknowledged within the text.

I also attest that the dissertation has been written by myself. Any help that I have received in my research work and the preparation of the dissertation itself has duly been acknowledged. In addition, I certify that all information sources and literature used are indicated in the dissertation.

This research is supported by an Australian Government Research Training Program Scholarship.

Signature of student:

Production Note:
Signature removed prior to publication.

Date: 23 March 2018

To my loved ones

Copyright notice

Acknowledgements

My doctorate journey would not have been made possible without the help of people mentioned in this acknowledgement section. First, I would like to express my utmost gratitude to my supervisors: Professor Igor Aharonovich, Prof. Milos Toth, and Associate Professor Charlene Lobo.

It has been my great honor to have an opportunity to work with Prof. Milos Toth whose knowledge in physics is unparalleled. He has taught me, a researcher majoring in materials sciences and chemical engineering, the physics of all kinds, from classical to quantum regime. More importantly, he patiently steps me through physical concepts that are very arduous to grasp. Outside working environment, he is a kind-hearted gentleman that mentally supports me significantly when I encounter social challenges in my early days in Australia. While I learn a great deal of physics from Prof. Toth, Prof. Aharonovich, on the other hand, has been showing me not only in-depth knowledge but also hands-on experience in quantum optics and photonics. Prof. Aharonovich is a lovely and dedicated advisor. He tirelessly guides me through individual equations and concepts in quantum optics and nanophotonics until I can completely understand those. He also gives me a plenty of opportunities to get to know experts in the field, network and collaborate with them. Thanks to these occasions, I have greatly improved my collaborative skills and become a more professional team player. I also want to extend my gratitude to Professor Lobo. She has dramatically helped me not only with technical problems but also with administrative matters.

My gratitude also goes to my thesis examiners, Assoc. Prof. Nick Vamivakas (University of Rochester), and Assoc. Prof. Paul Barclay (University of Calgary), for their time and effort spent on examining my thesis. Their comments and feedbacks help make my thesis better.

I would also like to thank other academic staff – Dr. Olga Shimoni, Dr. Jinghua Fang, Dr. Zai-quan (Sean) Xu, Dr. Sejeong Kim, Dr. Carlo Bradac, Dr. Angus Gentle and Dr. Gediminas Seniutinas – who get involved in my research, help me out with fruitful suggestions and share their invaluable experience. Without these dedicated staff, I could not have been able to finish the projects promptly.

The technical staff – Mr. Geoff McCredie, Ms. Katie McBean, Mr. Mark Berkahn and Mr, Herbert Yuan – also play a critical role in my Ph.D. journey. They have been maintaining, troubleshooting and upgrading to keep the facilities at their top performance; and they are very amiable, helpful and dedicated to all the students and staff in the Microstructure Analysis Unit (MAU). My gratitude also goes to the team in the mechanical workshop who help fabricate scientific tools that are invaluable to my experiments.

My academic journey would have missed most of its meaning without having the fellow students in MAU. They not only guide me through technical problems but also have become my companions in and outside the lab. I could still remember the daily morning coffee session and lunch break where we usually not only deepen our discussion into a specific scientific topic but also extend our arguments to general science. These moments will probably be with me for years down the road. I would, therefore, like to thank Mehran Kianinia, Amanuel Berhane, Kerem Bray, Russell Sandstrom, John Scott, Mika Tham Gleeson, Chris Elbadawi, James Bishop, Cameron Zachreson, Sumin Choi, Vikram Nikam, Daniel Totonjian, Minh Nguyen, Hanh Duong and Blake Reagan.

It has been my great pleasure to work with our collaborators from institutions around the globe: Prof. Dirk Englund, Dr. Gabriele Grosso, Tim Schroder, Dr. Hyowon Moon, and Mr. Benjamin Lienhard from Massachusetts Institute of Technology (MIT) for the work on quantum emitters in hexagonal boron nitride and silicon carbide; Prof. Michael Fuhrer and Dr. Changxi Zheng from Monash University, and Dr. Avi Bendavid from CSIRO for the study on single photon

emitters in oxidized tungsten diselenide; Dr. Andrea Schell, Prof. Shigeki Takeuchi and Dr. Hideaki Takashima for the investigation on non-linear optics and coupling to taper fiber of hBN quantum emitters; Prof. Teri Odom, Danqing Wang, and Ankun Yang for the work on hBN emitter - plasmonic lattice coupling; Prof. Alexander Kubanek for the investigation on resonant excitation of quantum emitters from hBN; Dr. Jingjie Zhang from ANSTO for the work on synthesis and optical properties of nuclear-related compounds.

No research could have been carried out without sufficient fundings. I, therefore, would like to extend my gratitude towards the Australian Research Council (ARC) and FEI company for their financial support to my Ph.D. candidature. I also want to thank the Research Training Program (RTP) scheme from the Department of Education and Training for funding my stipend in part.

Lastly, I want to thank my wife, Thao, my daughter, Sophia, my parents and my extended family for their endless support and understanding during my Ph.D. journey. They are the most important people in my life. They have always been with me during good times as well as hardships. Without them, I would not have been able to finish this challenging academic adventure.

List of Publications

Refereed journal publications

1) **Tran, T. T.**; Fang, J.; Zhang, H.; Rath, P.; Bray, K.; Sandstrom, R. G.; Shimoni, O.; Toth, M.; Aharonovich, I. "Facile Self-Assembly of Quantum Plasmonic Circuit Components." *Adv. Mater.* 2015, 27, 4048-4053.

2) **Tran, T. T.**; Bray, K.; Ford, M. J.; Toth, M.; Aharonovich, I. "Quantum Emission from Hexagonal Boron Nitride Monolayers." *Nat. Nanotechnol.* 2016, 11, 37-41.

3) **Tran, T. T.**; Elbadawi, C.; Totonjian, D.; Lobo, C. J.; Grosso, G.; Moon, H.; Englund, D. R.; Ford, M. J.; Aharonovich, I.; Toth, M. "Robust Multicolor Single Photon Emission from Point Defects in Hexagonal Boron Nitride." *ACS Nano* 2016, 10, 7331-7338.

4) **Tran, T. T.**; Zachreson, C.; Berhane, A. M.; Bray, K.; Sandstrom, R. G.; Li, L. H.; Taniguchi, T.; Watanabe, K.; Aharonovich, I.; Toth, M. "Quantum Emission from Defects in Single-Crystalline Hexagonal Boron Nitride." *Phys. Rev. Appl.* 2016, 5, 034005.

5) **Tran, T. T.**; Kianinia, M.; Nguyen, A.; Kim, S.; Xu, ZQ.; Kubanek, A.; Aharonovich, I.; Toth, M. "Resonant Excitation of Quantum Emitters in Hexagonal Boron Nitride." ACS Photonics 2017, ASAP, doi: 10.1021/acsphotonics.7b00977.

6) **Tran, T. T.**; Wang, D.; Xu, Z.-Q.; Yang, A.; Toth, M.; Odom, T. W.; Aharonovich, I. "Deterministic Coupling of Quantum Emitters in 2d Materials to Plasmonic Nanocavity Arrays." *Nano Lett.* 2017.

7) **Tran, T. T.**; Choi, S.; Scott, J. A.; Xu, Z.-Q.; Zheng, C.; Seniutinas, G.; Bendavid, A.; Fuhrer, M. S.; Toth, M.; Aharonovich, I. "Room-Temperature

Single-Photon Emission from Oxidized Tungsten Disulfide Multilayers." *Adv. Opt. Mater.* 2017, 5, 1600939.

8) **Tran, T. T.**; Kianinia, M.; Bray, K.; Kim, S.; Xu, Z.-Q.; Gentle, A.; Sontheimer, B.; Bradac, C.; Aharanovich, I. "Nanodiamonds with Photostable, Sub-Gigahertz Linewidths Quantum Emitters." *APL Photonics* 2017, 2, 116103.

9) Choi, S.; **Tran, T. T.**; Elbadawi, C.; Lobo, C.; Wang, X.; Juodkazis, S.; Seniutinas, G.; Toth, M.; Aharonovich, I. "Engineering and Localization of Quantum Emitters in Large Hexagonal Boron Nitride Layers." *ACS Appl. Mater. Interfaces* 2016, 8, 29642-29648.

10) Elbadawi, C.; **Tran, T. T.**; Kolibal, M.; Sikola, T.; Scott, J.; Cai, Q.; Li, L. H.; Taniguchi, T.; Watanabe, K.; Toth, M.; Aharonovich, I.; Lobo, C. "Electron Beam Directed Etching of Hexagonal Boron Nitride." *Nanoscale* 2016, 8, 16182-16186.

11) Lienhard, B.; Schröder, T.; Mouradian, S.; Dolde, F.; **Tran, T. T.**; Aharonovich, I.; Englund, D. "Bright and Photostable Single-Photon Emitter in Silicon Carbide." *Optica* 2016, 3, 768-774.

12) Schell, A. W.; **Tran, T. T.**; Takashima, H.; Takeuchi, S.; Aharonovich, I. "Non-Linear Excitation of Quantum Emitters in Hexagonal Boron Nitride Multiplayer." *APL Photonics* 2016, 1, 091302.

13) Scott, J. A.; Totonjian, D.; Martin, A. A.; **Tran, T. T.**; Fang, J.; Toth, M.; McDonagh, A. M.; Aharonovich, I.; Lobo, C. J. "Versatile Method for Template-Free Synthesis of Single-Crystalline Metal and Metal Alloy Nanowires." *Nanoscale* 2016, 8, 2804-2810.

14) Zhang, Y.; Cejka, J.; Lumpkin, G. R.; **Tran, T. T.**; Aharonovich, I.; Karatchevtseva, I.; Price, J. R.; Scales, N.; Lu, K. "Hydrothermal Synthesis, Structures and Properties of Two Uranyl Oxide Hydroxyl Hydrate Phases with Co(Ii) or Ni(Ii) Ions." *New J. Chem.* 2016, 40, 5357-5363.

15) Zhang, Y.; Clegg, J. K.; Lu, K.; Lumpkin, G. R.; **Tran, T. T.**; Aharonovich, I.; Scales, N.; Li, F. "Uranium(VI) Hybrid Materials with [(Uo2)3(μ3-O)(μ2-Oh)3]+ as the Sub–Building Unit Via Uranyl–Cation Interactions." *ChemistrySelect* 2016, 1, 7-12.

16) Zhang, Y.; Karatchevtseva, I.; Bhadbhade, M.; **Tran, T. T.**; Aharonovich, I.; Fanna, D. J.; Shepherd, N. D.; Lu, K.; Li, F.; Lumpkin, G. R. "Solvothermal Synthesis of Uranium(Vi) Phases with Aromatic Carboxylate Ligands: A Dinuclear Complex with 4-Hydroxybenzoic Acid and a 3d Framework with Terephthalic Acid." *J. Solid State Chem.* 2016, 234, 22-28.

17) Kianinia, M.; Regan, B.; Tawfik, S. A.; **Tran, T. T.**; Ford, M. J.; Aharonovich, I.; Toth, M. "Robust Solid-State Quantum System Operating at 800 K." *ACS Photonics* 2017.

18) Schell, A. W.; Takashima, H.; **Tran, T. T.**; Aharonovich, I.; Takeuchi, S. "Coupling Quantum Emitters in 2D Materials with Tapered Fibers." *ACS Photonics* 2017, 4, 761-767.

19) Tawfik, S. A.; Ali, S.; Fronzi, M.; Kianinia, M.; **Tran, T. T.**; Stampfl, C.; aharonovich, i.; Toth, M.; Ford, M. "First-Principles Investigation of Quantum Emission from hBN Defects." *Nanoscale* 2017, 9, 13575-13582.

20) Xu, Z.-Q.; Elbadawi, C.; **Tran, T. T.**; Kianinia, M.; Hoffman, T. B.; Edgar, J. H.; Toth, M.; Aharonovich, I. "Atomic Engineering of Single Photon Sources in 2D Boron Nitride." arXiv preprint arXiv:1704.05154 (2017), under review.

21) Kianinia, M.; Bradac, C.; Wang, F.; Sontheimer, B.; **Tran, T. T.**; Nguyen, M.; Kim, S.; Xu, Z.-Q.; Jin, D.; Schell, A. W. "All-optical control and super-resolution imaging of quantum emitters in layered materials." *Nat. Commun.* 2018, 9, (1), 874.

Conference oral presentations

Tran T. T. et. al., “Quantum Emission from Hexagonal Boron Nitride Monolayers”, International Conference of Nanoscience and Nanotechnology (ICONN), 2016, Canberra, Australia.

Tran T. T. et. al., “Quantum Emission from Hexagonal Boron Nitride Monolayers”, 5th International Symposium on Graphene Devices (ISGD-5), 2016, Brisbane, Australia.

Tran T. T. et. al., “Quantum Emission from Hexagonal Boron Nitride”, Conference on Optoelectronic and Microelectronic Materials and Devices (COMMAD), 2016, Sydney, Australia.

Tran T. T. et. al., “Quantum Emission from Hexagonal Boron Nitride”, Conference on Lasers and Electro-Optics (CLEO), 2017, San Jose, USA.

Patents

Bishop, J.; **Tran, T. T.**; Aharonovich, I.; Lobo, C.; Toth, M. “Nanofabrication Using a New Class of Electron Beam Induced Surface Processing Techniques.” US Patent: 2017; p US20170073814 A20170073811.

Contents

CERTIFICATE OF ORIGINAL AUTHORSHIP ..... **ii**
COPYRIGHT NOTICE ..... **iv**
ACKNOWLEDGEMENTS ..... **v**
LIST OF PUBLICATIONS ..... **viii**
CONTENTS ..... **xii**
LIST OF FIGURES ..... **xvi**
LIST OF TABLES ..... **xxxiii**
ABBREVIATIONS ..... **xxxiv**
ABSTRACT ..... **xxxvi**

1 INTRODUCTION AND BACKGROUND **1**
1.1 INTRODUCTION 1
1.2 BACKGROUND 5
1.2.1 Single Photon Sources *5*
1.2.1.1 Definition of photons and types of light sources 5
1.2.1.2 Second-order autocorrelation function 6
1.2.1.3 Emission rate and lifetime 9
1.2.1.4 Indistinguishability and Fourier-transform limited linewidths 10
1.2.2 Types of Single Photon Sources *11*
1.2.2.1 Atoms and trapped ions 12
1.2.2.2 Molecules, quantum dots, perovskite nanocrystals and carbon nanotubes . 13
1.2.2.3 Point-defect centers in wide-bandgap semiconductors 14
1.2.2.3.1 Color centers in diamond 14
1.2.2.3.2 Color centers in silicon carbide 16
1.2.2.3.3 Defect centers in zinc oxide 16
1.2.2.3.4 Color centers in rare-earth crystals 16
1.2.2.3.5 Defect-based centers in carbon nanotubes 17
1.2.2.3.6 Quantum emitters in two-dimensional limit 17
1.2.3 Two-dimensional Materials Optics *18*
1.2.4 Properties, Synthesis, & Characterization of Hexagonal Boron Nitride . *19*
1.2.4.1 Physical properties 19
1.2.4.2 Optical properties 21
1.2.4.3 Defects in hexagonal boron nitride 22
1.2.4.4 Synthesis of hexagonal boron nitride 23

1.2.4.4.1 Bulk crystals 23
1.2.4.4.2 Few-layer hBN flakes 23
1.2.4.5 Characterization of hexagonal boron nitride flakes 25
1.2.5 Laser Scanning Fluorescence Confocal Microscopy 26
1.2.5.1 Basics of wide-field and scanning confocal fluorescence microscopy 26
1.2.5.2 Typical laser scanning confocal fluorescence setup used in this thesis 28

2 QUANTUM EMISSION FROM HEXAGONAL BORON NITRIDE MONOLAYERS 31

2.1 ABSTRACT 31
2.2 INTRODUCTION 31
2.3 METHODS 32
2.3.1 Materials 32
2.3.2 Structural and elemental characterization 33
2.3.3 Photoluminescence analysis 33
2.3.4 Theoretical calculations 34
2.4 RESULTS AND DISCUSSION 35
2.5 CONCLUSION 50

3 ROBUST MULTICOLOR SINGLE PHOTON EMISSION FROM POINT DEFECTS IN HEXAGONAL BORON NITRIDE 51

3.1 ABSTRACT 51
3.2 INTRODUCTION 52
3.3 METHODS 53
3.3.1 Materials preparation: annealing process 53
3.3.2 Materials preparation: electron-beam irradiation 53
3.3.3 Optical characterization 53
3.3.4 Theoretical calculation 55
3.4 RESULTS AND DISCUSSION 57
3.5 CONCLUSIONS 72

4 QUANTUM EMISSION FROM SINGLE-CRYSTALLINE HEXAGONAL BORON NITRIDE 73

4.1 ABSTRACT 73
4.2 INTRODUCTION 73
4.3 METHODS 74
4.4 RESULTS AND DISCUSSION 75
4.5 CONCLUSIONS 85

5 RESONANT EXCITATION OF QUANTUM EMITTERS IN HEXAGONAL BORON NITRIDE 87

5.1 Abstract 87
5.2 Introduction 87
5.3 Methods 88
5.4 Results and Discussion 89
5.5 Conclusion 100

6 ENGINEERING AND LOCALIZATION OF QUANTUM EMITTERS IN LARGE HEXAGONAL BORON NITRIDE LAYERS 101

6.1 Abstract 101
6.2 Introduction 101
6.3 Methods 103
6.3.1 Sample preparation 103
6.3.2 Defect creation using femtosecond laser pulse irradiation 103
6.3.3 Electron beam irradiation of exfoliated hBN flakes 103
6.3.4 Ion implantation procedure 104
6.3.5 Optical measurements 104
6.4 Results and Discussion 105
6.5 Conclusions 114

7 DETERMINISTIC COUPLING OF QUANTUM EMITTERS IN 2D MATERIALS TO PLASMONIC NANOCAVITY ARRAYS 116

7.1 Abstract 116
7.2 Introduction 116
7.3 Methods 118
7.3.1 Sample preparation 118
7.3.2 Transfer process 118
7.3.3 Optical characterization 119
7.3.4 Modeling of plasmonic NP arrays 119
7.4 Results and Discussion 119
7.5 Conclusion 129

8 ROOM-TEMPERATURE SINGLE-PHOTON EMISSION FROM OXIDIZED TUNGSTEN DISULFIDE MULTILAYERS 130

8.1 Abstract 130
8.2 Introduction 130
8.3 Methods 131
8.4 Results and Discussion 132
8.5 Conclusion 140

9 GENERAL CONCLUSIONS AND OUTLOOKS 141

BIBLIOGRAPHY 144

List of Figures

Figure 1.1. *Schematic of photon temporal distribution of three types of photon sources, namely,* ***(a)*** *thermal light,* ***(b)*** *coherent light, and* ***(c)*** *single photon source.*

Figure 1.2. *Second-order autocorrelation functions for* ***(a)*** *thermal light,* ***(b)*** *coherent light, and* ***(c)*** *single photon source.*

Figure 1.3. *Typical solid-state quantum systems summarized in this thesis.* ***(a)*** *Defect centers in 3D bulk and nanocrystals, with host materials including diamond, silicon carbide, rare-earth and zinc oxide.* ***(b)*** *Quantum emitters in 2D hosts, namely tungsten diselenide (WSe_2) and hBN.* ***(c)*** *Defect-based single photon source in CNTs.* ***(d)*** *Nitride quantum dots embedded in a waveguide for emission enhancement.* ***(e)*** *Self-assembled InAs QDs The figure is reproduced with permission from Ref [16], published by Nature Publishing Group.*

Figure 1.4. *Schematic of a three-layer hBN flake showing the "lip-lip" (AA') stacking order.*

Figure 1.5. *Comparison between* ***(a)*** *wide-field and* ***(b)*** *confocal microscopy. Reproduced with permission from Ishikawa-Ankerhold et al., "Advanced Fluorescence Microscopy Techniques—Frap, Flip, Flap, Fret, and Flim.", 2012, 17, 4047; published by MDPI.*

Figure 1.6. *Schematic of a typical scanning confocal fluorescence setup used in this work. HBT: Hanbury-Brown and Twiss; BS: beamsplitter; FT: band-pass or long-pass filters; λ/2: half waveplate; Pol: linear polarizer; SPCAPD: single photon counting avalanche photodiode. The spectrometer is not displayed here for simplicity of the setup. The top and bottom panel showing different viewing angles on the same setup.*

Figure 2.1. *Structural characterization of hBN.* ***(a)*** *Schematic illustration of a hBN monolayer.* ***(b)*** *TEM image of the corner of a single hBN sheet. The inset shows the hBN lattice.* ***(c)*** *A corresponding SAED pattern.* ***(d)*** *Raman scattering spectra of monolayer, multilayer and bulk hBN (blue, green and red squares, respectively) on a silicon substrate. Solid lines are Lorentzian fits to the experimental data.*

Figure 2.2. *EDX maps of multilayer hBN annealed in argon at 850°C.* ***(a)*** *A representative SEM image of multilayer hBN. Corresponding EDX mappings of boron* ***(b)****, nitrogen* ***(c)****, carbon* ***(d)****, oxygen* ***(e)****, and silicon element* ***(f)****.*

Figure 2.3. *Optical characterization of single photon emitters in hBN.* ***(a)*** *Scanning confocal map of a multilayer hBN sample showing bright luminescent spots that correspond to emission from single defects.* ***(b)*** *Room temperature PL spectra of a defect center in an hBN monolayer (blue trace) and a multilayer hBN (red trace).* ***(c)*** *PL spectrum taken at 77K of a defect center in a multilayer hBN. The inset shows the zero-phonon line.* ***(d)*** *Antibunching curves from an individual defect center in a hBN monolayer (blue, open circles) and a multilayer hBN (red, open circles), corresponding to the spectra shown in* ***(b)****. The $g^2(\tau)$ curves were acquired using an excitation power of 300 μW, an acquisition time of 10 sec, and were normalized and offset vertically for clarity. The solid blue and red lines are fits obtained using* ***Eq. 2.1.***

Figure 2.4. *Representative PL spectrum taken from an ensemble of emitters in hBN monolayers at 77 K.*

Figure 2.5. *Line profile of the 532 nm CW laser used as the excitation source in this study.*

Figure 2.6. *Second-order autocorrelation functions of 15 SPEs found at random in multilayer hBN. The $g^2(0)$ value is shown for each emitter. Each curve was acquired for 10 min using a 300 μW, 532 nm CW laser as the excitation source.*

Figure 2.7. *Histogram of the $g^2(0)$ values shown in* ***Fig. 2.6****.*

Figure 2.8. *(**a**) The confocal map presented in **Fig. 2.3a.** (**b**) A close-up showing a typical single color center. (**c**) Line profile (indicated by the dashed line in (**b**) of the defect center shown in b. The circles and the solid traces are the experimental data and a Gaussian fit, respectively. (**d**) Antibunching curve obtained from the defect show in b. The Gaussian fit in b has a full width at half maximum of 429 nm. This value is expected from a single emitter given that the ZPL wavelength is ~623 nm, the PSB extends out to ~700 nm, and a background emission is present, as indicated by the $g^2(\tau)$ curve shown in (**d**).*

Figure 2.9. *Photophysical properties of single photon emitters in multilayer hBN. (**a**) Fluorescence saturation curve obtained from a single defect, showing a maximum emission rate of 4.26 Mcps. (**b**) Fluorescence lifetime measurement exhibiting an excited state lifetime of 3.1 ns. (**c**) Excitation (open, red circles) and emission (open, blue squares) polarization curves from a single defect. The solid red and blue lines are fits obtained using a $\cos^2(\theta)$ function. (**d**) Fluorescence intensity as a function of time demonstrating the photostability of a single defect at 1 mW excitation power. All the measurements were performed at room temperature using a 532 nm excitation laser.*

Figure 2.10. *Proposed defect models in the hBN lattice. Schematics of (**a**) the nitrogen-vacancy, V_N and (**d**) the anti-site nitrogen vacancy, N_BV_N. Simulated electronic structures of (**b**) V_N, and (**e**) N_BV_N. Black and grey arrows represent occupied and unoccupied states, respectively. Calculated imaginary dielectric tensors of the two components, namely, X (red trace) and Y (blue trace) of (**c**) V_N (**f**) N_BV_N.*

Figure 2.11. *Spin-resolved calculation of the imaginary dielectric tensor for X and Y components of the N_BV_N defect center. Red, blue, green, and purple solid lines represent spin-up of the X and Y components, and spin-down of the X and Y components, respectively.*

Figure 2.12. *Electronic band diagram of* ***(a)*** V_N, *and* ***(b)*** N_BV_N *defect centers hosted in the middle layer of three-layer hBN. Black and grey arrows represent occupied and unoccupied states, respectively.*

Figure 2.13. *Schematic illustration of the proposed extended three-level model used to interpret the temporal population dynamics of the defect center in hBN.*

Figure 2.14. (a) *Second-order autocorrelation function obtained versus laser power from an SPE in multilayer hBN. The* $g^2(\tau)$ *traces are normalized and shifted vertically for clarity.* ***(b)*** *The parameter a,* ***(c)*** *radiative lifetime* τ_1 *and* ***(d)*** *metastable state lifetime* τ_2 *of the defect center as a function of laser power.*

Figure 3.1. *Density functional theory calculation of the effects of strain on the optical response of the* N_BV_N *color center in hBN.* ***(a)*** *X-component of the in-plane imaginary dielectric tensor plotted as a function of compressive (negative percentages) and tensile (positive percentages) strain in an hBN multilayer.* ***(b)*** *Corresponding difference in the ZPL energy of* N_BV_N *versus compressive and tensile strain.*

Figure 3.2. *Generation of emitters in hBN.* ***(a)*** *Schematic illustration of two independent processes that yield emitters – annealing and electron beam irradiation. As-grown, drop-cast hBN flakes are either annealed in an argon environment, or irradiated by an electron beam in a low vacuum* H_2O *environment.* ***(b)*** *Normalized number of stable, bright single emitters as a function of annealing temperature found in hBN multilayers. Each data point was taken from a unique sample that was annealed at a single temperature.* ***(c, d)*** *Examples of PL spectra from emitters fabricated by an electron beam. Each pair shows data recorded from a fixed sample region before (black curve) and after (red curve) electron irradiation.*

Figure 3.3. *Stability of the emitters.* ***(a,c)*** *Normalized luminescence recorded at room temperature from two emitters (E1 and E2) after sequential annealing in*

argon, hydrogen, oxygen and ammonia. ***(b, d)*** *Corresponding antibunching measurements proving that the quantum nature of the defects persists after the sequential set of 30 min anneals performed in H_2, O_2 and NH_3 environments. Emitters E1 and E2 belong to Group 1 and 2, respectively. The Groups are defined in* ***Fig. 3.3****.*

Figure 3.4. (a, c, e) *Additional 25 PL spectra taken from Group 1 emitters.* ***(b, d)*** *Additional 13 PL spectra taken from Group 2 emitters. Additional antibunching curves acquired from* ***(f)*** *a Group 1 emitter, with a $g^2(0) = 0.08$, and from (g) a Group 2 emitter, with $g^2(0) = 0.26$. The nine PL spectra presented in* ***Fig. 3.3*** *of the main text are not shown here. The antibunching curves were obtained using a 532 nm CW at 300 μW as an excitation source and were not background-corrected. The acquisition time each antibunching curve is 60 sec. A neutral density filter was used to attenuate the signal used to generate the curve in* ***(f)****.*

Figure 3.5. *Emitter creation and destruction upon sequential annealing at 500ºC for 30 min each in H_2, O_2 and NH_3 environments. The sample was first annealed in Ar at 850ºC to generate emitters, and the black spectra in* ***(a-c)*** *were acquired from three different sample regions.* ***(a)*** *The green spectrum was acquired after annealing in H_2 from the same region as the black spectrum, and shows the disappearance of a number of emission lines (indicated by red arrows).* ***(b)*** *The red spectrum was acquired after the final annealing step in NH_3 from the same region as the black spectrum, and shows the appearance of a number of emission lines (indicated by green arrows).* ***(c)*** *The green and blue spectra were acquired after annealing in H_2 and O_2, respectively, and show the appearance and disappearance of a number of emission lines. We note that no systematic trends were observed as a function of gas species. Instead, annealing in all three reactive environments caused the generation and quenching of some emission lines, and on average, more emitters were generated than destroyed after each annealing step. This behavior is expected based on the Ar annealing data shown in* ***Fig. 3.1(b)*** *of*

the main paper. The quenching of some of the emitters is also not surprising. It merely indicates that some of the emitters are unstable, possibly because they are located in the topmost monolayers or edges of hBN flakes and hence sensitive to the annealing treatments.

Figure 3.6. *Multicolor photoluminescence from point defects in hBN.* ***(a)*** *Simplified schematic of the photoluminescence setup showing the excitation and emission of a defect center in an hBN lattice. The objective lens, dichroic mirror, excitation source, and emission are denoted by Obj., DM, Exc., and Emi., respectively.* ***(b)*** *Five examples of emitters in Group 1 with ZPLs at 576 nm (2.15 eV), 583 nm (2.13 eV), 602 nm (2.06 eV), 633 nm (1.96 eV), and 652 nm (1.90 eV).* ***(c)*** *Four examples of emitters in Group 2 with ZPLs at 681 nm (1.82 eV), 696 nm (1.78 eV), 714 nm (1.74 eV), and 762 nm (1.63 eV).* ***(d)*** *Histogram of ZPL energy for numerous emitters in group 1 (red) and group 2 (blue). Each spectrum was acquired from a separate sample region at room temperature using a 300μW CW 532 nm laser.* ***(e)*** *Second-order autocorrelation functions showing that $g^{(2)}(0)$ = 0.39 and 0.34, respectively. The $g^{(2)}(\tau)$ functions were acquired using an excitation power of 300 μW, an acquisition time of 20 sec, and were normalized (without background correction) and offset vertically for clarity. A neutral density filter was used to attenuate the signal generated by the 633 nm emitter.* ***(f)*** *Difference in the energy of the ZPL and PSB versus ZPL energy. The shaded band in* ***(f)*** *is a guide to the eye. In* ***(b)*** *and* ***(c)****, high energy portions of some spectra were cut from the graph for clarity, to avoid overlaps between the spectra.*

Figure 3.7. *Photophysical properties of the defects.* ***(a)*** *Time-resolved fluorescence measurements showing radiative transition lifetimes of the emitters. An 80 μW, 510 nm pulsed laser with a repetition rate of 20 MHz and a pulse width of 100 ps was used as the excitation source. The solid lines are fits obtained using single exponential decay functions.* ***(b)*** *Fluorescence saturation curves and corresponding theoretical fits calculated using a three-level model.* ***(c, d)*** *Second-*

order autocorrelation function, $g^{(2)}(\tau)$, recorded over a longer time scale from the two color centers presented in ***Fig. 3.6*** *with ZPLs at 633 (c) nm and 714 nm (d). The corresponding solid traces are theoretical fits to the experimental data. Insets show the fitting residue χ^2 versus the number of exponentials used in the fitting functions. The yellow bands indicate optimal fits realized when the number of exponentials and the residues are simultaneously minimized.*

Figure 3.8. *Short timescale second-order autocorrelation function, $g^{(2)}(\tau)$, obtained versus excitation power from the two color centers shown in* ***Fig. 3.6(e)*** *of the main text with ZPLs at* ***(a)*** *633 nm, and* ***(b)*** *714 nm. The $g^{(2)}(\tau)$ functions were acquired using a CW 532 nm laser, an acquisition time of 30 sec, and were normalized (without background correction) and offset vertically by 1 unit each for clarity. Solid traces represent theoretical fits of the experimental data obtained using a typical three-level model expression. The corresponding $g^2(0)$ values are 0.48 and 0.43, corresponding to single photon generation probabilities of 52% and 57% above saturation.*

Figure 3.9. *Plot of the power-dependent emission lifetime, τ_1, and metastable state lifetime, τ_2, (obtained by fitting the data in* ***Fig. 3.8****) versus excitation power for the emitters with ZPLs at* ***(a)*** *633 nm and* ***(b)*** *714 nm, respectively. The emission lifetime, τ^0_1, and metastable state, τ^0_2, were deduced by extrapolating the data to zero excitation power.*

Figure 3.10. *Room (295 K) and low (14 K) temperature spectra of representative emitters from* ***(a)*** *Group 1 (dashed and solid red traces), and* ***(b)*** *Group 2 (dashed and solid blue traces), respectively. At 14 K the line widths approach 3.87 and 1.17 meV.*

Figure 4.1. (a) *Optical microscope image of bulk hBN. The scale bar indicates 100 μm.* ***(b)*** *Raman scattering spectrum obtained with a 633 nm He-Ne laser showing a peak at 1365 cm^{-1} with a FWHM of 8.2 cm^{-1}.*

Figure 4.2. *Optical microscope images of bulk hBN samples with* ***(a)*** *a high density of dislocation defects (Bulk1), and* ***(b)*** *a low density of dislocation defects (Bulk2). Numerous planar stacking faults can be clearly seen in sample Bulk1. The scale bars indicate 100 μm.* ***(c)*** *Raman scattering spectra obtained with a 633 nm He-Ne laser showing a peak at 1365 cm^{-1} with a FWHM of 8.2 cm^{-1} for each sample.* ***(d)*** *NEXAFS spectra around the B K-edge spectral region. The inset details a spectral region in which sample Bulk1 shows higher intensity peaks compared to Bulk2 (i.e., a higher concentration of defects relative to Bulk2).*

Figure 4.3. *Cathodoluminescence spectra acquired at 295 K (red trace) and 77 K (blue trace) from sample* ***(a)*** *Bulk1 and* ***(b)*** *Bulk2. The inset is a schematic illustration of the CL setup.*

Figure 4.4. *Optical characterization performed with a 532 nm continuous wave (CW) laser and a 568 nm long pass filter in the collection pathway.* ***(a)*** *A typical confocal map of bulk hBN showing a number of isolated emission centers and ensembles of these centers. The scale bar indicates 10 μm.* ***(b)*** *A room-temperature photoluminescence spectrum of the isolated emission circled in the PL confocal map. The solid red and dotted grey traces represent emitter and background spectra, respectively. The emitter spectrum reveals a pair of peaks at 618 nm and 629 nm that are potentially the zero-phonon lines of the defect transition.* ***(c)*** *An antibunching curve recorded from the defect center in* ***(b)*** *showing a dip of ~ 0.35, proving the single photon emission nature of the defect. The bin size in* ***(c)*** *is 128 ps.*

Figure 4.5. *Normalized excitation (red trace) and emission (blue trace) polarization plot of defect center similar to that in* ***Fig. 4.6.*** *of the main text. The excitation source was a CW 300 μW, 675 nm laser.*

Figure 4.6. (a) *A typical confocal map showing isolated emission centers and ensembles of emitters.* The scale bar indicates 10 μm. ***(b)*** *A room-temperature PL*

spectrum of the isolated emission that is circled in the PL confocal map, revealing a broad emission band at ~ 770 – 900 nm. The solid red and dotted grey traces represent emitter and background spectra, respectively. ***(c)*** *An antibunching curve recorded by continuous wave excitation of the defect center in* ***(b)*** *showing a dip of ~0.37, proving the quantum nature of the defect. The inset shows a similar antibunching curve obtained by pulsed excitation.* ***(d)*** *Time-resolved fluorescence measurement of the defect center in* ***(b)*** *revealing a very short radiative lifetime of ~ 1.0 ns. All measurements were done using a 675 nm CW laser at room temperature, with a 855 ± 110 nm bandpass filter. Pulsed* $g^2(\tau)$ *and lifetime measurements (d) were conducted using a 675 nm laser with a pulse width of 45 ps, a power of 200 μW, and repetition rate of 80 MHz. The bin size in* ***(b)*** *and* ***(d)*** *is 128 ps.*

Figure 4.7. (a) *Long time-scale second-order autocorrelation function (recorded up to 0.1 s) reveals at least three possible metastable states of the defect center characterized in* ***Fig. 4.3****. The inset illustrates the possible excited electronic configuration of the defect center, including the existence of three metastable states. Temporal fluorescence intensity fluctuations at* ***(b)*** *150 μW,* ***(d)*** *600 μW, and* ***(f)*** *2000 μW and the corresponding histograms at* ***(c)*** *150 μW,* ***(e)*** *600 μW, and* ***(g)*** *2000 μW. The black traces in* ***(c)****,* ***(e)****, and* ***(g)*** *are corresponding simulated Poisson distributions, shown for comparison. The time-bin size in* ***(b)****,* ***(d)*** *and* ***(f)*** *is 50 ms.*

Figure 4.8. *Histogram of fluorescence OFF (blue trace) and ON (red trace) time (%) for the emitter presented in* ***Fig. 4.****3 of the main text. A cut-off threshold of 10 % of maximum fluorescence intensity was used to define the OFF state and generate the histogram.*

Figure 5.1. (a) *Cryogenic confocal PL setup. HBT: Hanbury-Brown and Twiss; BS: beamsplitter; FT: band-pass or long-pass filters; λ/2: half-wave plate; Pol: linear polarizer.* ***(b)*** *Confocal PL map recorded with 700-nm laser excitation at*

300 μW. The bright spot corresponds to a single emitter. The measurement was acquired at 8 K. ***(c)*** *Normalized PL spectrum taken from the same emitter at 8 K (blue trace) and 298 K (red trace) with a 300g/mm grating. The green-highlighted box indicates the collected spectral range for the PLE experiment in* ***Fig. 5.3****. The inset shows a higher resolution spectrum taken from the same emitter (with a 1800g/mm grating).* ***(d)*** *Second-order autocorrelation function (black open circles) acquired for the emitter using a 700 nm laser at 100 μW power as the excitation source, acquired for 5 minutes. The measurement was conducted at 8 K. The red solid line is the fitting for the* $g^{(2)}(0)$ *function using a three-level model convoluted by a Gaussian jitter response (see main text). The* $g^{(2)}(0)$ *value of 0.16 ± 0.01, without any background correction, indicates that the emission is from a single emitter. The standard deviation was based on the standard deviation taken from the long delay region. A band-pass filter was used in the measurements of confocal PL in (b) and the photon second-order autocorrelation function (d) to minimize the background PL contribution.*

Figure 5.2. (a) *Spectra showing maximum (red trace) and minimum (blue trace) emission polarization from the emitter taken with the use of a linear polarizer. The data was taken using an excitation laser power of 300 μW with a 5 s acquisition time. The visibility was determined to be unity.* ***(b)*** *Power-dependent fluorescence saturation curve (red open circles). The fit (solid red line) produces values of* I_{max} *and* P_{sat} *of 1.3 Mcounts/sec and 1.6 mW, respectively. The measurement was acquired with a band pass filter (760 ± 12) nm. All the measurements were conducted at room temperature.*

Figure 5.3. (a) *Simplified diagram of the hBN emitter where the excited state can be accessed via either off-resonance or on-resonance excitation, with the former pathway on the left, and the latter pathway on the right. Black and grey arrows indicate excitation towards the higher vibronic states, followed by vibronic relaxation towards the excited ground state. The green arrow indicates on-*

resonance excitation, followed by spontaneous emission denoted by the wavy red arrow in both pathways. ***(b)*** *Resonance photoluminescence excitation measurements on the single emitter with a ZPL peak at 766.186 nm. The excitation power used was 150 nW. Only photons from the PSB were collected using a long pass filter. The experimental data is plotted as the red trace. Five repetitive scans were averaged out to get the final data. The data was fit with either a Gaussian function (black solid line). The measurement was done at 8 K.* ***(c)*** *Additional survey PLE scans showing multiple local maxima with FWHM below 2 GHz. The grey arrows show representative spectral features that are asymmetrical.* ***(d)*** *Time-resolved PL measurements (red open circles) of the same single emitter measured at room temperature. A single-exponential fit gives rise to a lifetime of 3.6 ns for the emitter's excited state. The measurement was done with a 675 nm pulsed laser (100 μW, 10 MHz repetition rate, 100 ps pulse width).*

Figure 5.4. *Optical characterization of another defect center.* ***(a)*** *High- and low-resolution (inset) PL spectra taken from the emitter by off-resonant excitation at 700-nm with 300μW laser power.* ***(b)*** *Five repeated scans over 60 GHz range showing some complete optical resonance features as well as some asymmetrical features.* ***(c)*** *On-resonant excitation with the laser fixed at 787.592 nm (red solid line) and 2-nm detuned from the on-resonance excitation wavelength (black solid line). The calculated* $\tau_{ON}/\tau_{OFF} = 0.09$ *indicates that the emitter is mostly in unexcited states.*

Figure 5.5. (a) *PL intensity vs time for on-resonance (red line) and 2 nm detuned (black) excitation of the same emitter. The blue dash line represents the cut-off threshold (1800 count/sec) for calculating* τ_{on} *and* τ_{off}*. The* τ_{on} / τ_{off} *ratio was calculated to be 0.47. The data are vertically shifted for clarity.* ***(b)*** *Histogram of on-resonance time extracted from an on-resonance trace of* ***(a)****. The calculated average spectral diffusion time,* $\tau_{avg\ spec\ diff} = 102 \pm 65$ *ms.* ***(c)*** *Confocal PL map with the laser staying on-resonance (left panel) and 2 nm detuned (right panel)*

from the resonance. The measurements in ***(a)*** *and* ***(b)*** *were carried out at the excitation power of 150 nW.* ***(d)*** *On-resonance photon second-order correlation function (black open circles) acquired for the emitter at 1 μW excitation power for three hours. The red solid line is the fitting for the* $g^{(2)}_{meas}(0)$ *function using the Gaussian-convoluted three-level model, resulting in an antibunching dip value of 0.11 ± 0.04. The standard deviation was based on the standard deviation taken from the long delay time region. It must be noted that no smoothing procedure was implemented for this measurement. All the measurements were conducted at 8 K.*

Figure 6.1. (a) *Optical image of exfoliated hBN flakes.* ***(b)*** *Table of the investigated samples comprised of a reference sample, four samples that were implanted by ions, one processed by a laser beam and one by an electron beam.*

Figure 6.2. (a-d) *PL spectra from hBN flakes implanted with B, BN, O and Si ions. The insets are second-order autocorrelation functions,* $g^{(2)}(\tau)$*, recorded from each sample, demonstrating the emitters are single photon sources. A spectrum from a reference sample and a corresponding* $g^{(2)}(\tau)$ *function are shown in the (****Fig. 6.8****).*

Figure 6.3. (a) *A table comparing the number of formed emitters found in each ion-implanted sample and a reference sample that was only subjected to annealing.* ***(b, c)*** *Examples of stability curves from a single emitter in an ion implanted flake* ***(b)*** *and in a reference flake* ***(c)****. Blinking followed by bleaching was much more common in the reference sample than in the implanted samples.*

Figure 6.4. *Confocal maps from* ***(a-c)*** *B,* ***(d-f)*** *BN,* ***(g-i)*** *O and* ***(j-l)*** *Si implanted hBN flakes, demonstrating unambiguously that the emitters are always localized at flake edges. Large bright features seen away from flake edges, as in map* ***(i)****, do not exhibit photon antibunching, and do not possess the spectral characteristics of the single photon emitters discussed in this study.*

Figure 6.5. (a-d) *Example of excitation (red circles) and emission (blue squares) polarization plots of single emitters* from each of the implanted samples. All the emitters exhibit dipole like behavior in both excitation and emission.

Figure 6.6. *Fabrication of emitters using laser processing.* ***(a)*** *Confocal map of the hBN flakes. The white circle indicates the presence of the location of a single photon emitter.* ***(b)*** *PL spectrum recorded from the emitter. Inset:* $g^{(2)}(\tau)$ *curve confirming it is indeed a single photon emitter.* ***(c)*** *excitation and emission polarization curves (red circles and blue squares, respectively,) recorded from this emitter.*

Figure 6.7. *Fabrication of emitters by electron beam irradiation. Confocal map of the same flake before* ***(a)*** *and after* ***(b)*** *electron beam irradiation. The energy of the beam is 15 keV.* ***(c)*** *Spectra recorded from a particular location before (blue curve) and after (red curve) irradiation. Inset, a* $g^{(2)}(\tau)$ *curve confirming the formed defect is a single photon source.* ***(d)*** *Excitation and emission polarization from the same defect. The sample was not annealed after electron irradiation.*

Figure 7.1. *Hexagonal boron nitride flakes and their transfer process onto plasmonic lattice substrates.* ***(a)*** *Schematic illustration of the wet process used to transfer a selected hBN flake with an emitter of choice (exemplified by the red dot) from a thermal silicon oxide substrate onto a plasmonic NP array using PMMA as the carrier.* ***(b)*** *SEM image of the mechanically exfoliated hBN flake positioned atop of a silver plasmonic lattice on silica and* ***(c)*** *optical image of the same flake on the plasmonic lattice.* ***(d)*** *FDTD simulation of the lateral (in-plane) electric field intensity distribution* $|E|^2$ *of a 400 nm-spacing silver plasmonic lattice structure.*

Figure 7.2. *Finite-difference time-domain simulation of the vertical (cross-sectional) electric field intensity distribution* $|E|$ *of a silver nanoparticle (NP) array with 400-nm spacing.*

Figure 7.3. *Confocal PL map* ***(a)*** *and its corresponding larger field-of-view SEM image* ***(b)*** *shown in main text* ***Fig. 6.2a****. A good spatial correlation between the confocal map and the SEM image can be observed. The SEM image unarguably shows that the flakes are positioned atop the gold plasmonic NP array.*

Figure 7.4. *Coupling between a quantum emitter in a tape exfoliated hBN flake and a gold NP array on silica.* ***(a)*** *PL confocal map of a flake containing a single photon emitter (red circled). Inset, SEM image of part of the flake on top of the gold plasmonic lattice. The scale bar represents 2 μm.* ***(b)*** *PL spectra of the pristine (red trace) and coupled (blue trace) single photon emitter, and a transmission spectrum of the plasmonic lattice (green trace) with the plasmonic resonance at 640 nm.* ***(c)*** *Second-order autocorrelation functions obtained from the pristine (red circles) and coupled (blue open squares) system. In both cases, the dip at zero delay time falling well below 0.5 implies single photon emission. Background correction was employed to correct the antibunching curves due to high PL background coming from the hBN flake. The* $g^{(2)}(0)$ *values for emission from pristine and coupled emitters are at 0.02 and 0.04, respectively. Red and blue solid lines are fits obtained using a three-level model.* ***(d)*** *Time-resolved PL measurements from the pristine (red open circles) and coupled (blue open squares) systems. Red and blue solid lines are double exponential fits. A 532 nm continuous-wave laser was used in* ***(a)****,* ***(b)*** *and* ***(c)****. A 512 nm pulsed laser with a repetition rate of 10 MHz and 100 ps pulse width was used in* ***(d)****.*

Figure 7.5. *A full-range transmission spectrum of a gold array in Fig. 7.4. The solid line implies the 532 nm excitation laser used in this study. There is a negligible pump absorption by the plasmonic array according to the spectrum.*

Figure 7.6. *Confocal PL maps of before and after the solvent-exfoliated flakes being transferred onto the plasmonic NP array. The two maps show a good agreement on the spatial location and relative orientation of the flakes to one another, confirming that the same flakes were examined.*

Figure 7.7. *Coupling between a quantum emitter in a solvent exfoliated hBN flake and a gold NP array on a silica substrate.* ***(a)*** *PL spectra of a pristine (red trace) and coupled (blue trace) single photon emitter, and a transmission spectrum of the gold lattice (green trace). Inset: SEM image of the hBN flakes ontop the gold NP array.* ***(b)*** *Second-order autocorrelation functions obtained from the pristine (red open circles) and coupled (blue open squares) systems. The* $g^{(2)}(0)$ *values for emission from pristine and coupled emitters are 0.23 and 0.47, respectively. In both cases, the dip at zero delay time falling well below 0.5 implies single photon emission. Red and blue solid lines are fits obtained using a three-level model.* ***(c)*** *Time-resolved PL measurements from the pristine (red open circles) and coupled (blue open squares) systems. Red and blue solid lines are double exponential fits.* ***(d)*** *Fluorescence saturation curves obtained from the pristine (red open circles) and coupled (blue open squares) systems. Red and blue solid lines are fits obtained using equation 2. A 532 nm continuous-wave laser was used in* ***(a)****,* ***(b)*** *and* ***(d)****. A 512 nm pulsed laser with a repetition rate of 10 MHz and 100 ps pulse width was used in* ***(c)****.*

Figure 7.8. *Coupling between a quantum emitter in a solvent exfoliated hBN flake and a silver NP array on a silica substrate.* ***(a)*** *PL spectra of a pristine (red trace) and coupled (blue trace) single photon emitter, and a transmission spectrum of the silver lattice (green trace).* ***(b)*** *Second-order autocorrelation functions obtained from the pristine (red open circles) and coupled (blue open squares) systems. In both cases, the dip at zero delay time falling well below 0.5 implies single photon emission. Red and blue solid lines are fits obtained using a three-level model. The* $g^{(2)}(0)$ *values for emission from pristine and coupled emitters are 0.06 and 0.29, respectively.* ***(c)*** *Time-resolved PL measurements from the pristine (red open circles) and coupled (blue open squares) systems. Red and blue solid lines are double exponential fits.* ***(d)*** *Fluorescence saturation curves for obtained from the pristine (red open circles) and coupled (blue open squares) systems. Red and blue*

solid lines are fits obtained using equation 2. A 532 nm continuous-wave laser was used in ***(a)****,* ***(b)*** *and* ***(d)****. A 512 nm pulsed laser with a repetition rate of 10 MHz and 100 ps pulse width was used in* ***(c)****.*

Figure 8.1. *Characterization of the multilayers.* ***(a)*** *Optical image of annealed WS_2 multilayers. The scale bar is 10 μm. No visible difference could be seen before and after annealing.* ***(b)*** *Raman spectra of a pristine monolayer (red), pristine multilayer (green), and multilayers that were annealed in argon at 550°C (blue). The grey and yellow highlighted boxes denote E_{2g} and 2LA mode, and A_{1g} vibration mode of WS_2.* ***(c)*** *TEM image of an annealed flake and* ***(d)*** *the corresponding selected area electron diffraction taken from* ***(c)****. The diffraction pattern indicates the cubic phase of WO_3.* ***(e-g)*** *XPS spectra of WS_2 annealed at 550°C in an Argon atmosphere, showing spectral regions that contain the O_{1s}, S_{2p} and W_{4f} peaks, respectively. In* ***(c)*** *the presence of a WO_x phase is clearly observed.*

Figure 8.2. *Bright-field optical images of WS_2 flakes after being annealed at 550°C in argon for 30 min. The scale bars are 10 μm. The WS_2 flakes have lateral size of ~0.3 – 3 μm and thickness of ~5 – 300 nm.*

Figure 8.3. *Single photon emission from annealed multilayers.* ***(a)*** *A typical confocal photoluminescence map showing several bright spots corresponding to localized defects.* ***(b)*** *Photoluminescence spectra taken from three bright spots. A spectrum from monolayer WS_2 is plotted for comparison* ***(c)*** *Second-order autocorrelation measurement obtained from the three emitters. The curves are offset vertically for clarity.* ***(d)*** *Time-resolved photoluminescence measurement recorded from the three emitters, yielding excited state lifetimes of 3.5 ns, 4.6 ns, and 4.4 ns, respectively for emitters S1, S2 and S3. The pump power used in* ***(a, b, c)*** *was 300 μW at 532 nm while the pulsed measurement was done using a 512 nm laser (10 MHz, 50 μW).*

Figure 8.4. *Fluorescence saturation and polarization of emitter S1.* ***(a)*** *Fluorescence intensity as a function of pump power. The red open circles and grey open triangles denote background-corrected fluorescence profile of emitter S1 and background fluorescence taken at an area adjacent to the emitter (in* ***Fig. 8.3****). The solid lines are corresponding fitted curves. The saturated intensity is 347,000 cps with the saturated pump at 1.9 mW.* ***(b)*** *Excitation (red open circles) and emission (blue open squares) measurement for emitter S1. Solid lines are corresponding fits.* ***(c)*** *Fluorescence stability measurement over 10 minutes at an excitation power of 1mW. No bleaching or blinking could be seen from the measurement. Measurements taken in* ***(a-c)*** *were done with CW 532 nm laser.*

Figure 8.5. *Additional polarization data taken from three different single photon emitters from the annealed WS_2 sample. Red open circles and blue open squares denote excitation and emission measurement, respectively. Solid lines are corresponding fits. Measurements were done with CW 532 nm laser.*

Figure 8.6. (a) *Antibunching curves as a function of pump power. Solid lines are fitted profile using the standard three-level model.* ***(b)*** *Emission (τ_1) and metastable (τ_2) lifetime plotted as a function of excitation power. By applying linear fitting and extrapolating the fits to vanishing excitation power, emission (τ_1) and metastable (τ_2) lifetime are calculated to be 4.5 ns and 9.3 ns, respectively.* ***(c)*** *Proposed three-level diagram of the emitters with a ground state, an excited state, and a metastable state. Black, red and grey arrows represent excitation, emission, and non-radiative transitions.*

List of Tables

Table 3.1. *Additional metastable states associated with the investigated emitters.*

Abbreviations

0D – zero dimensional

1D – one dimensional

2D – two dimensional

3D – three dimensional

APD – avalanche photodiode

CL – cathodoluminescence

CVD – chemical vapor deposition

CW – continuous wavelength

EPR – electron paramagnetic resonance

FIB – focused ion beam

FWHM – full width at half maximum

hBN – hexagonal boron nitride

HBT – Hanbury Brown and Twiss

IRF – instrument response function

NIR – near infra-red

PL – photoluminescence

PSB – phonon sideband

ODMR – optically detected magnetic resonance

QDs – quantum dots

QE – quantum efficiency

QIP – quantum information processing

QKD – quantum key distribution

SEM – scanning electron microscope

SPS – single photon source

SRIM – stopping and range of ions in matter

WS_2 – tungsten disulfide

ZPL – zero phonon line

Abstract

Realization of quantum technologies demands successful assembly of crucial building blocks. Quantum light sources, lying at the heart of this architecture, have attracted a great deal of research focus during the last several decades. Optically active defect-based centers in wide bandgap materials such as diamond and silicon carbide have been proven to be excellent candidates due to their high brightness and photostability. Integration of quantum emitters on an on-chip integrated circuit, however, favors low dimensionality of the host materials. Single photon sources embedded in two-dimensional lattices are, therefore, highly desired. In this thesis, we introduce a class of novel quantum systems hosted in hexagonal boron nitride (hBN) – a wide bandgap semiconductor in the two-dimensional (2D) limit. First, we demonstrate experimentally that the quantum systems possess a record high single photon count rate, exceeding 4 MHz at room temperature. Polarization and time-resolved spectroscopy reveal their full emission polarization and short excited state lifetime (~3 ns). Besides, the emitters from this class of quantum system also show extremely high stability under high excitation at ambient conditions. By employing spin-resolved density functional theory (DFT) calculation, we suggest that the defect center is an antisite nitrogen vacancy (N_BV_N). A multicolor phenomenon where there is a wide distribution of zero-phonon lines (ZPL) from different emitters is also observed and can be attributed to strain field in the hBN lattice thanks to DFT calculation. Additionally, we demonstrate the ability to create the emitters by means of thermal treatment or electron beam induced etching. Under harsh environments, strikingly, most of the emitters survive and preserve their quantum properties. Resonant excitation spectroscopy reveals a linewidth of ~6 GHz, and a high single photon purity confirmed from an emitter by on-resonance antibunching measurements. Studies on bulk hBN crystals reveal that the emitters tend to locate at dislocations or stacking faults in the crystals. We also demonstrate ion implantation and laser

ablation as means of increasing formation yield of the emitters in mechanically exfoliated hBN flakes. Next, the coupling of quantum emitters in hBN to plasmonic particles arrays is demonstrated, showing several times Purcell enhancement factor. Lastly, we show that another 2D material - tungsten disulfide (WS_2) – when being oxidized also hosts quantum emitters at room temperature. This observation, therefore, opens a new avenue for studying quantum emitters embedded in other 2D materials.

1 Introduction and Background

1.1 Introduction

Living at the beginning of the 21st century, we are using the Internet for a wide range of purposes: from design, work, education to personal communications and entertainment. Rapid information exchange is one of the most important tasks that the world-wide-web offers, enabling us to, for instance, send emails or share photos/videos with our colleagues or families by just a few mouse clicks. In such information exchange process, it is very crucial that the content of the exchange be known only by the sender and the recipient. Seemingly trivial, this requirement is indeed very difficult to achieve since it is almost always possible for an eavesdropper to intercept and steal the exchanged information. To achieve absolutely secured information transfer, one of the most promising ways is to employ polarization states of single photons. In a typical scheme, known as Bennett and Brassard in 1984 or BB84 [1-2], the sender, called Alice, sends encoded single photons to the receiver, called Bob, through an optical fiber channel. Alice randomly picks one of the four polarization states of photons being transmitted, namely 0, 45, 90 and 135 degrees, to encode them. As each of the individual photons arrives at Bob's location, he randomly selects a linear polarizer filter, namely rectilinear or diagonal to measure these photons. Bob then publicly mentions to Alice the type of filter he used without revealing what results he gets for each measurement. Alice, in turn, lets Bob know which filter orientation is correct. While photons incorrectly measured are to be abandoned, photons correctly determined with filters are used to form bits depending upon their associated orientation. These bits are used to form the one-time key for Alice to exchange the encrypted information to Bob securely. Both Alice and Bob know this key exactly despite the random nature of the key generation process. To see how single photons assure absolutely secure key distribution, let us assume the presence of the eavesdropper, called Eve. The only way that Eve could steal the

information of the exchanged key is to intercept and measure the photons. Since there is only one photon being sent at any given time, Eve has to send a photon back to Bob whenever she measures a photon from Alice, to avoid Bob's suspicion. However, due to the no-cloning theorem, it is impossible for Eve to perfectly duplicate an unknown quantum system [3]. Due to this peculiar quantum nature of the no-cloning principle, quantum key distribution using single photons is absolutely secured. For this reason, in recent decades, extensive research effort has been spent on creating an on-demand, bright, polarized single photon source.

Among discovered quantum light sources, solid-state based single photon emitters are highly sought after thanks to their ease of handling and superb stability. Diamond color centers are such examples that have been studied extensively. The color centers are atomic-sized optically active defects in a three-dimensional (3D) crystal lattice of diamonds. The fact that the quantum emitters are embedded in a 3D crystal, however, poses some technical disadvantages such as total internal reflection, control of the position of the emitters within the lattice, difficulty in coupling with cavity or waveguide. It is, therefore, desirable to establish a new class of quantum emitters hosted in a two-dimensional (2D) lattice. In such a system, the emitter is positioned within a single sheet of the host crystal and thus could overcome the aforementioned challenges associated with those in 3D hosts. In this thesis, we report the first investigation of room-temperature quantum emitters in a 2D material, namely hexagonal boron nitride (hBN), and their coupling to optical cavities. In addition, we also show that by oxidizing tungsten diselenide (WS_2) – another 2D material, quantum emitters could also be generated, and hence this opens up a possibility to discover and engineer quantum emitters in other 2D materials.

The structure of this thesis is organized as followings:

Chapter 1 presents the introduction and the scope of the thesis. It also goes through some background about single photon source, 2D materials, and physical and optical properties and synthesis of hBN material.

Chapter 2 introduces the discovery and understanding of optically active defect centers from multilayer and monolayer hBN. Significant portions of this chapter are copied verbatim from the peer reviewed article "*Quantum Emission from Hexagonal Boron Nitride Monolayers*, **Tran, T. T.**; Bray, K.; Ford, M. J.; Toth, Nat. Nanotechnol. 2016, 11, 37-41" [4].

Chapter 3 deals with a deeper understanding of photophysics of quantum emitters in hBN multilayers, the engineering of these emitters using thermal treatment and electron-beam irradiation, and their stability and possible strain-induced optical transition shifts. Significant portions of this chapter are copied verbatim from the peer-reviewed article "*Robust Multicolor Single Photon Emission from Point Defects in Hexagonal Boron Nitride*, **Tran, T. T.**; Elbadawi, C.; Totonjian, D.; Lobo, C. J.; Grosso, G.; Moon, H.; Englund, D. R.; Ford, M. J.; Aharonovich, I.; Toth, M. ACS Nano 2016, 10, 7331-7338" [5].

Chapter 4 shows that quantum emitters in hBN are also be found in bulk hBN crystals. Their photophysical properties are shown with some distinct differences from their counterparts hosted in multilayer and monolayer hBN flakes. Significant portions of this chapter are copied verbatim from the peer-reviewed article "*Quantum Emission from Defects in Single-Crystalline Hexagonal Boron Nitride*, **Tran, T. T.**; Zachreson, C.; Berhane, A. M.; Bray, K.; Sandstrom, R. G.; Li, L. H.; Taniguchi, T.; Watanabe, K.; Aharonovich, I.; Toth, M. Phys. Rev. Appl. 2016, 5, 034005" [6].

Chapter 5 presents resonant excitation from a quantum emitter in hBN. The optical linewidth of the emitter is directly measured with photoluminescence excitation technique. On-resonance fluorescence with single photon characteristics is demonstrated by resonantly exciting the emitter. Significant portions of this chapter are copied verbatim from the peer-reviewed article "*Resonant Excitation of Quantum Emitters in Hexagonal Boron Nitride*, **Tran, T. T.**; Kianinia, M.; Nguyen, A.; Kim, S.; Xu, ZQ.; Kubanek, A.; Aharonovich, I.; Toth, M. ACS Photonics 2017, ASAP, doi: 10.1021/acsphotonics.7b00977."[7].

Chapter 6 demonstrates the engineering of quantum emitters in tape-exfoliated hBN flakes from bulk hBN crystals presented in Chapter 4. By using high-energy ion-implantation with different species as well as ultrashort pulse-laser-ablation techniques, quantum emitters are generated more efficiently, and preferentially located at the boundaries or extended defects of the flakes. Significant portions of this chapter are copied verbatim from the peer-reviewed article "*Engineering and Localization of Quantum Emitters in Large Hexagonal Boron Nitride Layers*, Choi, S.; **Tran, T. T.**; Elbadawi, C.; Lobo, C.; Wang, X.; Juodkazis, S.; Seniutinas, G.; Toth, M.; Aharonovich, I. ACS Appl. Mater. Interfaces 2016, 8, 29642-29648" [8].

Chapter 7 demonstrates the deterministic coupling phenomena of the quantum emitter in hBN with particle array plasmonic cavities by wet-transfer technique. In this work, single photon emitters in hBN with suitable optical transitions are selected and coupled to gold and silver nanoparticle arrays. A fluorescence enhancement of more than two-fold is achieved via Purcell effect. Significant portions of this chapter are copied verbatim from the peer-reviewed article "*Deterministic Coupling of Quantum Emitters in 2D Materials to Plasmonic Nanocavity Arrays***, Tran, T. T.**; Wang, D.; Xu, Z.-Q.; Yang, A.; Toth, M.; Odom, T. W.; Aharonovich, I. Nano Lett. 2017" [9].

Chapter 8 presents the study of quantum emitters found in oxidized WS_2 multilayers, implying opportunities for exploration of defect-based quantum emitters in other 2D materials. Significant portions of this chapter are copied verbatim from the peer-reviewed article "*Room-Temperature Single-Photon Emission from Oxidized Tungsten Disulfide Multilayers*, **Tran, T. T.**; Choi, S.; Scott, J. A.; Xu, Z.-Q.; Zheng, C.; Seniutinas, G.; Bendavid, A.; Fuhrer, M. S.; Toth, M.; Aharonovich, I. Adv. Opt. Mater. 2017, 5, 1600939" [10].

Chapter 9 summarizes all the studies in the thesis and gives a suggestive outlook on the new field of quantum emitters in 2D materials.

1.2 Background

This section introduces some background on single photon sources, 2D materials optics, physical and optical properties of hBN, and sub-bandgap excitation confocal microscope setup.

1.2.1 Single Photon Sources

Single photon source is of central to this thesis. This part of the thesis is discussed on definition and types of single photon sources, and also the associated challenges in achieving an ideal single photon source.

1.2.1.1 Definition of photons and types of light sources

The term photon was coined by Gilbert Lewis [11] in 1926 following the formulating of blackbody radiation by Planck in 1900 and the discovery of photoelectric effect by Einstein in 1905. The current interpretation of a photon is a quantum of an excited quantized electromagnetic field with an energy E:

$$E = h\upsilon \quad (1.1)$$

where h is the Planck's constant and ν is the photon frequency.

When we discuss photons, we should not only concern about their collective intensity but also about their temporal fluctuations. The fluctuations of photons in time are called photon statistics, and this characteristic of photons help define the types of photon sources. There are, in general, three types of photon sources, namely, thermal light (e.g., from an incandescent bulb), coherent light (e.g., from a laser diode) and single photon emission (i.e., a single photon at a time). The photon statistics of the three types of photon sources are described in **Fig. 1.1**. While thermal light shows the super-Poissonian distribution or photon bunching behavior - a situation whereby multiple photons are emitted by a source at the same time (**Fig. 1.1a**), coherent light obeys the Poissonian distribution (**Fig. 1.1b**). Single photon source, however, presents a non-classical behavior: a sub-Poissonian distribution or photon antibunching characteristic – a circumstance whereby strictly one photon is emitted by a source at a time (**Fig. 1.1c**). The way

to determine types of photon source will be discussed in the section 1.2.1.2 Second-order autocorrelation function.

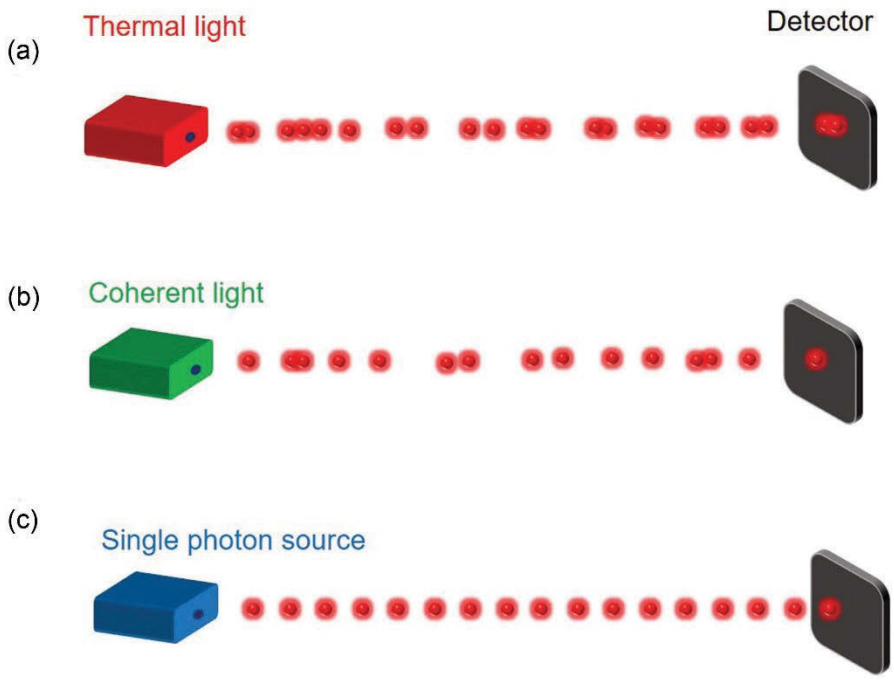

Figure 1.1. *Schematic of photon temporal distribution of three types of photon sources, namely,* ***(a)*** *thermal light,* ***(b)*** *coherent light, and* ***(c)*** *single photon source.*

An ideal single photon source is, thus, defined as a "photon gun" that emits a single photon upon a single trigger (either optically or electrically) at 100 % fidelity.

1.2.1.2 Second-order autocorrelation function

To understand photon temporal statistic, we need to measure the second-order autocorrelation function or the second-order coherence of photons. While the first-order coherence of photons, $g^{(1)}(\tau)$, measures the coherence of two electric fields such as those measurements conducted with Michelson interferometer, the second-order coherence, $g^{(2)}(\tau)$, concerns temporal fluctuation of intensity.

First, the electric field at position vector $\vec{r}$ can be written as the sum of the negative and positive frequency components [12]:

$$\vec{E}(\vec{r}) = \vec{E}^{(-)}(\vec{r}) + \vec{E}^{(+)}(\vec{r}) \quad (1.2)$$

By including the time-dependence in the quantum mechanical view point, the field operator becomes:

$$\vec{E}^{(-)}(\vec{r},\vec{t}) = i\sum_{\vec{k},\vec{\varepsilon}} \frac{\hbar\omega_k}{2\varepsilon_0 L^3}\vec{\varepsilon}a^{+}_{\vec{k},\vec{\varepsilon}}e^{i(\vec{k}\cdot\vec{r}-\omega_k t)} \quad (1.3)$$

Ignoring the spatial coherence properties, the instantaneous intensity is written as:

$$I(t) = 2\varepsilon_0 c\langle E^{(-)}(t)E^{(+)}(t)\rangle \quad (1.4)$$

Additionally, the first- and second-order autocorrelation are described as:

$$g^{(1)}(\tau) = \frac{\langle E^{(-)}(t+\tau)E^{(+)}(t)\rangle}{\langle E^{(-)}(t)E^{(+)}(t)\rangle} \quad (1.5)$$

$$g^{(2)}(\tau) = \frac{\langle I(t+\tau)I(t)\rangle}{\langle I(t)\rangle^2} = \frac{\langle E^{(-)}(t)E^{(-)}(t+\tau)E^{(+)}(t+\tau)E^{(+)}(t)\rangle}{\langle E^{(-)}(t)E^{(+)}(t)\rangle^2} \quad (1.6)$$

With the photon creation operator, $\hat{a}^\dagger$, and annihilation operator, $\hat{a}$, the first-order and second-order coherence are expressed as following [13]:

$$g^{(1)}(\tau) = \frac{\langle \hat{a}^\dagger(t)\,\hat{a}(t+\tau)\rangle}{\langle \hat{a}^\dagger(t)\,\hat{a}(t)\rangle} \quad (1.7)$$

$$g^{(2)}(\tau) = \frac{\langle \hat{a}^\dagger(t)\,\hat{a}^\dagger(t+\tau)\,\hat{a}(t+\tau)\,\hat{a}(t)\rangle}{\langle \hat{a}^\dagger(t)\,\hat{a}(t)\rangle^2} \quad (1.8)$$

where t is the arrival time of the first photon and t + τ is the arrival time of the second photon; $\hat{a}^\dagger$ and $\hat{a}$ are creation and annihilation operators for the photons.

From the **Eq. 1.2.**, it is clear that the first-order coherence is independent of the photon statistics as this expression only concerns the average photon number $\langle n\rangle = \langle \hat{a}^\dagger\hat{a}\rangle$. This means that a filtered thermal light and a coherent source with the same $\langle n\rangle$ yield the same first-order coherence. Essentially, the first-order coherence indicates the coherence time (or coherence length) of a light source – the duration that consecutive photons still preserve their phase. The second-order coherence, however, differentiates the two sources. For a number state $|n\rangle$ of the electromagnetic field, we have:

$$g^{(2)}(0) = \frac{\langle n|\hat{a}^\dagger\hat{a}^\dagger\hat{a}\hat{a}|n\rangle}{\langle n|\hat{a}^\dagger(t)\hat{a}(t)|n\rangle^2} = 1 - \frac{1}{n} \quad (1.9)$$

If we consider a true single photon source, i.e. plug in n = 1 into **Eq 1.4.**, we arrive at $g^{(2)}(0) = 0$. By employing **Eq. 1.4.**, we can also determine how many single photon emitters are being investigated based on the values of $g^{(2)}(0)$. For example, if two single photon emitters are examined optically, we will have $g^{(2)}(0) = 1 - \frac{1}{2} = 0.5$, and if there are three quantum emitters under investigation, we will obtain $g^{(2)}(0) = 1 - \frac{1}{3} = 0.67$, and so on.

For coherent light (i.e., a laser source), we have:

$$g^{(2)}(0) = \frac{\langle\alpha|\hat{a}^\dagger\hat{a}^\dagger\hat{a}\hat{a}|\alpha\rangle}{\langle\alpha|\hat{a}^\dagger(t)\hat{a}(t)|\alpha\rangle^2} = 1 \quad (1.10)$$

For thermal light source, we arrive at:

$$g^{(2)}(0) = \frac{(\Delta n)^2 - \langle n\rangle}{\langle n\rangle^2} = 2 \quad (1.11)$$

The theoretical second-order autocorrelation functions of thermal light, coherent light and single photon source are shown in **Fig. 1.2**.

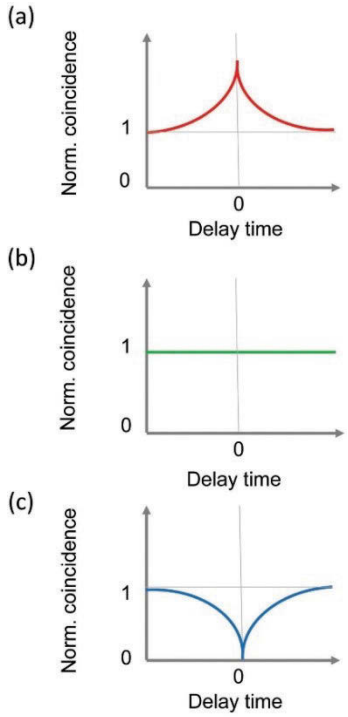

Figure 1.2. *Second-order autocorrelation functions for* ***(a)*** *thermal light,* ***(b)*** *coherent light, and* ***(c)*** *single photon source.*

To this end, we see that second-order photon coherence is one of the most important measurements to determine whether a source has the single photon nature. In an ideal situation, we expect $g^{(2)}(0) = 0$. However, in reality, it is very difficult to achieve this absolute zero value due to three main reasons, namely, (1) contribution of other surrounding emitters, (2) background fluorescence from the substrate or the host materials, and (3) timing jitter of the system. The discussion about these three factors contributing to the non-zero antibunching dip will be presented in the Appendix section (at the end of this thesis). Practically speaking, it is widely accepted that a source shows a $g^{(2)}(0)$ value < 0.5 is considered a single photon emitter [14]. The same judgement criterion is adopted throughout this thesis.

1.2.1.3 **Emission rate and lifetime**

When excited with continuous-wave (CW) laser, a quantum emitter can generate single photons at a maximum rate determined by the inversion of its natural lifetime and the refractive index of the environment [13]:

$$\Gamma_{rad} = \frac{1}{\tau_f} = \frac{4n}{3}\frac{|\mu_{21}|^2}{4\pi\varepsilon_0\hbar}\left(\frac{\omega_{12}}{c}\right)^3 \quad (1.12)$$

where Γ_{rad}, τ_f , n, μ_{12}, ε_0, ω_{12} and c are spontaneous emission rate, lifetime, refractive index of the environment, transition dipole moment between ground and excited states, vacuum permittivity, transition frequency, and the speed of light, respectively.

In vacuum, a two-level quantum emitter in its excited state decays into its ground state due to vacuum fluctuation, arisen from the energy fluctuation at any given point in space following the well-known Heisenberg's time-energy uncertainty principle. The spontaneous fluctuation in electric field at the location of the quantum system induces the decay of the system into its ground state. When the emitter is placed in an environment with higher refractive index than vacuum, it generates single photons at a higher rate, directly proportional to the refractive index value. The rise in the emission rate is due to the increase in the local density of photonic states (LDOPS) – the ability of the environment to support modes of

the electromagnetic field in classical view, or the frequency of vacuum fluctuations from the quantum mechanical approach.

1.2.1.4 Indistinguishability and Fourier-transform limited linewidths

Two photons are considered indistinguishable when they possess the same energy, momentum and polarization. The same energy criterion requires the two photons to have Fourier-transform limited (FT) linewidths – the linewidths achievable when radiative decay is the sole contributor to the broadening. In practice, this natural linewidth value is difficult to achieve for most of the solid-state single photon sources because of dephasing and spectral diffusion process. The dephasing time, T_2, excited state lifetime, T_1, and pure dephasing time, T_2^* of a quantum source are related through the following expression [13]:

$$\frac{1}{T_2} = \frac{1}{2T_1} + \frac{1}{T_2^*} \quad (1.13)$$

It must be noted that pure dephasing is the process in which the system interacts with the phonon bath elastically. With negligible spectral diffusion process, the full-width-at-half-maximum (FWHM) of the zero-phonon line (ZPL) of the emitter reads [13]:

$$\Delta\upsilon = \frac{1}{2\pi T_1} + \frac{1}{\pi T_2^*} \quad (1.14)$$

When the dephasing is negligible, i.e. $T_2^* = \infty$, we arrive at the FT limited linewidth of [13]:

$$\Delta\upsilon_{FT} = \frac{1}{2\pi T_1} \quad (1.15)$$

For most of solid-state quantum emitters, the optical linewidth is several orders of magnitude larger than the natural linewidth value at room temperature. Therefore, the cryogenic temperature is needed to minimize the effect of dephasing into the phonon bath. In addition, the effort also needs to be taken to eliminate spectral diffusion, a broadening mechanism that is independent of temperature. It is widely

accepted that spectral diffusion in condensed-matter systems is mainly caused by trapped charges in the lattice inducing random Stark shifts [15].

Regarding application of indistinguishable photons, two-photon quantum interference is demonstrated when two indistinguishable photons hit a perfectly semi-transparent beamsplitter from its two sides that result in a "bunching" behavior of the two photons, i.e., they output on the same side of the beamsplitter. This experiment is also called Hong-Ou-Mandel (HOM) test [16], and the output photon pair can be used as a quantum bit (qubit) for quantum information processing (QIP).

1.2.2 Types of Single Photon Sources

In this section, we will discuss a wide spectrum of different quantum light sources, including atoms, trapped ions, molecules, quantum dots (QDs), defects in carbon nanotubes (CNTs), defect-based color centers in 3D bulk crystals as well as in 2D domains. **Figure 1.3** summarizes schematics of the host materials along with their embedded quantum emitters. For a detailed discussion on solid-state quantum emitters, the readers are advised to refer to Ref [17].

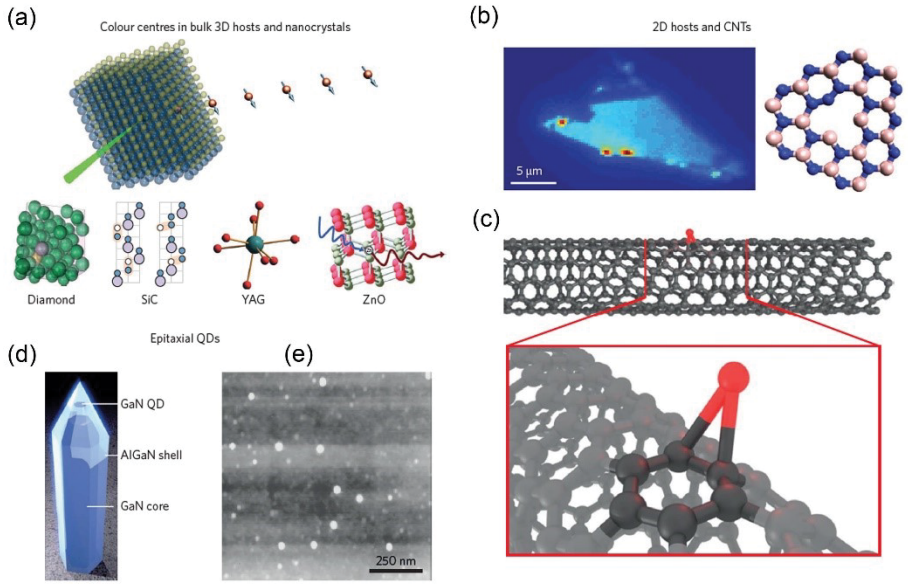

Figure 1.3. Typical solid-state quantum systems summarized in this thesis. **(a)** Defect centers in 3D bulk and nanocrystals, with host materials including diamond, silicon carbide, rare-earth and zinc oxide. **(b)** Quantum emitters in 2D

hosts, namely tungsten diselenide (WSe_2) and hBN. **(c)** Defect-based single photon source in CNTs. **(d)** Nitride quantum dots embedded in a waveguide for emission enhancement. **(e)** Epitaxial InAs QDs. The figure is reproduced from Ref [17], published by Nature Publishing Group.

1.2.2.1 Atoms and trapped ions

Atoms and ions are among two of the earliest classes of quantum emitters that were employed in quantum experimentation. Many fundamental quantum physics demonstrations such as squeezed atomic states [18], quantum Rabi oscillation [19], "Schrödinger Cat" superposition states [20], generation of Einstein-Podolsky-Rosen (EPR) photon pairs [21], multiparticle entanglement [22], and violation of Bell's inequality [23] are indeed conducted with atoms and ions. Thanks to these ground-breaking experiments on quantum control of atoms and ions, Serge Haroche and David J. Wineland won the Nobel Prize in Physics in 2012.

In a typical experiment, a beam of atoms are captured, cooled and magneto-optically trapped (MOT) inside a high vacuum chamber [24]. As the MOT is turned off, the atoms fall freely under gravity through a high Q cavity. It is crucial that only one atomic emitter pass the cavity at a time, and the atom is resonantly excited by the laser pump. The high Q cavity enables a strong coupling between the atom and the single cavity-mode. A single photon is repeatedly exchanged between the atom and the emitter for many cycles before it escapes the cavity. For the case of single ions, an individual ion is magneto-optically trapped and optically investigated, and hence minimizing the chances of exciting multiple emitters at a time.

The main advantage of atoms and ions as quantum emitters is that they are all identical, and thus they produce indistinguishable photons at cryogenic temperature. For this reason, atoms and ions are considered as nearly ideal single photon sources [12]. However, manipulation and handling these classes of single photon emitters are indeed a daunting task [12]. The instrumentation required for controlling a single qubit is very expensive, and therefore a large-scale architecture comprised of multiple qubits would require an extremely costly investment.

1.2.2.2 Molecules, quantum dots, perovskite nanocrystals and carbon nanotubes

Fluorescent molecules are arguably the earliest class of solid-state quantum emitters to be investigated thoroughly [25-27]. In general, fluorescent molecules are dispersed in a host matrix that serves to protect the optically active molecules from chemically interacting with substances in the ambient environment. Single molecules have been studied extensively by many research groups due to their ease of manipulation and storage compared to that of atoms and ions. The first observations of photon antibunching in single fluorescent molecules using second-order autocorrelation function set the experimental standards for the field of single photon generation [26, 28-29]. Though embedded in the host materials, the stability of these fluorescence molecules remains one of the biggest weaknesses that hinder their implementation in quantum applications [24].

After the discovery of photon antibunching from single molecules, colloidal and epitaxial quantum dots (QDs) were extensively researched. The quantum emission from QDs is due to their discrete energy levels that are formed by quantum confinement effect, making them considered as atom-like emitters. Non-classical generation of light [30], triggered single photon emission [31] and quantum cascades of photons [32] were demonstrated by several research groups. Colloidal QDs, however, suffer from spectral intermittency, or in other words, spectral blinking as a result of the non-radiative Auger recombination [33]. On the other hand, research on epitaxial QDs has gained tremendous momentum thanks to their high stability, high brightness, the absence of blinking and minor spectral diffusion. Among these semiconductor QDs, InAs/GaAs QDs have emerged as an all-around single photon emission performance [31, 34-35]. Under resonant excitation, a very high single photon purity of 99 % and photon indistinguishability of > 98 % have been reported [36].

Unlike the two aforementioned zero-dimensional (0D) and 3D hosts, carbon nanotubes - a one-dimensional material - widely studied for their superior mechanical properties, have been proven recently to show single photon emission

- as a result of the bound-exciton states [37-39]. Though it is interesting to study their optical properties at the fundamental levels, these emitters, however, are relatively dim and require cryogenic temperatures to generate non-classical light. At room temperature, the thermal energy is significantly higher than the trap potential, enabling the thermal ionization process to take place, diminishing the probability of generating single photons.

With rapid progress in chemical synthesis, a recent class of single photon emitters has been introduced – semiconductor perovskite nanocrystals (NCs) [40-41]. Semiconductor perovskites can be described as ABX_3, where A is an organic or inorganic cation, B is a metal cation and X is a halide anion. The quantum emission from perovskite NCs arises from the quantum confinement effect where the crystal sizes are smaller than the exciton Bohr radius, similar to the case of semiconductor quantum dots. Likewise, the perovskite NCs are highly prone to spectral blinking owing to the non-radiative Auger recombination pathway. Research on improvement of this detrimental effect is underway.

1.2.2.3 Point-defect centers in wide-bandgap semiconductors

Another class of single photon source is optically active defect centers in wide-bandgap semiconductors such as diamond, silicon carbide, rare-earth crystals and carbon nanotubes. These centers are point-defects in the crystal lattice that introduce new, discrete energy levels within the bandgap of the materials. Thanks to the large energy gaps between the defect's energy levels and the conduction band or valence band, the systems are energetically isolated from the host materials, and hence they are optically stable even under ambient conditions. This section briefly highlights the optical properties of these point-defect centers.

1.2.2.3.1 Color centers in diamond

Color centers in diamond have been attracting a great deal of research focus during the last several decades. These color centers are, in general, stable under room temperature, and produce single photon emission at ambient condition owing superb protection from the diamond lattice. Among over 500 hundred optically

active defect centers in diamond reported to date [42], the negatively charged nitrogen-vacancy center (NV^-), a substitutional nitrogen atom adjacent to a vacancy in the diamond lattice, has garnered most of the scientific attention [43]. Thanks to the C_{3v} defect symmetry, the center possesses the unique electronic structures with triplet ground and excited states, and singlet ground and excited states [44]. The triplet ground state of the center has a paramagnetic behavior and can be employed to perform optically detected magnetic resonance (ODMR) [45]. Negatively charged NV centers have been used to demonstrate a range of exotic physical capabilities including: detection of weak electric field [46], an elementary charge [47] and a single electron spin [48], temperature sensing [49], nanoscale magnetometry [50], nanoscale nuclear magnetic resonance (NMR) [51-52], a quantum register [53]. One of the main weakness of NV^- center is, however, its small photon contribution into the ZPL. Attempts towards coupling the center to optical cavities are underway, showing a promise to mitigate this issue [54-56]. An alternative approach is to find different color centers with the same ODMR capabilities like NV^- does. The second drawback of the NV^- center lies at its high spectral diffusion owing to its permanent dipole moments.

Another well-studied point-defect system is the negatively charged silicon vacancy center (SiV^-). The system comprises of an institutional silicon atom with two adjacent vacancies and has a D_{3d} symmetry. The SiV^- color center shows a high photon contribution into the ZPL of up to 80 %, and is very bright with some cases reportedly exceeding 4 Mcounts/sec for nanodiamonds grown on Iridium substrates [57]. It must be noted that the reproducibility of this type of samples is still under debate as no other research group manages to repeat such results to date. Due to its inversion symmetry, the center is immune to first-order Stark effect, and thus it is not susceptible to spectral diffusion [58]. Recently, a great deal of research has been dedicated to creating identical SiV- single photon emitters for two-photon quantum interference experiments [58-59]. Coherent quantum control has also been demonstrated on this system [60-61], showing a promise for its future use in quantum technologies. The effort to deterministically position

individual centers as well as enhance its brightness on non-metal substrates is underway [59, 62].

1.2.2.3.2 Color centers in silicon carbide

Silicon carbide (SiC) is another wide-bandgap semiconductor that hosts several different color centers to date. As silicon carbide is a well-established material in the semiconductor industry, it is very tempting to integrate quantum emitters into on-chip photonic circuits. Recently, color centers in silicon carbide with high brightness at room temperature have been reported [63-65]. A tentative defect structure has been suggested to be $C_{Si}V_C$ in a recent report [63]. This center is bright, however, not photo-stable. In a recent demonstration, ODMR is observed on the T_{V2} center in 4H-SiC at room temperature, making the defect center a promising platform for quantum sensing and quantum communication [66].

1.2.2.3.3 Defect centers in zinc oxide

Zinc oxide (ZnO) is 3.4 eV bandgap II-VI semiconductor material which offers an extra degree of control over embedded single photon emitters, namely, piezoelectricity and spintronics. The mature growth processes of ZnO is another compelling point for this material. Single photon emitters in ZnO nanoparticles and films have been reported by several research groups [67-69]. The origin of this defect center, however, has been a subject of debate [17]. Another obstacle for employment of this defect center in more complex quantum experiments is its blinking and photo-instability. These intrinsic issues have to be resolved before it is considered as a promising platform for quantum applications.

1.2.2.3.4 Color centers in rare-earth crystals

Much of research attention on color centers from rare-earth crystals, such as yttrium aluminium garnet (YAG) and yttrium orthosilicate (YOS), stems from the well-established fabrication process of these materials in the field of solid-state laser gain media [70-72]. These color centers have been shown to exhibit ODMR [73], and possesses a relatively long spin coherence times [74-76]. Their potential application in quantum communication and quantum sensing is, however,

hindered by their low brightness owing to a long excited state lifetime and multiple competing non-radiative relaxation pathways.

1.2.2.3.5 Defect-based centers in carbon nanotubes

Unlike the aforementioned shallowly-trapped exciton states in CNTs, defect-based quantum emitters arisen from a solidary dopant in CNTs has been reported recently, exhibiting room temperature single photon emission [77]. Interestingly, the emission appears to be in the near infrared (IR) range, making these emitters very compelling for quantum telecommunication. More research effort is expected to focus on improvement of the brightness of these color centers to enable their utilization in quantum information science.

1.2.2.3.6 Quantum emitters in two-dimensional limit

Very recently, defect-pinned localized exciton states in WSe_2 have been reported independently by four research groups [78-82]. Due to a localized defect structure, the created exciton is effectively trapped in a shallow potential well, on the order of tens of millielectronvolts. This shallow trap potential creates discrete energy levels, resulting in single photon emission. Interestingly, while the delocalized excitons in monolayer WSe_2 exhibit valley-dependent circularly polarized emission, defect-bound excitons show linearly polarized emission. At high magnetic fields, however, emitted photons from these excitons return to circular polarization states, similarly observed from the delocalized counterparts. Another interesting point is that these bound-excitons possess very high g factors (a dimensionless quantity characterizing the magnetic moment and gyromagnetic ratio of a particle) of 7 – 10, much larger than that of the delocalized excitons (~5). Recent research efforts have been focused on employing these emitters in electrically-driven single photon generation or deterministic creation of these quantum sources for potential uses in integrated photonic circuits [83-88]. One of the major drawbacks of these quantum emitters, however, is their lack of the room-temperature operation, facilitating optical investigation at ambient conditions.

Color centers in hexagonal boron nitride, an emerging class of quantum emitters, enable operations at ambient conditions with ultrahigh brightness and extreme stability. These quantum emitters are the primary topic of this thesis, and therefore will be discussed in details in the following sessions and chapters.

1.2.3 Two-dimensional Materials Optics

We now turn our attention to the field of 2D materials and briefly highlight their optical properties.

The quest for fabricating 2D materials was a long desired goal as such materials theoretically hold a great promise not only for fundamental experimental physics but also for practical implementations [89]. Vastly deferent from their 3D counterparts, 2D materials were expected to possess optical, electrical and mechanical properties that are unachievable with bulk materials thanks to their quantum confinement effect in one dimension. Two-dimensional materials were initially theorized to be structurally unstable under ambient condition. In 2004, however, Geim and Novoselov made a break-through experimental realization of few-layer of graphene by the Scotch-tape exfoliation method, proving that 2D materials are indeed stable in room temperature condition [90]. As expected, the experimental data matched with theoretical prediction very well, showing the Dirac massless fermions characteristic of carriers in graphene. Following this pioneering demonstration of graphene exfoliation, a wide range of other 2D materials was isolated by the same mechanical exfoliation approach [91]. These materials include transition metal dichacogenides (TMDs), with the chemical formula MX_2, and phosphorene, the semiconductor counterparts of graphene, and hBN, the isoelectric analogous to graphene. While graphene has a zero bandgap, TMDs, phosphorene, and hBN have finite bandgaps, enabling them to exhibit photoluminescence [92]. Owing to the confinement in one dimension, 2D semiconductors such as TMDs behave exotic electronic properties including indirect-to-direct bandgap transition and valleytronics [92-97]. Interestingly, indirect-to-direct bandgap switching has also been demonstrated using applied strain on few-layer TMD flakes [98], opening up possibilities for optomechanical

engineering of TMD-based devices. Valleytronics in TMDs is another gaming-changing characteristic that holds promises to enable quantum information processing thanks to the optically accessible spin control in these 2D semiconductors [99]. Furthermore, by employing chemical treatment, a near-unity quantum yield in MoS_2 has been demonstrated recently [100]. Additionally, they also exhibit some other compelling properties such as layer-dependent piezoelectricity owing to their lack of inversion symmetry [101]. By coupling TMDs to external optical cavities such as photonic crystals [102], microdisks [103], or micropillar [104] strong-coupling exciton-polaritons and ultralow-threshold lasings have been demonstrated.

Phosphorene, or in other words, few-layer black phosphorus, unlike TMDs, has direct bandgap transitions regardless of the number of layers, and layer-dependent emission wavelengths [105-106]. This material also possesses anisotropic optical responses, owing to its in-plane anisotropic chemical structure. Starkly different from TMDs and phosphorene, hBN has a much larger bandgap of around 5.9 eV, making them not only a natural insulator but also an attractive candidate for ultraviolet (UV) generation. As hBN is the material of interest in this thesis, a more detailed discuss about its physical and optical properties will appear in Sec. 1.5. In overall, by assembling different types of these 2D semiconductors and graphene, it is possible to arrive at a wide range of ultrathin vertical optoelectronic devices that are of great interest for applications such as high-density electronics or wearable optoelectronic equipment [107].

1.2.4 Properties, Synthesis, and Characterization of Hexagonal Boron Nitride

1.2.4.1 Physical properties

Hexagonal boron nitride is an isoelectric analog to graphene with a honeycomb lattice structures where boron and nitrogen atoms alternately bond to one another. While the nature of the B-N bond within a single layer of hBN is both covalent and ionic, the out-of-plane interaction between the layers is mostly van der Waals, with a small ionic contribution. Unlike the stacking sequence of graphene which

is the AB configuration, the stacking order of hBN layers is the "lip-lip" or AA' sequence, i.e., the boron atom at the bottom layer is perfectly aligned with the nitrogen atom at the top layer [108]. **Fig. 1.4** shows a schematic of a three-layer hBN flake with its AA' stacking order. Due to this structural configuration, the in-plane lattice constant, a, is 0.25 nm, and the out-of-plane lattice constant, c, is ~0.333 nm [109]. Moreover, owing to this layered structure, it is possible to exfoliate into hBN few-layer or monolayer from bulk crystals by either tape-exfoliation [91], ball-milling [110], molten hydroxide or solvent exfoliation [111]. It must be noted that isolation of monolayer or few-layer hBN using any top-down method is more difficult than that from graphene due to the stronger AA' interaction.

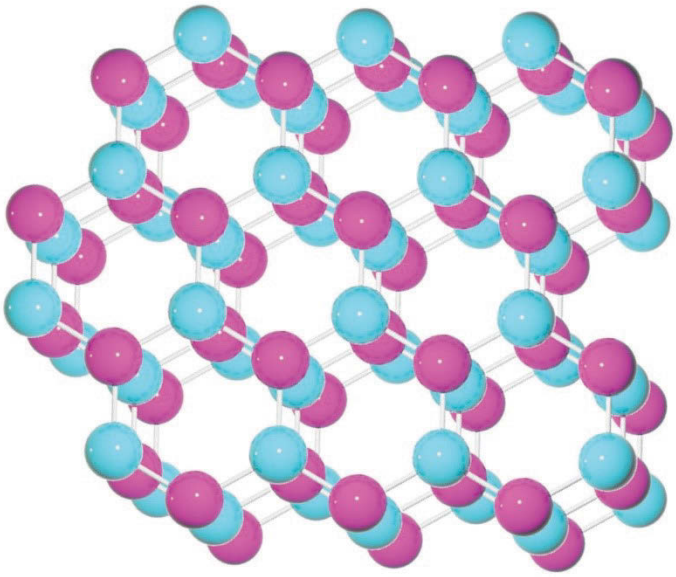

Figure 1.4. *Schematic of a three-layer hBN flake showing the "lip-lip" (AA') stacking order.*

With a bandgap of ~5.9 eV, hBN does not show any absorption in the visible and near IR, rendering its powder form a white color [112-113]. This wide bandgap value also makes the material a good insulator for other 2D materials including graphene, TMDs, and phosphorene. Due to the lower defect density, hBN has been shown to significantly boost the carrier mobility in graphene and 2D semiconductors [114]. Moreover, as hBN possesses a moderate dielectric, it serves

as an excellent tunneling barrier [115] for various types of optoelectronic devices at few-layers limit [83-84].

Hexagonal boron nitride is a superb thermal conductor, with a conductivity ~ 300 – 2000 $Wm^{-1}K^{-1}$ [116], despite being an electric insulator. The high thermal conductivity values are due to its highly energetic in-plane phonon modes arisen from the strong B-N bonds as well as the low atomic numbers of boron and nitrogen. Interestingly, the conductivity in monolayer hBN is higher than that from few-layered ones owing to the decreased interlayer phonon scattering.

Mechanical properties of hBN are other compelling points of this material. Monolayer hBN is predicted to be one of the strongest materials, similar to that of single layer of graphene. The in-plane stiffness values of a single layer hBN were predicted to be ~267 N m^{-1}, slightly lower than that of individual graphene sheet at 335 N m^{-1} [117].

1.2.4.2 **Optical properties**

Though hBN has been used as a dry lubricant for industrial purposes, its optical properties gained an accelerating research momentum only after the first report of direct-bandgap emission from bulk hBN in 2004 by Kenji Watanabe et al. [118]. In their report, UV lasings were also demonstrated by accelerated electron excitation, making hBN an emerging material for nanophonics in the UV spectral regime. The same research group further transformed the UV emission of hBN into a handheld far UV device for the first time [119], opening new possibilities for employing hBN as the active material in UV-related photonic systems. Hexagonal boron nitride, thought for more than a decade as a direct-bandgap material, has recently demonstrated to be an indirect-bandgap material following the report by Cassabois et al. in 2016 [120]. The report has spurred much of debates on whether hBN is indeed an indirect bandgap material as there are several questions on its excitonic spectra that remains unanswered.

In addition to its band-edge emission, impurities-driven bound-excitons recombination give rise to lower-energy photons of ~4 eV as shown in previous reports [121-122]. Although extended defects such as stacking faults [123] have

been proposed as the cause of this lower-energy emission, the origin of these impurities, however, remains largely speculative to date. Recent research has also been devoted to investigating the phonon-exciton coupling in hBN to further understand its complex optical properties [124-125].

Another exotic property of hBN that has been uncovered recently is its natural hyperbolicity [126] arisen from the difference between the in-plane (positive) and out-of-plane (negative) refractive index [127]. When being excited with frequencies in between the longitudinal optical (LO) and transverse optical (TO) modes, or in other words the "Reststrahlen" band, surface phonon-polariton (SPhP) modes are launched within the hBN crystals [128]. By employing SPhP modes, superlensing as well as sub-diffraction guiding and focusing of light have been realized experimentally [129-130]. These demonstrations open up exciting avenues for maneuvering infrared and terahertz light deep below the diffraction-limit [131].

1.2.4.3 **Defects in hexagonal boron nitride**

Complex defects such as Stone-Wales pentagon-heptagon rings on hBN are not thermodynamically stable due to the necessity of forming B-B or N-N bonds [132-136]. This property is in stark contrast to graphene or CNTs where Stone-Wales defects are very common. More favorable defects in hBN are vacancy-based or point-based defects. The former were observed with TEM mostly in well-defined triangular shapes, with a monovacancy of boron or nitrogen being the smallest configuration. These monovancy defects were controllably created by the use of high energy electrons in a TEM to deterministically knock the boron or nitrogen atoms off the hBN lattice [137-139]. It was calculated that the knock-on energy of a boron atom (74 keV) is slightly lower than that of a nitrogen atom (84 keV) [140], and hence the more dominating observance of boron vacancies. The existing of defects in hBN lattice induces changes in its thermal [141-143], electronic [144-147], magnetic [148] and optical properties [122, 149] as demonstrated in previous studies.

1.2.4.4 Synthesis of hexagonal boron nitride

1.2.4.4.1 Bulk crystals

High-quality bulk hexagonal boron nitride crystals are commonly synthesized by the high-temperature high pressure method (HTHP) [118, 150]. In a typical synthesis, a BN powder is heated at high temperature (> 2000°C) under inert gas environment to minimize residual oxygen. The powder is then compressed along with an alkali-metal BN solvent (e.g., $Ba_3B_2N_4$) in a molybdenum (Mo) chamber at 4 -5 GPa pressure and 1500 – 1650°C temperature for tens of hours. The Mo chamber is dissolved using hot aqua regia, and the hBN crystals are rinsed with water and collected. The harvested hBN crystals are colorless, implying the low-level of impurities, grain boundaries and extended defects embedded inside the crystal lattice. To date, the highest quality hBN crystals have been synthesized by Taniguchi et al. at the National Institute for Materials Science (NIMS). Samples fabricated in this group are widely used by the 2D material research community around the world owing to their superior purity and crystallinity.

1.2.4.4.2 Few-layer hBN flakes

Few-layer hexagonal boron nitride flakes can be synthesized either by top-down or bottom-up methods as will be discussed in the following sections.

For top-down approaches, bulk hBN is used as the starting material. In the first scheme, also known as the “Scotch tape method,” bulk hBN crystals of millimeter-sized are placed on a sticky tape and mechanically exfoliated by repeatedly peeling and attaching the two halves of the tape until the desired size and thickness are achieved. In the next step, the as-prepared substrate with hBN flakes is oxidized at ~400°C in air or oxygen to remove the residual adhesive. This tape exfoliated method has the advantage of convenience and ease of handling as well as low-defect density that is required for electronic implementations. It, however, suffers from the random distribution in dimensions of the exfoliated flakes and lack of scalability. To date, this tape-based exfoliated is primarily used in laboratories to understand the electro.

The second method employs the ball-milling process in which the hBN crystals are first well-grounded into micron-sized powder. The shear forces from the collision of oxide beads cause the hBN particles to be exfoliated. Though more scalable than the Scotch tape approach, this technique introduces a significantly higher defect density than that of tape exfoliation.

Similar to the second approach, the third method relies on sonication force and a solvent with appropriate surface energy to exfoliate the parent flakes into thinner ones. Coleman and co-workers reported this solvent-based direct exfoliation on a wide range of 2D materials including hBN, MoS_2, WS_2, $MoSe_2$ just to name a few [151]. Similarly, the same group also demonstrated surfactant-assisted aqueous exfoliation of these 2D materials [152]. Zhou et al. further improved the method by employing the mixed-solvent strategy, resulting in better thinner flakes and more stable solution [153]. For more detailed discussion, the readers may refer to the following topical review [111]. In general, this approach is inexpensive, facile and scalable and it provides the exfoliated materials with lower defect density than the second method. However, one of the drawbacks of this technique is its lack of control over the number of layers of the resultant hBN flakes. Therefore, more effort has to be dedicated to resolving such issue before solvent-based exfoliation can be employed for industrial applications.

On the contrary to top-down approaches, bottom-up approaches, which are chemical vapor deposition (CVD) techniques, offers a clear advantage of the high degree of control over thicknesses of the grown-hBN flakes [154]. In a typical CVD synthesis, single-crystalline metal facets such as Ru(001), Ni(111), Pd(111) and Pt(111) are used as substrates, and borazine is employed as a precursor [155-158]. Before the deposition, the substrates are cleaned with argon sputtering and heated at 800°C to remove surface contaminants. Borazine is subsequently flown into the chamber, thermally decomposed and deposited onto the substrate at 700 – 800°C. A monolayer of hBN is gradually formed on the surface of the metal substrate. Subsequent deposition of additional layers is strongly hindered due to the robust reduction reaction on the hBN surface. It is for this reason that makes this metal substrate based growth a favorable technique to get a monolayer hBN.

Upon having the grown hBN monolayer atop the substrate, the resultant substrate is spin-coated with a carrier polymer such as poly(methyl methacrylate) (PMMA) and etched away with an appropriate etchant, leaving behind the floated polymeric carrier and the monolayer hBN. The polymer film is then transferred onto a target substrate and washed off with organic solvents. The hBN monolayer is not ready for further fabrication or characterization. One of the main drawbacks of the CVD techniques is the low-quality of the resultant hBN film, namely, high amount of impurities and grain boundaries. On the other hand, the techniques have recently offered a route to growing of in-plane heterostructures between hBN and other 2D materials such as graphene [159].

1.2.4.5 Characterization of hexagonal boron nitride flakes

Among the techniques for characterizing hBN nanostructures, atomic force microscopy (AFM) stands out as a direct, convenient pathway to unveil the thickness and topological information of hBN structures. By using AFM, one can directly determine the thickness of an hBN flake as well as it surface roughness and other topological data. Another non-destructive technique is optical microscope (OM) that relies on the contrast difference between hBN flakes and the substrate [160-161]. For instance, Gorbachev and co-workers reported that an 80-nm thick SiO_2 on silicon substrate enabled the maximal contrast difference between hBN flakes and the substrate. Although the OM approach does not yield a highly accurate number of layers on an examined hBN flake, it is advantageous to other characterization techniques regarding speed and convenience. It can also be used as a quick check before another more accurate technique is employed for further in-depth characterization. Due to the hBN structure comprised of low atomic number elements, namely boron, and nitrogen, it supports strong optical phonon modes such as the in-plane stretching E_{2g} mode. As the number of layers increases, the interlayer van der Waals interactions rise, and hence the E_{2g} phonon mode is slightly reduced in frequency. By exploiting this characteristic, the number of layers in hBN flakes can be determined using Raman spectroscopy with high fidelity [160, 162]. Electron microscopy is another powerful characterization tool with the two main sub-divisions, that are scanning electron microscopy (SEM)

and transmission electron microscopy (TEM). While the use of SEM primarily remains at the topological level, TEM gives much deeper insights on structural level of hBN crystals. A common technique to determine layer number in hBN with TEM is to simply count the number of straight lines at the folded areas [109]. Structural information such as crystallinity, phase or lattice rotational is easily obtained with selected area electron diffraction (SAED) – a capability from TEM instrument. Alternatively, the crystal quality of hBN is determined by means of deep UV excitation. A high-quality crystal usually comprised of a set of well-defined PL peaks, including the strong band-edge excitonic emission arisen with the energy ~ 5.7 eV [118, 163]. Compositional characterization, on the other hand, is achievable by using energy dispersive X-ray (EDX) or electron energy loss spectroscopy (EELS), commonly equipped as a complementary feature in SEM and TEM. These chemical analysis techniques exploit the characteristic X-rays or energy loss of electrons from different elements to determine their composition quantitatively.

1.2.5 Laser Scanning Fluorescence Confocal Microscopy

1.2.5.1 Basics of wide-field and scanning confocal fluorescence microscopy

Wide-field fluorescence microscopy is one of the most basic optical microscopy techniques that has been used across disciplines such as biology, chemistry or solid state physics. In a basic setup for bio-imaging, an excitation source is focused through an objective with a chosen numerical aperture (NA) onto fluorescent dyes to excite them optically. The excitation volume is typically very large for this technique. Shortly after being excited, the molecules generates weak fluorescence light that is mixed with the strong reflected excitation light. The excitation pump is spectrally rejected by an interference filter, called dichroic beamsplitter, rendering the pure fluorescence photons detectable by an observer or a photodetector. Using wide-field fluorescence microscopy, it is possible to capture a live video of fluorescence dyes on the sample substrate as all the molecules

within the field of view are optically excited at once. This technique is, therefore, widely used in the field of biology and the related discipline.

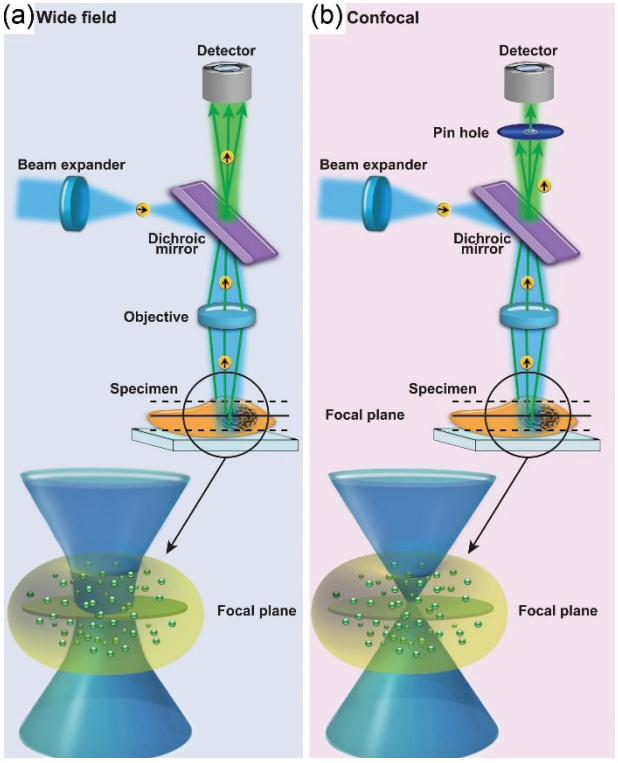

Figure 1.5. *Comparison between* ***(a)*** *wide-field and* ***(b)*** *confocal microscopy. Reproduced with permission from Ishikawa-Ankerhold et al., "Advanced Fluorescence Microscopy Techniques—Frap, Flip, Flap, Fret, and Flim.", 2012, 17, 4047; published by MDPI.*

Although this technique has an advantage of fast imaging, it suffers from a huge amount of background due to its large depth of field and non-selective excitation/collection, or in other words, non-confocality. To circumvent this shortcoming, confocal fluorescence microscopy is invented with the introduction of a pinhole at the detection path to significantly eliminate unwanted background fluorescence (**Fig. 1.5.**). In this scenario, the pinhole serves as a three-dimensional spatial filter that rejects fluorescence from all the points, except the focused point. With the aid of a two-dimensional steering mirror or an XYZ piezo sample stage, the excitation and collection spot is scanned over the area of interest. This working principle is why it is termed scanning fluorescence confocal microscopy. As there

is always only point being focused at a time, it takes a few orders of magnitude longer than that from wide-field fluorescence microscopy to complete a scan. The longer acquisition time is a direct trade-off to the very low fluorescence background that enables a so-called diffraction limited resolution – a term first coined by German physicist Ernst Abbe in 1873. The diffraction limited spot size, d, is dictated by the following equation:

$$d = 0.61\frac{\lambda}{NA} \quad (1.11)$$

where λ is the excitation wavelength; NA = n*sinθ with n is the environment refractive index, and θ is the solid angle of the focused laser beam. In our typical experiments, λ = 532 nm and NA = 0.9, and hence d ~ 360 nm. For a more detailed discussion on fluorescence imaging techniques, the readers are advised to refer to reference [164].

1.2.5.2 Typical laser scanning confocal fluorescence setup used in this thesis

The typical confocal fluorescence setup used in this thesis is shown in **Fig. 1.5**. The basic components of the setup is similar to the scanning confocal setup aforementioned, with some following modifications and add-on features. First, in our setup, instead of using a pinhole we employ the use of a graded-index multimode fiber (Thorlabs Inc.) with a core size of 62.5 μm to collect fluorescence light. The use of multimode fiber for collection enables us to fiber-couple light into either the spectrometer (Princeton Instrument Inc.) equipped with thermoelectrically-cooled visible and IR CCD cameras (Andor Inc.) or the single photon counting avalanche photodiode (SPCAPD, Excelitas Technologies Inc.). While the spectrometer allows for capturing the fluorescence spectra, the SPCADP permits not only counting single photons but also obtaining lifetime and photon second order autocorrelation measurements on a chosen quantum emitter through a dual-channel time tagger (PicoHarp 300, Picoquant Inc.). Second, polarization optics are also implemented to control the polarization of excitation and collection fluorescence light. Specifically, a half-wave plate is inserted in the excitation path

to manipulate the linear polarization state of the laser while a linear polarizer is placed at the collection side to determine the polarization of the collected fluorescence. In addition to these two modifications, for cryogenic PL measurement, a high-vacuum cryostat that is thermally cooled with cryogens, namely liquid nitrogen or liquid helium is used to control the sample temperature. In this setup configuration, the objective lens is hosted inside the cryo-chamber to minimize the distortion caused by the thin quartz window. The sample position is manipulated by using the vacuum-compatible XYZ piezo stage (Attocube Inc.). Scanning over the sample surface is established by using a fast steering mirror in the 4-f configuration, as shown in **Fig. 1.6**. The focal plane is controlled with a Z piezo holding the objective lens (Piezosystem Jena Inc.). Most of the hardware is controlled through an NI DAQ board (USB-6259 BNC, National Instruments Inc.) by a computer with LabView programming language.

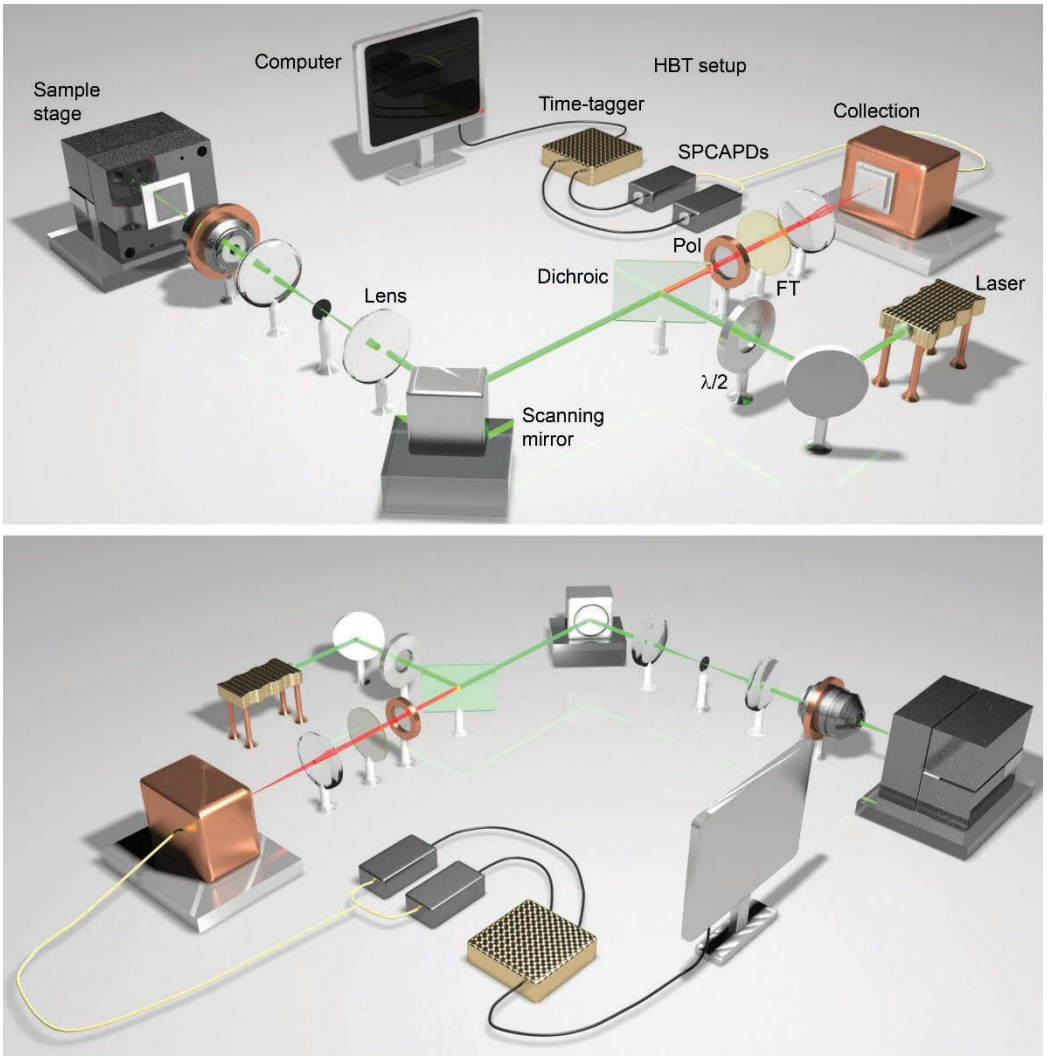

Figure 1.6. *Schematic of a typical scanning confocal fluorescence setup used in this work. HBT: Hanbury-Brown and Twiss; BS: beamsplitter; FT: band-pass or long-pass filters; λ/2: half waveplate; Pol: linear polarizer; SPCAPD: single photon counting avalanche photodiode. The spectrometer is not displayed here for simplicity of the setup. The top and bottom panel showing different viewing angles on the same setup.*

2 Quantum Emission from Hexagonal Boron Nitride Monolayers

This chapter presents the study of the first room-temperature defect centers embedded in a layered material, hexagonal boron nitride. In this chapter, the original idea of the project was conceived by Igor Aharonovich and Trong Toan Tran. Except for TEM characterization, all experimental work was done by Trong Toan Tran, with some assistance from Kerem Bray. The TEM characterization and analysis was conducted by Jinghua Fang. Data analysis and interpretation were carried out by Trong Toan Tran, Kerem Bray, Igor Aharonovich and Milos Toth. All simulation work was contributed by Michael J. Ford. The manuscript was written with contributions from all the authors.

2.1 Abstract

Artificial atomic systems in solids are widely considered the leading physical system for a variety of quantum technologies, including quantum communications, computing and metrology [165-166]. Room temperature quantum emitters have, however, thus far been observed only in wide bandgap semiconductors such as diamond [167] and silicon carbide [63], nanocrystal quantum dots[30, 168-169], and most recently carbon nanotubes [77]. Single photon emission from two-dimensional materials has been reported [170-173], but only at cryogenic temperatures. Here we demonstrate room temperature, polarized and ultrabright single photon emission from a color center in two-dimensional multilayer hexagonal boron nitride. Density Functional Theory (DFT) calculations indicate that vacancy-related centers are a likely source of the emission. Our results demonstrate the unprecedented potential of van der Waals crystals for large-scale nanophotonics and quantum information processing.

2.2 Introduction

Atomically thin van der Waals crystals have recently enabled new scientific and technological breakthroughs across a variety of disciplines in materials science,

nanophotonics and physics [91, 107]. These monolayers were utilized to realize phonon polaritons,[126, 128] super-resolution imaging, spin valley transport [95-96] and lasing [102]. Yet, an aspiring goal is to employ these materials in the quantum regime, where the photon emission can be non-classical, thereby enabling a major paradigm shift towards applications in quantum information processing [166].

In this work, we identify and study single photon emission from localized defects in monolayer hBN and multilayer hBN. The emitters are optically active at room temperature, thereby heralding the transformational application of 2D materials in quantum information applications with the potential to achieve scalable nanophotonic circuits on a single chip.

2.3 Methods

2.3.1 Materials

Monolayer and multilayer hBN samples were obtained from Graphene Supermarket™. The monolayer hBN sample was grown on a copper foil and transferred onto a silicon substrate using the following method. The sample was first spin-coated with 100 μL of 2% PMMA in chlorobenzene at 2000 rpm for 2 min. It was then dipped in 68% HNO_3 solution for 2 min to dissolve the copper foil substrate completely. The resultant membranes were placed on a silicon substrate and heated to 80°C under low acetone flow. The acetone flow was stopped once the PMMA was removed (~ 15 min). The sample was then rinsed thoroughly with copious amounts of acetone to remove any remaining contamination on the surface. Finally, the sample was dried under flowing N_2.

The multilayer hBN sample was annealed in argon to activate the color centers and to desorb surface contaminants. We tried a range of different annealing temperatures, and find that 850°C yields maximum fluorescence intensity. In a typical thermal treatment, a solution comprised of 20 μL of multilayer hBN in ethanol was drop-cast onto the silicon substrate and dried under ambient conditions. The sample was then placed in a high-temperature tube furnace

(Linberg/Blue M™), and annealed at 850°C for 30 min, under 1 Torr of argon (to prevent oxidation). The sample was then cooled to room-temperature overnight under 1 Torr of argon.

2.3.2 Structural and elemental characterization

SEM and EDX measurements were performed using a field emission gun SEM (Zeiss Supra 55VP FEG™) and a 20 mm^2 EDX (Oxford X-Max™) silicon drift detector. TEM and SAED analysis were conducted by using a Tecnai G2 TEM™) operating at 200 kV accelerating voltage. Raman spectroscopy was carried out using a Renishaw inVia Raman™ microscope.

2.3.3 Photoluminescence analysis

A continuous wave 532 nm laser (Gem 532™), Laser Quantum Ltd.) was used for excitation and scanning. The laser was directed through a Glan-Taylor polarizer (Thorlabs Inc.) and a half waveplate and focused onto the sample using a high numerical aperture (NA = 0.9, Nikon) objective lens. Scanning was performed either using an X-Y piezo scanning mirror (FSM-300™) or an X-Y-Z nanocube system (PI instruments). The collected light was filtered using a 532 nm dichroic mirror (532 nm laser BrightLine™), Semrock Inc.) and an additional long pass filter (Semrock™). The signal was then coupled into a graded index fiber, where the fiber aperture serves as a confocal pinhole. A fiber splitter was used to direct the light into a spectrometer (Acton SpectraPro™, Princeton Instrument Inc.) or two avalanche photodiodes (Excelitas Technologies™) used for single photon counting. Correlation measurements were done using a time-correlated single photon counting module (PicoHarp300™, PicoQuant™). Lifetime measurements were performed using a 510 nm pulsed laser excitation source (PiL051X™, Advanced Laser Diode Systems GmbH) with a 100 ps pulse width and an 80 MHz repetition rate.

Cryogenic PL was done using a Janis ST500™ cryostat. The cryostat is cooled with liquid N_2 and thermally regulated with a gold-plated heating stage. The setup is shown schematically in **Fig. 1.6** from the previous session.

2.3.4 Theoretical calculations

Vienna ab initio simulation package (VASP) [174],[175],[176] calculations were performed using the Generalised Gradient Approximation to the exchange-correlation functional proposed by Perdew, Burke and Ernzerhof [177]. All calculations are spin-polarized and use the projector augmented wave (PAW) pseudopotentials supplied with the VASP code. A plane-wave cutoff of 450 eV was used for all calculations; this is considerably higher than default values for the pseudopotentials used and represents a well-converged calculation.

Pristine single-layer hBN was first geometry optimized using the conventional cell and a 21 x 21 x 1 Monkhurst-Pack reciprocal space grid to an energy tolerance of 0.01 eV. A vacuum spacing of 20 Å was used to separate periodic images of the single layer and to ensure that interaction between these layers is negligible. Relaxation of the lattice vectors using a conjugate gradient approach or by hand plotting the energy as a function of lattice parameter give the same optimized unit cell. The computational conditions are clearly good enough that basis size effects are not important. The optimized lattice parameter is 2.5 Å, with a bond length of 1.447 Å.

2.4 Results and Discussion

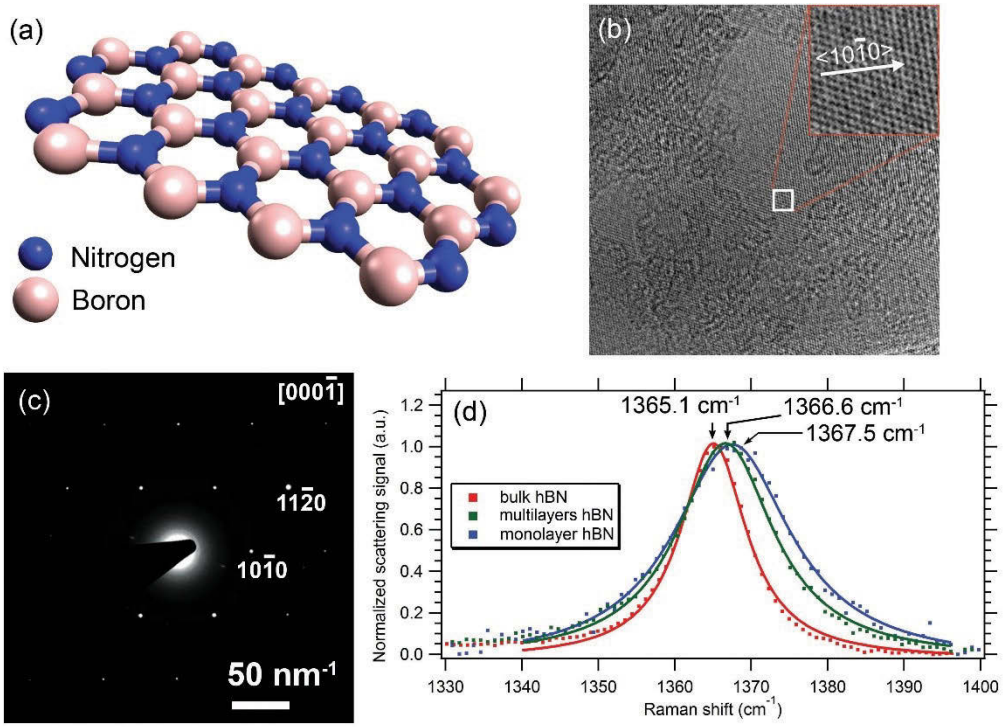

Figure 2.1. *Structural characterization of hBN.* ***(a)*** *Schematic illustration of an hBN monolayer.* ***(b)*** *TEM image of the corner of a single hBN sheet. The inset shows the hBN lattice.* ***(c)*** *A corresponding SAED pattern.* ***(d)*** *Raman scattering spectra of monolayer, multilayer, and bulk hBN (blue, green and red squares, respectively) on a silicon substrate. Solid lines are Lorentzian fits to the experimental data.*

Being a van der Walls crystal, monolayer hBN [162, 178] possesses similar structure to graphene where in-plane bonds are much stronger than out of plane bonds [179],[107]. **Fig. 2.1a** shows the 2D hexagonal lattice of hBN comprised of boron and nitrogen atoms. **Fig. 2.1b** and **Fig. 2.1c** show a transmission electron microscope image of hBN and a corresponding selected area electron diffraction pattern. The SAED pattern exhibits a sixfold symmetry attributed to single crystal hexagonal boron nitride with a [000-1] viewing zone axis.[162],[158],[180] **Fig. 2.1d** shows Raman spectra of an hBN monolayer, multilayer hBN and a bulk hBN reference sample. The Raman shifts are 1367.5 cm^{-1} (FWHM = 18.2 cm^{-1}), 1366.6 cm^{-1}, (FWHM = 15.2 cm^{-1}) and 1365.1 cm^{-1} (FWHM = 10.3 cm^{-1}), consistent with

a prior study [160]. In addition, energy dispersive X-ray (EDX) analysis suggests the existing of boron and nitrogen elements (**Fig. 2.2.**).

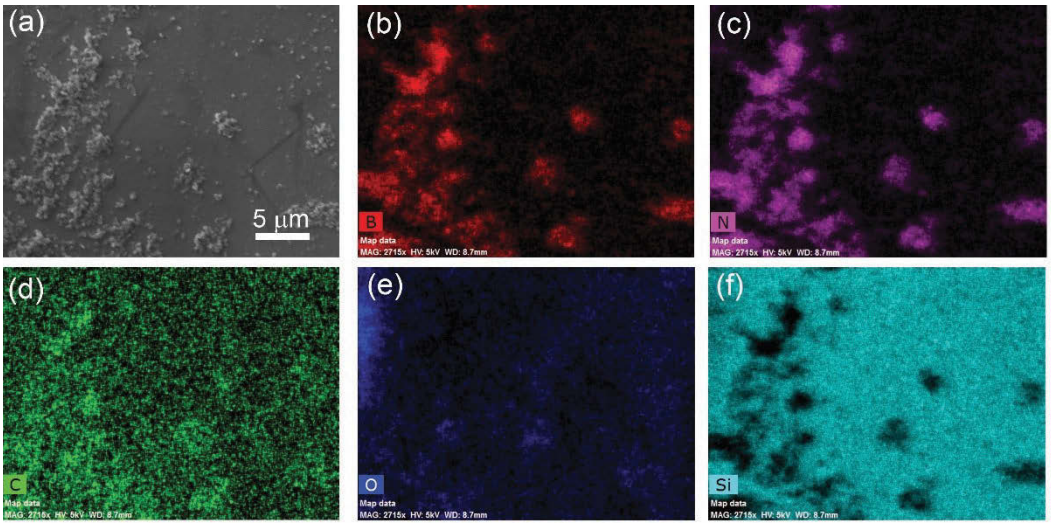

Figure 2.2. *EDX maps of multilayer hBN annealed in argon at 850°C.* ***(a)*** *A representative SEM image of multilayer hBN. Corresponding EDX mappings of boron* ***(b)****, nitrogen* ***(c)****, carbon* ***(d)****, oxygen* ***(e)****, and silicon element* ***(f)****.*

Hexagonal boron nitride has a wide bandgap of nearly 6 eV [92], which is much greater than that of most 2D materials and is expected to host optically active defects that have ground and excited states within the gap. To address such defects, optical measurements were performed using a low energy excitation laser emitting at 532 nm. The use of a sub-bandgap excitation source is key to probing individual defects whilst avoiding excitonic emissions [118].

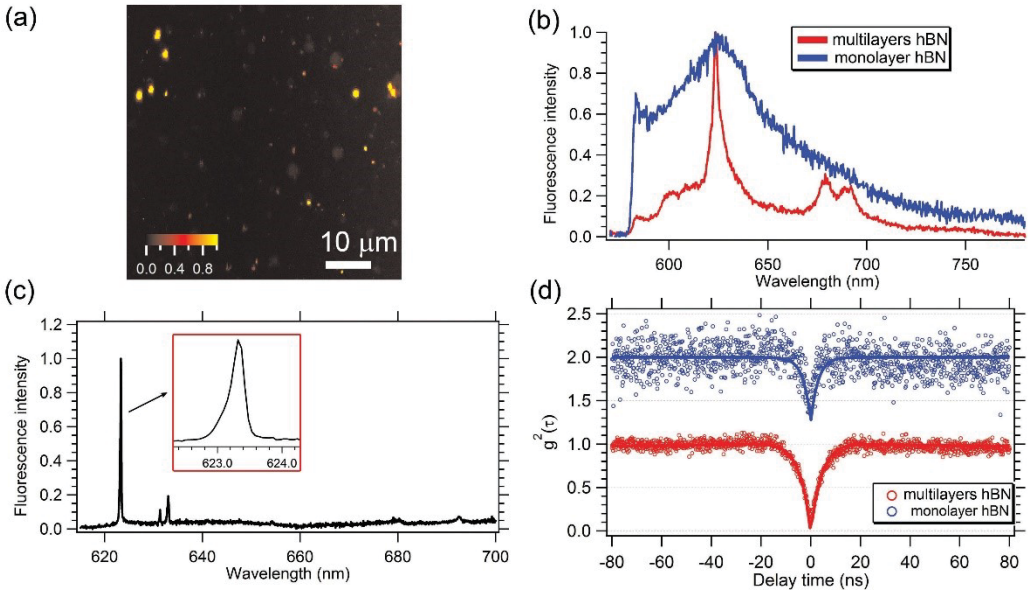

Figure 2.3. *Optical characterization of single photon emitters in hBN.* ***(a)*** *Scanning confocal map of a multilayer hBN sample showing bright luminescent spots that correspond to emission from single defects.* ***(b)*** *Room temperature PL spectra of a defect center in an hBN monolayer (blue trace) and a multilayer hBN (red trace).* ***(c)*** *PL spectrum taken at 77K of a defect center in a multilayer hBN. The inset shows the zero-phonon line.* ***(d)*** *Antibunching curves from an individual defect center in an hBN monolayer (blue, open circles) and a multilayer hBN (red, open circles), corresponding to the spectra shown in* ***(b)****. The* $g^2(\tau)$ *curves were acquired using an excitation power of 300 µW, an acquisition time of 10 sec, and were normalized and offset vertically for clarity. The solid blue and red lines are fits obtained using* ***Eq. 2.1.***

Fig. 2.3a shows a confocal photoluminescence (PL) map recorded at room temperature from multilayer hBN dispersed on a silicon dioxide substrate (see methods). The majority of the bright spots seen in the map are attributed to single defect centers hosted by multilayer hBN. **Fig. 2.3b** shows representative PL spectra recorded from an hBN monolayer and a multilayer hBN. In both cases, a bright emission is detected at ~ 623 nm (1.99 eV), attributed to the zero phonon line (ZPL) of the defect. The emission lines of multilayer hBN are much narrower than those of monolayers, and the emitters in multilayer BN are photostable (as is

discussed below). Spectra from multilayer hBN exhibit a phonon side band (PSB) doublet with well-resolved peaks at 680 nm (1.83 eV) and 693 nm (1.79 eV), respectively. The ZPL is asymmetric, possibly due to interactions with phonons analogous to those observed (at low temperatures) in carbon nanotubes [181]. **Fig. 2.3c** shows a low temperature spectrum of the defect in a multilayer BN (a corresponding spectrum obtained from a monolayer is shown in **Fig. 2.4**).

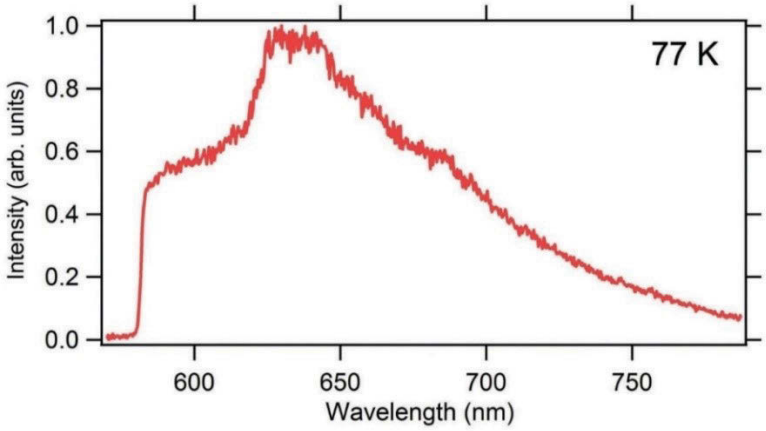

Figure 2.4. *Representative PL spectrum taken from an ensemble of emitters in hBN monolayers at 77 K.*

The ZPL from a multilayer hBN narrows dramatically and has a full width at half maximum (FWHM) of 0.25 nm at 77 K, limited by the width of the excitation laser line (shown in **Fig. 2.5**) and the resolution of the spectrometer. The two adjacent lines seen at 631 and 633 nm were not observed consistently across the sample and are attributed to the presence of other defects throughout the sample.

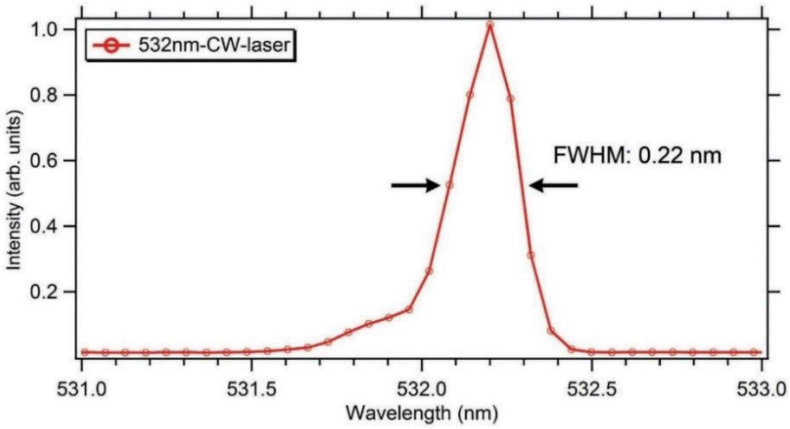

Figure 2.5. *Line profile of the 532 nm CW laser used as the excitation source in this study.*

To demonstrate single photon emission using the same luminescence signals, we recorded second order autocorrelation functions $g^2(\tau)$ using a Hanbury Brown and Twiss (HBT) interferometry setup. For a true single photon source, the $g^2(\tau)$ curve dips below 0.5 at zero delay time ($\tau = 0$).[12] Representative antibunching curves of the defect center in monolayer hBN (blue, open circles) and multilayer hBN (red, open circles) are shown in **Fig. 2.3d** (additional $g^2(\tau)$ curves acquired from other emitters and a $g^2(0)$ histogram are shown in **Fig. 2.6** and **2.7**).

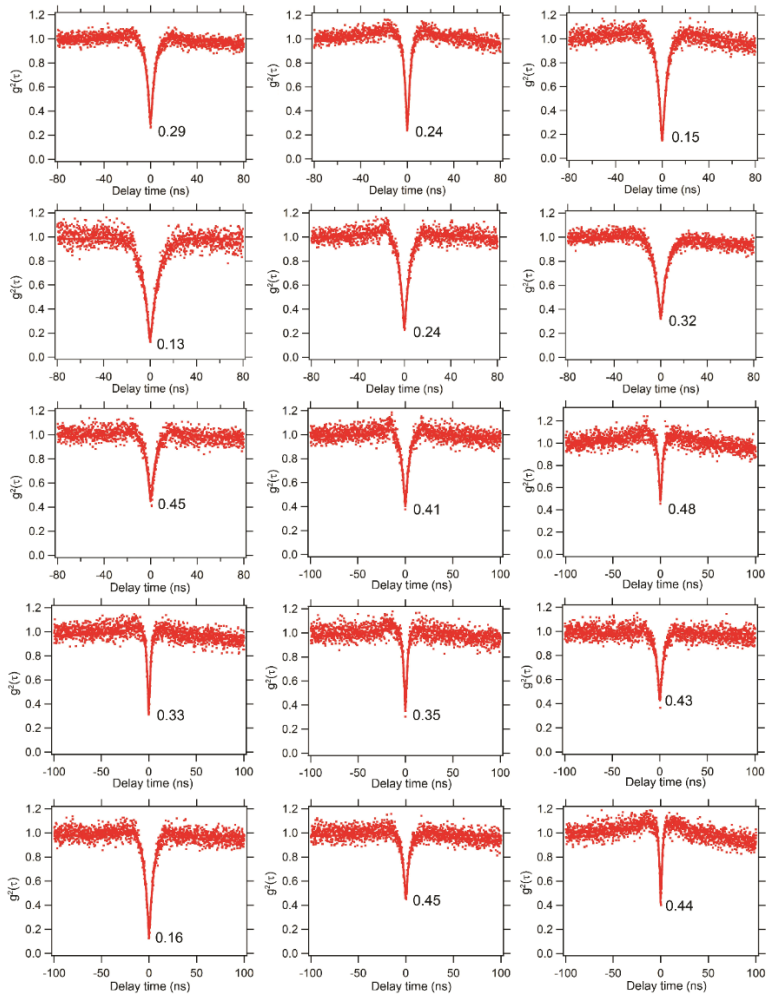

Figure 2.6. *Second-order autocorrelation functions of 15 SPEs found at random in multilayer hBN. The $g^2(0)$ value is shown for each emitter. Each curve was acquired for 10 min using a 300 μW, 532 nm CW laser as the excitation source.*

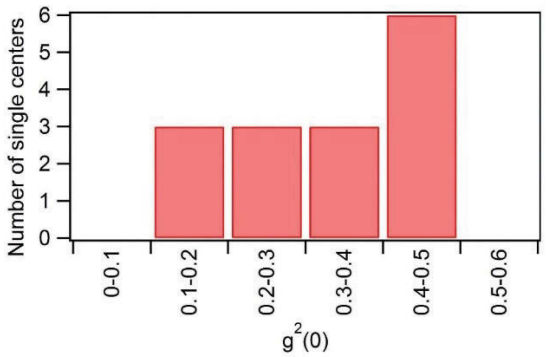

Figure 2.7. *Histogram of the $g^2(0)$ values shown in* ***Fig. 2.6****.*

In all cases, a dip below 0.5 is clearly seen at zero delay time ($\tau = 0$), confirming that each defect acts as a single photon emitter.[12] Each curve serves as direct evidence for quantum emission from a single defect in hBN, consistent with a spatial analysis of the confocal PL maps (see **Fig. 2.8**).

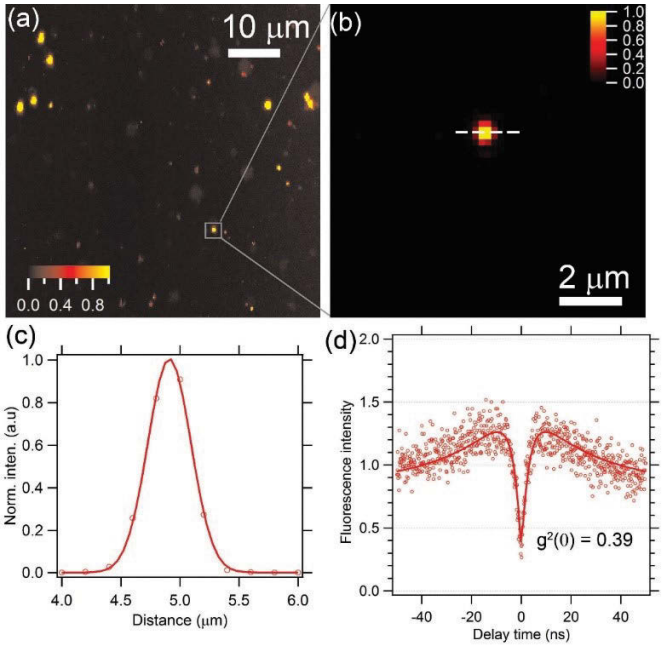

Figure 2.8. ***(a)*** *The confocal map presented in* ***Fig. 2.3a.*** ***(b)*** *A close-up showing a typical single color center.* ***(c)*** *Line profile (indicated by the dashed line in* ***(b)*** *of the defect center shown in b. The circles and the solid trace are the experimental data and a Gaussian fit, respectively.* ***(d)*** *Antibunching curve obtained from the defect show in b. The Gaussian fit in b has a full width at half maximum of 429 nm. This value is expected from a single emitter given that the ZPL wavelength is*

~623 nm, the PSB extends out to ~700 nm, and a background emission is present, as indicated by the $g^2(\tau)$ curve shown in ***(d)****.*

The experimental $g^2(\tau)$ data were fit using a three-level model (**Eq. 2.1)**). The parameters τ_1 and τ_2 are the lifetimes of the excited and metastable states, respectively. The fluorescence lifetime of the defect from these measurements, τ_1, is ~ 2.5 ns (and τ_2 is ~ 22.2 ns). A detailed analysis of this quantum system is presented in the methods section.

$$g^2(\tau) = 1 - (1 + a)e^{\frac{-|\tau|}{\tau_1}} + ae^{\frac{-|\tau|}{\tau_2}} \quad (2.1)$$

To understand the nature of the defect, detailed photophysical characterization of the emitters in multilayer hBN was performed. First, the Debye-Waller (DW) factor was calculated to understand the extent of electron-phonon coupling, i.e., the ratio of the ZPL intensity to that of the total emission.[57] Based on the PL measurements presented in **Fig. 2.3**, the DW factor is ~ 0.82. This value is amongst the highest reported for quantum emitters.[167] Centers with high DW factors are very useful for many applications including optoelectronics, nanophotonics, and bio-imaging, where there is a need for a strong, narrow band signal and a high signal to noise ratio.

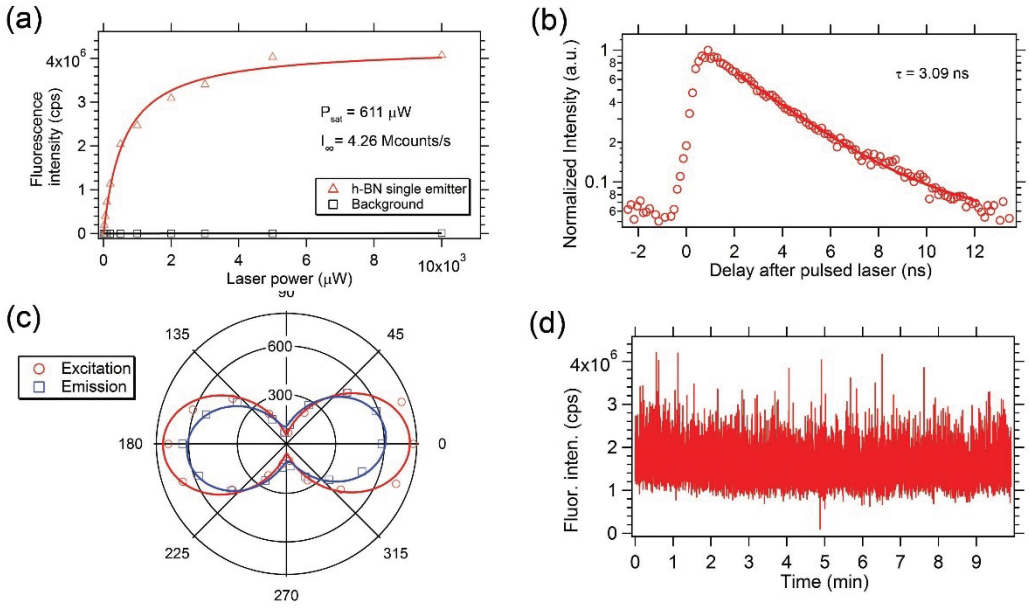

Figure 2.9. *Photophysical properties of single photon emitters in multilayer hBN.* ***(a)*** *Fluorescence saturation curve obtained from a single defect, showing a maximum emission rate of 4.26 Mcps.* ***(b)*** *Fluorescence lifetime measurement exhibiting an excited state lifetime of 3.1 ns.* ***(c)*** *Excitation (open, red circles) and emission (open, blue squares) polarization curves from a single defect. The solid red and blue lines are fits obtained using a $\cos^2(\theta)$ function.* ***(d)*** *Fluorescence intensity as a function of time demonstrating the photostability of a single defect at 1 mW excitation power. All the measurements were performed at room temperature using a 532 nm excitation laser.*

Fig. 2.9a shows the emission intensity of a single emitter as a function of excitation power. The experimental data were fit using **Eq. 2.2**:

$$I = {I_\infty P}/{(P + P_{sat})} \quad (2.2)$$

where I_∞ and P_{sat} are the emission rate and excitation power at saturation, respectively. The fitting yields $I_\infty \sim 4.2 \times 10^6$ counts/s at $P_{sat} \sim 611$ μW. This brightness is the highest reported for a quantum emitter in the visible spectral range, and similar to that of the brightest quantum emitters known to date.[57, 182] While several other systems exhibit comparable count rates, the availability of

hBN material in bulk quantities will enable wide usage of this material in emerging technologies.

Time-resolved fluorescence measurements were performed to directly measure the excited state lifetime. **Fig. 2.9b** shows the decay of the signal from a single quantum emitter with a ZPL at 623 nm. The experimental data were fit using a single exponential, and yields a lifetime of ~ 3 ns, consistent with the lifetime values deduced by measuring the second-order correlation function.

To understand whether the emission center consists of a single dipole or multiple dipoles, we performed excitation and emission polarization measurements. **Fig. 2.9c** shows the excitation (red circles) and emission (blue squares) polarization data obtained from a typical single emitter, and the corresponding fits obtained using a $\cos^2(\theta)$ fitting function.[183] The excitation and emission polarization visibility is calculated to be 86% and 71%, respectively. These results are characteristic of a single linearly polarized dipole transition.

The stability of a typical single emitter is shown in **Fig. 2.9d**. Even under a high excitation power of 1 mW, the defect exhibits a stable fluorescence emission signal over more than 10 min without any blinking or bleaching. Interestingly, while the emitters embedded in multilayer hBN exhibit absolute photo-stability, the emitters in monolayer hBN blink and bleach after several excitation cycles. We tentatively ascribe this behavior to modification of the defects caused by direct contact with the environment.

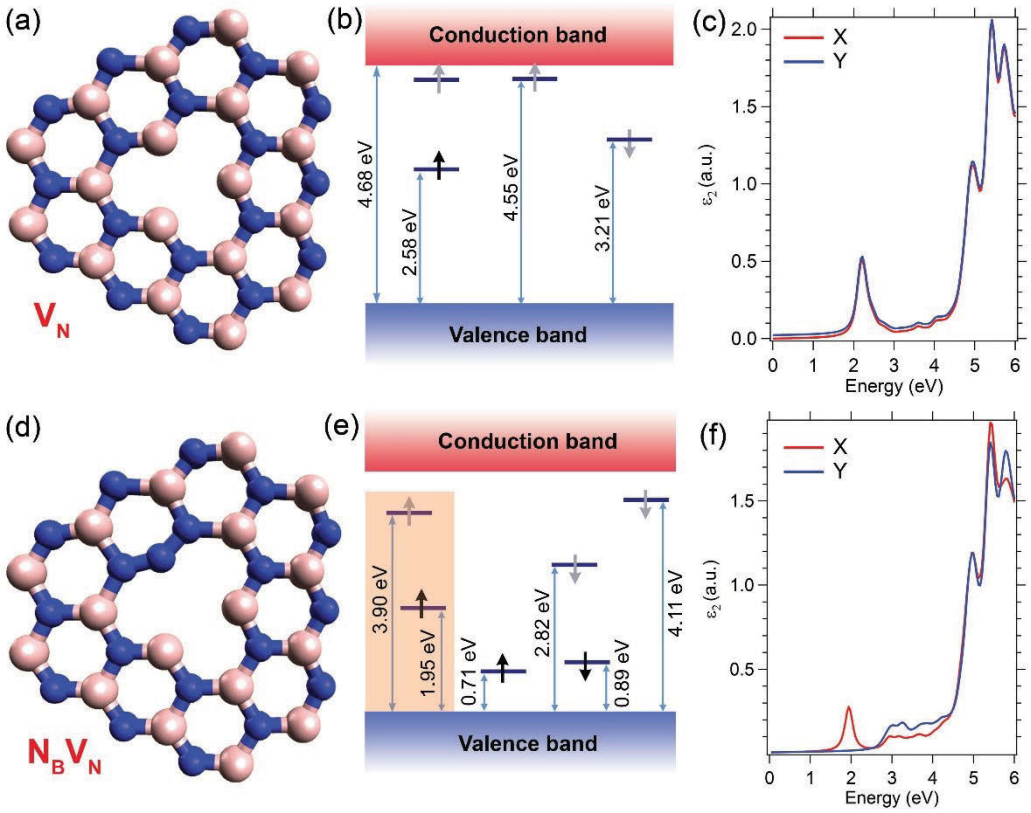

Figure 2.10. *Proposed defect models in the hBN lattice. Schematics of* ***(a)*** *the nitrogen-vacancy, V_N and* ***(d)*** *the anti-site nitrogen vacancy, N_BV_N. Simulated electronic structures of* ***(b)*** *V_N, and* ***(e)*** *N_BV_N. Black and grey arrows represent occupied and unoccupied states, respectively. Calculated imaginary dielectric tensors of the two components, namely, X (red trace) and Y (blue trace) of* ***(c)*** *V_N* ***(f)*** *N_BV_N.*

We now turn to the origin of the defect responsible for the observed single photon emission. Given that the quantum emission from this defect is observed in monolayers and multilayer hBN materials, the defect is most likely intrinsic. The most likely candidates are a nitrogen-vacancy (V_N), a boron vacancy (V_B) or an anti-site complex in which the nitrogen occupies the boron site, and there is a missing atom at the nitrogen site (N_BV_N).[184],[149] We exclude the possibility of a di-vacancy as those have been shown to be highly unstable.[185] The V_B has been theoretically predicted to have a UV absorption and emission band[149] that is inconsistent with our experimental data. We, therefore, used DFT to investigate

the V_N and the N_BV_N defects using the Vienna ab initio simulation package VASP[174] with the Perdew-Burke-Ernzerhof (PBE) exchange-correlation functional.[177] **Fig. 2.10a,d** show the structure of the V_N and N_BV_N defects, respectively. The V_N center has a missing nitrogen atom and the N_BV_N defect has a nitrogen atom at a Boron site neighboring a vacancy. **Fig. 2.10b,e** present the corresponding energy levels of the V_N (**Fig. 2.10b**) and N_BV_N (**Fig. 2.10e**) centers. Bearing in mind the shortcomings of DFT in predicting bandgaps and that the PBE is expected to underestimate this quantity, these calculations predict a number of transitions that are close to the measured photon energy. We assume that only spin preserving transitions are allowed. For the V_N defect, there is a single transition between a potential ground state 2.58 eV above the valence band to a potential excited state located at 4.55 eV above the valence band, resulting in a 1.97 eV transition. The N_BV_N defect exhibits potential internal transitions for the two spin channels that are nearly degenerate at 1.95 eV and 1.93 eV (shaded in **Fig. 2.10e**). Both of the two proposed centers, therefore, possess theoretical transition energies that match our experimental data (a ZPL centered on 623 nm, corresponding to ~ 2 eV).

To distinguish between the two defect possibilities, we simulate the optical responses of the defects. **Fig. 2.10c,f** show the calculated imaginary dielectric tensor for two components in the plane of the 2D sheet. The dielectric function corresponding to the V_N defect is isotropic and shows a single peak within the bandgap at 2.1 eV, consistent with a transition from the occupied defect level into the conduction band. The internal ground-to-excited state transition is either forbidden or extremely weak and hidden in the low-energy side of this transition. Therefore, the V_N defect is unlikely to be the studied emitter.

The N_BV_N defect is, by contrast, highly anisotropic and exhibits a peak at approximately 1.9 eV, corresponding to the internal ground-to-excited state transitions. This theoretical prediction is consistent with our experimental data, suggesting that the N_BV_N defect is the most likely candidate for the quantum emitter within hBN monolayers. Moreover, a spin-resolved calculation shows that the N_BV_N energy levels responsible for the optical transition are the ones between

the 1.95 eV (ground state) and the 3.90 eV (excited state) states above the valence band maximum. This transition is highlighted in **Fig. 2.10e**. The spin-resolved dielectric functions are provided in **Fig. 2.11**. We note that given the symmetry of the defect, tuning of the emission energy by both electric fields and strain is expected to be possible.

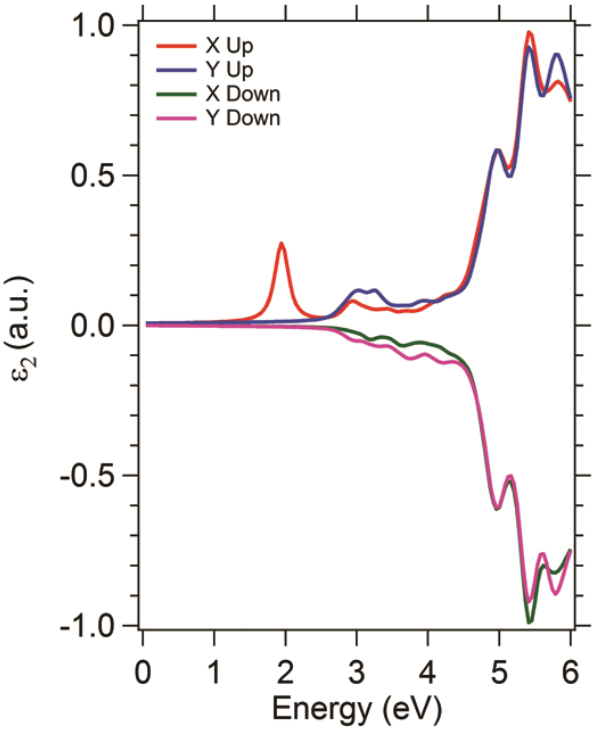

Figure 2.11. *Spin-resolved calculation of the imaginary dielectric tensor for X and Y components of the N_BV_N defect center. Red, blue, green, and purple solid lines represent spin-up of the X and Y components, and spin-down of the X and Y components, respectively.*

In order to ascertain that the simulation is also valid for multilayer hBN, we performed the same calculations using three-layer hBN where the middle layer contains the defect (**Fig. 2.12**). As expected, the results show that the weak interaction between the sheets has little effect, yielding an energy level structure that is very similar to that plotted in **Fig. 2.10.**

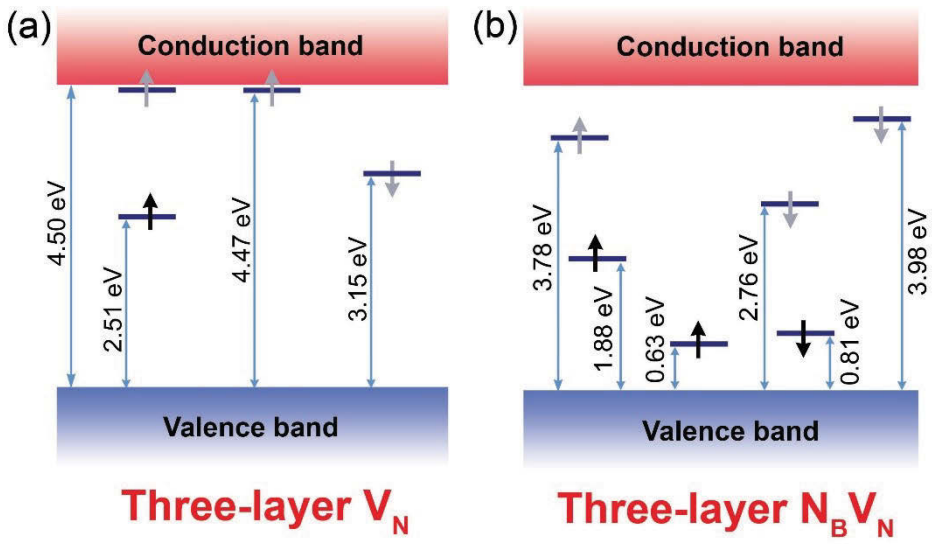

Figure 2.12. *Electronic band diagram of* ***(a)*** V_N, *and* ***(b)*** N_BV_N *defect centers hosted in the middle layer of three-layer hBN. Black and grey arrows represent occupied and unoccupied states, respectively.*

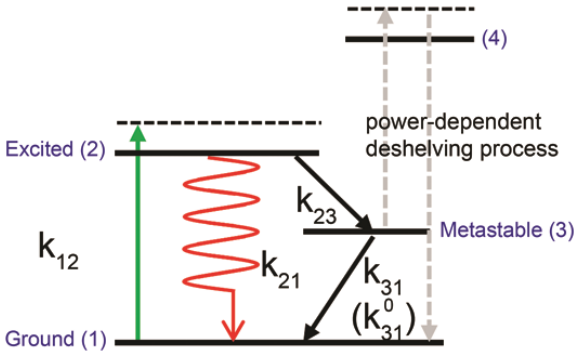

Figure 2.13. *Schematic illustration of the proposed extended three-level model used to interpret the temporal population dynamics of the defect center in hBN.*

Now we turn to the estimation of quantum efficiency of the defect center. The hBN quantum emitter was analyzed in the frame of an extended three level system [186] (see **Fig. 2.13**). To gain information about the level transition rates, the second order correlation function $g^2(\tau)$ was recorded as a function of excitation power. The results are shown in **Fig. 2.14a**. The $g^2(\tau)$ is given by **Eq. 2.1.**, where τ_1 and τ_2 represent the radiative transition lifetime and the metastable state lifetime, respectively, and *a* is a bunching factor [186].

We obtain the values of a, τ_1 and τ_2 by fitting the power-dependent $g^2(\tau)$ (**Fig. 2.14a**) using **Eq. 2.1.**. From these power-dependent values, we plot a (**Fig. 2.14b**), τ_1 (**Fig. 2.14c**) and τ_2 (**Fig. 2.14d**) as a function of excitation power. By fitting these curves (double exponential and single exponential fits for a and τ_1, and τ_2, respectively) and extrapolating them to extremely high and vanishing excitation powers, we arrive at $a_0 = -0.152$, $a_\infty = 0.349$, $\tau_1^0 = 2.196$ ns, $\tau_1^\infty = 0.175$ ns, $\tau_2^0 = 22.247$ ns, and $\tau_2^\infty = 17.567$ ns, where the superscripts ∞ and 0 signs denote extremely high and vanishing excitation powers.

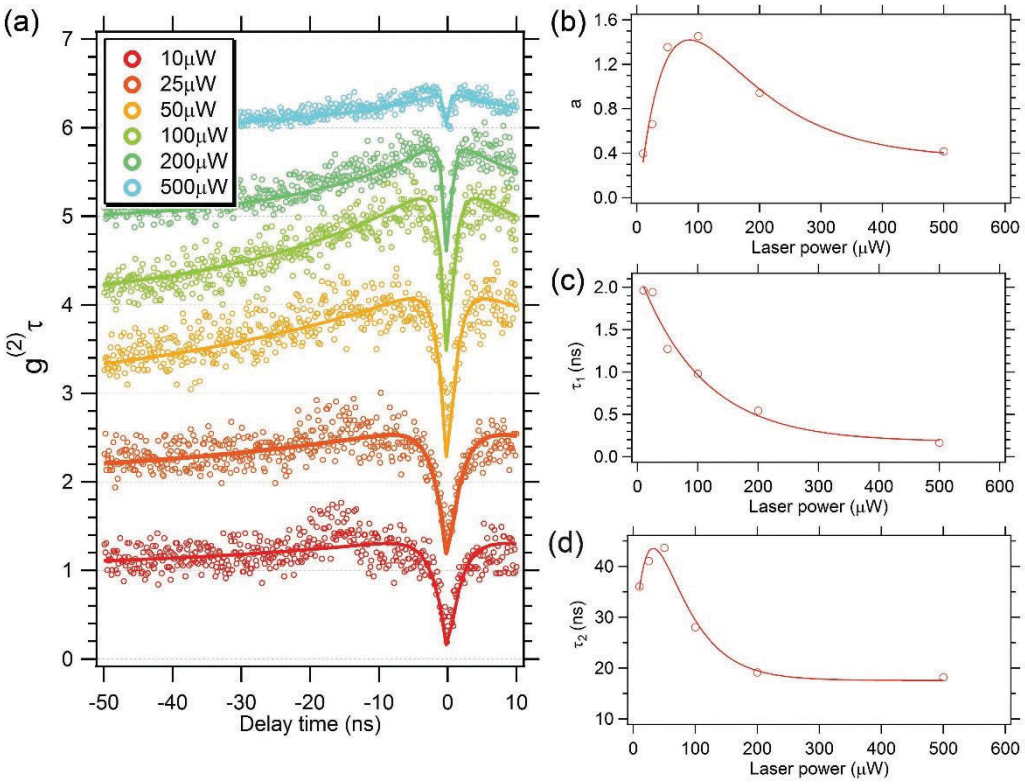

Figure 2.14. (a) *Second-order autocorrelation function obtained versus laser power from an SPE in multilayer hBN. The $g^2(\tau)$ traces are normalized and shifted vertically for clarity.* ***(b)*** *The parameter a,* ***(c)*** *radiative lifetime τ_1 and* ***(d)*** *metastable state lifetime τ_2 of the defect center as a function of laser power.*

The transition rates between the three levels, namely, pumping rate from the ground state (level 1) to the excited state (level 2), radiative decay rate from the excited state (level 2) to the ground state (level 1), shelving rate from the excited

state (level 2) to the metastable state (level 3), and de-shelving rate from the metastable state (level 3) to the ground state (level 1) are denoted by k_{12}, k_{21}, k_{23}, and k_{31}, respectively (**Fig. 2.13**). By measuring $g^2(\tau)$ as a function of excitation power, we can essentially deduce all of the above transition rates. Specifically, the parameters τ_1, τ_2 and *a* are deduced using **Eq. 2.3-2.6** [186].

$$\tau_{1,2} = \frac{2}{A \pm \sqrt{A^2-4B}} \quad (2.3)$$

$$A = k_{12} + k_{21} + k_{23} + k_{31} \quad (2.4)$$

$$B = k_{12}k_{23} + k_{12}k_{31} + k_{21}k_{31} + k_{23}k_{31} \quad (2.5)$$

$$a = \frac{(1-\tau_2 k_{31})}{k_{31}(\tau_2-\tau_1)} \quad (2.6)$$

Based on the moderate bunching behavior, we assume that k_{21}, and k_{31} are power-dependent transition rates, while k_{23} is assumed to be a power-independent rate. All the transition rates are given by **Eq. 2.7-2.11**.[186]

$$k_{31} = \frac{d.P}{P+c} + k_{31}^0 \quad (2.7)$$

$$k_{31}^0 = \frac{1}{\tau_2^0} \quad (2.8)$$

$$d = \frac{\frac{1}{\tau_2^\infty} - (1+a^\infty)\frac{1}{\tau_2^0}}{1+a^\infty} \quad (2.9)$$

$$k_{23} = \frac{1}{\tau_2^\infty} - k_{31}^0 - d \quad (2.10)$$

$$k_{21} = \frac{1}{\tau_1^0} - k_{23} \quad (2.11)$$

Here, P represents the excitation power, and the coefficients d and c the saturation behavior of transition k_{31}[186]. Using a combination of **Eq. 2.3-2.11**., we obtain k^0_{31} = 44.95 MHz, d = -2.75 MHz, k_{23} = 14.73 MHz, and k_{21} = 440.70 MHz.

Next, we estimate the quantum efficiency using **Eq. 2.12**:[186]

$$I_\infty = \eta_{det}\eta_{qe} \frac{k_{21}}{1+\frac{k_{23}}{k_{31}^0+d}} \quad (2.12)$$

where I_∞, η_{det}, and η_{qe} are the maximum fluorescence detected by the APDs, collection efficiency and fluorescence quantum efficiency, respectively. We measured the setup collection efficiency by accounting for the contribution of each component in the collection path: Dichroic mirrors (~ 95%), objective lens (~ 35%), lenses and coupling to optic fibers (~ 10%), and the APD efficiency at 630 nm (60%). The estimated collection efficiency for our setup is therefore η_{det} ~ 0.01995. This estimate is an upper limit (i.e. the actual quantum efficiency of the emitter can potentially be higher). To ensure that there is no loss due to dipole orientation misalignment of the emitter with respect to the laser, we only performed this calculation on emitters that are perfectly aligned with respect to the laser beam (based on polarization measurements). By inserting the above values into **Eq. 2.11.**, the quantum efficiency of the color center is ~ 65%.

2.5 Conclusion

To summarize, we unveiled a quantum emission from a point defect, N_BV_N, in monolayer hBN and multilayer hBN. The emitters are fully polarized and exhibit record rates of ~ 4 million counts/s at room temperature. Our results augment the scientific and technological importance of Van der Walls crystals - in particular, hBN. Single emitters in hBN will enable new applications in quantum technologies and optoelectronics based on 2D materials, and highlight the emerging potential of hBN devices.

3 Robust Multicolor Single Photon Emission from Point Defects in Hexagonal Boron Nitride

Following the discovery of quantum emitters in hBN materials presented in Chapter 2, this chapter reports a deeper understanding of photophysics of the quantum emitters in hBN multilayers, the engineering of these emitters using thermal treatment and electron-beam irradiation, and their photostability and possible strain-induced optical transition shifts. Trong Toan Tran, Milos Toth, and Igor Aharanovich conceived the idea. Christopher Elbadawi carried out and analyzed the electron-beam-induced creation of quantum emitters. Christopher Elbadawi and Daniel Totonjian conducted the stability tests of quantum emitters in different harsh environments. Trong Toan Tran performed the room-temperature optical characterization and analysis. The cryogenic PL measurements were carried out by Gabriele Grosso, Hyowon and Dirk Englund (MIT, USA). Michael J. Ford conducted and analyzed the DFT simulation of strain-induced energy shifts of quantum emission. All the authors discussed and wrote the manuscript.

3.1 Abstract

Hexagonal boron nitride is an emerging two dimensional material for quantum photonics owing to its large bandgap and hyperbolic properties. Here we report two approaches for engineering quantum emitters in hBN multilayers using either electron beam irradiation or annealing, and characterize their photophysical properties. The defects exhibit a broad range of multicolor room temperature single photon emissions across the visible and the near infrared spectral ranges, narrow line widths of sub 10 nm at room temperature, and a short excited state lifetime, and high brightness. We show that the emitters can be categorized into two general groups, but most likely possess similar crystallographic structure. Remarkably, the emitters are extremely robust and withstand aggressive annealing

treatments in oxidizing and reducing environments. Our results constitute the first step towards deterministic engineering of single emitters in 2D materials and hold great promise for the use of defects in boron nitride as sources for quantum information processing and nanophotonics.

3.2 Introduction

Hexagonal boron nitride is a van der Waals material that has recently emerged as a fascinating platform for room temperature quantum photonics due to the discovery of room temperature quantum emitters [4], realization of sub-diffraction focusing and guiding [128-129], super-resolution imaging [130], and tunable phonon polariton propagation [126]. While the optical properties of bulk hBN have been studied thoroughly [6, 118, 120], detailed photo-physical properties of its two-dimensional counterpart are scarce. In particular, the luminescent properties of hBN under sub-band-gap excitation remain largely unexplored.

In traditional 3D semiconductors, including diamond and silicon carbide, color centers have similar spectral properties in both bulk and nanostructured forms. This may be advantageous when controlled engineering of defects is required. Both materials can be doped during growth, resulting in deterministic formation of luminescent centers. However, in van der Walls crystals, the electronic and optical properties of two dimensional (single or few monolayer) flakes are significantly different from their bulk counterparts [162]. This often results in fascinating phenomena such as spin valley splitting [187] or strong exciton-phonon interactions that can be observed at room temperature [188], but poses major challenges for engineering and control of single color centers.

In this letter, we show that single emitters in hBN can be engineered using electron irradiation and withstand various aggressive annealing treatments in reactive gaseous environments, which do not change their spectral properties. We characterize the emitters and report an interesting phenomenon – namely, narrowband multicolor single photon emission from a 2D material. While known color centers and standard quantum dots (of a given, fixed chemical composition) luminesce at a particular wavelength or over a narrow spectral range, we show that

defects in hBN multilayers can emit over a broad range spanning over 200 nm. We also show that the emitters withstand various aggressive annealing treatments in reactive gaseous environments, which do not change their spectral properties. Our results pave the way for robust, room temperature quantum photonic devices that employ color centers in hBN as key building blocks.

3.3 Methods

3.3.1 Materials preparation: annealing process

Grid-marked native oxide Si (100) substrates were cleaned by ultrasonication in acetone and ethanol combined with light mechanical abrasion. Samples were prepared by drop-casting 100 μL of ethanol/water solution containing ~200 nm pristine h-BN flakes (Graphene Supermarket) onto marked substrates and allowed to dry.

Argon and O_2 annealing were carried out in a tube furnace (Lindberg Blue). The tube furnace was evacuated to low vacuum (~10^{-3} Torr) by means of a scroll pump then purged for 30 minutes under 10 sccm of Ar or O_2 flow with pressure regulated at 1 Torr. The substrate was then heated under 10 sccm of argon flow or 500°C under 10 sccm of O_2 flow and held at a fixed temperature for 30 minutes, then allowed to cool to room temperature under continuous gas flow.

H_2 and NH_3 annealing was carried out in dedicated vacuum chamber. The chamber was evacuated to high vacuum (~10^{-8} Torr) by means of a turbo molecular pump then purged for 30 minutes under 10 sccm of H_2 and NH_3 flow respectively with pressure regulated at 40 Torr. The substrate was then heated to 500°C under 10 sccm H_2 or NH_3 flow and held at this temperature for 30 minutes, then allowed to cool to room temperature under continuous gas flow.

3.3.2 Materials preparation: electron-beam irradiation

The substrates prepared for electron beam irradiation underwent photolithography procedures and subsequent metal deposition to create a hard mask grid. The substrates were then prepared as described above. The grid allowed for easy

identification of areas to characterize optically before and after electron beam irradiation.

Electron-beam irradiation experiments were performed in a variable pressure FEI field emission gun scanning electron microscope. A low vacuum environment of H_2O at a pressure of 8 Pa was used for all experiments. A focused beam was used in a raster scanning pattern to expose the hBN flakes as a function of time up to one hour over an area of 600 μm^2. An accelerating voltage of 15 kV and beam current of 1.4 nA were used for all electron beam irradiation experiments.

3.3.3 Optical characterization

A continuous wave 532 nm laser (Gem 532™, Laser Quantum Ltd.) was used for excitation and scanning. The laser was directed through a Glan-Taylor polarizer (Thorlabs Inc.) and a half waveplate, and focused onto the sample using a high numerical aperture (NA = 0.9, Nikon) objective lens. Scanning was performed either using an X-Y piezo scanning mirror (FSM-300™) or an X-Y-Z nanocube system (PI instruments). The collected light was filtered using a 532 nm dichroic mirror (532 nm laser BrightLine™, Semrock) and an additional long pass filter (Semrock). The signal was then coupled into a graded index fiber, where the fiber aperture serves as a confocal pinhole. A fiber splitter was used to direct the light to a spectrometer (Acton SpectraPro™, Princeton Instrument Inc.) or to two avalanche photodiodes (Excelitas Technologies™) used for single photon counting. Correlation measurements were done using a time-correlated single photon counting module (PicoHarp300™, PicoQuant™). The presented $g^{(2)}(\tau)$ curves were not corrected for background luminescence. Lifetime measurements were performed using a 510 nm pulsed laser excitation source (PiL051X™, Advanced Laser Diode Systems GmbH) with a 100 ps pulse width and a 20 MHz repetition rate. Low temperature PL spectroscopy was done at 14 K using a closed cycle refrigerating system cryostat (Janis CCS-XG-M/204N).

3.3.4 Theoretical calculation

VASP[174] calculations were performed using the Generalized Gradient Approximation to the exchange-correlation functional proposed by Perdew, Burke and Ernzerhof [177]. All calculations are spin-polarized and use the PAW pseudopotentials supplied with the VASP code. A plane-wave cutoff of 450 eV was used for all calculations, which is considerably higher than default values for the pseudopotentials used and represents a well-converged calculation. Pristine single-layer hBN was first geometry-optimized using the conventional cell and a 21×21×1 Monkhurst-Pack reciprocal space grid to an energy tolerance of 0.01 eV. A vacuum spacing of 20 Å was used to separate periodic images of the single layer and to ensure interaction between the layers is negligible. Relaxation of the lattice vectors using a conjugate gradient approach or by hand plotting the energy as a function of lattice parameter give the same optimized unit cell. The computational conditions are clearly good enough that basis size effects are not important. The optimized lattice parameter is 2.5 Å, with a bond length of 1.447 Å. A 7×7 supercell was used for the defective hBN monolayers with the reciprocal space grid reduced by a corresponding amount to 3×3×1. Defect structures were re-optimized. The imaginary component of the frequency dependent dielectric matrix was calculated in the Random Phase Approximation neglecting local field effects; the method is explained in detail in Ref 3[189]. The two orthogonal components of the dielectric tensor in the plane of the hBN monolayer are along and perpendicular to the axis of the N_BV_N defect.

A Gaussian smearing function is used with a small width of 0.05 eV. For the relatively large supercells used here, this should give good results. We have also tried the tetrahedron Blochl corrected, and an order-1 Methfessel-Paxton, smearing function, the latter with a considerably larger width of 0.2 eV (the default settings for VASP) with effectively no change in the calculated optical properties.

As this is a neutral defect, the interaction with replicas along the z-axis should be minimal. Total energy is well converged at this spacing. Similarly, the distance between replicas in the plane of the atoms is greater than 17 Å. The strain is applied

biaxially from -5% to + 5%. This range of strain is plausible according to recent studies[4, 5] of similar two-dimensional materials. The optical response is calculated through the imaginary components of the dielectric tensor. **Fig. 3.1a** shows plots of one in-plane component of this tensor for an hBN monolayer that contains an N_BV_N defect. The direction of this component is along a symmetry axis of the defect parallel to the B-N bonds within the sheet.

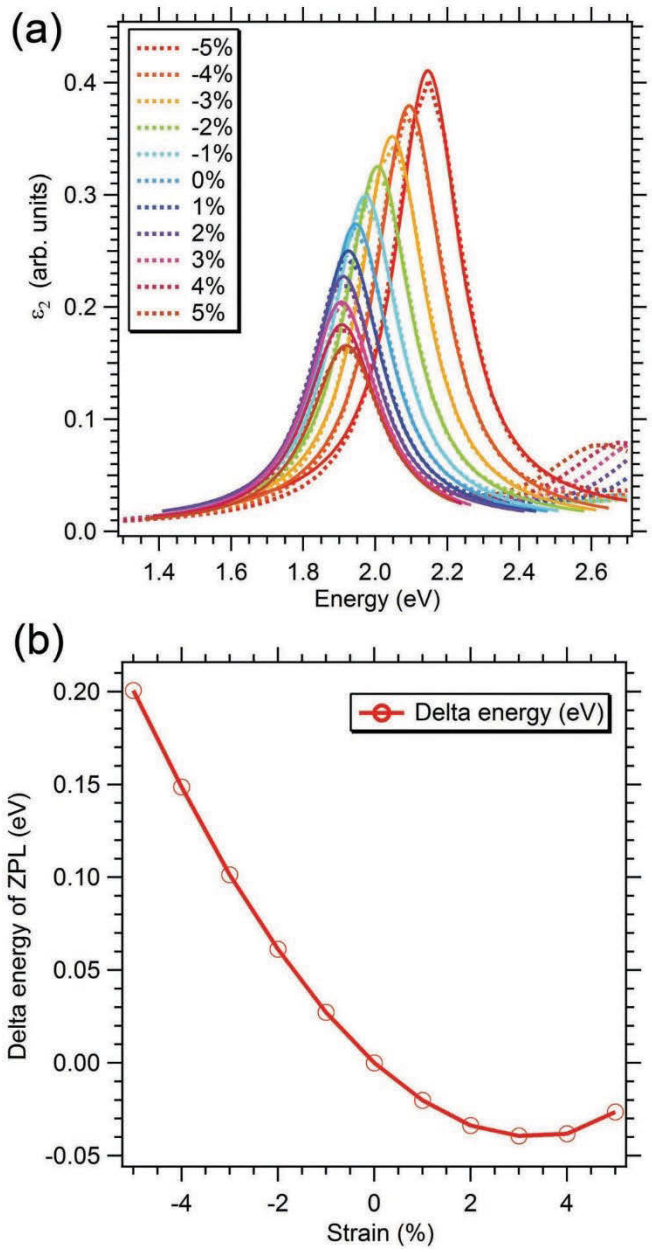

Figure 3.1. *Density functional theory calculation of the effects of strain on the optical response of the N_BV_N color center in hBN.* ***(a)*** *X-component of the in-plane*

imaginary dielectric tensor plotted as a function of compressive (negative percentages) and tensile (positive percentages) strain in a hBN multilayer. ***(b)*** *The corresponding difference in the ZPL energy of N_BV_N versus compressive and tensile strain.*

The calculated dielectric response was broadened with a 0.2 eV Gaussian smearing function. The peak in **Fig. 3.1a** corresponds to transitions that fall within the bandgap and are due to a defect level. This optical transition is polarized, the orthogonal component of the dielectric tensor does not exhibit a corresponding peak. The peaks in **Fig. 3.1a** were fitted with Lorentzian functions to extract the corresponding dependence of the optical transition energy on the strain. The resulting plot, shown in **Fig. 3.1b**, is indicative of the shift in ZPL energy versus the percentage of applied biaxial strain. As the strain increases from -5% to +5%, the optical transition energy (wavelength) changes from 2.15 to 1.91 eV (578 to 650 nm). We note that the energy shift is much more significant with compressive strain compared to tensile strain. This behavior is expected since the overlap between atomic orbitals scales super-linearly with strain [190-191].

3.4 Results and Discussion

We developed two different processes for engineering of the emitters, based on annealing and electron beam irradiation, illustrated schematically in **Fig. 3.2a**. Either method can be used to create the studied defects in hBN. The annealing method was optimized by varying the annealing temperature of as-grown flakes in an inert environment. Each annealing treatment was performed for 30 minutes under 1 Torr of argon. **Fig. 3.2b** shows that the number of stable color centers found by confocal PL increases with annealing temperature, indicating that defect diffusion and lattice relaxation occur in the flakes. This behavior is similar to the well-studied nitrogen-vacancy center in diamond [192-193].

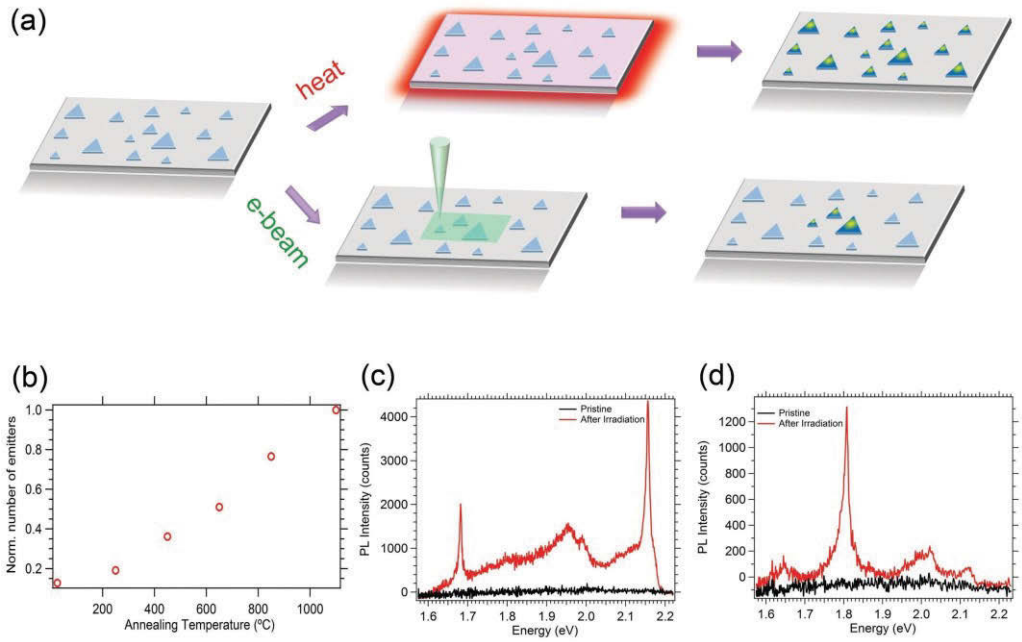

Figure 3.2. *Generation of emitters in hBN.* ***(a)*** *Schematic illustration of two independent processes that yield emitters – annealing and electron beam irradiation. As-grown, drop-cast hBN flakes are either annealed in an argon environment or irradiated by an electron beam in a low vacuum H_2O environment.* ***(b)*** *Normalized number of stable, bright single emitters as a function of annealing temperature found in hBN multilayers. Each data point was taken from a unique sample that was annealed at a single temperature.* ***(c, d)*** *Examples of PL spectra from emitters fabricated by an electron beam. Each pair shows data recorded from a fixed sample region before (black curve) and after (red curve) electron irradiation.*

The second process involves electron beam irradiation performed using a scanning electron microscope. The as-grown flakes were first deposited on a silicon substrate and pre-characterized by confocal PL mapping shown in **Fig. 2.3a**. Then, particular sample regions were irradiated by a 15 keV, 1.4 nA electron beam for one hour in a low vacuum, H_2O vapor environment [194] (the H_2O prevents electron beam deposition of carbon [195] that is luminescent and modifies PL spectra). A detailed description of the irradiation experiments is provided in the Experimental Methods section. There were no changes in Raman spectra of the flakes after these treatments. This observation is not unexpected considering the

high stability of hBN flakes [196]. The pre-characterized sample regions were then re-measured using the confocal PL microscope. **Fig. 3.2(c,d)** shows photoluminescence spectra recorded before (black curve) and after electron irradiation (red curve) from two sample regions. Luminescent defects were created by the electron beam in each case. Importantly, no annealing was performed before or after the electron beam irradiation treatments. Our results, therefore, demonstrate two distinct robust methodologies for engineering of the emitters in hBN.

Next, we proceeded to study the stability of the emitters in various gaseous environments. These properties are important both from a technological point of view, since the emitters can potentially be used as sensors or quantum light sources in harsh chemical environments, and for understanding their chemical origin, as annealing in different gases can modify defect emission properties [197-198]. First, we leveraged the defect fabrication study (**Fig. 3.2(b)**) to create emitters by annealing a sample for half an hour in Ar at 850°C. The sample was then characterized by confocal PL, annealed sequentially at 500°C for one hour each in hydrogen, oxygen and ammonia environments, and re-characterized by PL after each annealing step. To provide a direct comparison, we selected two specific defects (located using a grid) with different photon energies and compared their spectra and second-order autocorrelation functions before and after annealing in different environments. Spectra from two stable emitters are shown in **Fig. 3.3 (a)** and **(c)**, respectively (the emitters belong to two Groups defined in **Fig. 3.6**). The fluorescence from the emitters remains unmodified even after annealing in both oxidizing and reducing environments.

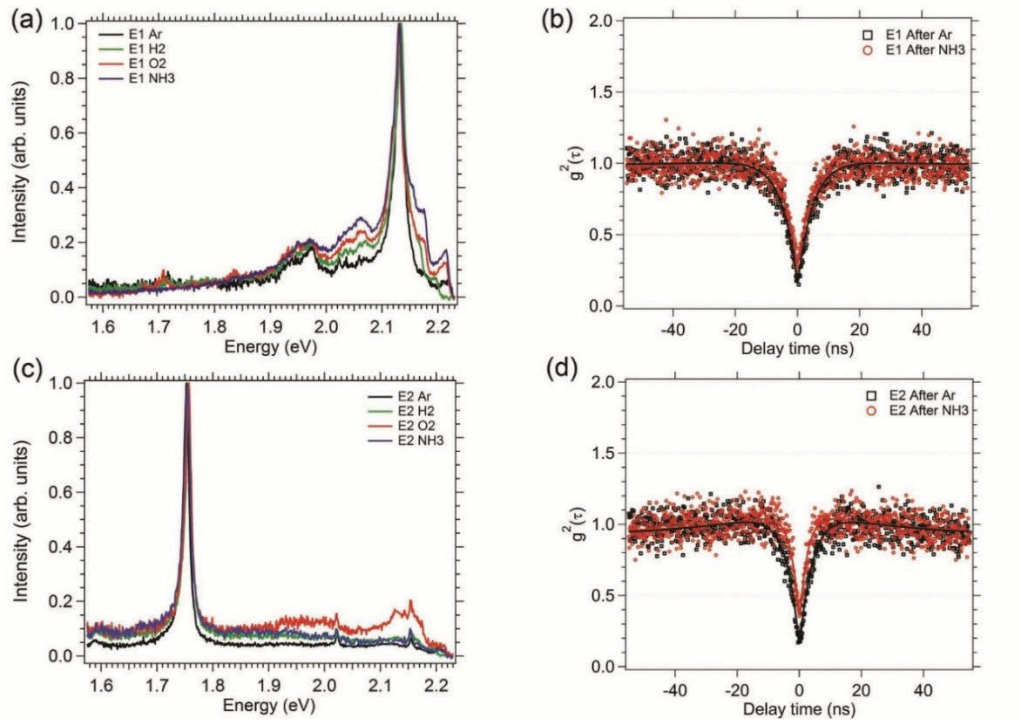

Figure 3.3. *Stability of the emitters.* ***(a,c)*** *Normalized luminescence recorded at room temperature from two emitters (E1 and E2) after sequential annealing in argon, hydrogen, oxygen, and ammonia.* ***(b, d)*** *Corresponding antibunching measurements proving that the quantum nature of the defects persists after the sequential set of 30 min anneals performed in H_2, O_2 and NH_3 environments. Emitters E1 and E2 belong to Group 1 and 2, respectively. The Groups are defined in* ***Fig. 3.3****.*

Fig. 3.2 (b, d) shows corresponding autocorrelation $g^{(2)}(\tau)$ curves for the two emitters recorded for each emitter after the initial argon annealing treatment (black curve) and after the final annealing step performed in an ammonia environment (red curve). All autocorrelation curves show that $g^{(2)}(0) < 0.5$, proving unambiguously that the emitters are point defects that act as single photon sources. The data convincingly prove the robustness of the emitters and the persistence of their quantum nature.

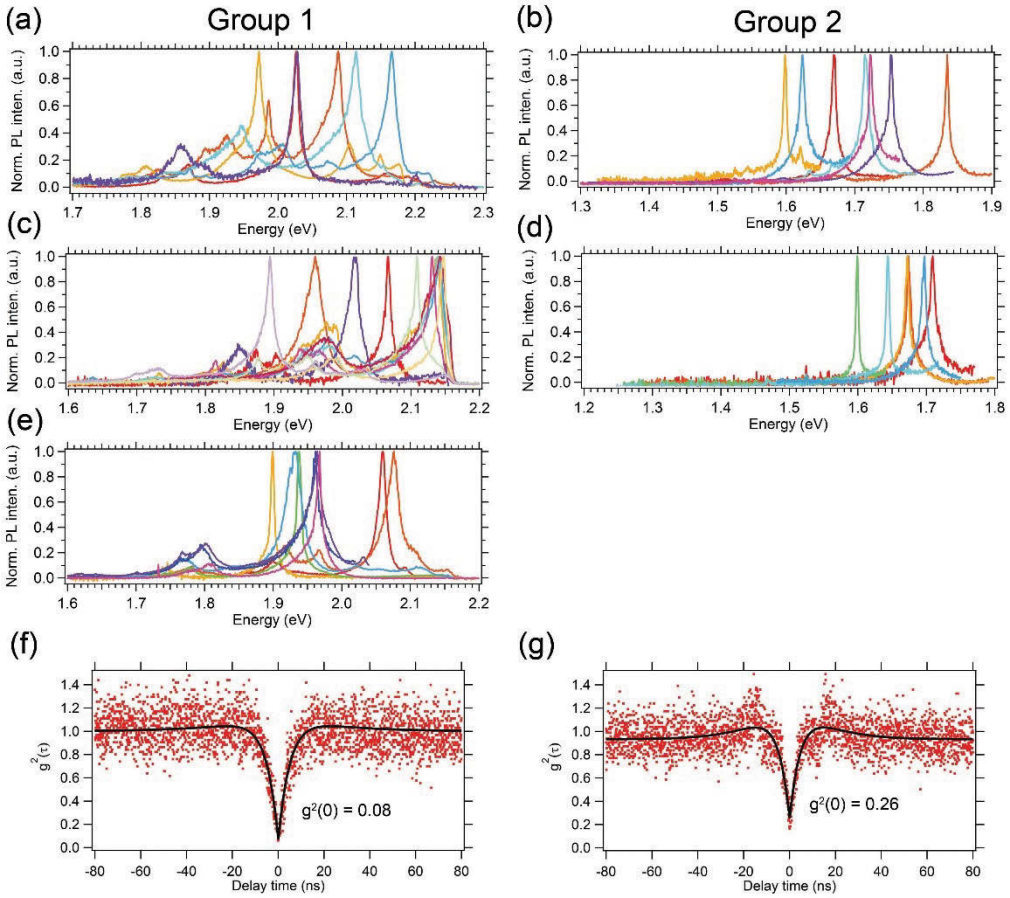

Figure 3.4. (a, c, e) *Additional 25 PL spectra taken from Group 1 emitters.* ***(b, d)*** *Additional 13 PL spectra taken from Group 2 emitters. Additional antibunching curves acquired from* ***(f)*** *a Group 1 emitter, with a* $g^2(0) = 0.08$*, and from (g) a Group 2 emitter, with* $g^2(0) = 0.26$*. The nine PL spectra presented in* ***Fig. 3.3*** *of the main text are not shown here. The antibunching curves were obtained using a 532 nm CW at 300 μW as an excitation source and were not background-corrected. The acquisition time each antibunching curve is 60 sec. A neutral density filter was used to attenuate the signal used to generate the curve in* ***(f)****.*

The annealing results provide important insights into the nature of the emitters. First, the luminescent defect is likely to have a vacancy in its crystallographic structure. This is because of the clear increase in formation probability with annealing temperature, a behavior that is very typical of vacancy-related complexes in solids [193, 199]. Second, it is likely that the emitters are charge neutral. If the emitters were negatively charged, annealing in a hydrogen

environment would have been expected to modify the charge state and modify or eliminate the emission. This behavior is exemplified by the NV center in diamond which switches from the negative to the neutral charge state upon annealing in hydrogen (and vice versa upon annealing in oxygen) [193, 199]. Similarly, many negatively charged emitters in GaN are switched off upon annealing in hydrogen [200]. Positively charged defects are not considered, as to the best of our knowledge positively charged single photon emitters in solids have not been observed. Finally, we believe that the emitters that are stable upon annealing cannot be surface states, as has been observed for some TMDs [201]. This is because surface states are often unstable, and are expected to be modified upon annealing in different reactive environments. We note, however, that while many of the emitters were absolutely stable and resisted all the annealing treatments, each annealing step did create some new emitters, and quench some emitters. Both of these effects are demonstrated in **Fig. 3.5**, and are not surprising, as is discussed later.

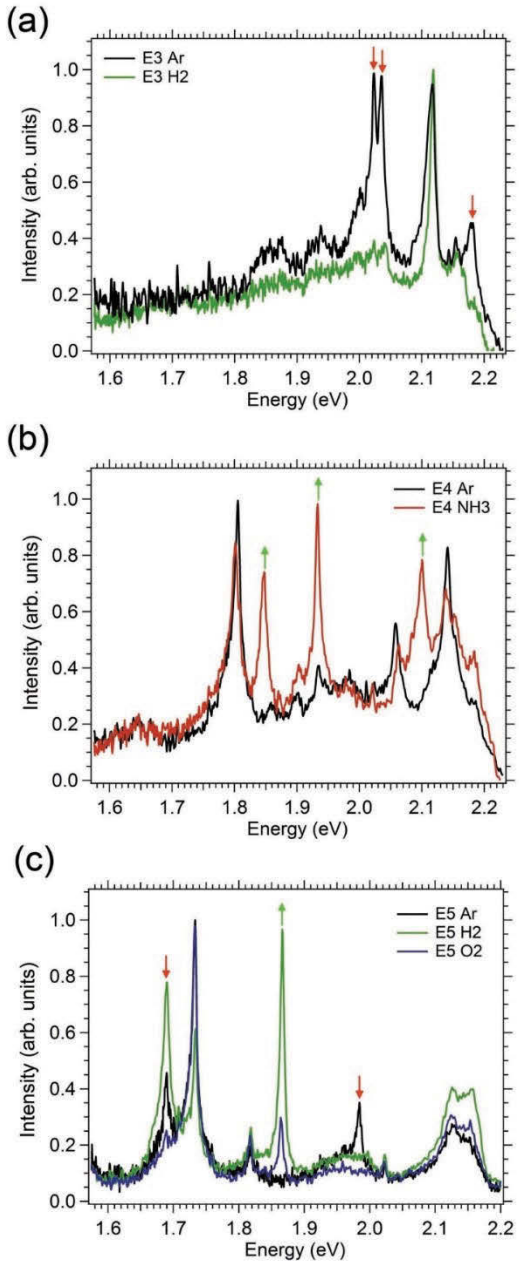

Figure 3.5. *Emitter creation and destruction upon sequential annealing at 500ºC for 30 min each in H_2, O_2 and NH_3 environments. The sample was first annealed in Ar at 850ºC to generate emitters, and the black spectra in* ***(a-c)*** *were acquired from three different sample regions.* ***(a)*** *The green spectrum was acquired after annealing in H_2 from the same region as the black spectrum, and shows the disappearance of a number of emission lines (indicated by red arrows).* ***(b)*** *The*

red spectrum was acquired after the final annealing step in NH_3 from the same region as the black spectrum, and shows the appearance of a number of emission lines (indicated by green arrows). ***(c)*** *The green and blue spectra were acquired after annealing in H_2 and O_2, respectively, and show the appearance and disappearance of a number of emission lines. We note that no systematic trends were observed as a function of gas species. Instead, annealing in all three reactive environments caused the generation and quenching of some emission lines, and on average, more emitters were generated than destroyed after each annealing step. This behavior is expected based on the Ar annealing data shown in* ***Fig. 3.1(b)*** *of the main paper. The quenching of some of the emitters is also not surprising. It merely indicates that some of the emitters are unstable, possibly because they are located in the topmost monolayers or edges of hBN flakes and hence sensitive to the annealing treatments.*

Unless noted otherwise, the measurements were performed at room temperature using either a 532 nm CW laser, or a 510 nm pulsed laser as an excitation source for lifetime measurements. We performed a PL survey and collected spectra of various single defect centers in hBN (which was annealed previously in argon at 850°C, as is discussed below). A representative range of room temperature PL spectra is shown in **Fig. 3.6(b, c)**. The emitters have narrow zero phonon lines (ZPLs) at energies in the range of ~1.6 – 2.2 eV (~ 565 – 775 nm).

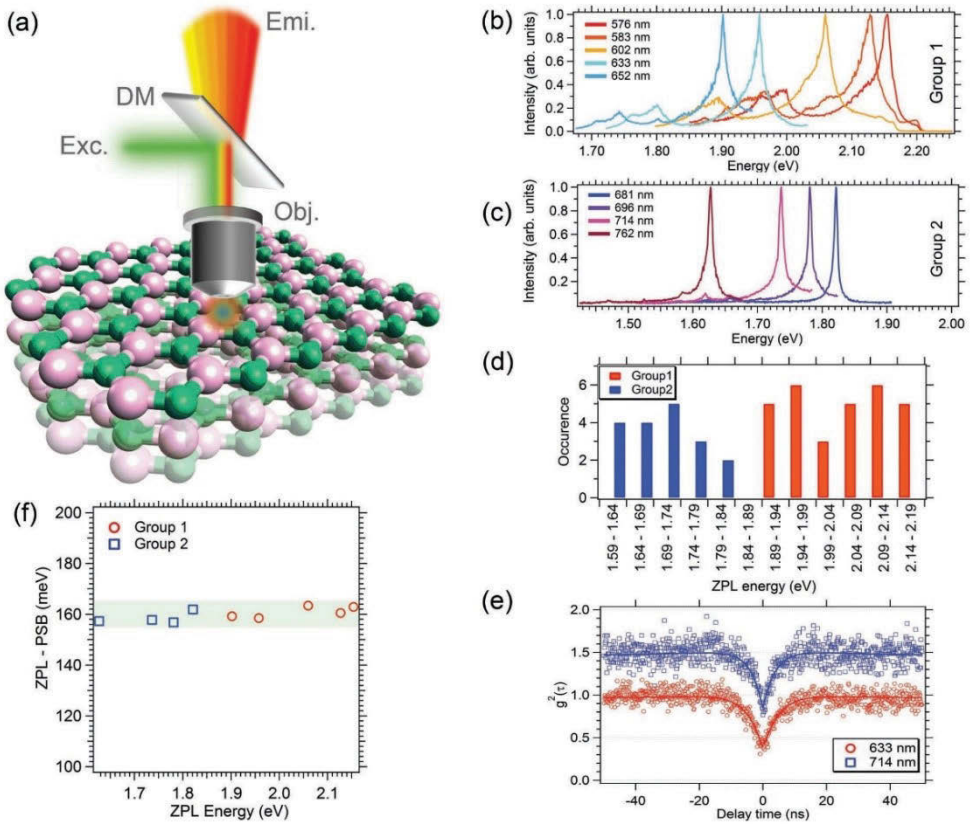

Figure 3.6. *Multicolor photoluminescence from point defects in hBN.* ***(a)*** *Simplified schematic of the photoluminescence setup showing the excitation and emission of a defect center in an hBN lattice. The objective lens, dichroic mirror, excitation source and emission are denoted by Obj., DM, Exc., and Emi., respectively.* ***(b)*** *Five examples of emitters in Group 1 with ZPLs at 576 nm (2.15 eV), 583 nm (2.13 eV), 602 nm (2.06 eV), 633 nm (1.96 eV), and 652 nm (1.90 eV).* ***(c)*** *Four examples of emitters in Group 2 with ZPLs at 681 nm (1.82 eV), 696 nm (1.78 eV), 714 nm (1.74 eV), and 762 nm (1.63 eV).* ***(d)*** *Histogram of ZPL energy for numerous emitters in group 1 (red) and group 2 (blue). Each spectrum was acquired from a separate sample region at room temperature using a 300μW CW 532 nm laser.* ***(e)*** *Second-order autocorrelation functions showing that $g^{(2)}(0)$ = 0.39 and 0.34, respectively. The $g^{(2)}(\tau)$ functions were acquired using an excitation power of 300 μW, an acquisition time of 20 sec, and were normalized (without background correction) and offset vertically for clarity. A neutral density filter was used to attenuate the signal generated by the 633 nm emitter.* ***(f)*** *The difference in the energy of the ZPL and PSB versus ZPL energy. The shaded band in* ***(f)*** *is a*

*guide to the eye. In **(b)** and **(c)**, high energy portions of some spectra were cut from the graph for clarity, to avoid overlaps between the spectra.*

The emitters can be classified into two general groups based on their ZPL energy and phonon side band (PSB) spectral shapes. Group 1 (**Fig. 3.6b**) consists of emitters with ZPL energies of 576 nm (2.15 eV), 583 nm (2.13 eV), 602 nm (2.06 eV), 633 nm (1.96 eV), and 652 nm (1.90 eV). Emitters in this group exhibit relatively broad and asymmetric ZPL line shapes with pronounced low energy tails. The spectra also contain pronounced doublet PSBs. Group 2 (**Fig. 3.6c**) is comprised of emitters at lower energies, with ZPLs centered on 681 nm (1.82 eV), 696 nm (1.78 eV), 714 nm (1.74 eV), and 762 nm (1.63 eV). Notably, these emitters have narrower, more symmetric ZPLs, with phonon sidebands that are weak compared to Group 1. A survey of ~ 40 emitters (**Fig. 3.4(a-e)**) in the sample annealed at 850°C revealed a relative abundance of ~70% and 30% of emitters in Groups 1 and 2, respectively. The low energy tails of the spectra taken from Group 1 are possibly due to low-energy interlayer phonon modes. **Fig. 3.6d** is a histogram showing the ZPL energies of emitters classified into the two groups.

A Hanbury Brown and Twiss (HBT) setup was used to verify single photon emission from these defects. **Fig. 3.6e** shows second-order autocorrelation functions ($g^{(2)}(\tau)$) recorded from representative emitters selected from each group, with ZPLs centered on 633 nm (Group 1 emitter), and 714 nm (Group 2 emitter). Both curves show that $g^{(2)}(0) < 0.5$, proving unambiguously that the defects are point defects that act as single photon emitters (an additional $g^{(2)}(\tau)$ from each group is shown in **Fig. 3.4f,g**. The data were not background-corrected,[202] fit using a three-level model, and offset vertically for clarity.

To calculate phonon mode energies coupled to the emission channel, we record the difference in energy between the ZPL maximum and the highest intensity measured in the PSB of each emitter. It is important to note that emitters in both groups exhibit a similar energy gap difference of 160 ± 5 meV between the ZPL and the PSB (**Fig. 3.6f**). These values indicate that the associated coupled localized vibrations (phonon modes) are very similar, and the defects responsible for all

spectra have similar crystallographic structure [42, 203]. Hence, the two groups likely correspond to two similar defects that reside in different local dielectric environments. The variation in ZPL position within each group may be contributed to by variations in local strain and dielectric environment, as is discussed below. We note that the spectra of emitters in Group 1 are very similar to those of a color center that was previously ascribed to the N_BV_N defect in hBN.[1]

Next, we present a detailed analysis of the photophysical properties of the two emitters whose $g^{(2)}(\tau)$ curves are shown in **Fig. 3.6(e)**, which are representative of emitters in each of the two groups shown in **Fig. 3.6(b,c)**. To obtain the optical transition lifetimes of these emitters, we performed a time-resolved fluorescence measurement using a 510 nm pulsed laser with a 20 MHz repetition rate and 100 ps pulse width. As is seen in **Fig. 3.7a**, the lifetimes of the two emitters were extracted using single exponential fits, yielding values of 2.9 and 6.7 ns for the centers with ZPLs at 633 nm and 714 nm, respectively (the onsets of the decay curves should be ignored since they correspond to the response of our experimental setup).

Fluorescence saturation behavior was characterized by measuring PL intensity as a function of excitation power. The results are shown in **Fig. 3.7b**, and the data were fit using **Eq. 2.2.** The resulting emission rates at saturation for the 633 nm and 714 nm emitters are 2.4×10^6 and 0.1×10^6 counts/s, at P_{sat} = 310 μW and 770 μW, respectively.

To gain further insights into the observed variation in emitter brightness, we measured the autocorrelation functions over longer time scales up to 0.1 seconds. These measurements provide information about the presence of other metastable states with longer decay times [204-206]. **Fig. 3.7(c, d)** shows long timescale photon antibunching curves for the two color centers. By applying an increasing number of components in the multi-exponential fitting function, we obtained a fitting function with the least number of exponentials and lowest fitting residue χ^2 for each center. **Tab. 3.1** summarizes the additional decay lifetimes obtained from the fits.

	ZPL= 633 nm	ZPL = 714 nm
τ_3 [μs]	0.46	5.4
τ_4 [μs]	6.4	25
τ_5 [μs]	----	62

Table 3.1. *Additional metastable states associated with the investigated emitters.*

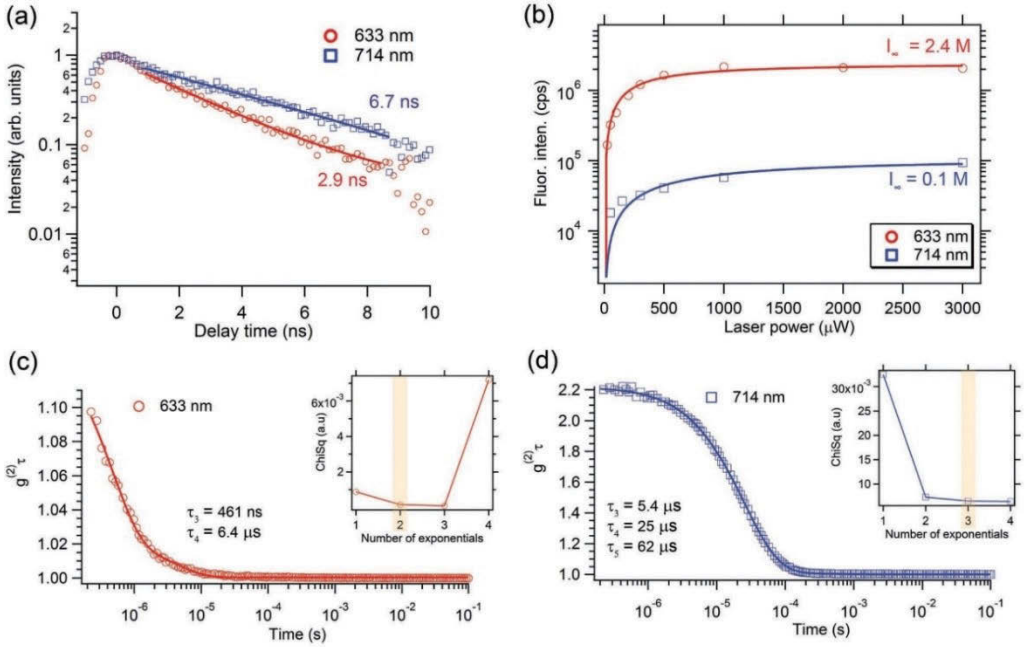

Figure 3.7. *Photophysical properties of the defects.* ***(a)*** *Time-resolved fluorescence measurements showing radiative transition lifetimes of the emitters. An 80 μW, 510 nm pulsed laser with a repetition rate of 20 MHz and a pulse width of 100 ps was used as the excitation source. The solid lines are fits obtained using single exponential decay functions.* ***(b)*** *Fluorescence saturation curves and corresponding theoretical fits calculated using a three-level model.* ***(c, d)*** *Second-order autocorrelation function, $g^{(2)}(\tau)$, recorded over a longer time scale from the two color centers presented in* ***Fig. 3.6*** *with ZPLs at 633 (c) nm and 714 nm (d).*

The corresponding solid traces are theoretical fits to the experimental data. Insets show the fitting residue χ^2 versus the number of exponentials used in the fitting functions. The yellow bands indicate optimal fits realized when the number of exponentials and the residues are simultaneously minimized.

These measurements account for the difference in the overall brightness of the two emitters. The brighter 633 nm defect has fewer metastable states with shorter lifetimes, while the 714 nm defect exhibits multiple additional metastable states with relatively long lifetimes. The differences in lifetimes of both radiative and non-radiative transitions between the two emitters are indicative of local environmental effects such as the presence of neighboring impurities or the proximity of a center to the surface or the edge of a multilayer hBN flake.

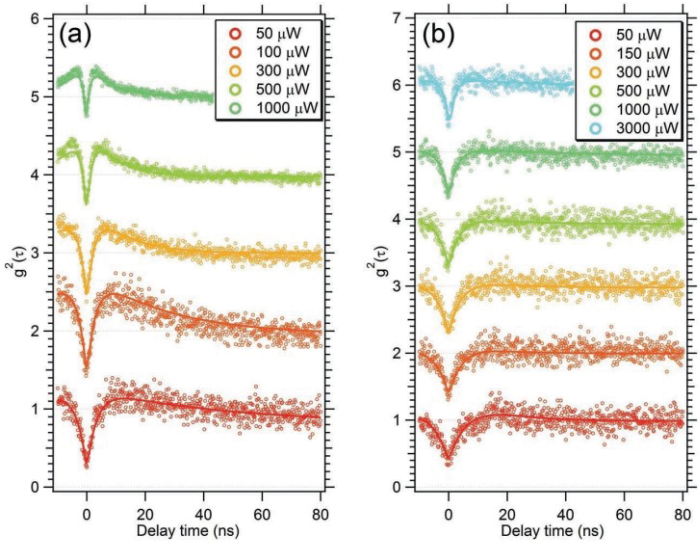

Figure 3.8. *Short timescale second-order autocorrelation function, $g^{(2)}(\tau)$, obtained versus excitation power from the two color centers shown in* ***Fig. 3.6(e)*** *of the main text with ZPLs at* ***(a)*** *633 nm, and* ***(b)*** *714 nm. The $g^{(2)}(\tau)$ functions were acquired using a CW 532 nm laser, an acquisition time of 30 sec, and were normalized (without background correction) and offset vertically by 1 unit each for clarity. Solid traces represent theoretical fits of the experimental data obtained using a typical three-level model expression. The corresponding $g^2(0)$ values are 0.48 and 0.43, corresponding to single photon generation probabilities of 52% and 57% above saturation.*

To further characterize the photodynamics of these emitters, we obtained photon antibunching curves *versus* excitation power (**Fig. 3.9**). By fitting the data using the three-level model (**Eq. 2.1.**), we obtained the power-dependent emission lifetimes, τ_1, and metastable state lifetimes, τ_2, as a function of excitation power [186, 207-208]. The corresponding lifetimes τ^0_1 and τ^0_2 were then obtained by extrapolating the data to zero excitation power [186, 207-208], (**Fig. 3.10**) yielding the values τ^0_1 = 3.3 and 8.1 ns, and τ^0_2 = 88.6 and 1.2 ns for the 633 nm and 714 nm emitters, respectively. The τ^0_1 values are in good agreement with those obtained by the direct time-resolved fluorescence lifetime measurements discussed earlier.

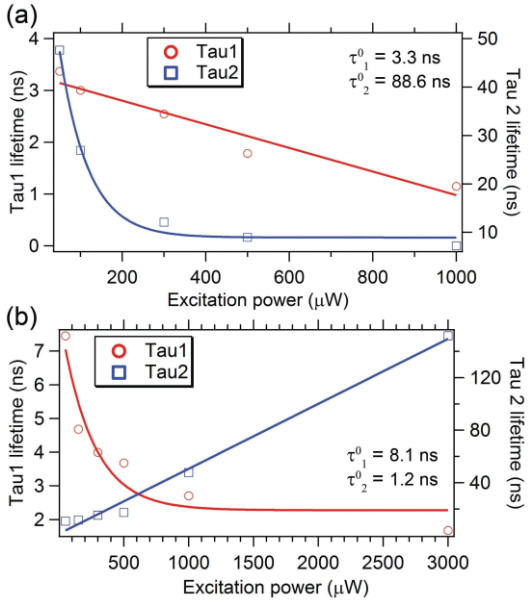

Figure 3.9. *Plot of the power-dependent emission lifetime, τ_1, and metastable state lifetime, τ_2, (obtained by fitting the data in* ***Fig. 3.8****) versus excitation power for the emitters with ZPLs at* ***(a)*** *633 nm and* ***(b)*** *714 nm, respectively. The emission lifetime, τ^0_1, and metastable state, τ^0_2, were deduced by extrapolating the data to zero excitation power.*

Finally, we obtained spectra of emitters from each group at cryogenic temperatures. **Fig. 3.10 (a, b)** shows room temperature and low temperature (14 K) spectra from emitters in Groups 1 and 2 respectively. As expected, the line

width is dramatically reduced and approaching 3.87 and 1.17 meV for emitters in Group 1 and Group 2, respectively. The spectra at low temperature confirm the difference in the ZPL shape for the two groups. In particular, the asymmetry of the ZPL in group 1 is maintained at low temperature highlighting a supplementary phonon side band for these emitters. On the other hand, the symmetry of the ZPL for group 2 is maintained at low temperature.

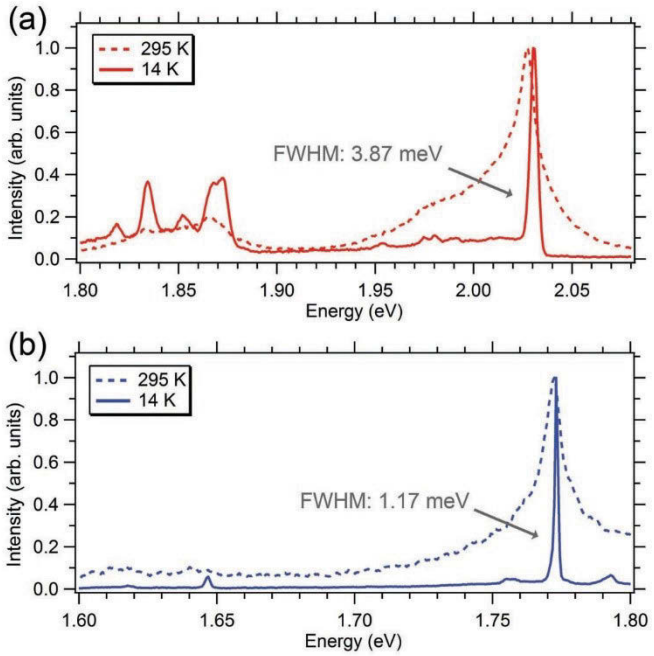

Figure 3.10. *Room- (295 K) and low- (14 K) temperature spectra of representative emitters from* ***(a)*** *Group 1 (dashed and solid red traces), and* ***(b)*** *Group 2 (dashed and solid blue traces), respectively. At 14 K the line widths approach 3.87 and 1.17 meV.*

We now turn back to the range of ZPL energies observed within each group shown in **Fig. 3.6(b, c)**. It is well known that strain can induce shifts in the electronic structure and hence the optical transitions [209]. Such effects can be modeled using DFT simulations, which we, therefore, used to calculate the optical response of a monolayer of hBN that contains the N_BV_N, and has similar photophysical properties to emitters in Group 2 of the present study. The DFT calculations (see **Fig. 3.1**) show that the range of ZPL positions expected from 5% strain is comparable to that observed in each of the two emitter Groups shown in **Fig. 3.6**.

These results are in accord with strain-induced exciton shifts that were observed for other 2D transition metal dichalcogenides, where strains of 3% resulted in 100 meV spectral shifts [98, 210]. Nonetheless, we acknowledge that the magnitude of strain needed to account for the entire observed range of ZPL positions within each group is high, and other effects such as variations in the dielectric environment of the emitters are likely to contribute to the observed shifts.

3.5 Conclusions

In conclusion, we present two robust methodologies to engineer room temperature multicolor single photon emission, based on annealing and electron beam irradiation. Moreover, we show that the emitters are stable even after annealing in harsh gaseous environments such as oxygen, hydrogen, and ammonia. By analyzing spectral features of these emitters, we could infer that there are at least two groups of defects. Although the emitters in the two groups exhibit significant differences in their spectral characteristics, they share similar local phonon energies and therefore are likely to have similar chemical structure. Our work opens up new possibilities for employing quantum emitters in 2D materials for emerging applications in nanophotonics and nanoscale sensing devices.

4 Quantum Emission from Single-Crystalline Hexagonal Boron Nitride

In Chapter 3, detailed photophysics of quantum emitters in hBN multilayers are reported. To further understand whether these emitters existing in the bulk materials, this chapter extends the scope of investigation of quantum emitters at the bulk level. The quantum emitters embedded in the bulk crystals exhibit different characteristics from those in solvent-based exfoliated flakes reported in Chapter 2 and 3. This work was conceived by Igor Aharonovich. The preparation of bulk hBN was done by Takashi Taniguchi and Kenji Watanabe (NIMS, Japan). Luhua Li did the near-edge x-ray absorption fine structure (NEXAFS). Cameron Zachreson and Amanuel Berhane conducted the cathodoluminescence (CL) measurements. Optical measurements and analysis were performed by Trong Toan Tran, with some assistance from Kerem Bray and Russell G. Sandstrom. All the authors discussed and wrote the manuscript.

4.1 Abstract

Bulk hexagonal boron nitride is a highly nonlinear natural hyperbolic material that attracts major attention in modern nanophotonics applications. However, studies of its optical properties in the visible part of the spectrum and quantum emitters hosted by bulk hBN have not been reported to date. In this work, we study the emission properties of hBN crystals in the red spectral range using sub-bandgap optical excitation. Quantum emission from defects is observed at room temperature and characterized in detail. Our results advance the use of hBN in quantum nanophotonics technologies and enhance our fundamental understanding of its optical properties.

4.2 Introduction

Recent studies have been focused on various wide-bandgap materials with superior chemical and thermal stability needed for optoelectronics and applications [109, 119, 167, 211-212]. Bulk hBN is one of these materials and offers excellent

thermal conductivity and bright luminescence in the deep ultraviolet (UV) region associated with band-edge transitions [118, 122-123, 213-215] which is highly advantageous for light emitting devices. Despite numerous studies of these emissions by X-Ray, electron energy loss and luminescence spectroscopy techniques, exact models of the emissions remain under debate. This is in part due to the complicated growth techniques (often high pressure and temperature) that can give rise to significant amounts of dislocations, stacking faults and impurity atoms, including oxygen and carbon. Furthermore, hBN is a naturally hyperbolic material. Its extreme optical anisotropy gives rise to potentially interesting applications based on sub-wavelength confinement and strong light-matter interactions [127-129]. However, to fully exploit the potential of hBN for quantum nanophotonics applications, true single photon emitters in this material must be identified.

Here, we report a comprehensive study of single photon emitters in the visible and near-infrared regions hosted by bulk hBN crystals. Our results promote the use of hBN as an interesting candidate for emerging applications in quantum technologies and nanophotonics.

4.3 Methods

The hBN single crystals used in this work were produced by the high-temperature and high-pressure process [150]. The hBN crystals were annealed for 30 min at 850°C under 0.5 Torr of Argon in a conventional tube furnace. The samples were heated at a ramp rate of 2°C/sec from room temperature. Upon completion, the samples were cooled to room temperature overnight. The annealing process was used to increase the number of luminescent defect centers. Optical images were obtained using a Zeiss optical microscope. Raman spectroscopy was conducted using a Renishaw in Via Raman™ microscope. The confocal maps and single photon spectroscopy were performed at room temperature using a continuous wave 532 nm laser (Gem 532™, Laser Quantum Ltd.). The laser was directed through a Glan-Taylor polarizer (Thorlabs Inc.) and a half waveplate and focused onto the sample using a high numerical aperture (NA = 0.9, Nikon) objective lens.

Scanning was performed using an X-Y piezo scanning mirror (FSM-300TM, Newport Corp.) or an X-Y-Z nanocube system (PI instruments). The collected light was filtered using a 532 nm dichroic mirror (532 nm laser BrightLine™, Semrock Inc.) and an additional long pass filter (SemrockTM). The signal was then coupled into a graded index fiber, where the fiber aperture serves as a confocal pinhole. A fiber splitter was used to direct the light into a spectrometer (Acton SpectraPro™, Princeton Instrument Inc.) or two avalanche photodiodes (Excelitas Technologies™) used for single photon counting. Correlation measurements were done using a time-correlated single photon counting module (PicoHarp300™, PicoQuant™). Lifetime measurements were performed using a 675 nm pulsed laser excitation source (PiL067X™, Advanced Laser Diode Systems™ GmbH) with a 45 ps pulse width.

4.4 Results and Discussion

We start by surveying the sample using conventional optical microscopy and Raman spectroscopy, as shown in **Fig. 4.1**. The bulk crystal shows a number of visible stacking disorder lines (**Fig. 4.1a**). Raman spectra of the sample exhibit the characteristic E_{2g} in-plane vibrational mode of bulk hexagonal boron nitride at 1365 cm-1, with a full width at half maximum (FWHM) of 8.2 cm-1 (**Fig. 4.1b**), indicating that the sample is a high-quality crystal [163].

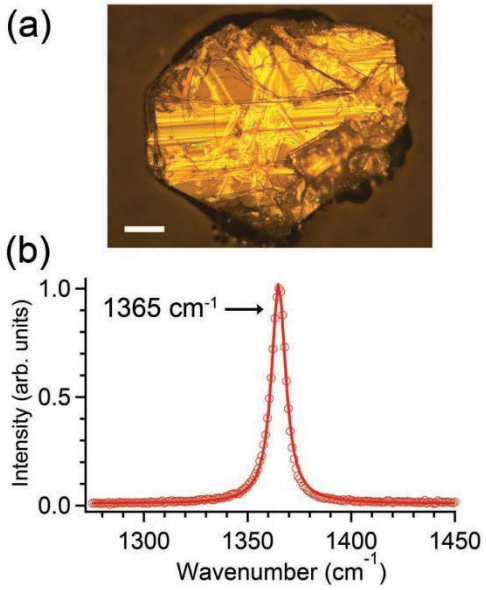

Figure 4.1. ***(a)*** *Optical microscope image of bulk hBN. The scale bar indicates 100 μm.* ***(b)*** *Raman scattering spectrum obtained with a 633 nm He-Ne laser showing a peak at 1365 cm^{-1} with an FWHM of 8.2 cm^{-1}.*

Additional characterization was performed using NEXAFS and CL spectroscopy [216]. The results are provided in **Fig. 4.2.**, along with corresponding data from a second sample that contained a lower concentration of defects (as per NEXAFS and optical microscopy data) [216]. We note that the single photon emitters characterized below (**Fig. 4.4, 4.6, 4.7**) were not found in this second sample (see **Fig. 4.2b)**.

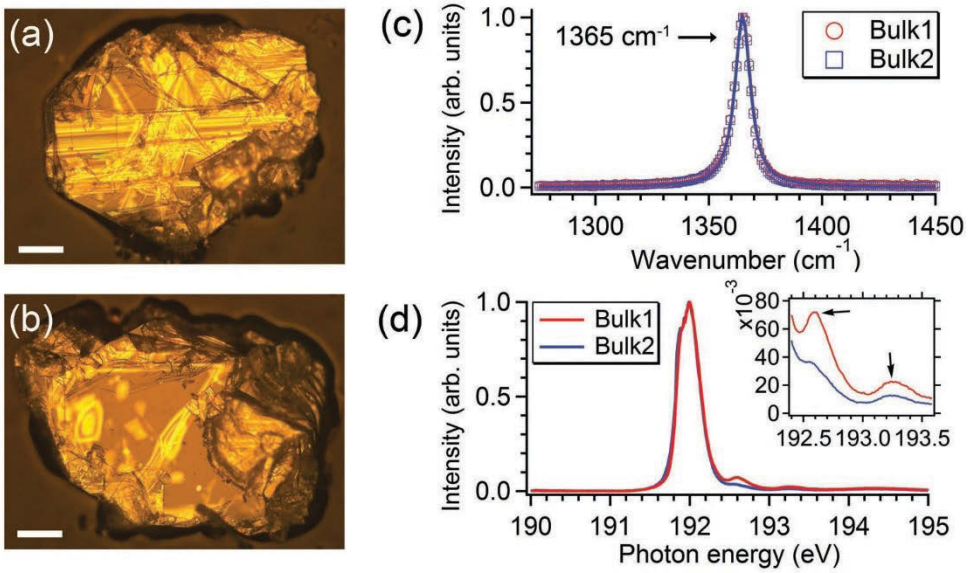

Figure 4.2. *Optical microscope images of bulk hBN samples with* ***(a)*** *a high density of dislocation defects (Bulk1), and* ***(b)*** *a low density of dislocation defects (Bulk2). Numerous planar stacking faults can be clearly seen in sample Bulk1. The scale bars indicate 100 μm.* ***(c)*** *Raman scattering spectra obtained with a 633 nm He-Ne laser showing a peak at 1365 cm^{-1} with an FWHM of 8.2 cm^{-1} for each sample.* ***(d)*** *NEXAFS spectra around the B K-edge spectral region. The inset details a spectral region in which sample Bulk1 shows higher intensity peaks compared to Bulk2 (i.e., a higher concentration of defects relative to Bulk2).*

Most prior luminescence studies of bulk hBN were performed using above band-gap excitation (as in **Fig. 4.3**), whereby the emission spectra are typically dominated by UV or near-UV luminescence **[216]**.

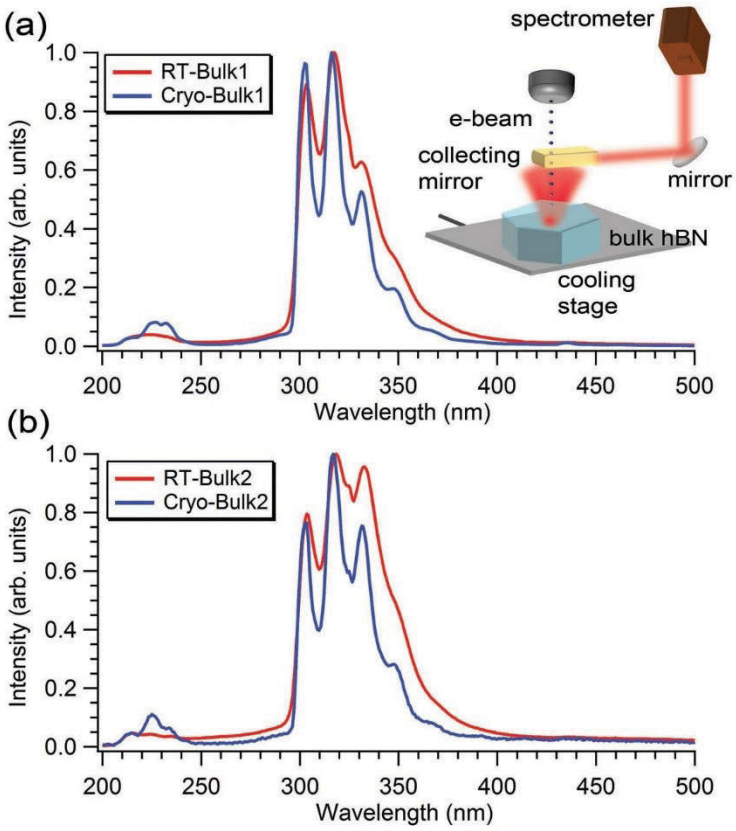

Figure 4.3. *Cathodoluminescence spectra acquired at 295 K (red trace) and 77 K (blue trace) from sample* ***(a)*** *Bulk1 and* ***(b)*** *Bulk2. The inset is a schematic illustration of the CL setup.*

On the contrary, in this letter, we adopt the techniques used for other wide bandgap materials, such as SiC and diamond, in order to access deep, defect-related levels preferentially and avoid transitions that entail the conduction and valence bands. **Fig. 4.4a** shows a typical confocal PL map of the hBN crystal obtained using a 532 nm excitation laser and a shallow confocal depth of a few hundred nanometers, revealing an isolated emission (circled in red) along with other ensemble emissions. A background spectrum (dotted grey trace) obtained from a region adjacent to the emitter is shown in **Fig. 4.4b**, revealing two Raman lines at 575 nm and 583 nm **[217]**. A PL spectrum taken from this particular defect (solid red trace

in **Fig. 4.4b**) reveals two sharp peaks at 618 nm and 629 nm. Both peaks are potentially the zero-phonon lines (ZPLs) of a color center and are relatively close to the emission line in our previous report **[4]**. Correlation spectroscopy using a Hanbury Brown & Twiss (HBT) interferometer was therefore used to prove that the two peaks correspond to an isolated defect that emits single photons. **Fig. 4.4c** displays the second-order autocorrelation measurement, $g^2(\tau)$, showing that at zero delay time, $g^2(0) \sim 0.35$ (**Fig. 4.4c**, where the red dots are experimental data while the solid line is a fit obtained using a three-level model). The $g^2(0)$ value of less than 0.5 proves unambiguously that the emitter is a single photon source **[12, 202, 218]** (we note that the data are not corrected for the background which comprises ~ 30% of the total light intensity). On average, we found two such isolated emitters in each 60 x 60 μm^2 area of the sample.

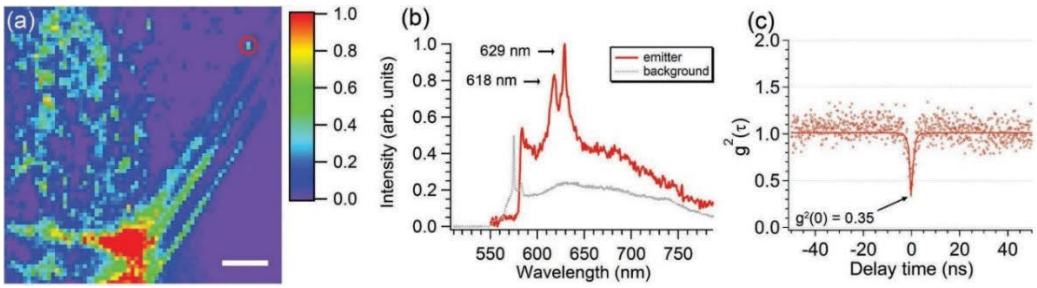

Figure 4.4. *Optical characterization performed with a 532 nm CW laser and a 568 nm long pass filter in the collection pathway.* ***(a)*** *A typical confocal map of bulk hBN showing a number of isolated emission centers and ensembles of these centers. The scale bar indicates 10 μm.* ***(b)*** *A room-temperature photoluminescence spectrum of the isolated emission circled in the PL confocal map. The solid red and dotted grey traces represent emitter and background spectra, respectively. The emitter spectrum reveals a pair of peaks at 618 nm and 629 nm that are potentially the zero-phonon lines of the defect transition.* ***(c)*** *An antibunching curve recorded from the defect center in* ***(b)*** *showing a dip of ~ 0.35, proving the single photon emission nature of the defect. The bin size in* ***(c)*** *is 128 ps.*

The emission associated with the defect characterized in **Fig. 4.4** bleached after several minutes of excitation at 532 nm. To gain additional insights into the occurrence of emitters in hBN, we employed a longer excitation wavelength of 675 nm. A typical confocal map is shown in **Fig. 4.6a** and contains several isolated emission spots. Similar to the previous case, we found an average of two isolated emitters in each 60 x 60 μm^2 area of the sample. A PL spectrum (solid red trace) taken from one of these spots (circled in red), shows a broad emission band in the range of ~770 – 900 nm (**Fig. 4.6b**). The dotted grey trace is the background luminescence **[217]**. We note that in **Fig. 4.6b** the line at ~ 745 nm is most likely background as it appears in the grey curve as well, while the line at ~ 760 nm is a potential ZPL. A second-order autocorrelation function, $g^2(\tau)$, is shown in **Fig. 4.6c** (the red dots are experimental data while the solid line is a fit obtained using a three-level model). A dip of ~ 0.37 at zero delay time confirms the single photon emission nature of the center. As our antibunching curve was obtained without background correction, the deviation from zero originates primarily from background emissions from the crystal. The inset of **Fig. 4.6c** demonstrates triggered single photon emission using pulsed excitation, which is important for many practical nanophotonics applications.

Measurements of fluorescence intensity from the same defect as a function of excitation power show that the fluorescence saturates at a count rate slightly greater than 200,000 counts/sec, comparable with other single photon emitters in bulk materials **[63]**. Time-resolved fluorescence measurements yield a lifetime of ~1.0 ns (**Fig. 4.6d**). This value is comparable to most conventional single emitters in bulk materials **[57, 63]**. Polarization measurements were conducted using a combination of a linear half-waveplate and/or a linear polarized filter **(**in **Fig. 4.5**) **[216]**. The results show the emission is fully linearly polarized.

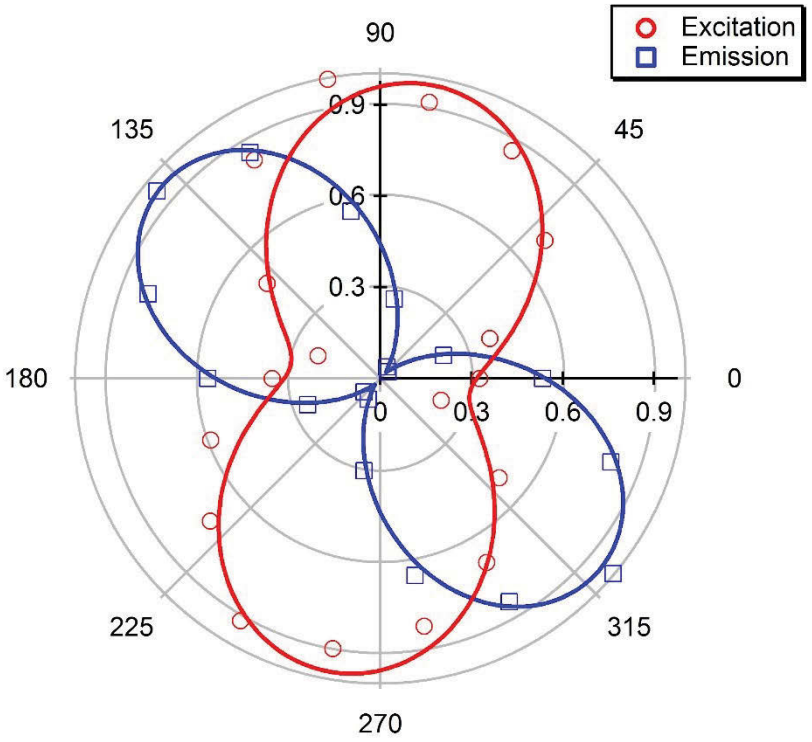

Figure 4.5. *Normalized excitation (red trace) and emission (blue trace) polarization plot of defect center similar to that in* ***Fig. 4.6.*** *of the main text. The excitation source was a CW 300 μW, 675 nm laser.*

The electron-phonon coupling characteristics of the two emitters were estimated using the Huang-Rhys (RH) factor. By fitting the PL spectra with multiple Lorentzian peaks, we calculated the RH factor to be 0.93 and 1.93 for the color centers shown in **Fig. 4.4** and **Fig. 4.6**, respectively (in the case of the former, the analysis was done using the combined intensity of the two ZPLs, and the total intensity of the broad phonon sideband emission which is assumed to consist of two overlapping sidebands corresponding to the ZPLs). These values are in good agreement with the prior literature **[122]**.

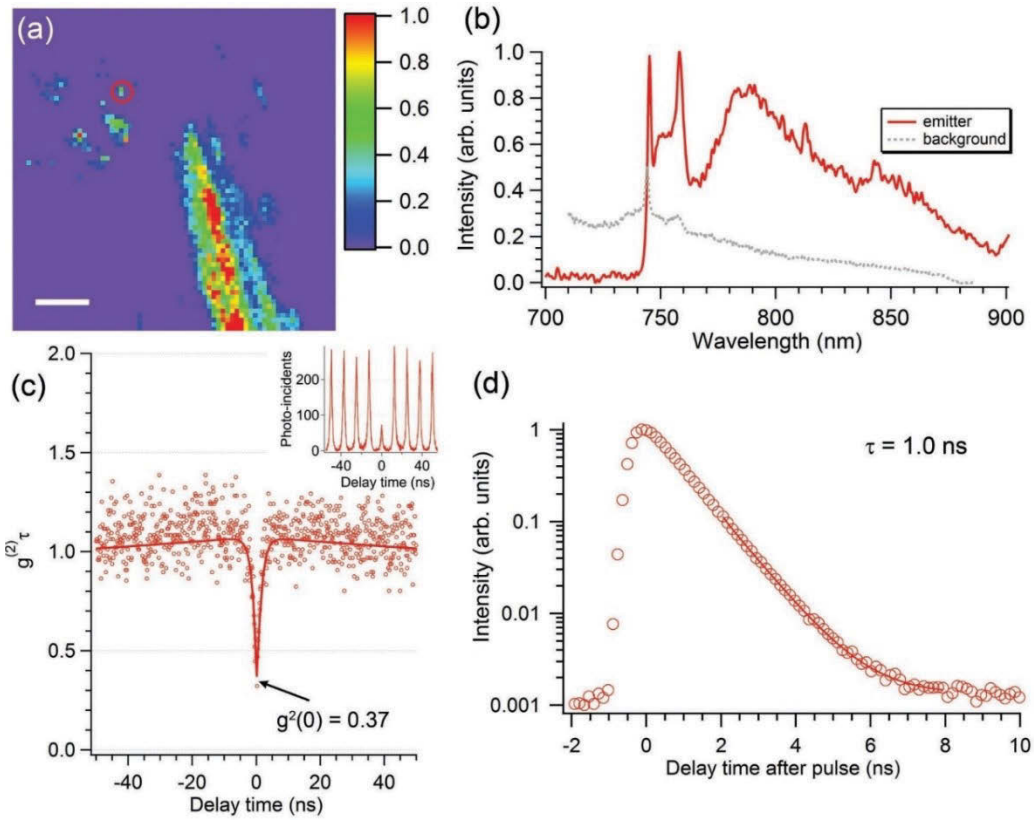

Figure 4.6. ***(a)*** *A typical confocal map showing isolated emission centers and ensembles of emitters.* The scale bar indicates 10 μm. ***(b)*** *A room-temperature PL spectrum of the isolated emission that is circled in the PL confocal map, revealing a broad emission band at ~ 770 – 900 nm. The solid red and dotted grey traces represent emitter and background spectra, respectively.* ***(c)*** *An antibunching curve recorded by continuous wave excitation of the defect center in* ***(b)*** *showing a dip of ~0.37, proving the quantum nature of the defect. The inset shows a similar antibunching curve obtained by pulsed excitation.* ***(d)*** *Time-resolved fluorescence measurement of the defect center in* ***(b)*** *revealing a very short radiative lifetime of ~ 1.0 ns. All measurements were done using a 675 nm CW laser at room temperature, with an 855 ± 110 nm bandpass filter. Pulsed* $g^2(\tau)$ *and lifetime measurements (d) were conducted using a 675 nm laser with a pulse width of 45 ps, a power of 200 μW, and repetition rate of 80 MHz. The bin size in* ***(b)*** *and* ***(d)*** *is 128 ps.*

To characterize the photodynamics of the defect shown in **Fig. 4.6** further, time-correlated measurements were performed on the emitter. The detected photons were time-tagged over a long time scale, and the results are shown in **Fig. 4.7a**. Three exponential components yield the best fit for the autocorrelation curve. This indicates that there are several additional metastable states associated with the electronic structure of this defect besides its principle radiative transition (i.e., between the ground state and the excited state). An illustration of such an excited electronic structure is shown in the inset of **Fig. 4.7a**, with lifetimes of the three additional metastable states of 480 ns, 5 μs, and 31 ms, respectively. The transition rates to these states are relatively low, which explains why the defect can be detected on a single photon level with reasonable brightness.

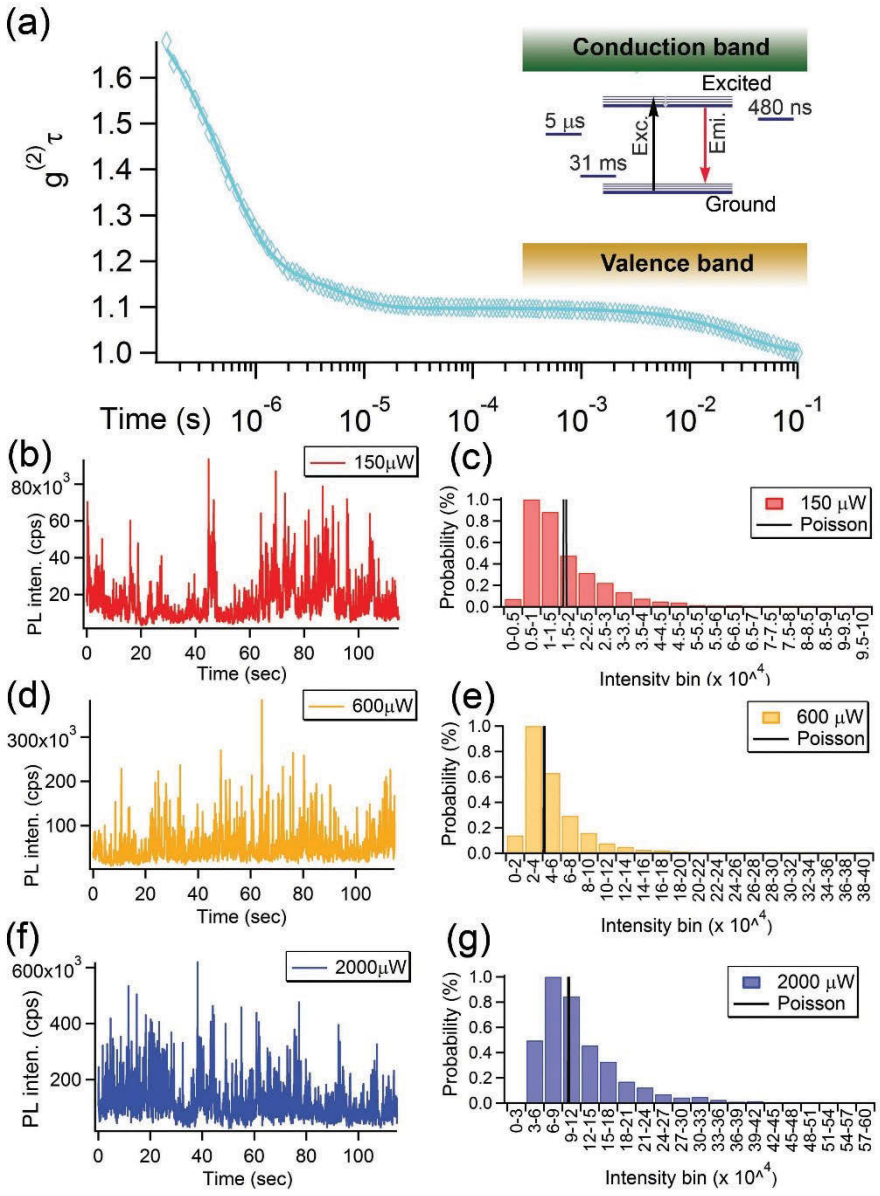

Figure 4.7. (a) *Long time-scale second-order autocorrelation function (recorded up to 0.1 s) reveals at least 3 possible metastable states of the defect center characterized in* ***Fig. 4.3****. The inset illustrates the possible excited electronic configuration of the defect center, including the existence of three metastable states. Temporal fluorescence intensity fluctuations at* ***(b)*** *150 μW,* ***(d)*** *600 μW, and* ***(f)*** *2000 μW and the corresponding histograms at* ***(c)*** *150 μW,* ***(e)*** *600 μW, and* ***(g)*** *2000 μW. The black traces in* ***(c)****,* ***(e)****, and* ***(g)*** *are corresponding simulated Poisson distributions, shown for comparison. The time-bin size in* ***(b)****,* ***(d)*** *and* ***(f)*** *is 50 ms.*

To elucidate the complex dynamics further, we characterized the blinking behavior of the defect at elevated excitation power. Plots of fluorescence intensity were recorded as a function of time at excitation powers of 150 μW (**Fig. 4.7b**), 600 μW (**Fig. 4.7d**) and 2000 μW (**Fig. 4.7f**). Blinking is clearly observed at all the investigated excitation powers. However, no bleaching of the defect is observed. This behavior is consistent with the autocorrelation function recorded in **Fig. 4.4a**, and confirms the power-dependence of the transition to the metastable states. Histograms of the fluorescence intensity (**Fig. 4.7c**, **4.7e**, and **4.7g**) reveal asymmetric distributions, rather than Poisson distributions expected from a non-blinking emitter, similar to that observed in ZnO nanoparticles [204]. Such behavior often referred to as ”photon bursts”, is characteristic of an intermittent bright state. The severe spectral diffusion, seen clearly in an OFF/ON histogram shown in **Fig. 4.8** [216], is likely associated with proximity of the emitter to the surface or to extended defects. Given the wide bandgap of hBN, it is expected that additional defects with other ZPL positions will be found, as in the case of shallow emitters in diamond [219].

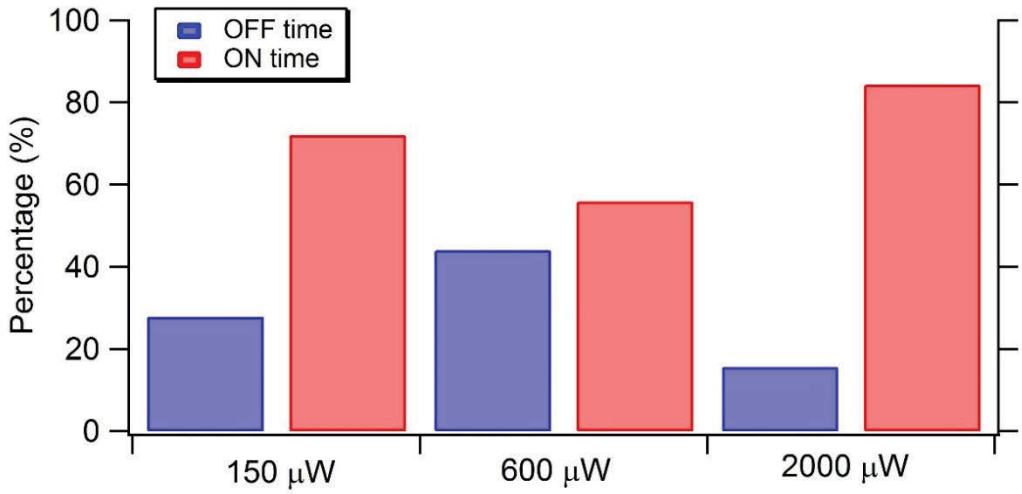

Figure 4.8. *Histogram of fluorescence OFF (blue trace) and ON (red trace) time (%) for the emitter presented in* ***Fig. 4.3*** *of the main text. A cut-off threshold of 10 % of maximum fluorescence intensity was used to define the OFF state and generate the histogram.*

We would like to highlight differences between the current work and a recent report of a quantum emitters in hBN [4]. First, the host materials are different, namely the bulk, three-dimensional hBN crystal shown in **Fig. 4.1a**, compared to two-dimensional hBN studied in [4]. Second, the emitters characterized in **Fig. 4.4, 4.6, 4.7** exhibit different photophysical properties and temporal dynamics. Specifically, the emitter reported in has characteristic PL spectra and photostability/photodynamics characteristics in monolayer hBN and few-layer 2D hBN, all of which are different from those of the two emitters in bulk hBN reported here.

In addition, 2D materials have strong confinement in the direction perpendicular to their basal plane and are not affected by adjacent layers via van der Waals forces [92, 97]. This may results in stronger dipole moments within the 2D monolayers. On the other hand, strain fields should be weaker in the 3D lattice, and emitters in bulk crystals are not expected to be affected as much by the environment. The unusual anisotropic dielectric environment in the 3D hBN lattice is predicted to provide extraordinary non-linear optical properties such as sub-diffraction focusing and guiding of emitted light that is of crucial importance for next-generation optoelectronic applications [126, 128].

Finally, we note that it is important to identify and study emitters in both bulk and nanoscale materials, as they are used for entirely different applications. For instance, the bulk hBN studied here could be exploited in monolithic on-chip integrated photonic circuits [220], and it has hyperbolic properties [126, 128] that do not exist in monolayer hBN.

4.5 Conclusions

In summary, room temperature single photon emission from bulk hBN was observed in the visible and the near-infrared spectral ranges. The longer wavelength center does not bleach and has a short lifetime of ~1 ns. The defect centers offer a new class of a single photon source to be realized based on bulk hBN. Our results enhance present understanding of fundamental quantum

phenomena in hBN and open the door to studies of light-matter interactions with quantum emitters in a hyperbolic medium.

5 Resonant Excitation of Quantum Emitters in Hexagonal Boron Nitride

This chapter presents the first demonstration of resonant excitation of quantum emitters in hBN flakes. Igor Aharonovich conceived the idea of the project. Trong Toan Tran and Mehran Kianinia constructed the resonant excitation setup. The optical measurements and analysis were done by Trong Toan Tran, with some assistance from Mehran Kianinia, Zai-quan Xu, Sejeong Kim, and Minh Nguyen. All the authors discussed and wrote the manuscript.

5.1 Abstract

Quantum emitters in layered hexagonal boron nitride have recently attracted a great deal of attention as promising single photon sources. In this work, we demonstrate resonant excitation of a single defect center in hBN, one of the most important prerequisites for employment of optical sources in quantum information processing applications. We observe spectral linewidths of an hBN emitter narrower than 1 GHz while the emitter experiences spectral diffusion. Temporal photoluminescence measurements reveal an average spectral diffusion time of around 100 ms. An on-resonance photon antibunching measurement is also realized. Our results shed light on the potential use of quantum emitters in hBN in nanophotonics and quantum information processing applications.

5.2 Introduction

Solid-state quantum emitters in low-dimensional hosts have emerged as promising candidates for quantum information and communications, owing to their strong PL and the potential use in integrated nanophotonics [17, 221-223]. Within this class of single photon emitters, optically active defect centers in layered hexagonal boron nitride, a two-dimensional dielectric, have gained tremendous research momentum due to outstanding characteristics such as high brightness at room temperature [4, 224-225], high photon contribution into ZPLs [5, 226], linearly polarized emission [227-229], high photo-stability even upon heating to 800 K

[230], and spectral tenability [5, 225]. Furthermore, integration of hBN emitters with plasmonic nanocavities [9] and tapered-fibers [231] have recently been demonstrated as the first step towards integrated on-chip circuits.

Recent cryogenic measurements revealed that some of the emitters have stable spectral lines as narrow as 45 μeV [226, 232]. It has also been shown that some emitters suffer from ultrafast spectral diffusion that causes broadening of the ZPLs [233]. However, to date, coherent resonant excitation of these quantum emitters has not been demonstrated. Resonant excitation is important for understanding the fundamental photophysical processes of solid-state quantum emitters, and vital for the realization of advanced quantum experiments, including generation of indistinguishable photons, entanglement and optical coherent control of quantum states [61, 223, 234-239].

In this work, we report resonant photoluminescence excitation (PLE) of a single hBN emitter at 8 K. The emitter shows optical linewidths of less than 1 GHz, but blinking and spectral diffusion result in a broader optical envelope that spans approximately 6.3 GHz. Despite the spectral diffusion, single photon emission is confirmed by recording an on-resonance second-order autocorrelation function. Our results shed light on outstanding challenges with this intriguing quantum system and represent a stepping stone towards the generation of indistinguishable photons for quantum information processing applications.

5.3 Methods

We employed hBN flakes (Graphene Supermarket, ~200 – 500 nm in diameter) that were drop-casted on a 1 x 1 cm^2 silicon substrate. The substrate was thermally treated in argon at 850°C for half an hour to activate defects in hBN optically [4]. These hBN flakes were well-characterized with SEM and AFM by previous reports [4, 227]. The sample was mounted on a three-dimensional piezo stage (Attocube Inc.) of a home-built open-loop cryostat with flowing liquid helium (**Fig. 5.1a**). The sample was excited with a computer-controlled CW Titanium:Sapphire (Ti:Sap) laser (SolsTis, M2 Inc.) with a narrow spectral linewidth of 50 kHz. Excitation and collection light was split by a 90:10

(transmission: reflection) non-polarizing beamsplitter and collected through an objective lens with (NA= 0.95), which was mounted inside the cryostat. Residual pump laser was rejected using the combination of a 715 nm longpass and 850 ± 105 nm bandpass filter (Semrock Inc.). It is noted that for both PLE and on-resonance excitation experiments, only the light from the PSB was collected, and not from the ZPL, to avoid collection of scattered laser light. Time-resolved PL was carried out with a pulsed 675 nm diode laser (~ 50 ps pulse width) with a repetition rate of 10 MHz and a power of 100 μW. Second-order autocorrelation measurements were performed with an HBT interferometer and a TCSPC module.

5.4 Results and Discussion

Quantum emitters in hBN flakes are known to display a wide range of ZPL energies spanning ~ 570 – 770 nm [5-6, 227-228, 240]. Making it possible to select and address a particular optical transition of interest within this range. We, therefore, conducted survey confocal PL mapping using a CW laser tuned at 700 nm to off-resonantly excite hBN emitters at 8 K and selected a bright emitter for further optical investigation (**Fig. 5.1b**, black arrow). The emitter, at room temperature, has a weak PSB, and an asymmetric ZPL shape, consistent with the literature [5]. While the FWHM of the emitter at room temperature was ~10 nm (5.1 THz), at 8 K, the ZPL width was limited by our spectrometer resolution of 25 GHz (**Fig. 5.1c**). It should be noted that the small peak at ~ 800 nm is likely a ZPL of another weak emitter within the excitation spot. The inset of **Fig. 5.1c** shows a higher resolution spectrum of the emitter, indicating a ZPL position of 766.8 nm (391.2 THz).

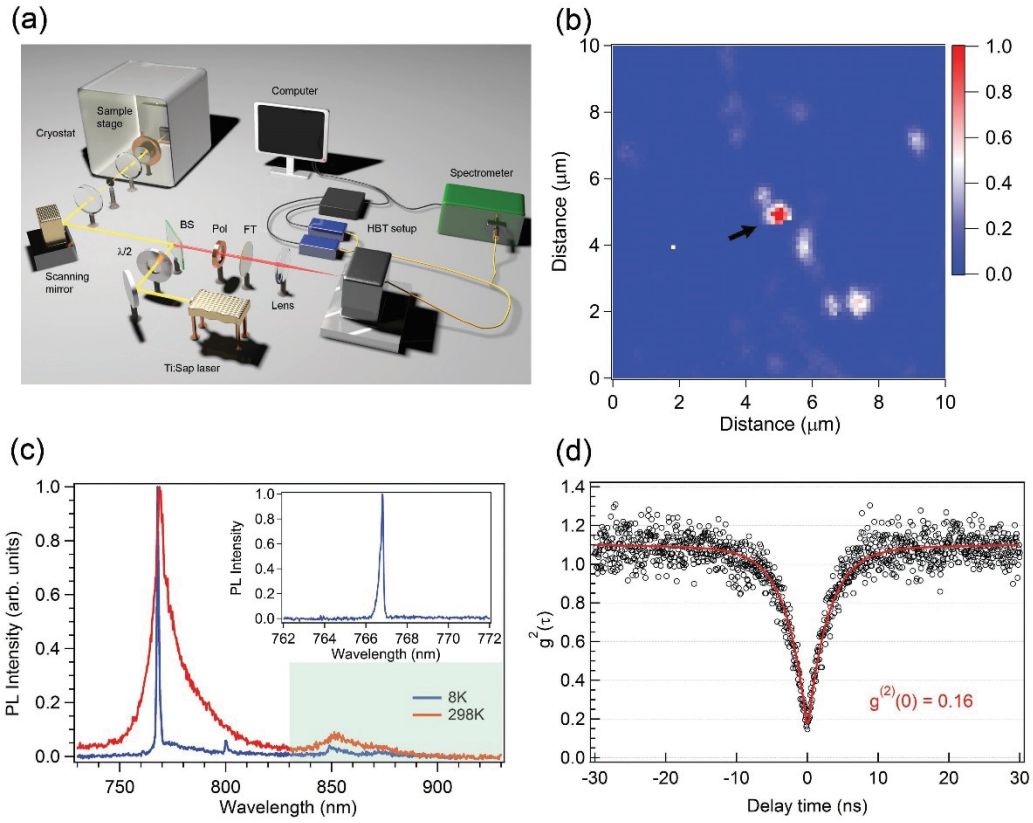

Figure 5.1. (a) *Cryogenic confocal PL setup. HBT: Hanbury-Brown and Twiss; BS: beamsplitter; FT: band-pass or long-pass filters; λ/2: half-wave plate; Pol: linear polarizer.* ***(b)*** *Confocal PL map recorded with 700-nm laser excitation at 300 μW. The bright spot corresponds to a single emitter. The measurement was acquired at 8 K.* ***(c)*** *Normalized PL spectrum taken from the same emitter at 8 K (blue trace) and 298 K (red trace) with a 300g/mm grating. The green-highlighted box indicates the collected spectral range for the PLE experiment in* ***Fig. 5.3****. The inset shows a higher resolution spectrum taken from the same emitter (with a 1800g/mm grating).* ***(d)*** *Second-order autocorrelation function (black open circles) acquired for the emitter using a 700 nm laser at 100 μW power as the excitation source, acquired for 5 minutes. The measurement was conducted at 8 K. The red solid line is the fitting for the $g^{(2)}(0)$ function using a three-level model convoluted by a Gaussian jitter response (see main text). The $g^{(2)}(0)$ value of 0.16 ± 0.01, without any background correction, indicates that the emission is from a single emitter. The standard deviation was based on the standard deviation taken*

from the long delay region. A band-pass filter was used in the measurements of confocal PL in (b) and the photon second-order autocorrelation function (d) to minimize the background PL contribution.

To verify the single photon purity of the defect under off-resonant excitation, we recorded the second-order autocorrelation function, $g^{(2)}(\tau)$, (**Fig. 5.1d)**. To quantify the jitter contribution in our detection scheme, we measured the standard deviation of the instrument response function (IRF) to be 0.5 ns by fitting a Gaussian to the IRF. We then used the Gaussian-convoluted three-level model to fit the data mentioned in the main text, taking into account the timing-jitter effect [207]:

$$g^{(2)}_{meas}(\tau) = \int_{-\infty}^{+\infty} g^{(2)}(\tau') J(\tau - \tau') d\tau' \quad \textbf{(5.1)}$$

with $g^{(2)}(\tau') = 1 - (1 + a)e^{-\tau'/\tau_1} + ae^{-\tau'/\tau_2}$ **(5.2)**, and $J(\tau - \tau') = \frac{1}{\sigma\sqrt{2\pi}} e^{\frac{-(\tau-\tau')^2}{2\sigma^2}}$ **(5.3)**

where $J(\tau - \tau')$ is the IRF, and σ is the standard deviation; *a* is the bunching factor, while τ_1 and τ_2 are the antibunching and bunching time, respectively.

From the convoluted three-level model fitting function, an antibunching dip or $g^{(2)}_{meas}(0)$) of 0.16 ± 0.01, with the deduced antibunching time value of $\tau_1 \sim 3$ ns was derived (red solid line). The $g^{(2)}_{meas}(0)$ value is well below 0.5 and thus clearly indicates the single photon nature of the emitter [241]. The small deviation from zero is mainly caused by the contribution of fluorescence background within the laser spot [186]. Polarization PL measurements showed that the transition dipole moment of the defect center is perpendicular to the optical axis (**Fig. 5.2a**). The emitter also exhibits high brightness with a saturated PL intensity in excess of 1×10^6counts/sec (**Fig. 5.2b**).

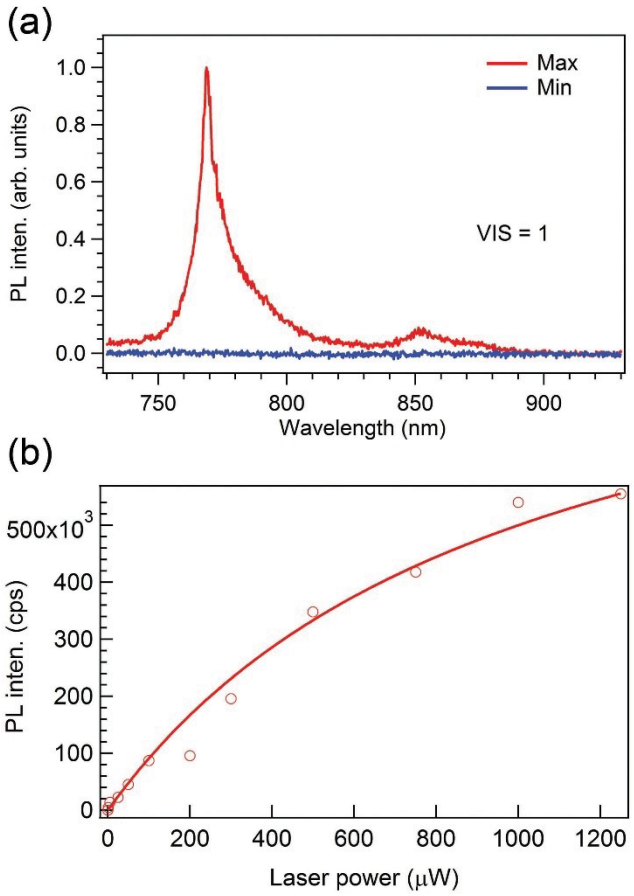

Figure 5.2. (a) *Spectra showing maximum (red trace) and minimum (blue trace) emission polarization from the emitter taken with the use of a linear polarizer. The data was taken using an excitation laser power of 300 μW with a 5 s acquisition time. The visibility was determined to be unity.* ***(b)*** *Power-dependent fluorescence saturation curve (red open circles). The fit (solid red line) produces values of* I_{max} *and* P_{sat} *of 1.3 Mcounts/sec and 1.6 mW, respectively. The measurement was acquired with a bandpass filter (760 ± 12) nm. All the measurements were conducted at room temperature.*

Although off-resonant excitation is convenient due to its relative insensitivity to excitation wavelength, the excited electron is required to vibrationally relax before spontaneous emission takes place (**Fig. 5.3a**). Resonant excitation, on the other hand, enables coherent access to manipulation of quantum states and is a practical means to realize photon indistinguishability. We, therefore, proceeded to investigate the emitter of interest resonantly. The Ti:Sap laser wavelength,

frequency-stabilized by a high-resolution external cavity (WS6, HighFinesse), was scanned across the ZPL, and the fluorescence signal was collected by a single photon counting avalanche photodiode (SPCAPD). To minimize laser scattering, we chose to spectrally filter out the residual pump laser with a 830 nm longpass filter and collect the red-shifted photons from the PSB (highlighted in the **Fig. 5.1c**), instead of using the cross-polarization technique [242].

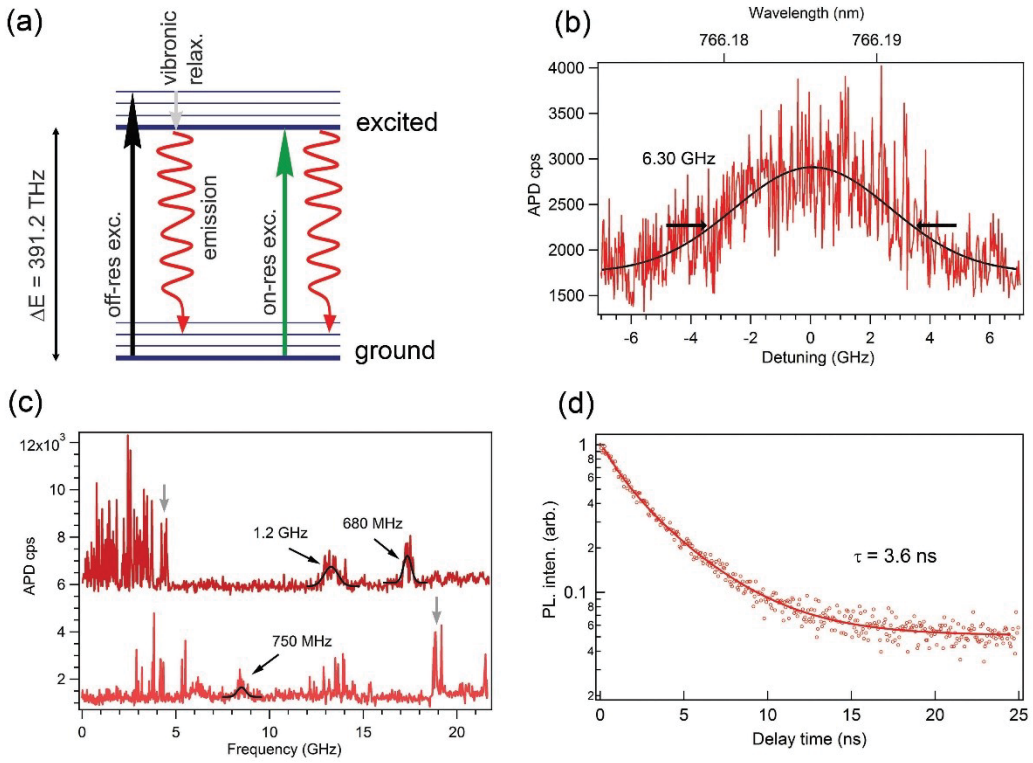

Figure 5.3. (a) *Simplified diagram of the hBN emitter where the excited state can be accessed via either off-resonance or on-resonance excitation, with the former pathway on the left, and the latter pathway on the right. Black and grey arrows, indicate excitation towards the higher vibronic states, followed by vibronic relaxation towards the excited ground state. The green arrow indicates on-resonance excitation, followed by spontaneous emission denoted by the wavy red arrow in both pathways.* ***(b)*** *Resonance photoluminescence excitation measurements on the single emitter with a ZPL peak at 766.186 nm. The excitation power used was 150 nW. Only photons from the PSB were collected using a long pass filter. The experimental data is plotted as the red trace. Five repetitive scans*

were averaged out to get the final data. The data was fit with either a Gaussian function (black solid line). The measurement was done at 8 K. ***(c)*** *Additional survey PLE scans showing multiple local maxima with FWHM below 2 GHz. The grey arrows show representative spectral features that are asymmetrical.* ***(d)*** *Time-resolved PL measurements (red open circles) of the same single emitter measured at room temperature. A single-exponential fit gives rise to a lifetime of 3.6 ns for the emitter's excited state. The measurement was done with a 675 nm pulsed laser (100 μW, 10 MHz repetition rate, 100 ps pulse width).*

Under our experimental conditions, only those emitters with lines above 700 nm were considered, because of the use of a Ti:SAP laser that is tunable from 700 – 900 nm. Out of the emitters that have a ZPL above 700 nm, approximately 20% of the investigated emitters showed stable spectrometer-limited or nearly spectrometer-limited lines that can be effectively filtered. Out of those, we attempted PLE on several emitters. All these emitters responded to the resonant excitation, though most exhibited severe spectral jumps (**Fig. 5.4**).

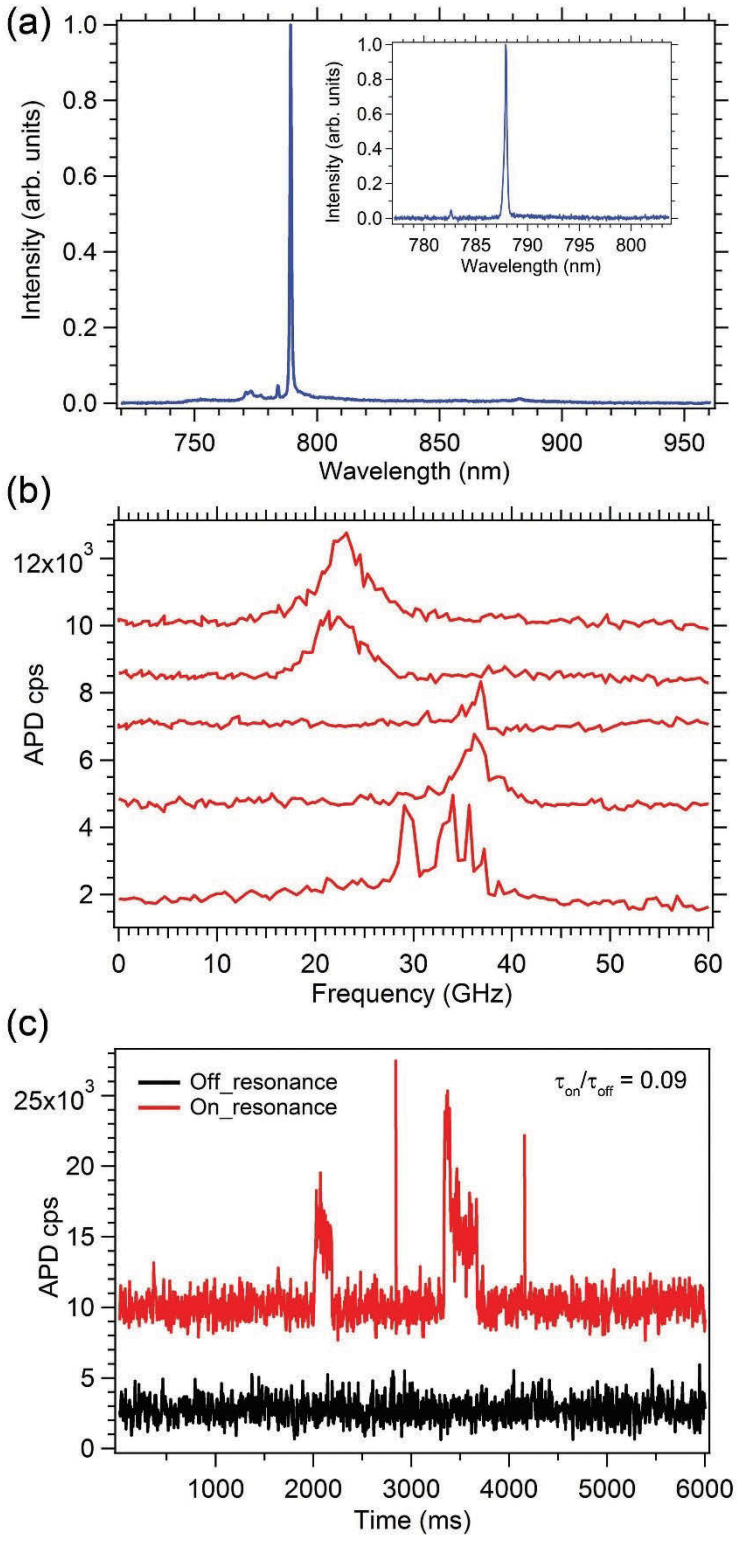

Figure 5.4. *Optical characterization of another defect center.* ***(a)*** *High- and low-resolution (inset) PL spectra taken from the emitter by off-resonant excitation at 700-nm with 300μW laser power.* ***(b)*** *Five repeated scans over 60 GHz range*

showing some complete optical resonance features as well as some asymmetrical features. ***(c)*** *On-resonant excitation with the laser fixed at 787.592 nm (red solid line) and 2-nm detuned from the on-resonance excitation wavelength (black solid line). The calculated* τ_{ON}/τ_{OFF} *= 0.09 indicates that the emitter is mostly in unexcited states.*

Fig. 5.3b shows a resonant PLE plot obtained by averaging five consecutive scans over the same 14 GHz range with 70 MHz resolution (each scan lasting for ~ 2 minutes). The laser power was kept at 150 nW to prevent power-induced broadening. A single broad peak was observed at 766.186 nm, with a Gaussian FWHM of 6.3 ± 0.3 GHz. A Gaussian function fits the experimental data better than a Lorentzian function, indicating that spectral diffusion is the primary mechanism responsible for the overall linewidth of the emission. Nevertheless, dephasing is also expected to play a role in the overarching broadening mechanism, as was recently reported [233]. The spectral fluctuations when averaged out, resulted in a broad Gaussian lineshape with an FWHM of 6.3 ± 0.3 GHz [241]. The average interval between two consecutive jumps appeared to be slow, on the order of milliseconds. Additional scans performed over a wider frequency range of 22 GHz using a scan speed of 200 MHz/second reveal numerous intermittent peaks, randomly distributed within the scan window (**Fig. 5.3c**). Most of these peaks are also fit best with Gaussian functions, suggesting that spectral diffusion is the dominant broadening mechanism (i.e., it is more pronounced than dephasing). The fits yield line widths in the range of ~700 – 1200 MHz (each of these features corresponds to a data acquisition time of a few seconds). Additional asymmetrical features seen in **Fig. 5.3c** (indicated by the gray arrows) likely correspond to rapid spectral diffusion/jumps over a broader spectral range or the situation where the emitter has undergone a transition to the dark state. The widths of the Gaussian peaks in **Fig. 5.3c** are significantly smaller than the time-averaged value of ~ 6.3 GHz seen in **Fig. 5.3b**, which indicates that the emitter is stable but exhibits rapid spectral jumps during excitation. Spectral jumps are expected from emitters with a permanent dipole moment such as the antisite vacancy defect N_BV_N, which has been suggested as the atomic structure of the

hBN SPEs [4] studied in this work. Indeed, the broadened PLE trace in **Fig. 5.3b** and the frequent spectral jumps indicate that the resonance pumping was intermittent. However, the emission instabilities seen in **Fig. 5.3b-c** may be mitigated, once the level structure of the emitters is fully understood, by a co-incident laser used to repump the defects, as has been done previously for NV centers in diamond [243].

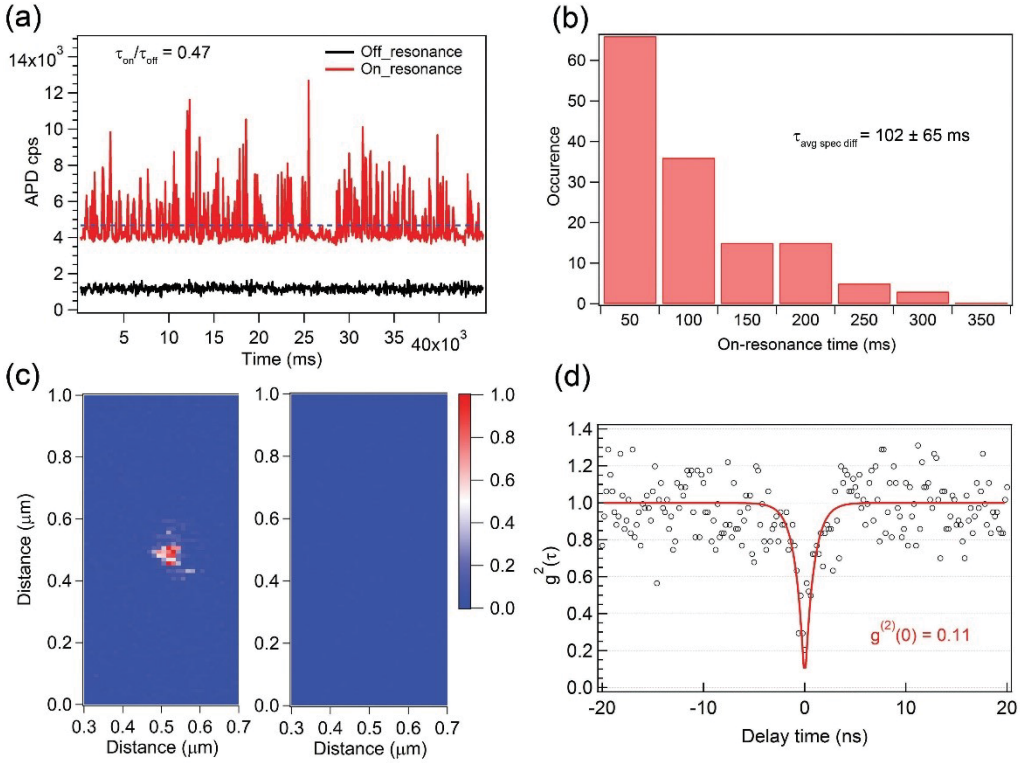

Figure 5.5. (a) *PL intensity vs. time for on-resonance (red line) and 2 nm detuned (black) excitation of the same emitter. The blue dash line represents the cut-off threshold (1800 count/sec) for calculating* τ_{on} *and* τ_{off}*. The* τ_{on} */* τ_{off} *ratio was calculated to be 0.47. The data are vertically shifted for clarity.* ***(b)*** *Histogram of on-resonance time extracted from an on-resonance trace of* ***(a)****. The calculated average spectral diffusion time,* $\tau_{avg\ spec\ diff}$ *= 102 ± 65 ms.* ***(c)*** *Confocal PL map with the laser staying on-resonance (left panel) and 2 nm detuned (right panel) from the resonance. The measurements in* ***(a)*** *and* ***(b)*** *were carried out at the excitation power of 150 nW.* ***(d)*** *On-resonance photon second-order correlation function (black open circles) acquired for the emitter at 1 μW excitation power for*

three hours. The red solid line is the fitting for the $g^{(2)}_{meas}(0)$ function using the Gaussian-convoluted three-level model, resulting in an antibunching dip value of 0.11 ± 0.04. The standard deviation was based on the standard deviation taken from the long delay time region. It must be noted that no smoothing procedure was implemented for this measurement. All the measurements were conducted at 8 K.

To compare the measured peak widths to the Fourier-transform (FT) lifetime limited linewidth, we conducted time-resolved PL measurements of the excited state lifetime using a pulsed excitation source. A lifetime of 3.6 ± 0.1 ns was extracted by fitting a single exponential function to the experimental data shown in **Fig. 5.3d**, yielding an FT limited linewidth of ~ 44 MHz, which is over an order of magnitude narrower than the measured linewidths in **Fig. 5.3b-c**. The observed broadening and spectral jumps are attributed primarily to low quality of the hBN host material and the chemically exfoliated, drop-casted flakes used in the present study. Currently available hBN crystals are known to host impurities introduced during synthesis processes [244-245]. Such impurities can undergo charge transitions during optical excitation, which can, in turn, give rise to intense local electric field fluctuations that interact strongly with the permanent transition dipole moment of emitters and cause spectral diffusion [15]. The latter can, in principle, be suppressed using dynamic Stark shift feedback techniques that have been demonstrated previously using nitrogen-vacancy (NV) centers in diamond [246]. A more direct approach is to prevent the underlying problem by improving the crystal purity of the hBN material. Indeed, initial PLE measurements from NV centers in nanodiamonds showed GHz linewidths [247-248], and subsequent realization of high-quality single crystal material yielded improved, stable and FT limited lines.

To characterize the emission dynamics further, we recorded the PL intensity as a function of time using a fixed excitation laser tuned to the emission resonance of 766.186 nm (red trace in **Fig. 5.5a**). Emission intermittency (blinking) is clearly evident when the laser is resonant with the optical transition of the emitter and gives rise to photon bursts [249] in the time-resolved PL signal. For reference, off-resonance excitation with the laser wavelength detuned by 2 nm is shown as a

black curve. In this case, the emitter was not excited and only a steady state, low-intensity background is observed.

The time-resolved PL trace enables quantification of the spectral diffusion time. By setting a threshold value of 1800 counts/sec (grey dashed line) to separate the ON and OFF-resonance times (τ_{on} and τ_{off}, respectively), the τ_{on} / τ_{off} ratio is equal to 0.47. This value indicates that the average amount of time during which the emitter is detuned from the excitation field is about twice as long as the ON-resonance time. By binning the ON-resonance time intervals (**Fig. 5.5b**), we obtain an average spectral diffusion time, $\tau_{avg\ spec\ diff}$, of approximately 102 ± 65 ms. We note, however, that spectral diffusion at the millisecond time scale cannot explain the line broadening observed in **Fig. 5.3**. Recent results show that emitters in hBN exhibit ultrafast spectral diffusion at a time scale of a few μs, and a coherence time of ~ 81 ps [233]. Further detailed studies are needed to fully understand and circumvent spectral diffusion of emitters in hBN.

With an average spectral diffusion time of ~ 100 ms, we demonstrated that an ON-resonance confocal PL map could be acquired, showing a clear bright spot in the center of the map (**Fig. 5.5c**, left panel), and the absence of background emissions present in the off-resonance confocal map shown in **Fig. 5.1b**. In contrast, when the resonant excitation laser was detuned by 2 nm, no PL signal is observed (**Fig. 5.5c**, right panel).

Finally, to confirm the resonance single photon nature, we acquired an on-resonance antibunching curve from the emitter using a laser power of 1 μW (**Fig. 5.5d**). An acquisition time of three hours was needed to achieve an adequate signal-to-noise ratio, due to the spectral diffusion and blinking which also prevented the observation of Rabi oscillations in our data. A fit based on the Gaussian-convoluted three-level model (red solid line) resulted in a $g^{(2)}(0)$ value of 0.11 ± 0.04, which is comparable to that from off-resonance excitation (**Fig. 5.1d**), and confirms the single photon nature of the emitter. Notably, the on-resonance antibunching time (~0.87 ns) is less than a third of the off-resonance antibunching time (3.0 ns).

5.5 Conclusion

To summarize, we demonstrated resonant excitation of a quantum emitter in hBN. The emitter has a time-averaged optical linewidth of ~ 6 GHz. Using individual scans, we were able to resolve narrower transitions, down to ~ 700 MHz, despite the presence of spectral diffusion. An average spectral diffusion time of ~ 100 ms was observed, which is sufficiently long to realize more complex experiments such as the Hong-Ou-Mandel two-photon quantum interference effect [16]. Measurement of the second-order autocorrelation function under resonant excitation was demonstrated, confirming the single photon nature of the source. Our results provide important insights into coherent properties of quantum emitters in hBN and motivate further spectroscopic and materials engineering work aimed at improving the optical linewidths of quantum emitters in hBN.

6 Engineering and Localization of Quantum Emitters in Large Hexagonal Boron Nitride Layers

This chapter reports the engineering of quantum emitters in exfoliated hBN flakes *via* ion implantation, laser ablation and electron beam induced etching. Igor Aharonovich conceived the work. The ion implantation was performed by the Department of Electronic Materials Engineering (ANU). The laser ablation was carried out by Xuewen Wang and Saulius Juodkazis (Swinburne University of Technology). Christopher Elbadawi conducted the electron beam induced etching of hBN flakes and analyzed the data. Optical measurements and analysis were done by Sumin Choi and Trong Toan Tran, with some assistance from Gediminas. All the authors discussed and wrote the manuscript.

6.1 Abstract

Hexagonal boron nitride is a wide bandgap van der Waals material that has recently emerged as promising platform for quantum photonics experiments. In this work, we study the formation and localization of narrowband quantum emitters in large flakes (up to tens of microns wide) of hBN. The emitters can be activated in as-grown hBN by electron irradiation or high-temperature annealing, and the emitter formation probability can be increased by ion implantation or focused laser irradiation of the as-grown material. Interestingly, we show that the emitters are always localized at edges of the flakes, unlike most luminescent point defects in 3D materials. Our results constitute an important step on the road map of deploying hBN in nanophotonics applications.

6.2 Introduction

In recent years layered materials, also known as van der Walls crystals, have attracted major attention across multiple fields of nanoscale science and technology [92, 107, 250-252]. For instance, transition metal carbides and nitrides

(MXens) have been promising building blocks for energy storage and capacitors,[250, 253]. Similarly, transition metal dichalcogenides (TMDs) have been explored in nanoelectronics and nanophotonic applications mainly due to a unique transition from an indirect to a direct bandgap as their thickness is reduced to a single monolayer [92, 102, 254-256].

Hexagonal boron nitride is a van der Walls crystal that has so far been used primarily as a capping or a separating layer for graphene and TMDs devices [107, 245, 257]. However, hBN has recently been shown to be the first known material that is naturally hyperbolic (meaning that the dielectric constants in the plane and out of plane have opposite signs), a property that has been leveraged to demonstrate sub-diffraction polariton propagation and sub-wavelength imaging with a nanoscale resolution [126, 258]. hBN also possesses a wide bandgap of ~6 eV, that results in its ability to host many optically active defects over a wide spectral range [122, 259]. Research into isolated point defects of hBN has recently accelerated, and several isolated defects have been characterized by scanning tunneling microscopy [260] and optical confocal microscopy [6, 261-262]. Indeed, one of the fascinating properties of hBN is the ability to host ultrabright, room temperature single photon emitters that originate from localized defect states within the bandgap.

In this work, we study the formation and localization of defects that act as single photon emitters in large (tens of microns wide) hBN layers. Ion implantation and laser processing are shown to enhance the formation probability of the defects. We study the photophysical properties of the emitters, showing their photoluminescence spectra, polarization properties, and photon emission statistics (autocorrelation functions). We use hBN flakes that are much larger than the spatial resolution of confocal photoluminescence microscopy and show that the emitters are always localized at boundaries or flake edges, in contrast to emitters in traditional 3D materials which are typically located away from surfaces and interfaces.

6.3 Methods

6.3.1 Sample preparation

hBN layers were exfoliated from a bulk hBN material using standard scotch tape techniques. **Fig. 6.1a** shows an optical image of the exfoliated material. Flakes with diameters of up to tens of microns were obtained. A reference sample and six substrates with exfoliated flakes were prepared for processing by ion implantation, laser ablation, and electron irradiation. Ion implantation was explored using boron (B), boron-nitrogen (BN) complexes, silicon and oxygen ions. B and BN were selected to test whether the formation probability of intrinsic defects would increase, generating mostly vacancies and interstitials, while silicon and oxygen atoms were chosen to determine whether the emitters are related to common impurities. Indeed, oxygen is known to be trapped within hBN lattice during growth and exfoliation [263]. A summary of the sample processing details is shown in **Fig. 6.1b**. The laser ablation and electron beam irradiation treatments are described below. Unless noted otherwise, the presented data is from samples that were annealed for 30 minutes at 850^0C in an argon environment [261, 264] either after exfoliation (reference sample) or after ion/laser processing.

6.3.2 Defect creation using femtosecond laser pulse irradiation

A Pharos laser system (Light Conversion Co. Ltd.) with a tunable pulse duration from t_p=230 fs to 10 ps, and an average power of 10 W, operated using a repetition rate of 200 kHz was used for laser processing of hBN. The second harmonic beam with a wavelength of 515 nm was focused onto the sample surface by an oil immersion objective with an NA of 1.4 (Olympus). The focus spot is around 450 nm ($d=1.22\lambda/NA$). The pulse energy was varied in 10% steps from 225 nJ to 90 nJ. A single pulse was delivered to each sample area, and the irradiated areas were separated by 5 μm.

6.3.3 Electron beam irradiation of exfoliated hBN flakes

Bulk hBN was mechanically exfoliated onto a Si (111) substrate covered with a native oxide layer. The exfoliated flakes were rinsed with acetone and IPA and

dried under flowing N2. The Samples were then loaded into a variable pressure FEI field-emission-gun scanning electron microscope. The system was pumped down to high vacuum, and the chamber was filled with water vapour at a pressure of 8 Pa. The hBN flakes were then located using a magnetic field assisted gas ionization cascade detector, and electron beam irradiation was performed using a focused Gaussian electron beam which was scanned for one hour over an area of 600 μm^2. An accelerating voltage of 15 kV was used and the electron beam fluence delivered to the exposed area was 5×10^{18} e-/cm^2 (this is much lower than that needed to cause electron beam induced etching of hBN). The irradiation process is stopped by electron beam blanking.

6.3.4 Ion implantation procedure

Ion implantation was performed using a conventional NEC implanter (located at Australian National University). A suitable powder containing the desired material (B, BN, Si and O) is first pressed densely into a small copper cylindrical cathode. A source of negative ions by cesium sputtering is used to generate the ion beam. The cathode is biased to typically 6 V which attracts the negative ions, and the pressed powder is sputtered. The beam is accelerated by an extractor voltage and an Einzel lens which is used to focus the beam. Using a 90° magnet, only the ions with a specific mass to charge ratio and energy are selected. The beam is then electrostatically raster scanned to ensure a homogeneous distribution over the desired implantation region, which can be modified by an aperture. The samples are affixed to a hollow nickel block with clamps. A cylindrical copper shield surrounding the target is cooled to 80 K to reduce contamination build up on the sample surface. The sample holder is biased to -300 V with respect to the target for charge suppression. Prior to each implantation cycle, the system was pumped down below 5×10^{-7} Torr.

6.3.5 Optical measurements

Single photon emission characteristics were measured at room temperature using scanning confocal microscopy with a continuous-wave 532-nm laser (Gem 532™, Laser Quantum Ltd.). The laser was directed through a half wave plate and focused

on the sample through a high numerical aperture objective lens (NA 0.9, Nikon). Scanning was performed using an X-Y piezo scanning mirror (FSM-300TM, Newport Corp.).The emission was collected using the same objective, filtered through a 532nm dichroic mirror and a long pass filter (Semrock), and coupled into a multimode fiber that served as a confocal aperture. Then a fiber splitter was used to split the light path to two avalanche photodiodes (APDs) (Excelitas Technologies™) for single photon counting and into a spectrometer (Acton SpectraPro™, Princeton Instrument Inc.). While the emission spectra were measured using the spectrometer, single photon detection was performed using a using a time-correlated single-photon-counting module (PicoHarp300™, PicoQuant™). Excitation polarization of the single photon emitters was controlled using a half-wave plate, while the emission polarization was measured using a linear polarizer at maximum excitation polarization. The collected $g^{(2)}(\tau)$ curves were fit using a three-level system **Eq. 2.1**.

The polarization behavior is fit by **Eq. 6.1.**:

$$I = I_0 \cos^2 \theta_i \tag{6.1}$$

where I_0 is the initial intensity and θ_i is the angle between the initial polarization direction of light and the transmission axis of the polarizer.

6.4 Results and Discussion

All optical characterization of the hBN emitters was performed at room temperature. **Fig. 6.2a-d** shows PL spectra recorded from samples implanted with B, BN, O and Si ions. The spectra in all cases are similar, showing a ZPL at ~ 600 nm and a weaker second peak near 650 nm. While some variation in the position of the ZPLs was observed, an absolute majority of the spectra exhibited two peaks. An investigation of 50 emitters revealed a similar range of spectra from each sample investigated in this work (i.e., there are no statistically meaningful differences between the reference sample and samples processed by the various ion, laser and electron beam irradiation treatments). Interestingly, the difference between the two peaks seen in each spectrum is approximately 160 meV,

indicating that all the emitters have a similar structure within the hBN lattice [261-262].

To ensure that the emission originates from localized single defects, we recorded the second order autocorrelation function, $g^{(2)}(\tau)$, from each emitter. The functions are shown as insets in **Fig. 6.2**. The dips at zero delay time (τ=0) confirm that the luminescence originates from single photon emitters. The data (blue dots) was fit using a standard three-level model (solid black line) [261]. The deviations from zero at τ=0 are attributed to background emissions.

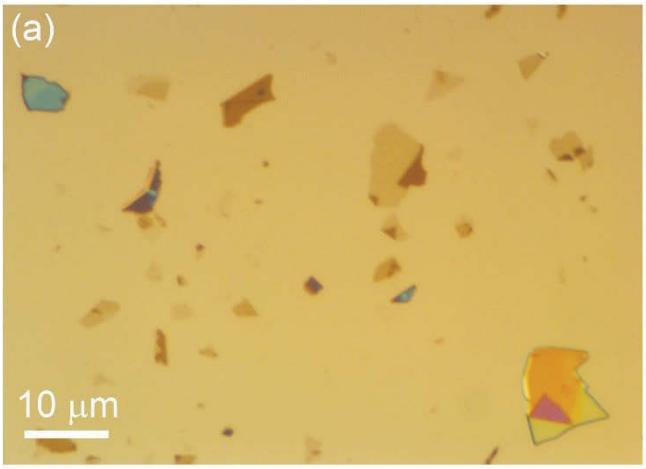

(b)

Sample	Irradiation	Annealing
B^- irradiated	energy: 50 keV, fluence: 10^{10} ion/cm^2, temp: RT	850°C 30 min 1 Torr Ar
BN^- irradiated	energy: 50 keV, fluence: 10^{10} ion/cm^2, temp: RT	
O^- irradiated	energy: 70 keV, fluence: 10^{10} ion/cm^2, temp: RT	
Si^- irradiated	energy: 50 keV, fluence: 10^{10} ion/cm^2, temp: RT	
Reference	—	
Laser ablation	λ: 515 nm, pulse width: 230 fs number of pulse: 1, temp: RT	
e-beam	energy: 15keV, e-fluence: 5 x 10^{18} (e/cm2) temp: RT	—

Figure 6.1. ***(a)*** *Optical image of exfoliated hBN flakes.* ***(b)*** *Table of the investigated samples comprised of a reference sample, four samples that were implanted by ions, one processed by a laser beam and one by an electron beam.*

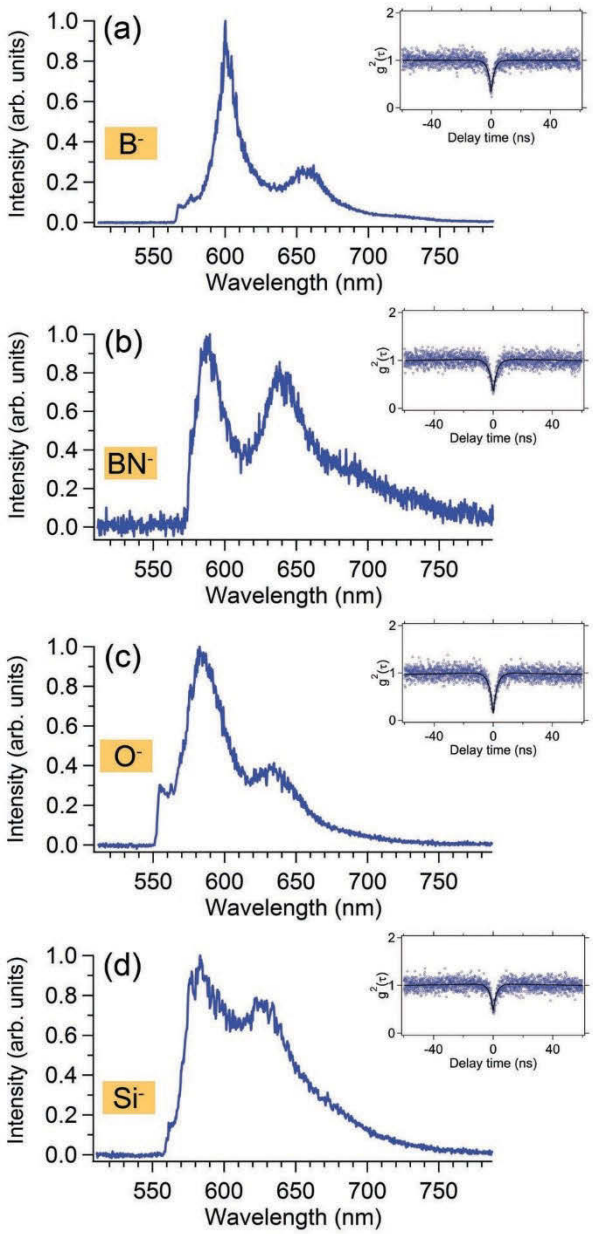

Figure 6.2. (a-d) *PL spectra from hBN flakes implanted with B, BN, O and Si ions. The insets are second-order autocorrelation functions, $g^{(2)}(\tau)$, recorded from each sample, demonstrating the emitters are single photon sources. A spectrum from a reference sample and a corresponding $g^{(2)}(\tau)$ function are shown in the (**Fig. 6.8**).*

Fig. 6.3a shows a comparison of the number of single emitters found in the implanted flakes versus the reference sample (which has undergone the same annealing treatment used to activate the emitters,[261, 264] but without ion implantation). The implanted flakes show considerably more emitters than the

reference. However, the ion species have little influence on the formation probability of the defects. This indicates that the main role of the bombarding ions is to introduce vacancies and to activate already present intrinsic point defects, rather than the introduction of a foreign florescent defects (i.e., such as in the case of nitrogen implantation into diamonds to produce nitrogen-vacancy centers [265]). In addition, we observed that the emitters in the implanted flakes are mostly optically stable and do not exhibit blinking, while almost 50% of the emitters in the reference flakes show severe blinking and eventual bleaching. **Fig. 6.3** (b, c) shows typical intensity traces from a stable defect in an ion implanted flake and a blinking emitter in a reference sample. We, therefore, conclude that implantation can be used to increase the emitter activation probability as well as increase their photo-stability.

(a)

Sample	Number of Emitters	Number of Flakes examined
B	10	7
BN	10 (3 were blinking)	12
O	10	12
Si	11 (3 were blinking)	8
Ref.	7 (3 were blinking)	16

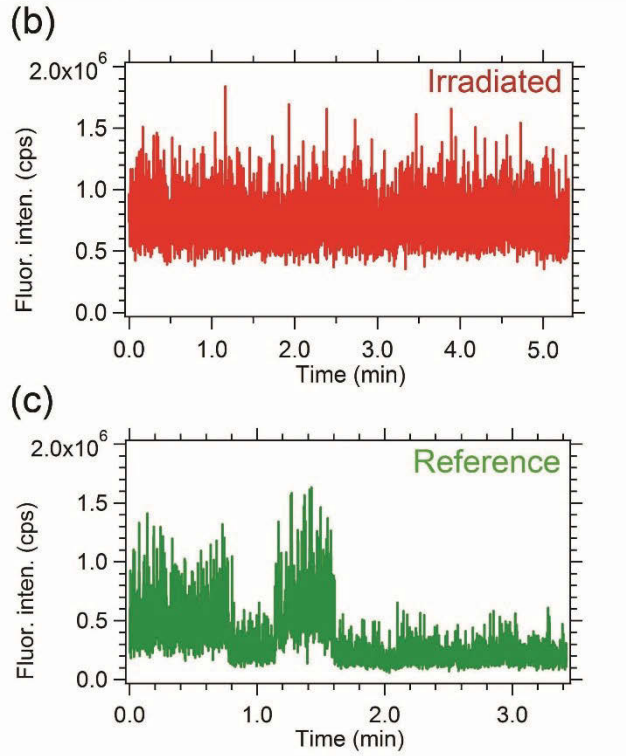

Figure 6.3. (a) *A table comparing the number of formed emitters found in each ion-implanted sample and a reference sample that was only subjected to annealing.* ***(b, c)*** *Examples of stability curves from a single emitter in an ion implanted flake* ***(b)*** *and a reference flake* ***(c)****. Blinking followed by bleaching was much more common in the reference sample than in the implanted samples.*

Another important observation is the location of the emitters within the flakes. In contrast to prior work done using small (~ 200 nm wide) flakes of hBN, the samples used here are sufficiently large to resolve emitter locations within the flakes by confocal microscopy. **Fig. 6.4** shows three confocal maps from each implantation batch. White circles indicate quantum emitters. Remarkably, in all

cases, the emitters are localized at flake edges or grain boundaries. While similar behavior was reported for excitons in TMDs [82, 201, 266], such defect localization is an unexpected phenomenon for stable luminescent defects in semiconductors. Indeed, in 3D materials, the formation of stable, luminescent point defects near crystal edges and surfaces is extremely challenging, and the most stable and bright emitters are typically located in the bulk, deep within the crystal [267-269]. Emitter localization at interfaces is desirable for device fabrication as it can improve ultimate control over emitter placement and coupling to photonic and plasmonic cavities. We note that due to the finite resolution of the confocal microscope, which is ~ 300 nm in our experimental setup, we cannot conclusively say how far the emitters are from the flake edges. However, there is no compelling reason to suggest that point defects are localized tens or hundreds of nanometers away from an edge, and it is, therefore, most likely that the emitters decorate the edges and crystal boundaries. Interestingly, extended line defects in BN with different chemical terminations and geometrical variations have been modeled and predicted to have unique optoelectronic properties that can result in confined, optically active systems [270]. Detailed atomistic modelling and super-resolution imaging will be required to elucidate this behavior further.

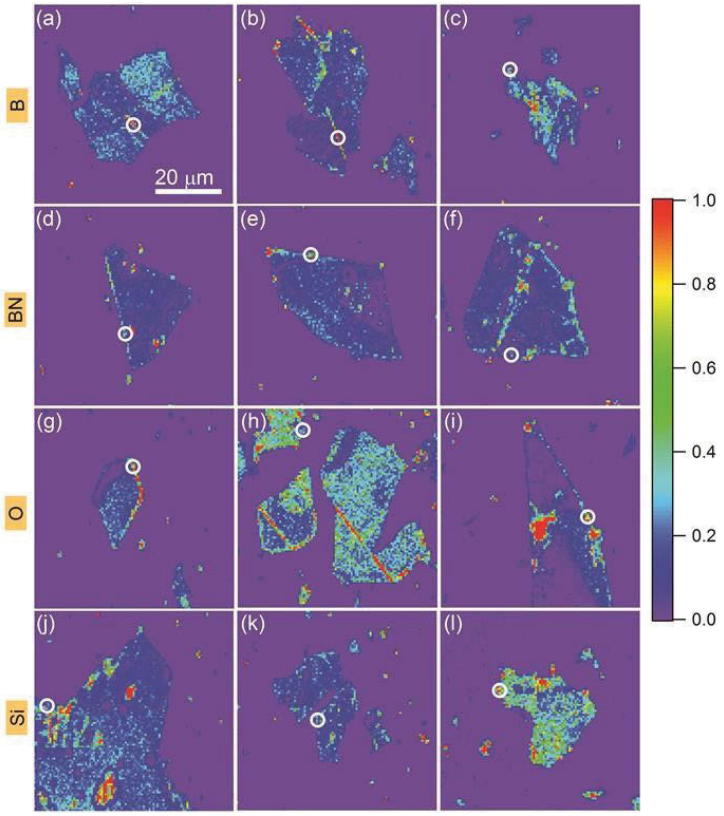

Figure 6.4. *Confocal maps from* ***(a-c)*** *B,* ***(d-f)*** *BN,* ***(g-i)*** *O and* ***(j-l)*** *Si implanted hBN flakes, demonstrating unambiguously that the emitters are always localized at flake edges. Large bright features seen away from flake edges, as in map* ***(i)****, do not exhibit photon antibunching, and do not possess the spectral characteristics of the single photon emitters discussed in this study.*

Fig. 6.5 (a-d) show examples of excitation and emission polarization recorded for different emitters from different implantation batches. More examples are shown in the SI. While most of the emitters are fully polarized in both excitation and emission, we did observe numerous emitters that did not show full extinction. This is most likely because the flakes were not properly adhered to the substrate post-exfoliation, creating an angle between the flake and the excitation laser beam. The polarization behavior is therefore indicative of a dipole-like emitter, with a fast polarization axis, in accord with the earlier studies [261-262]. The misalignment between the excitation and the emission polarization is likely due to redistribution of the excited electronic states.

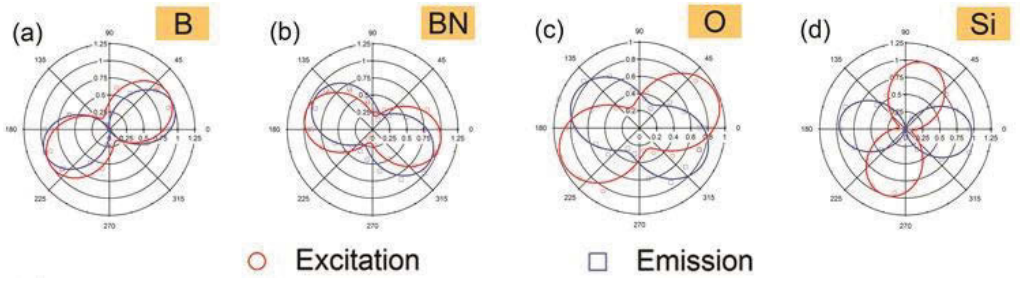

Figure 6.5. (a-d) *Example of excitation (red circles) and emission (blue squares) polarization plots of single emitters* from each of the implanted samples. All the emitters exhibit dipole like behaviour in both excitation and emission.

Next, we characterize flakes that were processed using an ultrafast pulsed laser operated at a power just below the threshold for rapid ablation[271]. Ultra-short laser pulses are efficient sources of free electron acceleration due to high peak intensities. Free electrons accelerated to energies larger than the bandgap are efficient in defect formation and chemical bond breaking. Colour center formation in dielectric materials is typical under fs-laser irradiation at such fluence/irradiance[272]. **Fig. 6.6a** shows a confocal map of the sample, while **Fig. 6.6b** shows a photoluminescence spectrum recorded from a single emitter found in these flakes. The inset is a corresponding $g^{(2)}(\tau)$ curve that confirms single photon emission from this defect. Similarly to the ion implantation case, the emitter exhibits full polarization behavior in both excitation and emission as is seen in **Fig. 6.6(c)**.

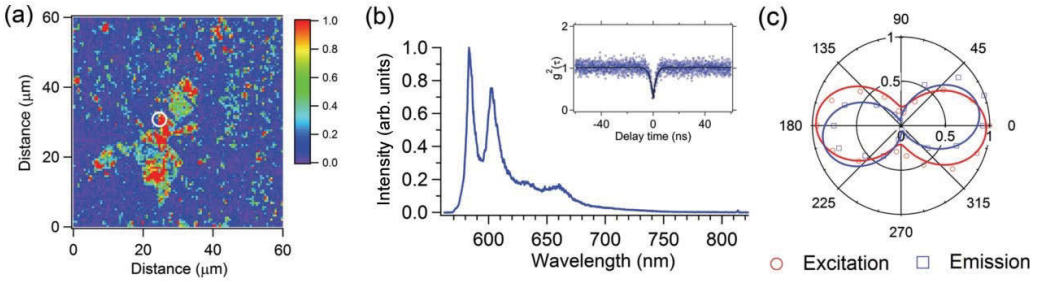

Figure 6.6. *Fabrication of emitters using laser processing.* ***(a)*** *Confocal map of the hBN flakes. The white circle indicates the presence of the location of a single photon emitter.* ***(b)*** *PL spectrum recorded from the emitter. Inset:* $g^{(2)}(\tau)$ *curve confirming it is indeed a single photon emitter.* ***(c)*** *excitation and emission*

polarization curves (red circles and blue squares, respectively,) recorded from this emitter.

The original size of the flakes was large, similarly to the ones shown in **Fig. 6.1a**. However, the laser process caused some of the flakes to break up into many small fragments. This resulted in more observed emitters per similar scan area.

Finally, we use a deterministic electron beam induced irradiation technique to fabricate the emitters in specific hBN flakes (this technique has been used previously to fabricate emitters in sub-micron hBN flakes that were too small to determine emitter locations within the limits of diffraction-limited confocal microscopy[264]). **Fig. 6.7a,b** shows a flake before and after electron beam irradiation by a 15 keV electron beam in an H_2O vapor environment (see methods). **Fig. 6.7c** shows photoluminescence spectra recorded from the pristine flake (blue) and after the irradiation treatment (red). Note that the spectra were recorded at the same location, as indicated by the white circles in (a) and (b). The inset is a $g^{(2)}(\tau)$ function that proves the probed emitter is a single photon source. **Fig. 6.7d** shows the corresponding polarization measurements from the same emitter. This sample was not annealed after electron beam irradiation because the annealing is not required for emitter activation, in contrast to emitters generated by the ion and laser irradiation treatments. This can be explained by the fact that ion implantation and laser irradiation generates significant damage in the hBN lattice that partly recovers during annealing. On the other hand, irradiation by 15 keV electrons in H_2O vapor is a more subtle process that chemically reforms the lattice, with minimal damage to the surrounding crystallographic environment. The electron beam approach is therefore appealing as it allows emitter fabrication and localization in a single step, without the use of lithographic masks or post-processing treatments. The emitters fabricated by an electron beam had the same spectral and polarization characteristics as those made by ion and laser irradiation, and they were located consistently at flake edges and grain boundaries. Further work is needed to determine whether the electron beam creates new defects or activates pre-existing defects that are present in as-grown hBN.

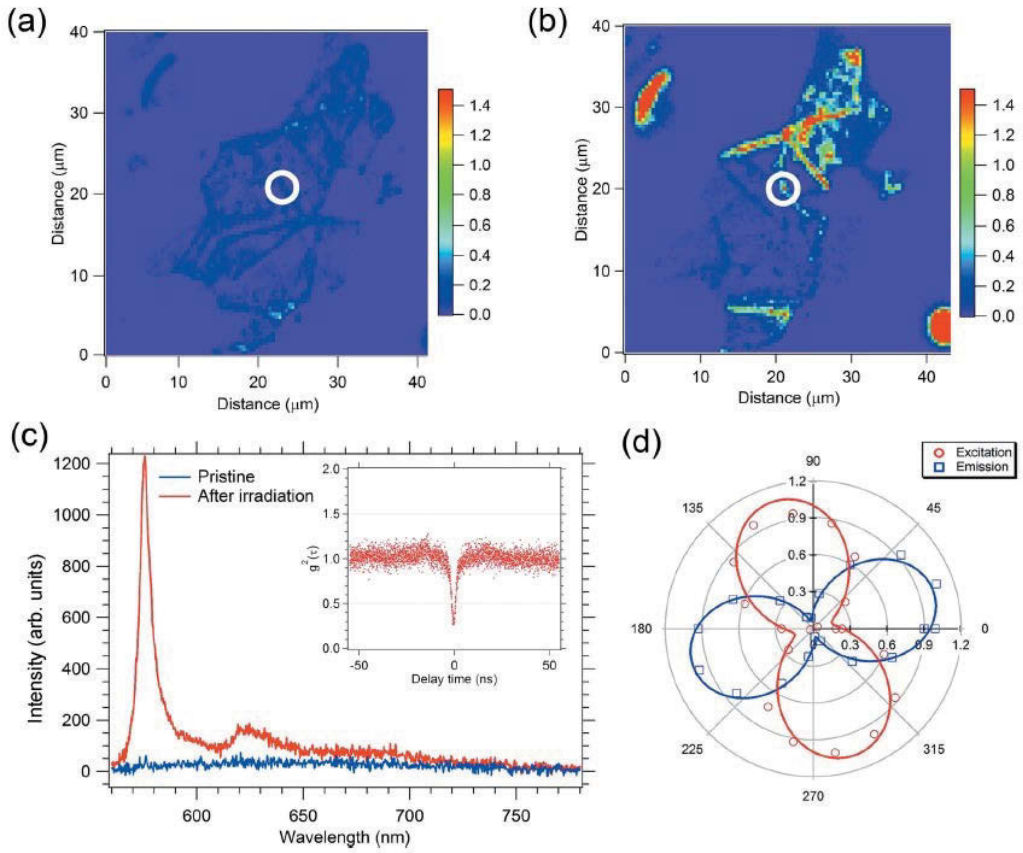

Figure 6.7. *Fabrication of emitters by electron beam irradiation. Confocal map of the same flake before* ***(a)*** *and after* ***(b)*** *electron beam irradiation. The energy of the beam is 15 keV.* ***(c)*** *Spectra recorded from a particular location before (blue curve) and after (red curve) irradiation. Inset, a* $g^{(2)}(\tau)$ *curve confirming the formed defect is a single photon source.* ***(d)*** *Excitation and emission polarization from the same defect. The sample was not annealed after electron irradiation.*

6.5 Conclusions

To summarize, we presented a comprehensive study of single emitters in large layered hBN. We find that ion implantation, laser ablation, and annealing are efficient methods to generate the emitters. However, the implantation species have little influence. We also observe that the emitters are always localized at flake edges, indicating that a flake morphological defects may play a role in the formation of these quantum emitters. Finally, we showed that electron beam irradiation can be used to fabricate the emitters in a particular flake. Overall, the

emitters are polarized and optically photostable and therefore are very promising for future quantum photonics and quantum optoelectronic applications. Further studies are required to unveil the exact structure of the single emitters large layered hBN.

7 Deterministic coupling of quantum emitters in 2D materials to plasmonic nanocavity arrays

This chapter reports the weak coupling of quantum emitters in hBN flakes and plasmonic particle arrays. The project was conceived by Igor Aharonovich and Teri Odom. The plasmonic particle arrays were fabricated and characterized by Danqing Wang and Ankun Yang (Northwestern University). Coupling experiments and analysis were performed by Trong Toan Tran and Zai-quan Xu. All the authors discussed and wrote the manuscript.

7.1 Abstract

Quantum emitters in two-dimensional materials are promising candidates for studies of light-matter interaction and next generation, integrated on-chip quantum nanophotonics. However, the realization of integrated nanophotonic systems requires coupling of emitters to optical cavities and resonators. In this work, we demonstrate hybrid systems in which quantum emitters in 2D hexagonal boron nitride are deterministically coupled to high-quality plasmonic nanocavity arrays. The plasmonic nanoparticle arrays offer a high quality, low loss cavity in the same spectral range as the quantum emitters in hBN. The coupled emitters exhibit enhanced emission rates and reduced fluorescence lifetimes, consistent with Purcell enhancement in the weak coupling regime. Our results provide the foundation for a versatile approach to achieving scalable, integrated hybrid systems based on low loss plasmonic nanoparticle arrays and 2D materials.

7.2 Introduction

Hybrid plasmonic – photonic systems are attracting increasing attention in studies of light-matter interaction at the nanoscale, coherent and incoherent light amplification, and as media for achieving enhanced emission and absorption rates [273-277]. To this extent, the coupling of SPEs, which are vital components of

future quantum technologies [17], to plasmonic cavities was demonstrated for 3D crystals including color centers in diamond [278-279], 1D carbon nanotubes (CNTs) [280] and 0D quantum dots [281-283]. Recently, isolated defects in 2D hexagonal boron nitride [5, 228, 261, 284] have emerged as a new class of room temperature SPEs. These emitters are embedded in 2D flakes of layered hBN and therefore offer an excellent platform for integration with photonic elements, making them promising constituents of next-generation nanophotonics and optoelectronic devices.

One specific plasmonic resonator is a periodic metal nanoparticle (NP) array (for instance silver or gold) in a homogeneous dielectric environment [285-286]. This geometry supports narrow lattice plasmon resonances at the band-edge with suppressed radiative loss and strong sub-wavelength localized field enhancement around the NPs (< 50 nm). The plasmonic cavity modes can strongly enhance the emission rates of emitters in the hot spot regions, and the resonance wavelengths can be tailored by changing the NP periodicity and the dielectric environment [285]. Additionally, compared to the limited pattern area in other plasmonic cavity designs by e-beam lithography (< 100 μm), these periodic metal NP arrays can be readily fabricated in cm^2 scale with a large-scale fabrication process based on soft interference lithography (SIL) [287]. Thus, large-scale plasmonic NP arrays provide a flexible platform for coupling to SPEs without a need for precise control over the emitter location. Such lattices have been used to demonstrate strong light-matter coupling, directional emission and lasing actions [280, 286, 288]. Integration of plasmonic NP arrays with deterministically selected quantum emitters in 2D materials will constitute a new platform for integrated on-chip flat optics.

In this work, we report for the first time a hybrid quantum 2D material system integrated with a plasmonic NP array. Specifically, we deterministically couple individual emitters of choice in 2D hBN hosts to gold or silver NP arrays (**Fig. 7.1a**). We demonstrate an enhancement in the spontaneous emission rate, along with an enhanced count rate and modified ultrafast dynamics. Our results open up new intriguing possibilities to explore quantum plasmonics with 2D materials.

7.3 Methods

7.3.1 Sample preparation

Two types of hBN flakes were studied: commercial solvent-exfoliated hBN flakes (Graphene Laboratories) with a diameter of ~300 nm and tape exfoliated flakes from bulk hBN. In both cases, the flakes were deposited onto 1 x 1 cm^2, 300 nm thick oxide silicon substrates. The substrates were then annealed at 850°C for half an hour in an argon atmosphere (1Torr) to activate optically active color centers. Gold markers (fabricated by photolithography prior to drop casting) were used to locate specific emitters.

Commercial poly(methyl methacrylate) (PMMA, Microchem A3) was spin coated onto the substrates at 3000 rpm for 1 min to form ~ 200 nm of PMMA. The substrates were then baked at 120°C for 20 min using a hot plate to cure the polymer and thus enhance adhesion of the PMMA. In our experiments, all characterization of pristine and coupled emitters was performed in the presence of PMMA which functions as an index-matching medium for plasmonic particle arrays.

7.3.2 Transfer process

We first pre-characterized numerous flakes to match the emission of hBN emitters to the plasmonic resonance. Overall, one out of ten emitters (~ 10 %) will satisfy the criteria of being a single, bright and match the plasmonic resonance. For the transfer, the substrates were gently floated on the surface of a 2M NaOH solution in a glass beaker. The beaker was then heated to 90°C for two hours to accelerate the silicon etching process. After that, the PMMA-coated hBN flakes were completely detached from the substrates and floating on the surface of the alkaline solution. The membranes were rinsed in deionized water, loaded onto plasmonic lattice substrates and dried at 40°C on a hot plate. The substrates were then baked at 120°C for 20 min to bring the emitters closer to the plasmonic surfaces and increase adhesion between the PMMA membrane and the substrate surface.

7.3.3 Optical characterization

A continuous wave 532 nm laser (Gem 532™, Laser Quantum Ltd.) was used for excitation and scanning. The laser was directed through a Glan-Taylor polarizer (Thorlabs Inc.) and a half waveplate and focused onto the sample using a high numerical aperture (NA = 0.9, Nikon) objective lens. Scanning was performed using an X-Y piezo scanning mirror (FSM-300™). The collected light was filtered using a 532 nm dichroic mirror (532 nm laser BrightLine™, Semrock) and an additional long pass filter (Semrock). The signal was then coupled into a graded index fiber, where the fiber aperture serves as a confocal pinhole. A fiber splitter was used to direct the light to a spectrometer (Acton SpectraPro™, Princeton Instrument Inc.) or two avalanche photodiodes (Excelitas Technologies™) used for collection of spectra and photon counting. Correlation measurements were done using a time-correlated single photon counting module (PicoHarp300™, PicoQuant™). The presented $g^2(\tau)$ curves in **Fig. 7.4** were corrected for background luminescence while the those in **Fig. 7.7** and **7.8** were not background corrected. Lifetime measurements were performed using a 512 nm pulsed laser excitation source (PiL051X™, Advanced Laser Diode Systems GmbH) with a 100 ps pulse width and a 10 MHz repetition rate.

7.3.4 Modeling of plasmonic NP arrays

We used FDTD calculations based on a commercial software (FDTD solutions, Lumerical Inc.) to simulate the linear optical properties and near-field enhancement of Au and Ag NP arrays. The optical constants of gold and silver were from Johnson and Christy (400 – 1000 nm)[289]. The cylindrical NPs had height h = 50 nm and diameter d = 80 nm. A uniform mesh size of 2 nm was used in x, y and z directions to ensure the accuracy of electric field simulations inside the metal NPs.

7.4 Results and Discussion

Fig. 7.1b shows a scanning electron microscopy image of a pristine hBN flake. The flakes were exfoliated using scotch tape from highly crystalline bulk hBN. To

match the emission peaks (~ 560 nm – 700 nm), we select silver or gold NP arrays with a NP spacing of 400 nm. The corresponding optical image is shown in **Fig. 7.1c**. Based on finite-difference time-domain (FDTD) modeling (**Fig. 7.1d**), the near-field electric field at lattice plasmon resonance is enhanced with respect to incident light in plasmonic hot spots. The electric field distribution along the vertical axis suggests that the field enhancement is still reasonably high for vertical distance of several tens of nanometers away from the edge of NPs (see **Fig. 7.2**). Such hot-spot regions are well-suited for the hBN flakes used in this study. Quantum emitters embedded in hBN flakes exhibit a broad distribution of zero-phonon lines (ZPL) in the range of ~ 560 – 700 nm, that are likely due to strain fields or inhomogeneity in the local dielectric environment [5]. In order to match with this property of the emitters, we designed plasmonic arrays with lower Q factor than our previous work [290], and hence broader resonance width, covering most of the emission spectral range of the hBN emitters.

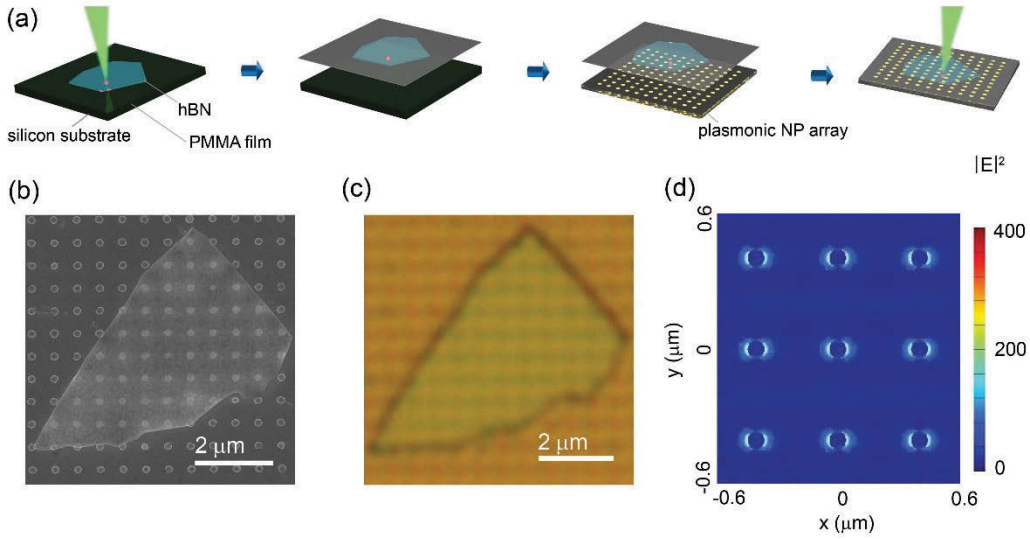

Figure 7.1. *Hexagonal boron nitride flakes and their transfer process onto plasmonic lattice substrates.* ***(a)*** *Schematic illustration of the wet process used to transfer a selected hBN flake with an emitter of choice (exemplified by the red dot) from a thermal silicon oxide substrate onto a plasmonic NP array using PMMA as the carrier.* ***(b)*** *SEM image of the mechanically exfoliated hBN flake positioned atop of a silver plasmonic lattice on silica and* ***(c)*** *optical image of the same flake on the plasmonic lattice.* ***(d)*** *FDTD simulation of the lateral (in-plane) electric*

field intensity distribution $|E|^2$ of a 400 nm-spacing silver plasmonic lattice structure.

To transfer hBN flakes onto plasmonic NP arrays, we employed the wet transfer method depicted in **Fig. 7.1a** (see methods for details)[291]. Briefly, an SPE at a frequency matching the plasmonic lattice array was identified and pre-characterized. A poly(methyl methacrylate) (PMMA) membrane was used to lift off the flakes and position them on top of a plasmonic lattice to achieve index-matching condition for high-quality lattice plasmon resonances. Lithographically defined substrates enabled identification and characterization of the same emitter before and after the transfer process.

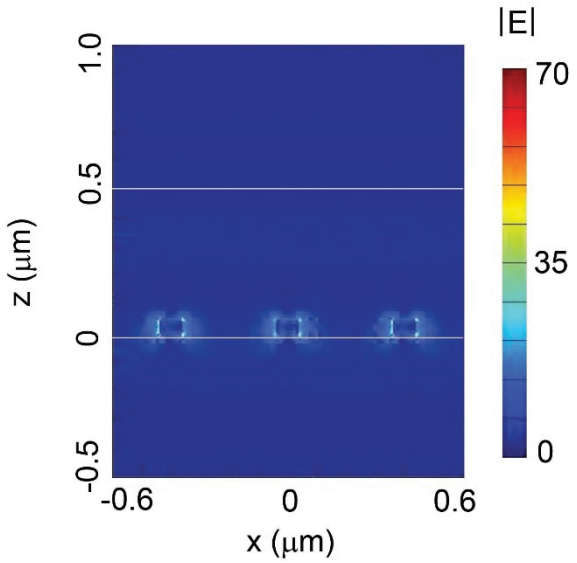

Figure 7.2. *Finite-difference time-domain simulation of the vertical (cross-sectional) electric field intensity distribution |E| of a silver nanoparticle (NP) array with 400-nm spacing.*

The optical properties of the emitters were recorded at room temperature using a home-built confocal microscope with a Hanbury Brown and Twiss interferometer (see methods for details). **Fig. 7.4a** shows a confocal PL map of a pristine hBN flake with a selected single emitter, marked by a red circle. A larger field-of-view scanning electron microscope (SEM) image of the hBN flakes atop the gold NP array can be found in **Fig. 7.3**.

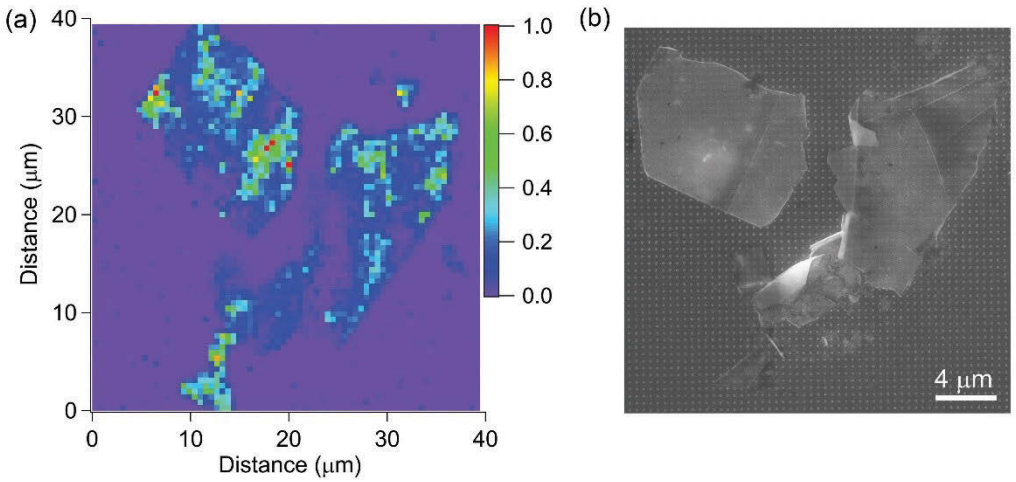

Figure 7.3. *Confocal PL map* ***(a)*** *and its corresponding larger field-of-view SEM image* ***(b)*** *shown in main text* ***Fig. 6.2a****. A good spatial correlation between the confocal map and the SEM image can be observed. The SEM image unarguably shows that the flakes are positioned atop the gold plasmonic NP array.*

Fig. 7.4b shows a transmission curve of the Au NP array (green) with the plasmonic resonance at 640 nm, a PL spectrum of the SPE circled in **Fig. 7.4a** with a zero phonon line (ZPL) at ~ 600 nm and a phonon sideband at ~ 640 nm (red curve). While the exact crystallographic structure of the emitters is still under debate, it has been proposed to be associated with the antisite nitrogen-vacancy defect (N_BV_N)[261]. **Fig. 7.4c** shows a second order correlation function, $g^2(\tau)$, from the emitter that dips to 0.02 at zero delay time (after background correction) [292], thus confirming that the emitter is indeed a single photon source. The data are fit using a three-level model **Eq. 2.1.**

We used the same model to fit all autocorrelation measurements in this work.

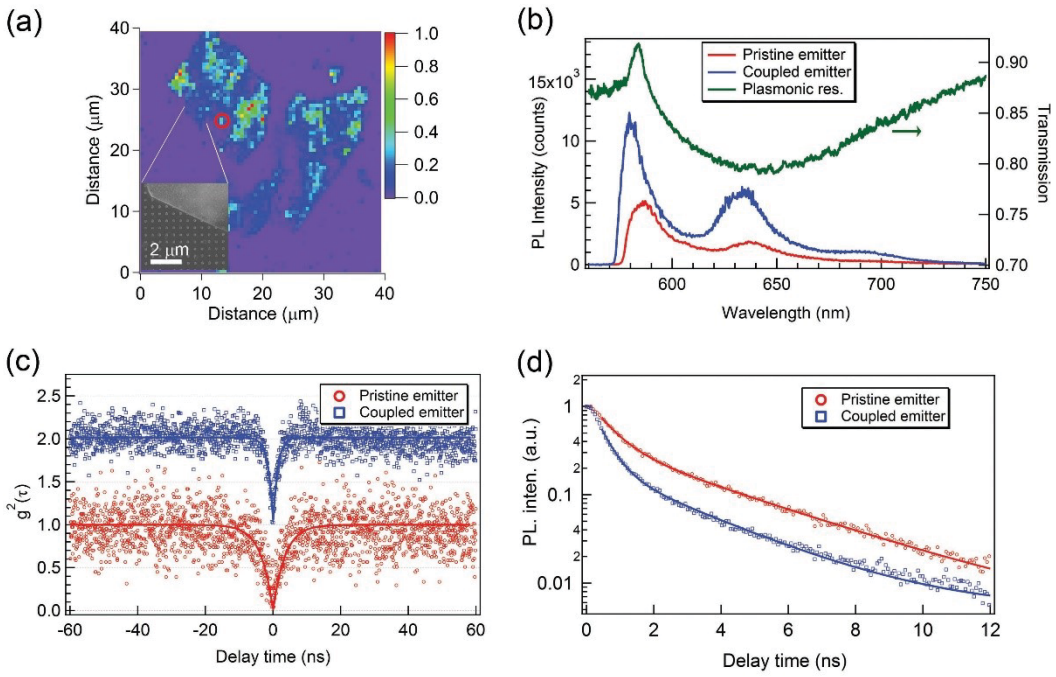

Figure 7.4. *Coupling between a quantum emitter in a tape exfoliated hBN flake and a gold NP array on silica.* ***(a)*** *PL confocal map of a flake containing a single photon emitter (red circled). Inset, SEM image of part of the flake on top of the gold plasmonic lattice. The scale bar represents 2 μm.* ***(b)*** *PL spectra of the pristine (red trace) and coupled (blue trace) single photon emitter, and a transmission spectrum of the plasmonic lattice (green trace) with the plasmonic resonance at 640 nm.* ***(c)*** *Second-order autocorrelation functions obtained from the pristine (red circles) and coupled (blue open squares) system. In both cases, the dip at zero delay time falling well below 0.5 implies single photon emission. Background correction was employed to correct the antibunching curves due to high PL background coming from the hBN flake. The* $g^{(2)}(0)$ *values for emission from pristine and coupled emitters are at 0.02 and 0.04, respectively. Red and blue solid lines are fits obtained using a three-level model.* ***(d)*** *Time-resolved PL measurements from the pristine (red open circles) and coupled (blue open squares) systems. Red and blue solid lines are double exponential fits. A 532 nm continuous-wave laser was used in* ***(a)***, ***(b)*** *and* ***(c)***. *A 512 nm pulsed laser with a repetition rate of 10 MHz and 100 ps pulse width was used in* ***(d)***.

Once the selected emitter was pre-characterized, it was transferred onto the plasmonic lattice with a matching resonance at λ = 641 nm (green curve, **Fig. 7.4b**). A full transmission spectra of the gold plasmonic array can be found in **Fig. 7.5**.

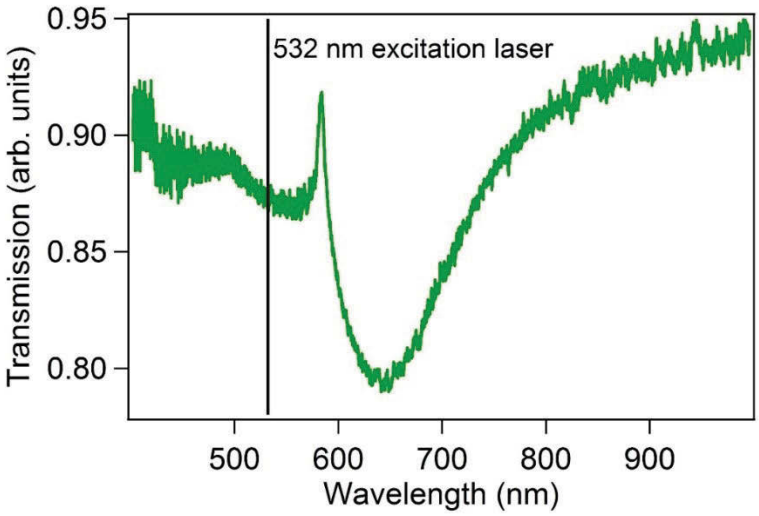

Figure 7.5. *A full-range transmission spectrum of a gold array in* ***Fig. 7.4.****. The solid line implies the 532 nm excitation laser used in this study. There is a negligible pump absorption by the plasmonic array according to the spectrum.*

Inset of **Fig. 7.4a** shows the SEM image of the same flake hosting the single emitter atop the gold array system. After being transferred atop the gold lattice, the emitter emission was enhanced by a factor of ~ 2.5 (blue curve, **Fig. 7.4b**), while still maintaining its quantum nature, as evident from the $g^2(\tau)$ function (blue curve, **Fig. 7.4c**). Because of better overlap of lattice plasmon resonance and the photon sideband, we observed stronger enhancement (~ 3) than the peak at zero phonon line. To achieve a more quantitative analysis of the enhancement, a lifetime measurement of the emitter was recorded before and after the transfer using a pulsed laser (see methods). **Fig. 7.4d** plots the lifetime results obtained using a picosecond pulsed laser. By using a double exponential fitting function, we obtained the values of $\tau_{1P} = 0.63$ ns, $\tau_{2P} = 3.4$ ns, and $\tau_{1C} = 0.42$ ns, $\tau_{2C} = 2.6$ ns for the pristine and coupled emitter, respectively. The PL intensity increase was in

good agreement with the lifetime reduction for the emitter, confirming the coupling to the plasmonic array.

To match the SPE frequency with the plasmonic NP array, we chose an emitter emitting at 652 nm. The same unique features on the confocal maps taken for pristine and coupled emitters (**Fig. 7.6**) suggests that the same location of the emitter is addressed. **Fig. 7.7a** shows a PL spectrum of the pristine SPE, and the same emitter coupled to the gold NP array. The emitter maintained its quantum nature, after being coupled to the plasmonic lattice, evident by the dips below 0.5 from the antibunching curves (**Fig. 7.7b**).

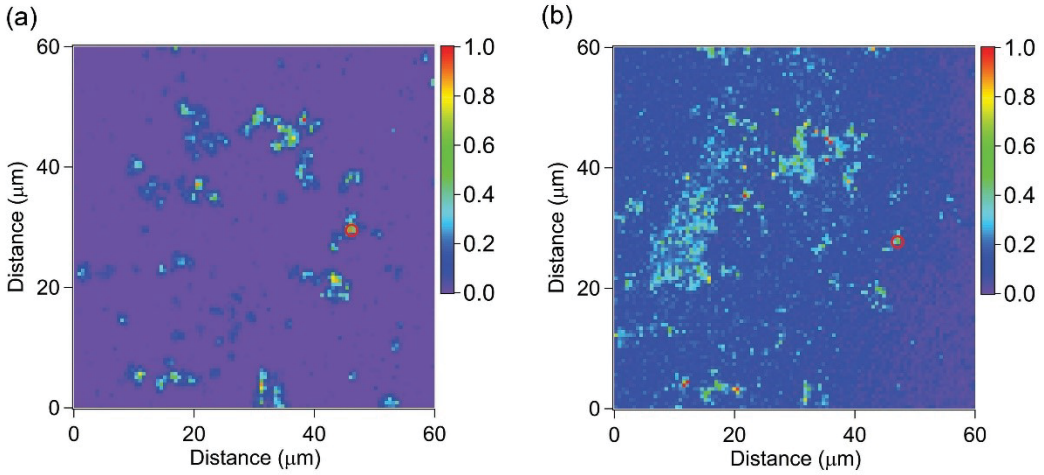

Figure 7.6. *Confocal PL maps of before and after the solvent-exfoliated flakes being transferred onto the plasmonic NP array. The two maps show a good agreement on the spatial location and relative orientation of the flakes to one another, confirming that the same flakes were examined.*

The reduction in the $g^{(2)}(0)$ value of the coupled emitter compared to the pristine emitter is due to background fluorescence from traces of PMMA residues after the transfer process. This effect is more obvious in the solvent hBN exfoliated rather than mechanically exfoliated flakes because of their smaller sizes compared to the laser spot size. From the time-resolved measurements, the lifetime of the emitter is reduced after being transferred onto the gold NP array - from 4 ns to 0.6 ns (**Fig. 7.7c**). This reduction in lifetime implies that there is an increase in local density of optical states (LDOS) due to higher concentration of electric field surrounding the

emitter. **Fig. 7.7d** shows saturation measurements recorded from the pristine and the coupled flake, exhibiting saturation count rates of 0.37×10^6 and 0.89×10^6 counts/s, respectively, with an overall enhancement factor of 2.4. The data are fit to a three-level model, using **Eq. 2.2.** The higher brightness is thus in good agreement with the decrease in the lifetime of the emitter.

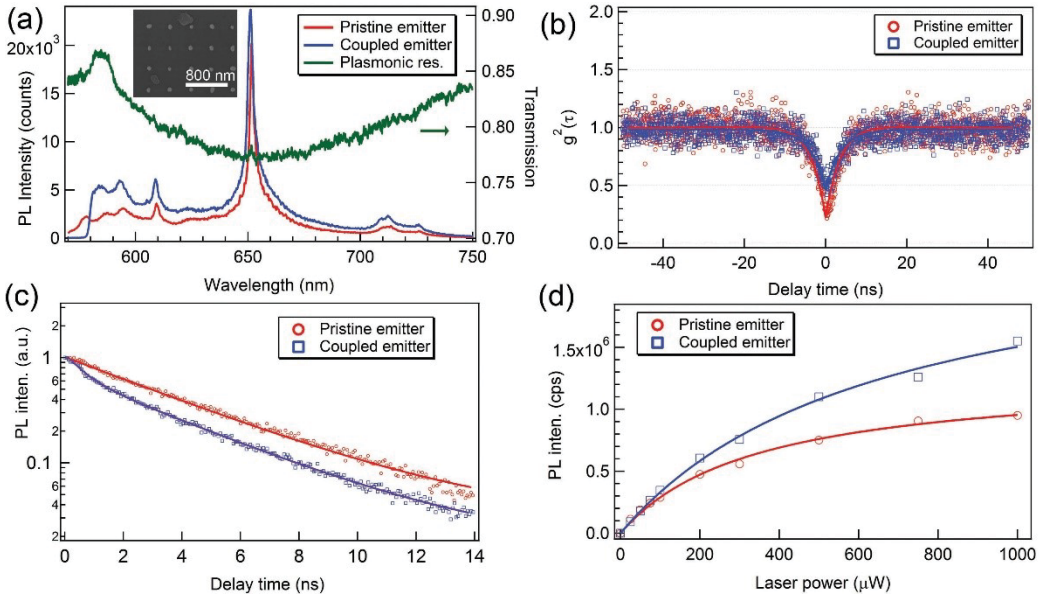

Figure 7.7. *Coupling between a quantum emitter in a solvent exfoliated hBN flake and a gold NP array on a silica substrate.* ***(a)*** *PL spectra of a pristine (red trace) and coupled (blue trace) single photon emitter, and a transmission spectrum of the gold lattice (green trace). Inset: SEM image of the hBN flakes ontop the gold NP array.* ***(b)*** *Second-order autocorrelation functions obtained from the pristine (red open circles) and coupled (blue open squares) systems. The $g^{(2)}(0)$ values for emission from pristine and coupled emitters are 0.23 and 0.47, respectively. In both cases, the dip at zero delay time falling well below 0.5 implies single photon emission. Red and blue solid lines are fits obtained using a three-level model.* ***(c)*** *Time-resolved PL measurements from the pristine (red open circles) and coupled (blue open squares) systems. Red and blue solid lines are double exponential fits.* ***(d)*** *Fluorescence saturation curves obtained from the pristine (red open circles) and coupled (blue open squares) systems. Red and blue solid lines are fits obtained using* ***Eq. 2.1.*** *A 532 nm continuous-wave laser was used in* ***(a)****,* ***(b)*** *and* ***(d)****. A 512*

nm pulsed laser with a repetition rate of 10 MHz and 100 ps pulse width was used in ***(c)***.

While gold NP arrays can produce sharp lattice plasmon resonances in the NIR region, they suffer losses from interband transitions in the red region and thus exhibit broad resonances with lower quality factors. In contrast, silver NP arrays maintain narrow lattice plasmon resonances in the red spectral region with stronger near-field enhancement, better mode quality and larger Purcell factor compared to gold NPs. We, therefore, employed a silver NP array with 400 nm spacing coated with a 5-nm protective alumina layer. A strong resonance peak at $\lambda = 638$ nm with a full-width-at-half-maximum (FWHM) of 50 nm was obtained from this structure (**Fig. 7.8a**). To match this lattice, we identify a single emitter with a ZPL at 680 nm. The flake was then transferred onto the plasmonic array using the method shown in **Fig. 7.1c**. **Fig. 7.8a** shows a PL spectrum of the pristine single emitter, and the same emitter coupled to the silver plasmonic lattice array. **Fig. 7.8b** confirms that the emitter is an SPE, and the non-classical emission is maintained after the transfer, with $g^{(2)}(0)$ at 0.06 and 0.29 before (red curve) and after (blue curve) the transfer, respectively.

The lifetime of the pristine emitter is $\tau_{1P} = 8.5$ ns while the lifetime of the same emitter coupled to the plasmonic lattice significantly reduced at a shorter time scale, to $\tau_{1C} = 0.27$ ns (**Fig. 7.8c**), characteristic of the coupling to silver NP array. Only the first component in the decay curve of the coupled system was used for comparison because the second component simply arises from the uncoupled part of fluorescence emission. We note that the lifetimes of the pristine solvent exfoliated and tape exfoliated flakes may differ most likely due to the different dielectric environments in the materials.

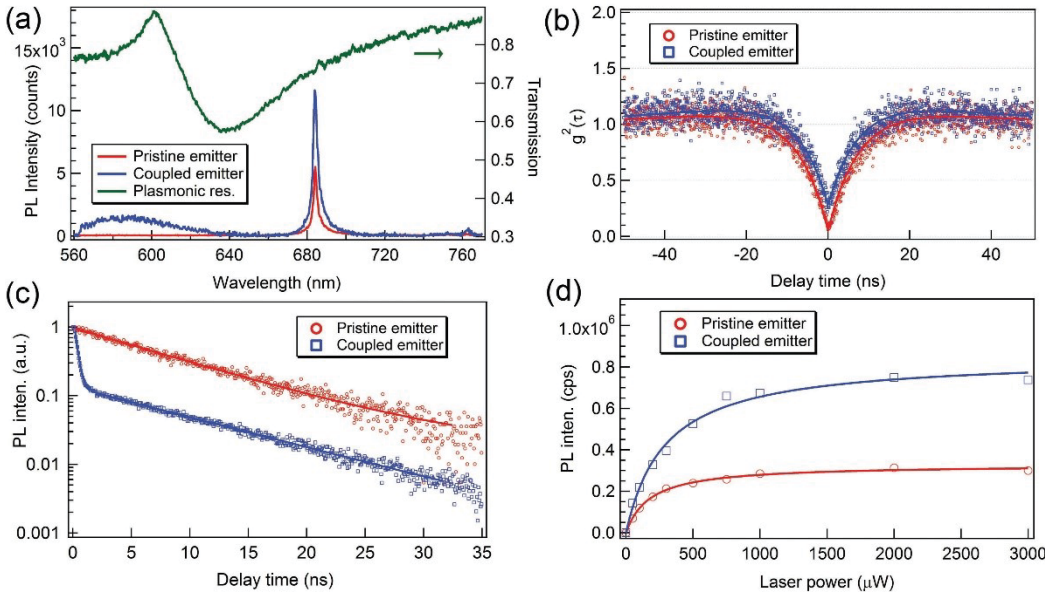

Figure 7.8. *Coupling between a quantum emitter in a solvent exfoliated hBN flake and a silver NP array on a silica substrate.* ***(a)*** *PL spectra of a pristine (red trace) and coupled (blue trace) single photon emitter, and a transmission spectrum of the silver lattice (green trace).* ***(b)*** *Second-order autocorrelation functions obtained from the pristine (red open circles) and coupled (blue open squares) systems. In both cases, the dip at zero delay time falling well below 0.5 implies single photon emission. Red and blue solid lines are fits obtained using a three-level model. The* $g^{(2)}(0)$ *values for emission from pristine and coupled emitters are 0.06 and 0.29, respectively.* ***(c)*** *Time-resolved PL measurements from the pristine (red open circles) and coupled (blue open squares) systems. Red and blue solid lines are double exponential fits.* ***(d)*** *Fluorescence saturation curves for obtained from the pristine (red open circles) and coupled (blue open squares) systems. Red and blue solid lines are fits obtained using* ***Eq. 2.1.*** *A 532 nm continuous-wave laser was used in* ***(a)****,* ***(b)*** *and* ***(d)****. A 512 nm pulsed laser with a repetition rate of 10 MHz and 100 ps pulse width was used in* ***(c)****.*

Fig. 7.8d shows saturation measurements recorded from the pristine and the coupled flake, exhibiting saturation count rates of 0.33×10^6 and 0.85×10^6 counts/s, respectively, with an overall factor of 2.6 enhancement. The measured enhancement is lower than the one predicted from the ratios of the spontaneous decays before and after coupling to the plasmonic lattice ($E_F = \tau_{1P}/\tau_{1C} \approx 30$). This

is likely due to less optimal spatial position of the emitters with respect to the hot cavity field, the spectral overlap between lattice plasmon resonance and hBN emission, or the contribution of the non-radiative decay pathways of the coupled system.

7.5 Conclusion

To summarize, we presented a robust and versatile approach to couple SPEs in 2D hBN to plasmonic nanocavity arrays. In particular, we developed a robust approach to transfer deterministically a pre-characterized quantum emitter of choice in hBN onto plasmonic gold and silver lattice arrays. An enhancement of a factor of ~ 2 is observed, associated with a fast lifetime reduction to demonstrate plasmonic-enhanced SPE emission. We note that the hBN emitters are already bright in their pristine form, with high QE and strong radiative component, which makes it more challenging to achieve high enhancement using plasmonic or dielectric cavities. The approach is an enabler to enhance emission from emitters in 2D materials and paves the way to hybrid planar quantum optics with 2D materials and plasmonic resonators.

.

8 Room-Temperature Single-Photon Emission from Oxidized Tungsten Disulfide Multilayers

This chapter reports single photon emitter in oxidized tungsten disulfide flakes. The project was conceived by Trong Toan Tran and Igor Aharonovich. The monolayer WS_2 samples were prepared by Changxi Zheng (Monash University). John A. Scott conducted transmission electron microscopy characterization and analysis. Avi Bendavid performed the XPS measurements and analysis. Optical characterization was done by Trong Toan Tran, with some assistance from Sumin Choi and Gediminas Seniutinas. All the author discussed and wrote the manuscript.

8.1 Abstract

Two dimensional systems offer a unique platform to study light-matter interaction at the nanoscale. In this work, we report on robust quantum emitters fabricated by thermal oxidation of tungsten disulfide multilayers. The emitters show robust, optically stable, linearly polarized luminescence at room temperature, can be modeled using a three-level system, and exhibit moderate bunching. Overall, our results provide important insights into the understanding of defect formation and quantum emitter activation in 2D materials.

8.2 Introduction

Two-dimensional materials have recently emerged as a promising platform for optoelectronics[97] and nanophotonics [92] owing to their layer-dependent properties, strong light-matter interactions, and weak van der Waals interlayer bonding. Among these layered materials, TMDs such as molybdenum disulfide (MoS_2), tungsten disulfide, molybdenum diselenide ($MoSe_2$), and tungsten diselenide (WSe_2) have garnered the most research interest thanks to their direct bandgaps (for monolayers), large carrier mobility, tunable emission and

mechanical flexibility.[89, 293-294] The recent discoveries of single photon sources in the form of quantum dots in WSe_2 [78-82, 295] has further spurred intensive research into the use of TMDs for quantum information and processing. The 2D nature of these crystals and the know-how gained from work on manipulation of graphene, enabled rapid engineering of electrically triggered quantum light emitting diodes [83].

However, due to the shallow binding energies of several millielectron volts (meV), these quantum dots exhibit single photon emission only at cryogenic temperature. Furthermore, the nature of the quantum emitters is still under debate. On the other hand, room temperature single photon emission was recently observed from monolayers, few layers and bulk hBN [4-6, 8, 224, 227-228]. hBN has a wide bandgap of almost 6 eV and can, therefore, host a variety of localized defects with deep states that enable single photon emission at room temperature. In this letter, we report on quantum emission observed from annealed WS_2 multilayers. We show that annealing at a temperature of 550°C gives rise to partial oxidation of the flakes and the formation of localized stable optically active defects. We characterize the nature of the emissions and propose several models for the origin of the emitters.

8.3 Methods

Commercial solvent-exfoliated tungsten disulfide samples (Graphene Laboratories) were drop-cast on a 1 cm^2 native oxide (a few nm thick SiO_2) silicon chip. The chip was annealed in a tube furnace (Lindberg/Blue M) at 550°C for 30 min under 1 Torr of flowing Argon and subsequently cooled down to room temperature before being subject to photoluminescence measurement. Similar to other TMDs, crystal structures of tungsten disulfide can be studied using Raman spectroscopy (in Via Renishaw microscope) with three typical vibrational phonon modes E_{2g}, A_{1g} and 2LA.

8.4 Results and Discussion

While the first two arise from in-plane stretching optical phonon modes at Brillouin zone center, the latter comes from a longitudinal acoustic mode.[296] **Fig. 8.1a** shows a typical optical image of the annealed WS_2 multilayers on a native oxide silicon substrate (no difference was seen before and after the annealing process). The WS_2 flakes have a lateral size of ~0.3 – 3 μm and thickness of ~5 – 300 nm. Additional images could be referred to **Fig. 8.2.** We conducted Raman scattering measurement of the sample before and after thermal annealing at 550°C in an inert environment. A Raman spectrum from a high-quality monolayer WS_2 sample is used as a reference. **Fig. 8.1b** presents Raman scattering plots for the three samples. Both the monolayer (red trace) and the pristine multilayers (green trace) show clear E_{2g} and 2LA modes (grey highlighted), and A_{1g} mode (orange highlighted), confirming the characteristic lattice vibrations of WS_2.[296] The annealed WS_2 sample, however, does not show these lattice vibration characteristics, implying that the flakes underwent compositional changes upon annealing.

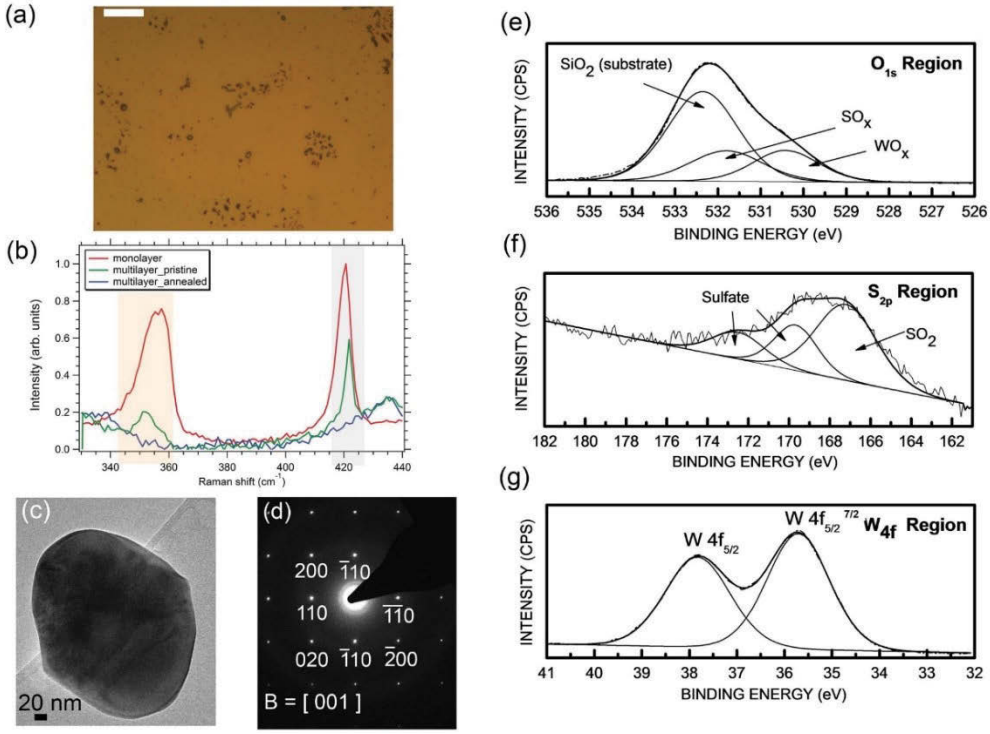

Figure 8.1. *Characterization of the multilayers.* ***(a)*** *Optical image of annealed WS_2 multilayers. The scale bar is 10 μm. No visible difference could be seen before and after annealing.* ***(b)*** *Raman spectra of a pristine monolayer (red), pristine multilayer (green), and multilayers that were annealed in argon at 550°C (blue). The grey and yellow highlighted boxes denote E_{2g} and 2LA mode, and A_{1g} vibration mode of WS_2.* ***(c)*** *TEM image of an annealed flake and* ***(d)*** *the corresponding selected area electron diffraction taken from* ***(c)****. The diffraction pattern indicates the cubic phase of WO_3.* ***(e-g)*** *XPS spectra of WS_2 annealed at 550°C in an Argon atmosphere, showing spectral regions that contain the O_{1s}, S_{2p} and W_{4f} peaks, respectively. In* ***(c)*** *the presence of a WO_x phase is clearly observed.*

To understand the crystal structure of the treated flakes, we employed TEM and SAED. The SAED pattern along the [001] zone axis showed that the flake was a single crystal with the cubic structure. D-spacing measurements of 0.261 nm and 0.185 nm matched the {110} and {200} planes of cubic WO_3 (Pm-3m). These measurements suggest that the diffraction pattern comes from the cubic phase of WO_3. In addition, X-ray photoelectron spectroscopy (XPS) was used to elucidate the composition of the annealed WS_2 sample. **Fig. 8.1e, 1f** and **1g** show photoelectron binding energies at O_{1s}, S_{2p} and W_{4f} regions, respectively. The three spectra suggest the presence of WO_x phase, supporting the electron diffraction data. The oxidation forms during the annealing process of WS_2, likely as a result of traces of residual water and oxygen molecules in the quartz tube. This behavior is consistent with previous studies on oxidation of WS_2.[297-298]

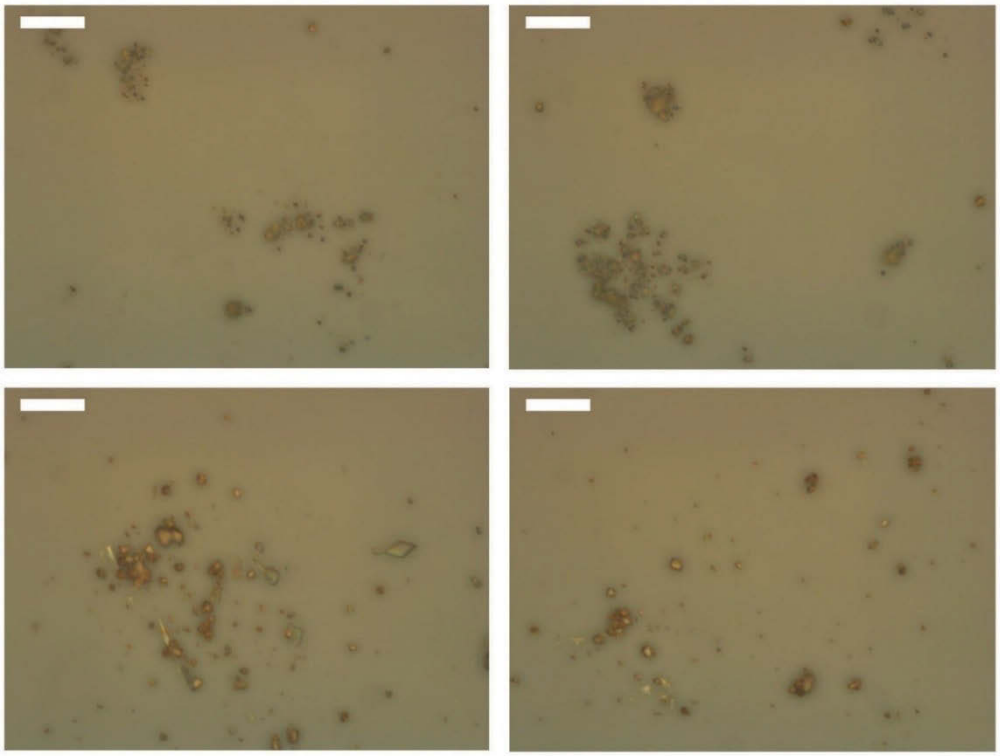

Figure 8.2. *Bright-field optical images of WS_2 flakes after being annealed at 550°C in argon for 30 min. The scale bars are 10 μm. The WS_2 flakes have a lateral size of ~0.3 – 3 μm and thickness of ~5 – 300 nm.*

To characterize the annealed flakes further, we perform micro-photoluminescence (μPL) measurements using a typical home-built confocal microscope equipped with a high numerical aperture objective (NA = 0.9). The excitation of the samples is performed using a 532 nm CW laser, and the collected signal is directed into two single photon detectors or imaged using a spectrometer. The details of the setup can be found elsewhere[4]. To examine the sample, we first conduct a confocal map scan over a 60 x 60 μm^2 area (**Fig. 8.3a**). Several bright spots are observed in the confocal map, and their spectral properties are shown in **Fig. 8.3b**. The PL spectra show single peaks at 600 nm (yellow trace), 650 nm (purple trace) and 730 nm (red trace), with peak widths broader than that of the excitonic emission line from the monolayer WS_2 sample (black trace). Note also that the yellow trace appears at higher energies than the excitonic transition of the WS_2 monolayer, further confirming that a new phase has formed. **Fig. 8.3c** shows the

three corresponding second order autocorrelation ($g^{(2)}(\tau)$) plots taken from the three centers described in **Fig. 8.3b**. The $g^{(2)}(0)$ values are well below 0.5 at zero delay time, indicating that all three centers are indeed single photon sources.[13, 14] For convenience, we name the three emitters S1 (red), S2 (yellow) and S3 (purple). Note that emitters S1 and S3 exhibit similar spectral and temporal properties (i.e., no bunching at the same excitation power, and FWHM of 31 nm and 19 nm, respectively) while emitter S2 exhibits bunching and a much broader emission spectrum. To measure the excited state lifetimes of these color centers, we employed time-resolved PL with a 512 nm pulse laser (100 ps pulse width and 10 MHz repetition rate) as an excitation source. By using double exponential fitting, we obtained excited state lifetimes of 3.5, 4.6, and 4.4 ns for emitter S1, S2 and S3, respectively.

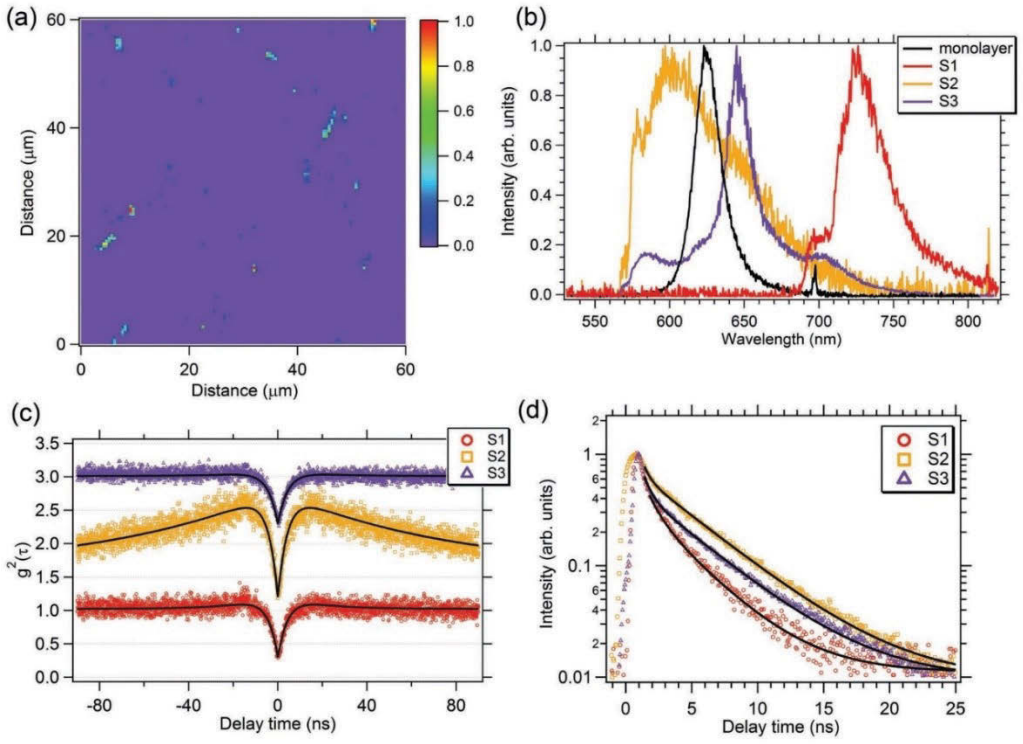

Figure 8.3. *Single photon emission from annealed multilayers.* ***(a)*** *A typical confocal photoluminescence map showing several bright spots corresponding to localized defects.* ***(b)*** *Photoluminescence spectra taken from three bright spots. A spectrum from monolayer WS_2 is plotted for comparison* ***(c)*** *Second-order autocorrelation measurement obtained from the three emitters. The curves are*

offset vertically for clarity. ***(d)*** *Time-resolved photoluminescence measurement recorded from the three emitters, yielding excited state lifetimes of 3.5 ns, 4.6 ns, and 4.4 ns, respectively for emitters S1, S2 and S3. The pump power used in* ***(a, b, c)*** *was 300 μW at 532 nm while the pulsed measurement was done using a 512 nm laser (10 MHz, 50 μW).*

We proceed with further detailed characterization of emitter S1. A fluorescence saturation curve is recorded as a function of excitation power, and the data are shown in **Fig. 8.4a**. To fit the data, we employ a standard three-level system that has a ground, excited and a long-lived metastable state. Consequently, the data are fit using **Eq. 2.2.**, yielding a saturated intensity, I_∞, of 350 kcps at a saturation power, P_{sat}, of 1.9 mW (**Fig. 8.4a**). This brightness is comparable with room temperature emitters in diamond, ZnO, and SiC.[67-68, 292, 299].

We then conducted an excitation and emission polarization study of emitter S1. By using a half-wave plate for excitation polarization measurement, and both a half-wave plate and a polarizing filter for emission polarization measurement, we obtained plots of excitation (red open circles) and emission (blue open squares) polarization for emitter S1 (**Fig. 8.4b**). Fitting the two curves with a $\cos^2(\theta)$, indicates that the center is only partially polarized. The visibility of excitation and emission polarization of the defect were determined to be 0.32 and 0.79, respectively.

The fact that the emission polarization has higher visibility than excitation polarization probably suggests that either the excitation dipole is not aligned along the laser path, or there are two orthogonal absorption dipole moments that take process during the non-resonant excitation of the emitter. The emission is almost fully polarized, suggesting that only one dipole is involved in the emission process. Polarization data taken from three other emitters confirms similar behavior (**Fig. 8.5**).

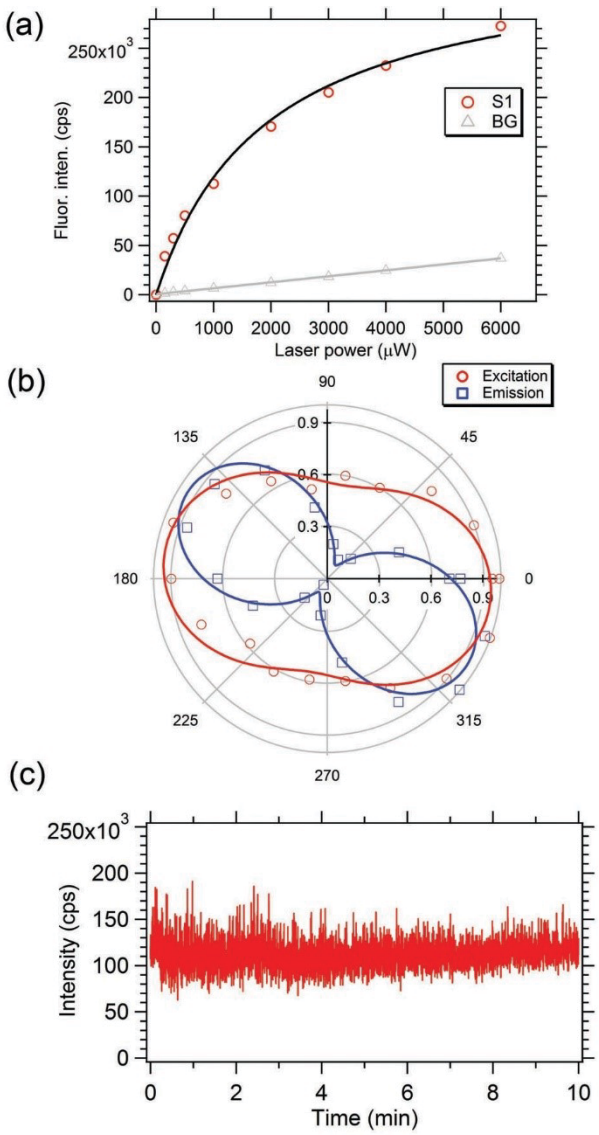

Figure 8.4. *Fluorescence saturation and polarization of emitter S1.* ***(a)*** *Fluorescence intensity as a function of pump power. The red open circles and grey open triangles denote background-corrected fluorescence profile of emitter S1 and background fluorescence taken at an area adjacent to the emitter (in* ***Fig. 8.3****). The solid lines are corresponding fitted curves. The saturated intensity is 347,000 cps with the saturated pump at 1.9 mW.* ***(b)*** *Excitation (red open circles) and emission (blue open squares) measurement for emitter S1. Solid lines are corresponding fits.* ***(c)*** *Fluorescence stability measurement over 10 minutes at an excitation power of 1mW. No bleaching or blinking could be seen from the measurement. Measurements taken in* ***(a-c)*** *were done with CW 532 nm laser.*

Fluorescence stability for the emitter is shown in **Fig. 8.4c**. The emitter is stable and does not exhibit blinking or bleaching under 1 mW of continuous laser excitation over the course of the measurement (10 minutes).

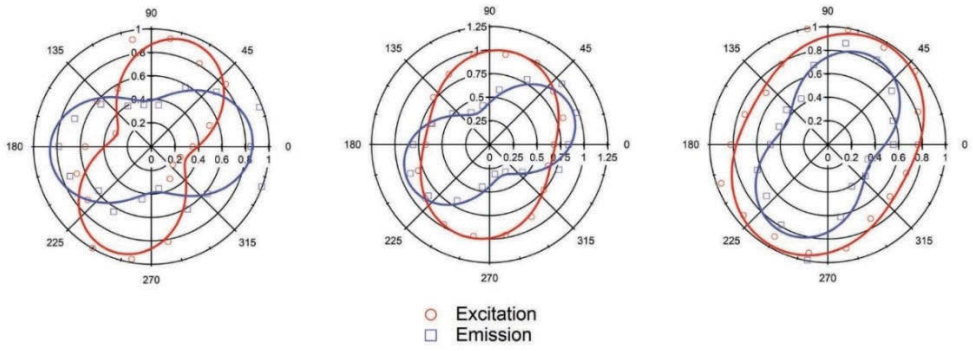

Figure 8.5. *Additional polarization data taken from three different single photon emitters from the annealed WS_2 sample. Red open circles and blue open squares denote excitation and emission measurement, respectively. Solid lines are corresponding fits. Measurements were done with CW 532 nm laser.*

To understand the photophysics of the emitter further, we measured $g^{(2)}(\tau)$ as a function of excitation power. This measurement is helpful to understand important photophysical parameters of quantum emitters such as their excited state (τ_1) and metastable state (τ_2) lifetimes which must be known in order to estimate the quantum yield of the centers. Such a measurement is shown in **Fig. 8.6a**. At high power (> 2mW), the emitter exhibits photo-bunching, indicating that its electronic structure includes at least one metastable state.[218, 300] The curves are, therefore, fitted with a three-level model following **Eq. 2.1.**

By plotting τ_1 and τ_2 as a function of excitation power, we arrive at the graph shown in **Fig. 8.6b**. The data are well fitted with single exponential [186], yielding τ_1 and τ_2 values of 4.5 and 9.3 ns, respectively. It must be noted that the excited state lifetime obtained by this method is in relatively good agreement with that from the time-resolved PL measurement.

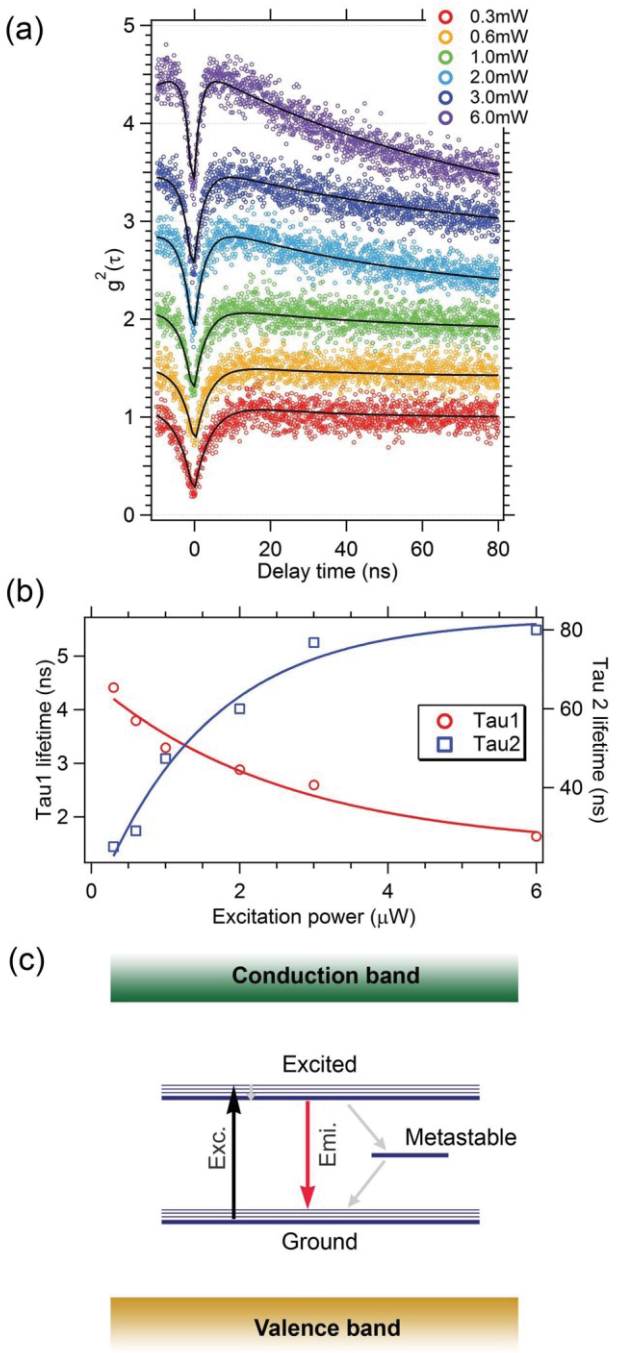

Figure 8.6. (a) *Antibunching curves as a function of pump power. Solid lines are fitted profile using the standard three-level model.* ***(b)*** *Emission (τ_1) and metastable (τ_2) lifetime plotted as a function of excitation power. By applying linear fitting and extrapolating the fits to vanishing excitation power, emission (τ_1) and metastable (τ_2) lifetime are calculated to be 4.5 ns and 9.3 ns, respectively.* ***(c)*** *Proposed three-level diagram of the emitters with a ground state, an excited*

state, and a metastable state. Black, red and grey arrows represent excitation, emission, and non-radiative transitions.

We now turn to the possible origin of the single photon source. Single photon emission could only be observed from the thermally treated flakes, namely the WO_3 layers, but not on the pristine WS_2 samples. Single photon emission was also observed at energies higher than of the direct bandgap excitonic emission from a monolayer WS_2 (i.e., S2). From these two observations, it is reasonable to attribute the single photon emission to a deep trap state of a WO_3 (not a shallow bound exciton state, as it is not thermally ionized and its quantum optical properties are preserved at room temperature). Indeed, the bandgap of WO_3 can be substantially higher, up to 3.6 eV[301-302] in the case of WO_3, than the bandgap of WS_2 (~ 2 eV). These higher bandgaps can facilitate localized defects with ground and excited state energies within the bandgap (see **Fig. 8.6c** and corresponding transitions that can be driven using a 2.4 eV green laser. Similar behavior of quantum emission from oxides was observed for zinc oxide (ZnO) that has a comparable bandgap of 3.2 eV also exhibits quantum emitters at room temperature.[67, 303-304]

8.5 Conclusion

To summarize, we identified several quantum emitters in annealed WS_2 multilayers. Raman and XPS measurements suggest a phase transition to a WO_3 cubic phase via oxidation. The new layers host optically stable quantum emitters. The origin of the emitters is likely a deep trap defect state within the bandgap of the WO_3. The quantum emitters show relatively high brightness and a short excited state lifetime suitable for photonic applications. A detailed study of various tungsten oxide materials, as well as dedicated modeling and temperature, resolved measurements are needed to understand the origin and the chemical structure of the defects. However, even at this point, our results emphasize the breadth of emitters available within 2D materials and their promise to host new optically active defects.

9 General conclusions and Outlook

In summary, I introduce a new class of room-temperature quantum emitters embedded in the layered material - hexagonal boron nitride. I demonstrate that the quantum emitters exhibit ultrahigh brightness with cases exceeding 4 MHz emission rate without the aid of optical cavities or solid immersion lenses – the brightest defect-based quantum emitters to date. The harvested quantum light shows full polarization, suggesting a single fixed transition dipole moment. Lifetimes from these emitters are measured to be around 3 ns, roughly five-fold shorter than that of NV centers in diamond. In addition, the quantum emitters are extremely stable even when tested at elevated temperature (as high as 500°C) with reactive gaseous environments. I also demonstrate the control of density and locality of the emitters on hBN flakes by means of thermal energy, electron beam induced etching, ion beam irradiation or laser ablation. Moreover, I prove that the quantum emitters are observed on all forms of hBN materials, from solvent-exfoliated nanoflakes, micron-sized flakes to bulk crystals, confirming the reproducibility of the single photon sources. Using resonant excitation, I show that the linewidth of ~6 GHz is recorded, a promising sign for further work to couple these emitters to high Q factor dielectric cavities. When being resonantly excited, the emitters still produce single photon emission, confirmed by the photon antibunching behavior. With spin-polarized DFT simulation, I propose the defect configuration to be N_BV_N. Additionally, this defect symmetry is predicted to allow for tuning the optical resonance by applied stress along the direction of the dipole moment. Finally, I demonstrate that another 2D material, namely WS_2, upon thermally oxidized, also host room-temperature, stable single photon emitters. This observation implies that there might be possible to create quantum emitters in other 2D semiconductors such as TMDs.

At this end, I have shown in this work that quantum emitters in hBN emerge as a new promising class of single photon source owing to its room-temperature operation, ultrahigh polarized emission, high single photon purity, possible tuning of optical resonance, integrat-ability to external optical cavities and ease of

fabrication. More investigations on these defect centers, however, are awaited. On the one hand, future works should be focused on determining the level structures of the color centers so that a full coherent quantum control scheme can be realized experimentally to manipulate quantum states of the defect centers. This determination could be done by optical investigation guided by a combination of different simulation toolkits such as DFT, group theory, and a linear combination of atomic orbitals (LCAO) – the same approach used to unveil the level structure of NV centers in diamond. In fact, following my first studies, there have been several recent reports proposing different defect configurations such as carbon-antisite vacancy (C_BV_N) [305-306] or negatively charged boron vacancy (V^-_B) [307]. The origin of the defect centers is, however, still under debate.

In addition, optical experiments involved high magnetic and electric fields are expected to play a crucial role to uncover quantum properties of these systems such as spin-spin and spin-orbit interactions and spin-selection rules. Once the level structures of these quantum sources are unambiguously determined, more advanced quantum demonstrations including two-photon quantum interference can be executed. In case the electron spins of the systems can be optically addressed, it is possible to attempt ODMR-driven nanoscale and formation of quantum logic gates as having been demonstrated on NV centers in diamond. On the other, schemes with more precise engineering and control of the spatial position of the emitters in hBN flakes need to be pursued, to enable on-chip integrated optical circuit based on quantum emitters in hBN. The approaches include the use of energy-controlled focused ion beam (FIB) with a wide range of trial species such as argon, helium, silicon, oxygen, and so on, and employment of high-energy electron bombardment from TEM.

Before the final remark, a summary of the literature on quantum emitters in hBN is presented to provide the readers with an overall picture of this active topic. Inspired by our pioneering works, several research groups around the globe have been pursuing further studies of the quantum emitter in hBN. Fuchs and co-workers [227], and Wrachtrup and co-workers [228] demonstrated detailed photophysics of quantum emitters in solvent- and tape-exfoliated hBN flakes.

Bright quantum emission from defects in bulk hBN was reported by Jacques et al. [224]. Quantum emitters in hBN emitting in the UV spectral region were also presented using CL by Zobelli and co-workers [240]. Bassett et al. reported the photodynamics, polarization and electron-phonon coupling studies on suspended hBN flakes [229]. Fuchs and co-workers took a step further on the polarization study to suggest that the misalignment between the absorption and emission dipole is due to the different transition pathways involved [232]. Magneto-optical measurements were attempted by Strauf et. al. [226] and Koperski et. al. [308], however, there were no signs of magnetic-field interaction with the quantum emitters in hBN, even at magnetic field as high as 14 T. The extraction of quantum emission from the quantum emitters into tapered-fiber and multimode fiber were demonstrated by Schell et. al. [231] and Vogl et. al. [309], respectively. Schell and co-workers [310], on a different investigation, performed two-photon absorption for a single defect center in hBN flakes. Coherence times of the quantum emitters were studied by Benson et al. [233], showing coherence times around 81 ps. A couple of follow-up studies from our group (not shown in this thesis) were focused on the stability of the quantum emitters at a temperature as high as 800 K [230], and super-resolution using ground-state depletion (GSD) technique [311]. On the other hand, several simulation studies employing first-principle calculation or group theory were also reported, suggesting a variety of defect configurations [305-307].

To sum up, I believe that this current work lays a strong foundation for future investigations into single photon source from the hexagonal boron nitride in particular and in the two-dimensional limit in general, where the physics is rich, and the applicability is widely opened.

Bibliography

1. Bennett, C. H.; Brassard, G., *Proceedings of the IEEE International Conference on Computers, Systems and Signal Processing* **1984**, 175-179.

2. Bennett, C. H.; Brassard, G., Quantum cryptography: Public key distribution and coin tossing. *Theoretical Computer Science* **2014,** *560*, 7-11.

3. Wootters, W. K.; Zurek, W. H., A single quantum cannot be cloned. *Nature* **1982,** *299* (5886), 802-803.

4. Tran, T. T.; Bray, K.; Ford, M. J.; Toth, M.; Aharonovich, I., Quantum Emission from Hexagonal Boron Nitride Monolayers. *Nat. Nanotechnol.* **2016,** *11* (1), 37-41.

5. Tran, T. T.; Elbadawi, C.; Totonjian, D.; Lobo, C. J.; Grosso, G.; Moon, H.; Englund, D. R.; Ford, M. J.; Aharonovich, I.; Toth, M., Robust Multicolor Single Photon Emission from Point Defects in Hexagonal Boron Nitride. *ACS Nano* **2016,** *10* (8), 7331-7338.

6. Tran, T. T.; Zachreson, C.; Berhane, A. M.; Bray, K.; Sandstrom, R. G.; Li, L. H.; Taniguchi, T.; Watanabe, K.; Aharonovich, I.; Toth, M., Quantum Emission from Defects in Single-Crystalline Hexagonal Boron Nitride. *Phys. Rev. Appl.* **2016,** *5* (3), 034005.

7. Tran, T. T.; Kianinia, M.; Nguyen, M.; Kim, S.; Xu, Z.-Q.; Kubanek, A.; Toth, M.; Aharonovich, I., Resonant Excitation of Quantum Emitters in Hexagonal Boron Nitride. *ACS Photonics* **2017**, ASAP, doi: 10.1021/acsphotonics.7b00977.

8. Choi, S.; Tran, T. T.; Elbadawi, C.; Lobo, C.; Wang, X.; Juodkazis, S.; Seniutinas, G.; Toth, M.; Aharonovich, I., Engineering and Localization of Quantum Emitters in Large Hexagonal Boron Nitride Layers. *ACS Appl. Mater. Interfaces* **2016,** *8* (43), 29642-29648.

9. Tran, T. T.; Wang, D.; Xu, Z.-Q.; Yang, A.; Toth, M.; Odom, T. W.; Aharonovich, I., Deterministic Coupling of Quantum Emitters in 2D Materials to Plasmonic Nanocavity Arrays. *Nano Lett.* **2017,** *17* (4), 2634-2639.

10. Tran, T. T.; Choi, S.; Scott, J. A.; Xu, Z.-Q.; Zheng, C.; Seniutinas, G.; Bendavid, A.; Fuhrer, M. S.; Toth, M.; Aharonovich, I., Room-Temperature Single-Photon Emission from Oxidized Tungsten Disulfide Multilayers. *Adv. Opt. Mater.* **2017,** *5* (5), 1600939-n/a.

11. Lewis, G. N., The conservation of photons. *Nature* **1926,** *118*, 874-875.

12. Lounis, B.; Orrit, M., Single-photon sources. *Rep. Prog. Phys.* **2005,** *68* (5), 1129-1179.

13. Buckley, S.; Rivoire, K.; Vučković, J., Engineered quantum dot single-photon sources. *Rep. Prog. Phys.* **2012,** *75* (12), 126503.

14. Aharonovich, I.; Castelletto, S.; Simpson, D. A.; Su, C. H.; Greentree, A. D.; Prawer, S., Diamond-based single-photon emitters. *Rep. Prog. Phys.* **2011,** *74* (7), 076501.

15. Wolters, J.; Sadzak, N.; Schell, A. W.; Schröder, T.; Benson, O., Measurement of the Ultrafast Spectral Diffusion of the Optical Transition of Nitrogen Vacancy Centers in Nano-Size Diamond Using Correlation Interferometry. *Phys. Rev. Lett.* **2013,** *110* (2).

16. Hong, C. K.; Ou, Z. Y.; Mandel, L., Measurement of subpicosecond time intervals between two photons by interference. *Phys. Rev. Lett.* **1987,** *59* (18), 2044-2046.

17. Aharonovich, I.; Englund, D.; Toth, M., Solid-state single-photon emitters. *Nat. Photon.* **2016,** *10* (10), 631-641.

18. Wineland, D. J.; Bollinger, J. J.; Itano, W. M.; Heinzen, D. J., Squeezed atomic states and projection noise in spectroscopy. *Phys. Rev. A* **1994,** *50* (1), 67-88.

19. Brune, M.; Schmidt-Kaler, F.; Maali, A.; Dreyer, J.; Hagley, E.; Raimond, J. M.; Haroche, S., Quantum Rabi Oscillation: A Direct Test of Field Quantization in a Cavity. *Phys. Rev. Lett.* **1996,** *76* (11), 1800-1803.

20. Monroe, C.; Meekhof, D. M.; King, B. E.; Wineland, D. J., A "Schrödinger Cat" Superposition State of an Atom. *Science* **1996,** *272* (5265), 1131-1136.

21. Hagley, E.; Maître, X.; Nogues, G.; Wunderlich, C.; Brune, M.; Raimond, J. M.; Haroche, S., Generation of Einstein-Podolsky-Rosen Pairs of Atoms. *Phys. Rev. Lett.* **1997,** *79* (1), 1-5.

22. Rauschenbeutel, A.; Nogues, G.; Osnaghi, S.; Bertet, P.; Brune, M.; Raimond, J.-M.; Haroche, S., Step-by-Step Engineered Multiparticle Entanglement. *Science* **2000,** *288* (5473), 2024-2028.

23. Rowe, M. A.; Kielpinski, D.; Meyer, V.; Sackett, C. A.; Itano, W. M.; Monroe, C.; Wineland, D. J., Experimental violation of a Bell's inequality with efficient detection. *Nature* **2001,** *409* (6822), 791-794.

24. Eisaman, M. D.; Fan, J.; Migdall, A.; Polyakov, S. V., Invited review article: Single-photon sources and detectors. *Rev. Sci. Instrum.* **2011,** *82* (7), 071101.

25. Orrit, M.; Bernard, J., Single pentacene molecules detected by fluorescence excitation in a p-terphenyl crystal. *Phys. Rev. Lett.* **1990,** *65* (21), 2716-2719.

26. Basché, T.; Moerner, W. E.; Orrit, M.; Talon, H., Photon antibunching in the fluorescence of a single dye molecule trapped in a solid. *Phys. Rev. Lett.* **1992,** *69* (10), 1516-1519.

27. Betzig, E.; Chichester, R. J., Single Molecules Observed by Near-Field Scanning Optical Microscopy. *Science* **1993,** *262* (5138), 1422-1425.

28. Brunel, C.; Lounis, B.; Tamarat, P.; Orrit, M., Triggered Source of Single Photons based on Controlled Single Molecule Fluorescence. *Phys. Rev. Lett.* **1999,** *83* (14), 2722-2725.

29. Lounis, B.; Moerner, W. E., Single photons on demand from a single molecule at room temperature. *Nature* **2000,** *407* (6803), 491-493.

30. Michler, P.; Imamoglu, A.; Mason, M. D.; Carson, P. J.; Strouse, G. F.; Buratto, S. K., Quantum correlation among photons from a single quantum dot at room temperature. *Nature* **2000,** *406* (6799), 968-70.

31. Santori, C.; Pelton, M.; Solomon, G.; Dale, Y.; Yamamoto, Y., Triggered Single Photons from a Quantum Dot. *Phys. Rev. Lett.* **2001,** *86* (8), 1502-1505.

32. Moreau, E.; Robert, I.; Manin, L.; Thierry-Mieg, V.; Gérard, J. M.; Abram, I., Quantum Cascade of Photons in Semiconductor Quantum Dots. *Phys. Rev. Lett.* **2001,** *87* (18), 183601.

33. Efros, A. L.; Nesbitt, D. J., Origin and control of blinking in quantum dots. *Nat. Nanotechnol.* **2016,** *11* (8), 661-71.

34. Strauf, S.; Stoltz, N. G.; Rakher, M. T.; Coldren, L. A.; Petroff, P. M.; Bouwmeester, D., High-frequency single-photon source with polarization control. *Nat. Photon.* **2007,** *1* (12), 704-708.

35. Sun, S.; Kim, H.; Solomon, G. S.; Waks, E., A quantum phase switch between a single solid-state spin and a photon. *Nat. Nanotechnol.* **2016,** *11* (6), 539-544.

36. Ding, X.; He, Y.; Duan, Z. C.; Gregersen, N.; Chen, M. C.; Unsleber, S.; Maier, S.; Schneider, C.; Kamp, M.; Höfling, S.; Lu, C.-Y.; Pan, J.-W., On-Demand Single Photons with High Extraction Efficiency and Near-Unity Indistinguishability from a Resonantly Driven Quantum Dot in a Micropillar. *Phys. Rev. Lett.* **2016,** *116* (2), 020401.

37. Galland, C.; Högele, A.; Türeci, H. E.; Imamoğlu, A., Non-Markovian Decoherence of Localized Nanotube Excitons by Acoustic Phonons. *Phys. Rev. Lett.* **2008,** *101* (6), 067402.

38. Vialla, F.; Chassagneux, Y.; Ferreira, R.; Roquelet, C.; Diederichs, C.; Cassabois, G.; Roussignol, P.; Lauret, J. S.; Voisin, C., Unifying the Low-Temperature Photoluminescence Spectra of Carbon Nanotubes: The Role of Acoustic Phonon Confinement. *Phys. Rev. Lett.* **2014,** *113* (5), 057402.

39. Sarpkaya, I.; Ahmadi, E. D.; Shepard, G. D.; Mistry, K. S.; Blackburn, J. L.; Strauf, S., Strong Acoustic Phonon Localization in Copolymer-Wrapped Carbon Nanotubes. *ACS Nano* **2015,** *9* (6), 6383-6393.

40. Hu, F.; Zhang, H.; Sun, C.; Yin, C.; Lv, B.; Zhang, C.; Yu, W. W.; Wang, X.; Zhang, Y.; Xiao, M., Superior Optical Properties of Perovskite Nanocrystals as Single Photon Emitters. *ACS Nano* **2015**.

41. Park, Y.-S.; Guo, S.; Makarov, N. S.; Klimov, V. I., Room Temperature Single-Photon Emission from Individual Perovskite Quantum Dots. *ACS Nano* **2015,** *9* (10), 10386-10393.

42. Zaitsev, A. M., Vibronic Spectra of Impurity-related Optical Centers in Diamond. *Phys. Rev. B* **2000,** *61* (19), 12909.

43. Doherty, M. W.; Manson, N. B.; Delaney, P.; Jelezko, F.; Wrachtrup, J.; Hollenberg, L. C. L., The nitrogen-vacancy colour centre in diamond. *Phys. Rep.* **2013,** *528* (1), 1-45.

44. Childress, L.; Walsworth, R.; Lukin, M., Atom-like crystal defects: From quantum computers to biological sensors. *Physics Today* **2014,** *67* (10), 38-43.

45. Gruber, A.; Dräbenstedt, A.; Tietz, C.; Fleury, L.; Wrachtrup, J.; Borczyskowski, C. v., Scanning Confocal Optical Microscopy and Magnetic Resonance on Single Defect Centers. *Science* **1997,** *276* (5321), 2012-2014.

46. Dolde, F.; Fedder, H.; Doherty, M. W.; Nöbauer, T.; Rempp, F.; Balasubramanian, G.; Wolf, T.; Reinhard, F.; Hollenberg, L. C. L.; Jelezko, F.; Wrachtrup, J., Electric-field sensing using single diamond spins. *Nat. Phys.* **2011,** *7* (6), 459-463.

47. Dolde, F.; Doherty, M. W.; Michl, J.; Jakobi, I.; Naydenov, B.; Pezzagna, S.; Meijer, J.; Neumann, P.; Jelezko, F.; Manson, N. B.; Wrachtrup, J., Nanoscale Detection of a Single Fundamental Charge in Ambient Conditions Using theNV−Center in Diamond. *Phys. Rev. Lett.* **2014,** *112* (9).

48. Grinolds, M. S.; Hong, S.; Maletinsky, P.; Luan, L.; Lukin, M. D.; Walsworth, R. L.; Yacoby, A., Nanoscale magnetic imaging of a single electron spin under ambient conditions. *Nat. Phys.* **2013,** *9* (4), 215-219.

49. Clevenson, H.; Trusheim, M. E.; Teale, C.; Schröder, T.; Braje, D.; Englund, D., Broadband magnetometry and temperature sensing with a light-trapping diamond waveguide. *Nat. Phys.* **2015,** *11* (5), 393-397.

50. Balasubramanian, G.; Chan, I. Y.; Kolesov, R.; Al-Hmoud, M.; Tisler, J.; Shin, C.; Kim, C.; Wojcik, A.; Hemmer, P. R.; Krueger, A.; Hanke, T.; Leitenstorfer,

A.; Bratschitsch, R.; Jelezko, F.; Wrachtrup, J., Nanoscale imaging magnetometry with diamond spins under ambient conditions. *Nature* **2008,** *455* (7213), 648-51.
51. Mamin, H. J.; Kim, M.; Sherwood, M. H.; Rettner, C. T.; Ohno, K.; Awschalom, D. D.; Rugar, D., Nanoscale Nuclear Magnetic Resonance with a Nitrogen-Vacancy Spin Sensor. *Science* **2013,** *339* (6119), 557-560.
52. Staudacher, T.; Shi, F.; Pezzagna, S.; Meijer, J.; Du, J.; Meriles, C. A.; Reinhard, F.; Wrachtrup, J., Nuclear Magnetic Resonance Spectroscopy on a (5-Nanometer)3 Sample Volume. *Science* **2013,** *339* (6119), 561-563.
53. Dutt, M. V. G.; Childress, L.; Jiang, L.; Togan, E.; Maze, J.; Jelezko, F.; Zibrov, A. S.; Hemmer, P. R.; Lukin, M. D., Quantum Register Based on Individual Electronic and Nuclear Spin Qubits in Diamond. *Science* **2007,** *316* (5829), 1312-1316.
54. Faraon, A.; Barclay, P. E.; Santori, C.; Fu, K.-M. C.; Beausoleil, R. G., Resonant enhancement of the zero-phonon emission from a colour centre in a diamond cavity. *Nat. Photon.* **2011,** *5* (5), 301-305.
55. Faraon, A.; Santori, C.; Huang, Z.; Acosta, V. M.; Beausoleil, R. G., Coupling of Nitrogen-Vacancy Centers to Photonic Crystal Cavities in Monocrystalline Diamond. *Phys. Rev. Lett.* **2012,** *109* (3).
56. Babinec, T. M.; Hausmann, B. J.; Khan, M.; Zhang, Y.; Maze, J. R.; Hemmer, P. R.; Loncar, M., A diamond nanowire single-photon source. *Nat. Nanotechnol.* **2010,** *5* (3), 195-9.
57. Neu, E.; Steinmetz, D.; Riedrich-Möller, J.; Gsell, S.; Fischer, M.; Schreck, M.; Becher, C., Single photon emission from silicon-vacancy colour centres in chemical vapour deposition nano-diamonds on iridium. *New J. Phys.* **2011,** *13* (2), 025012.
58. Evans, R. E.; Sipahigil, A.; Sukachev, D. D.; Zibrov, A. S.; Lukin, M. D., Narrow-Linewidth Homogeneous Optical Emitters in Diamond Nanostructures via Silicon Ion Implantation. *Phys. Rev. Appl.* **2016,** *5* (4), 044010.

59. Rogers, L. J.; Jahnke, K. D.; Teraji, T.; Marseglia, L.; Muller, C.; Naydenov, B.; Schauffert, H.; Kranz, C.; Isoya, J.; McGuinness, L. P.; Jelezko, F., Multiple intrinsically identical single-photon emitters in the solid state. *Nat. Commun.* **2014,** *5*, 4739.

60. Pingault, B.; Jarausch, D.-D.; Hepp, C.; Klintberg, L.; Becker, J. N.; Markham, M.; Becher, C.; Atatüre, M., Coherent control of the silicon-vacancy spin in diamond. *Nat. Commun.* **2017,** *8*, 15579.

61. Zhou, Y.; Rasmita, A.; Li, K.; Xiong, Q.; Aharonovich, I.; Gao, W.-b., Coherent control of a strongly driven silicon vacancy optical transition in diamond. *Nat. Commun.* **2017,** *8*, 14451.

62. Schroder, T.; Trusheim, M. E.; Walsh, M.; Li, L.; Zheng, J.; Schukraft, M.; Sipahigil, A.; Evans, R. E.; Sukachev, D. D.; Nguyen, C. T.; Pacheco, J. L.; Camacho, R. M.; Bielejec, E. S.; Lukin, M. D.; Englund, D., Scalable focused ion beam creation of nearly lifetime-limited single quantum emitters in diamond nanostructures. *Nat. Commun.* **2017,** *8*, 15376.

63. Castelletto, S.; Johnson, B. C.; Ivády, V.; Stavrias, N.; Umeda, T.; Gali, A.; Ohshima, T., A silicon carbide room-temperature single-photon source. *Nat. Mater.* **2014,** *13* (2), 151-156.

64. Castelletto, S.; Johnson, B. C.; Zachreson, C.; Beke, D.; Balogh, I.; Ohshima, T.; Aharonovich, I.; Gali, A., Room Temperature Quantum Emission from Cubic Silicon Carbide Nanoparticles. *ACS Nano* **2014,** *8* (8), 7938-7947.

65. Lienhard, B.; Schröder, T.; Mouradian, S.; Dolde, F.; Tran, T. T.; Aharonovich, I.; Englund, D., Bright and photostable single-photon emitter in silicon carbide. *Optica* **2016,** *3* (7), 768-774.

66. Widmann, M.; Lee, S. Y.; Rendler, T.; Son, N. T.; Fedder, H.; Paik, S.; Yang, L. P.; Zhao, N.; Yang, S.; Booker, I.; Denisenko, A.; Jamali, M.; Momenzadeh, S. A.; Gerhardt, I.; Ohshima, T.; Gali, A.; Janzen, E.; Wrachtrup, J., Coherent control of single spins in silicon carbide at room temperature. *Nat. Mater.* **2015,** *14* (2), 164-8.

67. Morfa, A. J.; Gibson, B. C.; Karg, M.; Karle, T. J.; Greentree, A. D.; Mulvaney, P.; Tomljenovic-Hanic, S., Single-Photon Emission and Quantum Characterization of Zinc Oxide Defects. *Nano Lett.* **2012,** *12* (2), 949-954.

68. Choi, S.; Johnson, B. C.; Castelletto, S.; Ton-That, C.; Phillips, M. R.; Aharonovich, I., Single photon emission from ZnO nanoparticles. *Appl. Phys. Lett.* **2014,** *104* (26), 261101.

69. Jungwirth, N. R.; Pai, Y. Y.; Chang, H. S.; MacQuarrie, E. R.; Nguyen, K. X.; Fuchs, G. D., A single-molecule approach to ZnO defect studies: Single photons and single defects. *J. Appl. Phys.* **2014,** *116* (4), 043509.

70. Kolesov, R.; Xia, K.; Reuter, R.; Stohr, R.; Zappe, A.; Meijer, J.; Hemmer, P. R.; Wrachtrup, J., Optical detection of a single rare-earth ion in a crystal. *Nat. Commun.* **2012,** *3*, 1029.

71. Utikal, T.; Eichhammer, E.; Petersen, L.; Renn, A.; Götzinger, S.; Sandoghdar, V., Spectroscopic detection and state preparation of a single praseodymium ion in a crystal. **2014,** *5*, 3627.

72. Emanuel, E.; Tobias, U.; Stephan, G.; Vahid, S., Spectroscopic detection of single Pr 3+ ions on the 3 H 4 − 1 D 2 transition. *New J. Phys.* **2015,** *17* (8), 083018.

73. Siyushev, P.; Xia, K.; Reuter, R.; Jamali, M.; Zhao, N.; Yang, N.; Duan, C.; Kukharchyk, N.; Wieck, A. D.; Kolesov, R.; Wrachtrup, J., Coherent properties of single rare-earth spin qubits. *Nat. Commun.* **2014,** *5*, 3895.

74. Kolesov, R.; Xia, K.; Reuter, R.; Jamali, M.; Stöhr, R.; Inal, T.; Siyushev, P.; Wrachtrup, J., Mapping Spin Coherence of a Single Rare-Earth Ion in a Crystal onto a Single Photon Polarization State. *Phys. Rev. Lett.* **2013,** *111* (12), 120502.

75. Zhong, T.; Kindem, J. M.; Miyazono, E.; Faraon, A., Nanophotonic coherent light–matter interfaces based on rare-earth-doped crystals. **2015,** *6*, 8206.

76. Longdell, J. J.; Fraval, E.; Sellars, M. J.; Manson, N. B., Stopped Light with Storage Times Greater than One Second Using Electromagnetically Induced Transparency in a Solid. *Phys. Rev. Lett.* **2005,** *95* (6), 063601.

77. Ma, X.; Hartmann, N. F.; Baldwin, J. K.; Doorn, S. K.; Htoon, H., Room-temperature single-photon generation from solitary dopants of carbon nanotubes. *Nat. Nanotechnol.* **2015,** *10*, 671–675.

78. He, Y.-M.; ClarkGenevieve; SchaibleyJohn, R.; He, Y.; ChenMing, C.; WeiYu, J.; DingXing; Zhang, Q.; Yao, W.; Xu, X.; Lu, C.-Y.; Pan, J.-W., Single quantum emitters in monolayer semiconductors. *Nat. Nanotechnol.* **2015,** *10* (6), 497-502.

79. Koperski, M.; Nogajewski, K.; Arora, A.; Cherkez, V.; Mallet, P.; Veuillen, J. Y.; Marcus, J.; Kossacki, P.; Potemski, M., Single photon emitters in exfoliated WSe2 structures. *Nat. Nanotechnol.* **2015,** *10* (6), 503-6.

80. Srivastava, A.; Sidler, M.; Allain, A. V.; Lembke, D. S.; Kis, A.; ImamoğluA, Optically active quantum dots in monolayer WSe2. *Nat. Nanotechnol.* **2015,** *10* (6), 491-496.

81. Chakraborty, C.; Kinnischtzke, L.; Goodfellow, K. M.; Beams, R.; Vamivakas, A. N., Voltage-controlled quantum light from an atomically thin semiconductor. *Nat. Nanotechnol.* **2015,** *10* (6), 507-511.

82. Tonndorf, P.; Schmidt, R.; Schneider, R.; Kern, J.; Buscema, M.; Steele, G. A.; Castellanos-Gomez, A.; van der Zant, H. S. J.; Michaelis de Vasconcellos, S.; Bratschitsch, R., Single-photon emission from localized excitons in an atomically thin semiconductor. *Optica* **2015,** *2* (4), 347.

83. Palacios-Berraquero, C.; Barbone, M.; Kara, D. M.; Chen, X.; Goykhman, I.; Yoon, D.; Ott, A. K.; Beitner, J.; Watanabe, K.; Taniguchi, T.; Ferrari, A. C.; Atatüre, M., Atomically thin quantum light-emitting diodes. *Nature Communications* **2016,** *7*, 12978.

84. Clark, G.; Schaibley, J. R.; Ross, J.; Taniguchi, T.; Watanabe, K.; Hendrickson, J. R.; Mou, S.; Yao, W.; Xu, X., Single Defect Light-Emitting Diode in a van der Waals Heterostructure. *Nano Lett.* **2016,** *16* (6), 3944-3948.

85. Schwarz, S.; Kozikov, A.; Withers, F.; Maguire, J. K.; Foster, A. P.; Dufferwiel, S.; Hague, L.; Makhonin, M. N.; Wilson, L. R.; Geim, A. K.; Novoselov,

K. S.; Tartakovskii, A. I., Electrically pumped single-defect light emitters in WSe 2. *2D Materials* **2016,** *3* (2), 025038.

86. Chakraborty, C.; Goodfellow, K. M.; Dhara, S.; Yoshimura, A.; Meunier, V.; Vamivakas, A. N., Quantum-Confined Stark Effect of Individual Defects in a van der Waals Heterostructure. *Nano Lett.* **2017,** *17* (4), 2253-2258.

87. Gabriella, D. S.; Obafunso, A. A.; Xiangzhi, L.; Zhu, X. Y.; James, H.; Stefan, S., Nanobubble induced formation of quantum emitters in monolayer semiconductors. *2D Materials* **2017,** *4* (2), 021019.

88. Palacios-Berraquero, C.; Kara, D. M.; Montblanch, A. R.; Barbone, M.; Latawiec, P.; Yoon, D.; Ott, A. K.; Loncar, M.; Ferrari, A. C.; Atature, M., Large-scale quantum-emitter arrays in atomically thin semiconductors. *Nat. Commun.* **2017,** *8*, 15093.

89. Butler, S. Z.; Hollen, S. M.; Cao, L.; Cui, Y.; Gupta, J. A.; Gutiérrez, H. R.; Heinz, T. F.; Hong, S. S.; Huang, J.; Ismach, A. F.; Johnston-Halperin, E.; Kuno, M.; Plashnitsa, V. V.; Robinson, R. D.; Ruoff, R. S.; Salahuddin, S.; Shan, J.; Shi, L.; Spencer, M. G.; Terrones, M.; Windl, W.; Goldberger, J. E., Progress, Challenges, and Opportunities in Two-Dimensional Materials Beyond Graphene. *ACS Nano* **2013,** *7* (4), 2898-2926.

90. Novoselov, K. S.; Geim, A. K.; Morozov, S. V.; Jiang, D.; Zhang, Y.; Dubonos, S. V.; Grigorieva, I. V.; Firsov, A. A., Electric Field Effect in Atomically Thin Carbon Films. *Science* **2004,** *306* (5696), 666-669.

91. Novoselov, K. S.; Jiang, D.; Schedin, F.; Booth, T. J.; Khotkevich, V. V.; Morozov, S. V.; Geim, A. K., Two-dimensional atomic crystals. *Proc. Natl. Acad. Sci.* **2005,** *102* (30), 10451-10453.

92. Xia, F.; Wang, H.; Xiao, D.; Dubey, M.; Ramasubramaniam, A., Two-dimensional material nanophotonics. *Nat. Photon.* **2014,** *8* (12), 899-907.

93. Mak, K. F.; Lee, C.; Hone, J.; Shan, J.; Heinz, T. F., Atomically ThinMoS2: A New Direct-Gap Semiconductor. *Phys. Rev. Lett.* **2010,** *105* (13).

94. Splendiani, A.; Sun, L.; Zhang, Y.; Li, T.; Kim, J.; Chim, C. Y.; Galli, G.; Wang, F., Emerging photoluminescence in monolayer MoS2. *Nano Lett.* **2010,** *10* (4), 1271-5.

95. Mak, K. F.; He, K.; Shan, J.; Heinz, T. F., Control of valley polarization in monolayer MoS2 by optical helicity. *Nat. Nanotechnol.* **2012,** *7* (8), 494-498.

96. Zeng, H.; Dai, J.; Yao, W.; Xiao, D.; Cui, X., Valley polarization in MoS2 monolayers by optical pumping. *Nat. Nanotechnol.* **2012,** *7* (8), 490-493.

97. Wang, Q. H.; Kalantar-Zadeh, K.; Kis, A.; Coleman, J. N.; Strano, M. S., Electronics and optoelectronics of two-dimensional transition metal dichalcogenides. *Nat. Nanotechnol.* **2012,** *7* (11), 699-712.

98. Desai, S. B.; Seol, G.; Kang, J. S.; Fang, H.; Battaglia, C.; Kapadia, R.; Ager, J. W.; Guo, J.; Javey, A., Strain-Induced Indirect to Direct Bandgap Transition in Multilayer WSe2. *Nano Lett.* **2014,** *14* (8), 4592-4597.

99. Schaibley, J. R.; Yu, H.; Clark, G.; Rivera, P.; Ross, J. S.; Seyler, K. L.; Yao, W.; Xu, X., Valleytronics in 2D materials. *Nature Reviews Materials* **2016,** *1* (11), 16055.

100. Amani, M.; Lien, D.-H.; Kiriya, D.; Xiao, J.; Azcatl, A.; Noh, J.; Madhvapathy, S. R.; Addou, R.; KC, S.; Dubey, M.; Cho, K.; Wallace, R. M.; Lee, S.-C.; He, J.-H.; Ager, J. W.; Zhang, X.; Yablonovitch, E.; Javey, A., Near-unity photoluminescence quantum yield in MoS2. *Science* **2015,** *350* (6264), 1065-1068.

101. Wu, W.; Wang, L.; Li, Y.; Zhang, F.; Lin, L.; Niu, S.; Chenet, D.; Zhang, X.; Hao, Y.; Heinz, T. F.; Hone, J.; Wang, Z. L., Piezoelectricity of single-atomic-layer MoS2 for energy conversion and piezotronics. *Nature* **2014,** *514* (7523), 470-474.

102. Wu, S.; Buckley, S.; Schaibley, J. R.; Feng, L.; Yan, J.; Mandrus, D. G.; Hatami, F.; Yao, W.; Vuckovic, J.; Majumdar, A.; Xu, X., Monolayer semiconductor nanocavity lasers with ultralow thresholds. *Nature* **2015,** *520* (7545), 69-72.

103. Ye, Y.; Wong, Z. J.; Lu, X.; Ni, X.; Zhu, H.; Chen, X.; Wang, Y.; Zhang, X., Monolayer excitonic laser. *Nat. Photon.* **2015**.

104. Liu, X.; Galfsky, T.; Sun, Z.; Xia, F.; Lin, E.-c.; Lee, Y.-H.; Kéna-Cohen, S.; Menon, V. M., Strong light–matter coupling in two-dimensional atomic crystals. *Nat. Photon.* **2014,** *9* (1), 30-34.

105. Zhang, S.; Yang, J.; Xu, R.; Wang, F.; Li, W.; Ghufran, M.; Zhang, Y.-W.; Yu, Z.; Zhang, G.; Qin, Q.; Lu, Y., Extraordinary Photoluminescence and Strong Temperature/Angle-Dependent Raman Responses in Few-Layer Phosphorene. *ACS Nano* **2014,** *8* (9), 9590-9596.

106. Yang, J.; Xu, R.; Pei, J.; Myint, Y. W.; Wang, F.; Wang, Z.; Zhang, S.; Yu, Z.; Lu, Y., Optical tuning of exciton and trion emissions in monolayer phosphorene. *Light: Science & Applications* **2015,** *4* (7), e312.

107. Geim, A. K.; Grigorieva, I. V., Van der Waals heterostructures. *Nature* **2013,** *499* (7459), 419-25.

108. Watanabe, K.; Taniguchi, T., Hexagonal Boron Nitride as a New Ultraviolet Luminescent Material and Its Application. *Int. J. Appl. Ceram. Technol.* **2011,** *8* (5), 977-989.

109. Lin, Y.; Connell, J. W., Advances in 2D boron nitride nanostructures: nanosheets, nanoribbons, nanomeshes, and hybrids with graphene. *Nanoscale* **2012,** *4* (22), 6908-39.

110. Li, L. H.; Chen, Y.; Behan, G.; Zhang, H.; Petravic, M.; Glushenkov, A. M., Large-scale mechanical peeling of boron nitride nanosheets by low-energy ball milling. *J. Mater. Chem.* **2011,** *21* (32), 11862.

111. Nicolosi, V.; Chhowalla, M.; Kanatzidis, M. G.; Strano, M. S.; Coleman, J. N., Liquid Exfoliation of Layered Materials. *Science* **2013,** *340* (6139), 1420-+.

112. Zhi, C.; Bando, Y.; Tang, C.; Kuwahara, H.; Golberg, D., Large-Scale Fabrication of Boron Nitride Nanosheets and Their Utilization in Polymeric Composites with Improved Thermal and Mechanical Properties. *Adv. Mater.* **2009,** *21* (28), 2889-2893.

113. Lin, Y.; Williams, T. V.; Connell, J. W., Soluble, Exfoliated Hexagonal Boron Nitride Nanosheets. *The Journal of Physical Chemistry Letters* **2010,** *1* (1), 277-283.

114. Dean, C. R.; Young, A. F.; Meric, I.; Lee, C.; Wang, L.; Sorgenfrei, S.; Watanabe, K.; Taniguchi, T.; Kim, P.; Shepard, K. L.; Hone, J., Boron nitride substrates for high-quality graphene electronics. *Nat. Nanotechnol.* **2010,** *5* (10), 722-6.

115. Britnell, L.; Gorbachev, R. V.; Jalil, R.; Belle, B. D.; Schedin, F.; Katsnelson, M. I.; Eaves, L.; Morozov, S. V.; Mayorov, A. S.; Peres, N. M.; Neto, A. H.; Leist, J.; Geim, A. K.; Ponomarenko, L. A.; Novoselov, K. S., Electron tunneling through ultrathin boron nitride crystalline barriers. *Nano Lett.* **2012,** *12* (3), 1707-10.

116. Sevik, C.; Kinaci, A.; Haskins, J. B.; Çağın, T., Characterization of thermal transport in low-dimensional boron nitride nanostructures. *Phys. Rev. B* **2011,** *84* (8), 085409.

117. Şahin, H.; Cahangirov, S.; Topsakal, M.; Bekaroglu, E.; Akturk, E.; Senger, R. T.; Ciraci, S., Monolayer honeycomb structures of group-IV elements and III-V binary compounds: First-principles calculations. *Phys. Rev. B* **2009,** *80* (15), 155453.

118. Watanabe, K.; Taniguchi, T.; Kanda, H., Direct-Bandgap Properties and Evidence for Ultraviolet Lasing of Hexagonal Boron Nitride Single Crystal. *Nat. Mater.* **2004,** *3* (6), 404-409.

119. Watanabe, K.; Taniguchi, T.; Niiyama, T.; Miya, K.; Taniguchi, M., Far-ultraviolet plane-emission handheld device based on hexagonal boron nitride. *Nat. Photon.* **2009,** *3* (10), 591-594.

120. Cassabois, G.; Valvin, P.; Gil, B., Hexagonal Boron Nitride is an Indirect Bandgap Semiconductor. *Nat. Photon.* **2016,** *10*, 262-266.

121. Silly, M. G.; Jaffrennou, P.; Barjon, J.; Lauret, J. S.; Ducastelle, F.; Loiseau, A.; Obraztsova, E.; Attal-Tretout, B.; Rosencher, E., Luminescence properties of hexagonal boron nitride: Cathodoluminescence and photoluminescence spectroscopy measurements. *Phys. Rev. B* **2007,** *75* (8), 085205.

122. Museur, L.; Feldbach, E.; Kanaev, A., Defect-related photoluminescence of hexagonal boron nitride. *Phys. Rev. B* **2008,** *78* (15), 155204.
123. Bourrellier, R.; Amato, M.; Galvão Tizei, L. H.; Giorgetti, C.; Gloter, A.; Heggie, M. I.; March, K.; Stéphan, O.; Reining, L.; Kociak, M.; Zobelli, A., Nanometric Resolved Luminescence in h-BN Flakes: Excitons and Stacking Order. *ACS Photonics* **2014,** *1* (9), 857-862.
124. Vuong, T. Q. P.; Cassabois, G.; Valvin, P.; Jacques, V.; Lee, A. V. D.; Zobelli, A.; Watanabe, K.; Taniguchi, T.; Gil, B., Phonon symmetries in hexagonal boron nitride probed by incoherent light emission. *2D Materials* **2016,** *4* (1), 011004.
125. Vuong, T. Q. P.; Cassabois, G.; Valvin, P.; Ouerghi, A.; Chassagneux, Y.; Voisin, C.; Gil, B., Phonon-Photon Mapping in a Color Center in Hexagonal Boron Nitride. *Phys. Rev. Lett.* **2016,** *117* (9), 097402.
126. Dai, S.; Fei, Z.; Ma, Q.; Rodin, A. S.; Wagner, M.; McLeod, A. S.; Liu, M. K.; Gannett, W.; Regan, W.; Watanabe, K.; Taniguchi, T.; Thiemens, M.; Dominguez, G.; Neto, A. H. C.; Zettl, A.; Keilmann, F.; Jarillo-Herrero, P.; Fogler, M. M.; Basov, D. N., Tunable Phonon Polaritons in Atomically Thin van der Waals Crystals of Boron Nitride. *Science* **2014,** *343* (6175), 1125-1129.
127. Caldwell, J. D.; Lindsay, L.; Giannini, V.; Vurgaftman, I.; Reinecke, T. L.; Maier, S. A.; Glembocki, O. J., Low-loss, infrared and terahertz nanophotonics using surface phonon polaritons. *Nanophotonics* **2015,** *4* (1), 44-68.
128. Caldwell, J. D.; Kretinin, A. V.; Chen, Y.; Giannini, V.; Fogler, M. M.; Francescato, Y.; Ellis, C. T.; Tischler, J. G.; Woods, C. R.; Giles, A. J.; Hong, M.; Watanabe, K.; Taniguchi, T.; Maier, S. A.; Novoselov, K. S., Sub-Diffractional Volume-Confined Polaritons in the Natural Hyperbolic Material Hexagonal Boron Nitride. *Nat. Commun.* **2014,** *5*, 5221.
129. Dai, S.; Ma, Q.; Andersen, T.; McLeod, A. S.; Fei, Z.; Liu, M. K.; Wagner, M.; Watanabe, K.; Taniguchi, T.; Thiemens, M.; Keilmann, F.; Jarillo-Herrero, P.; Fogler, M. M.; Basov, D. N., Subdiffractional Focusing and Guiding of Polaritonic Rays in a Natural Hyperbolic Material. *Nat. Commun.* **2015,** *6*, 6963.

130. Li, P.; Lewin, M.; Kretinin, A. V.; Caldwell, J. D.; Novoselov, K. S.; Taniguchi, T.; Watanabe, K.; Gaussmann, F.; Taubner, T., Hyperbolic Phonon-Polaritons in Boron Nitride for Near-Field Optical Imaging and Focusing. *Nat. Commun.* **2015,** *6*, 7507.

131. Caldwell, J. D.; Vurgaftman, I.; Tischler, J. G.; Glembocki, O. J.; Owrutsky, J. C.; Reinecke, T. L., Atomic-scale photonic hybrids for mid-infrared and terahertz nanophotonics. *Nat. Nanotechnol.* **2016,** *11* (1), 9-15.

132. Seifert, G.; Fowler, P. W.; Mitchell, D.; Porezag, D.; Frauenheim, T., Boron-nitrogen analogues of the fullerenes: electronic and structural properties. *Chem. Phys. Lett.* **1997,** *268* (5–6), 352-358.

133. Pokropivny, V. V.; Skorokhod, V. V.; Oleinik, G. S.; Kurdyumov, A. V.; Bartnitskaya, T. S.; Pokropivny, A. V.; Sisonyuk, A. G.; Sheichenko, D. M., Boron Nitride Analogs of Fullerenes (the Fulborenes), Nanotubes, and Fullerites (the Fulborenites). *J. Solid State Chem.* **2000,** *154* (1), 214-222.

134. Golberg, D.; Bando, Y.; Tang, C. C.; Zhi, C. Y., Boron Nitride Nanotubes. *Adv. Mater.* **2007,** *19* (18), 2413-2432.

135. Rao, C. N. R.; Govindaraj, A., Synthesis of Inorganic Nanotubes. *Adv. Mater.* **2009,** *21* (42), 4208-4233.

136. Wang, J.; Lee, C. H.; Yap, Y. K., Recent advancements in boron nitride nanotubes. *Nanoscale* **2010,** *2* (10), 2028-2034.

137. Meyer, J. C.; Chuvilin, A.; Algara-Siller, G.; Biskupek, J.; Kaiser, U., Selective Sputtering and Atomic Resolution Imaging of Atomically Thin Boron Nitride Membranes. *Nano Lett.* **2009,** *9* (7), 2683-2689.

138. Kotakoski, J.; Jin, C. H.; Lehtinen, O.; Suenaga, K.; Krasheninnikov, A. V., Electron knock-on damage in hexagonal boron nitride monolayers. *Phys. Rev. B* **2010,** *82* (11).

139. Ryu, G. H.; Park, H. J.; Ryou, J.; Park, J.; Lee, J.; Kim, G.; Shin, H. S.; Bielawski, C. W.; Ruoff, R. S.; Hong, S.; Lee, Z., Atomic-scale dynamics of

triangular hole growth in monolayer hexagonal boron nitride under electron irradiation. *Nanoscale* **2015,** *7* (24), 10600-5.

140. Zobelli, A.; Gloter, A.; Ewels, C. P.; Seifert, G.; Colliex, C., Electron knock-on cross section of carbon and boron nitride nanotubes. *Phys. Rev. B* **2007,** *75* (24), 245402.

141. Muralidharan, K.; Erdmann, R. G.; Runge, K.; Deymier, P. A., Asymmetric energy transport in defected boron nitride nanoribbons: Implications for thermal rectification. *AIP Advances* **2011,** *1* (4), 041703.

142. Yang, K.; Chen, Y.; Xie, Y.; Wei, X. L.; Ouyang, T.; Zhong, J., Effect of triangle vacancy on thermal transport in boron nitride nanoribbons. *Solid State Commun.* **2011,** *151* (6), 460-464.

143. Mortazavi, B.; Pereira, L. F. C.; Jiang, J.-W.; Rabczuk, T., Modelling heat conduction in polycrystalline hexagonal boron-nitride films. **2015,** *5*, 13228.

144. Tang, S.; Cao, Z., Theoretical study of stabilities and electronic properties of the vacancy and carbon-doping defects in zigzag boron nitride nanoribbons. *Computational Materials Science* **2010,** *48* (3), 648-654.

145. Chen, W.; Li, Y.; Yu, G.; Zhou, Z.; Chen, Z., Electronic Structure and Reactivity of Boron Nitride Nanoribbons with Stone-Wales Defects. *J. Chem. Theory Comput.* **2009,** *5* (11), 3088-3095.

146. Zhang, A.; Teoh, H. F.; Dai, Z.; Feng, Y. P.; Zhang, C., Band gap engineering in graphene and hexagonal BN antidot lattices: A first principles study. *Appl. Phys. Lett.* **2011,** *98* (2), 023105.

147. Anota, E. C.; Gutierrez, R. E.; Morales, A. E.; Cocoletzi, G. H., Influence of point defects on the electronic properties of boron nitride nanosheets. *J Mol Model* **2012,** *18* (5), 2175-84.

148. Yang, J.; Kim, D.; Hong, J.; Qian, X., Magnetism in boron nitride monolayer: Adatom and vacancy defect. *Surf. Sci.* **2010,** *604* (19-20), 1603-1607.

149. Attaccalite, C.; Bockstedte, M.; Marini, A.; Rubio, A.; Wirtz, L., Coupling of excitons and defect states in boron-nitride nanostructures. *Phys. Rev. B* **2011,** *83* (14).

150. Taniguchi, T.; Watanabe, K., Synthesis of high-purity boron nitride single crystals under high pressure by using Ba–BN solvent. *J. Cryst. Growth* **2007,** *303* (2), 525-529.

151. Coleman, J. N.; Lotya, M.; O'Neill, A.; Bergin, S. D.; King, P. J.; Khan, U.; Young, K.; Gaucher, A.; De, S.; Smith, R. J.; Shvets, I. V.; Arora, S. K.; Stanton, G.; Kim, H.-Y.; Lee, K.; Kim, G. T.; Duesberg, G. S.; Hallam, T.; Boland, J. J.; Wang, J. J.; Donegan, J. F.; Grunlan, J. C.; Moriarty, G.; Shmeliov, A.; Nicholls, R. J.; Perkins, J. M.; Grieveson, E. M.; Theuwissen, K.; McComb, D. W.; Nellist, P. D.; Nicolosi, V., Two-Dimensional Nanosheets Produced by Liquid Exfoliation of Layered Materials. *Science* **2011,** *331* (6017), 568-571.

152. Smith, R. J.; King, P. J.; Lotya, M.; Wirtz, C.; Khan, U.; De, S.; O'Neill, A.; Duesberg, G. S.; Grunlan, J. C.; Moriarty, G.; Chen, J.; Wang, J.; Minett, A. I.; Nicolosi, V.; Coleman, J. N., Large-scale exfoliation of inorganic layered compounds in aqueous surfactant solutions. *Adv. Mater.* **2011,** *23* (34), 3944-8.

153. Zhou, K.-G.; Mao, N.-N.; Wang, H.-X.; Peng, Y.; Zhang, H.-L., A Mixed-Solvent Strategy for Efficient Exfoliation of Inorganic Graphene Analogues. *Angewandte Chemie International Edition* **2011,** *50* (46), 10839-10842.

154. Xu, M.; Liang, T.; Shi, M.; Chen, H., Graphene-Like Two-Dimensional Materials. *Chem. Rev.* **2013,** *113* (5), 3766-3798.

155. Rokuta, E.; Hasegawa, Y.; Suzuki, K.; Gamou, Y.; Oshima, C.; Nagashima, A., Phonon Dispersion of an Epitaxial Monolayer Film of Hexagonal Boron Nitride on Ni(111). *Phys. Rev. Lett.* **1997,** *79* (23), 4609-4612.

156. Auwärter, W.; Suter, H. U.; Sachdev, H.; Greber, T., Synthesis of One Monolayer of Hexagonal Boron Nitride on Ni(111) from B-Trichloroborazine (ClBNH)3. *Chem. Mater.* **2004,** *16* (2), 343-345.

157. Müller, F.; Stöwe, K.; Sachdev, H., Symmetry versus Commensurability: Epitaxial Growth of Hexagonal Boron Nitride on Pt(111) From B-Trichloroborazine (ClBNH)3. *Chem. Mater.* **2005,** *17* (13), 3464-3467.

158. Shi, Y.; Hamsen, C.; Jia, X.; Kim, K. K.; Reina, A.; Hofmann, M.; Hsu, A. L.; Zhang, K.; Li, H.; Juang, Z. Y.; Dresselhaus, M. S.; Li, L. J.; Kong, J., Synthesis of few-layer hexagonal boron nitride thin film by chemical vapor deposition. *Nano Lett.* **2010,** *10* (10), 4134-9.

159. Liu, Z.; Ma, L.; Shi, G.; Zhou, W.; Gong, Y.; Lei, S.; Yang, X.; Zhang, J.; Yu, J.; Hackenberg, K. P.; Babakhani, A.; Idrobo, J.-C.; Vajtai, R.; Lou, J.; Ajayan, P. M., In-plane heterostructures of graphene and hexagonal boron nitride with controlled domain sizes. *Nat Nano* **2013,** *8* (2), 119-124.

160. Gorbachev, R. V.; Riaz, I.; Nair, R. R.; Jalil, R.; Britnell, L.; Belle, B. D.; Hill, E. W.; Novoselov, K. S.; Watanabe, K.; Taniguchi, T.; Geim, A. K.; Blake, P., Hunting for monolayer boron nitride: optical and Raman signatures. *Small* **2011,** *7* (4), 465-8.

161. Golla, D.; Chattrakun, K.; Watanabe, K.; Taniguchi, T.; LeRoy, B. J.; Sandhu, A., Optical thickness determination of hexagonal boron nitride flakes. *Appl. Phys. Lett.* **2013,** *102* (16), 161906.

162. Song, L.; Ci, L.; Lu, H.; Sorokin, P. B.; Jin, C.; Ni, J.; Kvashnin, A. G.; Kvashnin, D. G.; Lou, J.; Yakobson, B. I.; Ajayan, P. M., Large Scale Growth and Characterization of Atomic Hexagonal Boron Nitride Layers. *Nano Lett.* **2010,** *10* (8), 3209-3215.

163. Kubota, Y.; Watanabe, K.; Tsuda, O.; Taniguchi, T., Deep Ultraviolet Light-Emitting Hexagonal Boron Nitride Synthesized at Atmospheric Pressure. *Science* **2007,** *317* (5840), 932-934.

164. Ishikawa-Ankerhold, H. C.; Ankerhold, R.; Drummen, G. P. C., Advanced Fluorescence Microscopy Techniques—FRAP, FLIP, FLAP, FRET and FLIM. *Molecules* **2012,** *17* (4), 4047.

165. O'Brien, J. L.; Furusawa, A.; Vučković, J., Photonic quantum technologies. *Nat. Photon.* **2009,** *3* (12), 687-695.

166. Awschalom, D. D.; Bassett, L. C.; Dzurak, A. S.; Hu, E. L.; Petta, J. R., Quantum Spintronics: Engineering and Manipulating Atom-Like Spins in Semiconductors. *Science* **2013,** *339* (6124), 1174-1179.
167. Aharonovich, I.; Neu, E., Diamond Nanophotonics. *Adv. Opt. Mater.* **2014,** *2*, 911-928.
168. Mangum, B. D.; Wang, F.; Dennis, A. M.; Gao, Y.; Ma, X.; Hollingsworth, J. A.; Htoon, H., Competition between auger recombination and hot-carrier trapping in PL intensity fluctuations of type II nanocrystals. *Small* **2014,** *10* (14), 2892-901.
169. Pisanello, F.; Lemenager, G.; Martiradonna, L.; Carbone, L.; Vezzoli, S.; Desfonds, P.; Cozzoli, P. D.; Hermier, J. P.; Giacobino, E.; Cingolani, R.; De Vittorio, M.; Bramati, A., Non-blinking single-photon generation with anisotropic colloidal nanocrystals: towards room-temperature, efficient, colloidal quantum sources. *Adv. Mater.* **2013,** *25* (14), 1974-80.
170. Chakraborty, C.; Kinnischtzke, L.; Goodfellow, K. M.; Beams, R.; Vamivakas, A. N., Voltage-controlled quantum light from an atomically thin semiconductor. *Nat. Nanotechnol.* **2015**.
171. He, Y.-M.; Clark, G.; Schaibley, J. R.; He, Y.; Chen, M.-C.; Wei, Y.-J.; Ding, X.; Zhang, Q.; Yao, W.; Xu, X.; Lu, C.-Y.; Pan, J.-W., Single quantum emitters in monolayer semiconductors. *Nat. Nanotechnol.* **2015**.
172. Koperski, M.; Nogajewski, K.; Arora, A.; Cherkez, V.; Mallet, P.; Veuillen, J. Y.; Marcus, J.; Kossacki, P.; Potemski, M., Single photon emitters in exfoliated WSe2 structures. *Nat. Nanotechnol.* **2015**.
173. Srivastava, A.; Sidler, M.; Allain, A. V.; Lembke, D. S.; Kis, A.; Imamoğlu, A., Optically active quantum dots in monolayer WSe2. *Nat. Nanotechnol.* **2015**.
174. Kresse, G.; Hafner, J., Ab Initio Molecular-Dynamics Simulation of the Liquid-Metal-Amorphous-Semiconductor Transition in Germanium. *Phys. Rev. B* **1994,** *49* (20), 14251.

175. Kresse, G.; Furthmüller, J., Efficiency of ab-initio total energy calculations for metals and semiconductors using a plane-wave basis set. *Computational Materials Science* **1996,** *6* (1), 15-50.
176. Kresse, G.; Furthmüller, J., Efficient iterative schemes for ab initio total-energy calculations using a plane-wave basis set. *Phys. Rev. B* **1996,** *54* (16), 11169-11186.
177. Perdew, J. P.; Burke, K.; Ernzerhof, M., Generalized Gradient Approximation Made Simple. *Phys. Rev. Lett.* **1996,** *77* (18), 3865-3868.
178. Park, J.-H.; Park, J. C.; Yun, S. J.; Kim, H.; Luong, D. H.; Kim, S. M.; Choi, S. H.; Yang, W.; Kong, J.; Kim, K. K.; Lee, Y. H., Large-Area Monolayer Hexagonal Boron Nitride on Pt Foil. *ACS Nano* **2014,** *8* (8), 8520-8528.
179. Xu, M.; Liang, T.; Shi, M.; Chen, H., Graphene-like two-dimensional materials. *Chem. Rev.* **2013,** *113* (5), 3766-98.
180. Khan, M. H.; Huang, Z.; Xiao, F.; Casillas, G.; Chen, Z.; Molino, P. J.; Liu, H. K., Synthesis of Large and Few Atomic Layers of Hexagonal Boron Nitride on Melted Copper. *Sci. Rep.* **2015,** *5*.
181. Vialla, F.; Chassagneux, Y.; Ferreira, R.; Roquelet, C.; Diederichs, C.; Cassabois, G.; Roussignol, P.; Lauret, J. S.; Voisin, C., Unifying the Low-Temperature Photoluminescence Spectra of Carbon Nanotubes: The Role of Acoustic Phonon Confinement. *Phys. Rev. Lett.* **2014,** *113* (5).
182. Aharonovich, I.; Castelletto, S.; Simpson, D. A.; Stacey, A.; McCallum, J.; Greentree, A. D.; Prawer, S., Two-Level Ultrabright Single Photon Emission from Diamond Nanocrystals. *Nano Lett.* **2009,** *9* (9), 3191-3195.
183. Schietinger, S.; Barth, M.; Aichele, T.; Benson, O., Plasmon-Enhanced Single Photon Emission from a Nanoassembled Metal−Diamond Hybrid Structure at Room Temperature. *Nano Lett.* **2009,** *9* (4), 1694-1698.
184. Orellana, W.; Chacham, H., Stability of native defects in hexagonal and cubic boron nitride. *Phys. Rev. B* **2001,** *63* (12).

185. Jin, C.; Lin, F.; Suenaga, K.; Iijima, S., Fabrication of a Freestanding Boron Nitride Single Layer and Its Defect Assignments. *Phys. Rev. Lett.* **2009,** *102* (19).
186. Neu, E.; Agio, M.; Becher, C., Photophysics of Single Silicon Vacancy Centers in Diamond: Implications for Single Photon Emission. *Opt. Express* **2012,** *20* (18), 19956-19971.
187. Rostami, H.; Asgari, R., Valley Zeeman Effect and Spin-valley Polarized Conductance in Monolayer MoS2 in a Perpendicular Magnetic Field. *Phys. Rev. B* **2015,** *91* (7), 075433.
188. del Corro, E.; Botello_Mendez, A. R.; Gillet, Y.; Elías, A. L.; Terrones, H.; Feng, S.; Fantini, C.; Rhodes, D.; Pradhan, N. R.; Balicas, L., Atypical Exciton-Phonon Interactions in WS2 And WSe2 Monolayers Revealed by Resonance Raman Spectroscopy. *Nano Lett.* **2016,** *16* (4), 2363-2368.
189. Gajdoš, M.; Hummer, K.; Kresse, G.; Furthmüller, J.; Bechstedt, F., Linear Optical Properties in the Projector-augmented Wave Methodology. *Phys. Rev. B* **2006,** *73* (4), 045112.
190. Androulidakis, C.; Tsoukleri, G.; Koutroumanis, N.; Gkikas, G.; Pappas, P.; Parthenios, J.; Papagelis, K.; Galiotis, C., Experimentally Derived Axial Stress–strain Relations for Two-dimensional Materials Such as Monolayer Graphene. *Carbon* **2015,** *81*, 322-328.
191. Desai, S. B.; Seol, G.; Kang, J. S.; Fang, H.; Battaglia, C.; Kapadia, R.; Ager, J. W.; Guo, J.; Javey, A., Strain-Induced Indirect to Direct Bandgap Transition in Multilayer WSe2. *Nano Lett.* **2014,** *14* (8), 4592-4597.
192. Botsoa, J.; Sauvage, T.; Adam, M. P.; Desgardin, P.; Leoni, E.; Courtois, B.; Treussart, F.; Barthe, M. F., Optimal Conditions for NV−center Formation in Type-Ib Diamond Studied Using Photoluminescence and Positron Annihilation Spectroscopies. *Phys. Rev. B* **2011,** *84* (12), 125209.
193. Orwa, J. O.; Santori, C.; Fu, K. M. C.; Gibson, B.; Simpson, D.; Aharonovich, I.; Stacey, A.; Cimmino, A.; Balog, P.; Markham, M.; Twitchen, D.; Greentree, A. D.; Beausoleil, R. G.; Prawer, S., Engineering of Nitrogen-Vacancy Color Centers in

High Purity Diamond by Ion Implantation and Annealing. *J. Appl. Phys.* **2011,** *109* (8), 083530.

194. Thiel, B. L.; Toth, M.; Schroemges, R. P. M.; Scholtz, J. J.; van Veen, G.; Knowles, W. R., Two-stage Gas Amplifier for Ultrahigh Resolution Low Vacuum Scanning Electron Microscopy. *Rev. Sci. Instrum.* **2006,** *77* (3), 033705.

195. Toth, M.; Lobo, C. J.; Lysaght, M. J.; Vladár, A. E.; Postek, M. T., Contamination-Free Imaging by Electron Induced Carbon Volatilization in Environmental Scanning Electron Microscopy. *J. Appl. Phys.* **2009,** *106* (3), 034306.

196. Cui, Z.; Oyer, A. J.; Glover, A. J.; Schniepp, H. C.; Adamson, D. H., Large Scale Thermal Exfoliation and Functionalization of Boron Nitride. *Small* **2014,** *10* (12), 2352-2355.

197. Fu, K. M. C.; Santori, C.; Barclay, P. E.; Beausoleil, R. G., Conversion of Neutral Nitrogen-vacancy Centers to Negatively Charged Nitrogen-vacancy Centers Through Selective Oxidation. *Appl. Phys. Lett.* **2010,** *96* (12), 121907.

198. Shanley, T. W.; Martin, A. A.; Aharonovich, I.; Toth, M., Localized Chemical Switching of the Charge State of Nitrogen-vacancy Luminescence Centers in Diamond. *Appl. Phys. Lett.* **2014,** *105* (6), 063103.

199. Sébastien, P.; Detlef, R.; Dominik, W.; Jan, M.; Alexander, Z., Creation and Nature of Optical Centres in Diamond for Single-photon Emission—Overview and Critical Remarks. *New J. Phys.* **2011,** *13* (3), 035024.

200. Shuji, N.; Naruhito, I.; Masayuki, S.; Takashi, M., Hole Compensation Mechanism of P-Type GaN Films. *Jpn. J. Appl. Phys.* **1992,** *31* (5R), 1258.

201. Gutiérrez, H. R.; Perea-López, N.; Elías, A. L.; Berkdemir, A.; Wang, B.; Lv, R.; López-Urías, F.; Crespi, V. H.; Terrones, H.; Terrones, M., Extraordinary Room-Temperature Photoluminescence in Triangular WS2 Monolayers. *Nano Lett.* **2013,** *13* (8), 3447-3454.

202. Michler, P.; Kiraz, A.; Becher, C.; Schoenfeld, W. V.; Petroff, P. M.; Zhang, L.; Hu, E.; Imamoglu, A., A Quantum Dot Single-photon Turnstile Device. *Science* **2000,** *290* (5500), 2282-2285.

203. Huxter, V. M.; Oliver, T. A. A.; Budker, D.; Fleming, G. R., Vibrational and Electronic Dynamics of Nitrogen–Vacancy Centres in Diamond Revealed by Two-dimensional Ultrafast Spectroscopy. *Nat. Phys.* **2013,** *9* (11), 744-749.
204. Neitzke, O.; Morfa, A.; Wolters, J.; Schell, A. W.; Kewes, G.; Benson, O., Investigation of Line Width Narrowing and Spectral Jumps of Single Stable Defect Centers in ZnO at Cryogenic Temperature. *Nano Lett.* **2015,** *15* (5), 3024-3029.
205. Bernard, J.; Fleury, L.; Talon, H.; Orrit, M., Photon Bunching in the Fluorescence from Single Molecules: A Probe for Intersystem Crossing. *J. Chem. Phys.* **1993,** *98* (2), 850-859.
206. Fleury, L.; Segura, J. M.; Zumofen, G.; Hecht, B.; Wild, U. P., Nonclassical Photon Statistics in Single-Molecule Fluorescence at Room Temperature. *Phys. Rev. Lett.* **2000,** *84* (6), 1148-1151.
207. Aharonovich, I.; Castelletto, S.; Simpson, D. A.; Greentree, A. D.; Prawer, S., Photophysics of Chromium-related Diamond Single-photon Emitters. *Phys. Rev. A* **2010,** *81* (4), 043813.
208. Berthel, M.; Mollet, O.; Dantelle, G.; Gacoin, T.; Huant, S.; Drezet, A., Photophysics of Single Nitrogen-vacancy Centers in Diamond Nanocrystals. *Phys. Rev. B* **2015,** *91* (3), 035308.
209. Neu, E.; Fischer, M.; Gsell, S.; Schreck, M.; Becher, C., Fluorescence and Polarization Spectroscopy of Single Silicon Vacancy Centers in Heteroepitaxial Nanodiamonds on Iridium. *Phys. Rev. B* **2011,** *84* (20), 205211.
210. Castellanos-Gomez, A.; Roldan, R.; Cappelluti, E.; Buscema, M.; Guinea, F.; van der Zant, H. S.; Steele, G. A., Local Strain Engineering in Atomically Thin MoS2. *Nano Lett.* **2013,** *13* (11), 5361-5366.
211. Taniyasu, Y.; Kasu, M.; Makimoto, T., An aluminium nitride light-emitting diode with a wavelength of 210 nanometres. *Nature* **2006,** *441* (7091), 325-8.
212. Liu, C.; Hu, Z.; Wu, Q.; Wang, X.; Chen, Y.; Sang, H.; Zhu, J.; Deng, S.; Xu, N., Vapor−Solid Growth and Characterization of Aluminum Nitride Nanocones. *J. Am. Chem. Soc.* **2005,** *127* (4), 1318-1322.

213. Jaffrennou, P.; Barjon, J.; Lauret, J. S.; Attal-Trétout, B.; Ducastelle, F.; Loiseau, A., Origin of the excitonic recombinations in hexagonal boron nitride by spatially resolved cathodoluminescence spectroscopy. *J. Appl. Phys.* **2007,** *102* (11), 116102.

214. Pierret, A.; Loayza, J.; Berini, B.; Betz, A.; Plaçais, B.; Ducastelle, F.; Barjon, J.; Loiseau, A., Excitonic recombinations inh−BN: From bulk to exfoliated layers. *Phys. Rev. B* **2014,** *89* (3), 035414.

215. Meuret, S.; Tizei, L. H. G.; Cazimajou, T.; Bourrellier, R.; Chang, H. C.; Treussart, F.; Kociak, M., Photon Bunching in Cathodoluminescence. *Phys. Rev. Lett.* **2015,** *114* (19), 197401.

216. *See Supplemental Material at [URL] for additional charaterization data obtained using near-edge x-ray absorption fine structure spectroscopy, raman spectroscopy, cathodoluminescence spectroscopy, photoluminescence polarization and a histogram of fluorescene on and off times from an emitter in bulk hBN.*

217. Reich, S.; Ferrari, A. C.; Arenal, R.; Loiseau, A.; Bello, I.; Robertson, J., Resonant Raman scattering in cubic and hexagonal boron nitride. *Phys. Rev. B* **2005,** *71* (20), 205201.

218. Kurtsiefer, C.; Mayer, S.; Zarda, P.; Weinfurter, H., Stable Solid-state Source of Single Photons. *Phys. Rev. Lett.* **2000,** *85* (2), 290-293.

219. Gatto Monticone, D.; Traina, P.; Moreva, E.; Forneris, J.; Olivero, P.; Degiovanni, I. P.; Taccetti, F.; Giuntini, L.; Brida, G.; Amato, G.; Genovese, M., Native NIR-emitting single colour centres in CVD diamond. *New J. Phys.* **2014,** *16* (5), 053005.

220. Rath, P.; Ummethala, S.; Nebel, C.; Pernice, W. H. P., Diamond as a material for monolithically integrated optical and optomechanical devices. *Phys. Status Solidi A* **2015,** *212* (11), 2385–2399.

221. Akselrod, G. M.; Argyropoulos, C.; Hoang, T. B.; Ciracì, C.; Fang, C.; Huang, J.; Smith, D. R.; Mikkelsen, M. H., Probing the mechanisms of large Purcell enhancement in plasmonic nanoantennas. *Nat. Photon.* **2014,** *8* (11), 835-840.

222. Khasminskaya, S.; Pyatkov, F.; Słowik, K.; Ferrari, S.; Kahl, O.; Kovalyuk, V.; Rath, P.; Vetter, A.; Hennrich, F.; Kappes, M. M.; Gol'tsmanG; KorneevA; Rockstuhl, C.; Krupke, R.; Pernice, W. H. P., Fully integrated quantum photonic circuit with an electrically driven light source. *Nat. Photon.* **2016,** *advance online publication*.

223. Chu, X.-L.; Götzinger, S.; Sandoghdar, V., A single molecule as a high-fidelity photon gun for producing intensity-squeezed light. *Nat. Photon.* **2017,** *11* (1), 58-62.

224. Martínez, L. J.; Pelini, T.; Waselowski, V.; Maze, J. R.; Gil, B.; Cassabois, G.; Jacques, V., Efficient single photon emission from a high-purity hexagonal boron nitride crystal. *Phys. Rev. B* **2016,** *94* (12), 121405.

225. Grosso, G.; Moon, H.; Lienhard, B.; Ali, S.; Efetov, D. K.; Furchi, M. M.; Jarillo-Herrero, P.; Ford, M. J.; Aharonovich, I.; Englund, D., Tunable and high purity room-temperature single photon emission from atomic defects in hexagonal boron nitride. *arXiv preprint arXiv:1611.03515* **2016**.

226. Li, X.; Shepard, G. D.; Cupo, A.; Camporeale, N.; Shayan, K.; Luo, Y.; Meunier, V.; Strauf, S., Nonmagnetic Quantum Emitters in Boron Nitride with Ultranarrow and Sideband-Free Emission Spectra. *ACS Nano* **2017,** *11* (7), 6652-6660.

227. Jungwirth, N. R.; Calderon, B.; Ji, Y.; Spencer, M. G.; Flatté, M. E.; Fuchs, G. D., Temperature Dependence of Wavelength Selectable Zero-Phonon Emission from Single Defects in Hexagonal Boron Nitride. *Nano Lett.* **2016,** *16*, 6052-6057.

228. Chejanovsky, N.; Rezai, M.; Paolucci, F.; Kim, Y.; Rendler, T.; Rouabeh, W.; Fávaro de Oliveira, F.; Herlinger, P.; Denisenko, A.; Yang, S.; Gerhardt, I.; Finkler, A.; Smet, J. H.; Wrachtrup, J., Structural Attributes and Photodynamics of Visible Spectrum Quantum Emitters in Hexagonal Boron Nitride. *Nano Lett.* **2016,** *16* (11), 7037-7045.

229. Exarhos, A. L.; Hopper, D. A.; Grote, R. R.; Alkauskas, A.; Bassett, L. C., Optical Signatures of Quantum Emitters in Suspended Hexagonal Boron Nitride. *ACS Nano* **2017,** *11* (3), 3328.

230. Kianinia, M.; Regan, B.; Tawfik, S. A.; Tran, T. T.; Ford, M. J.; Aharonovich, I.; Toth, M., Robust Solid-State Quantum System Operating at 800 K. *ACS Photonics* **2017,** *4* (4), 768-773.

231. Schell, A. W.; Takashima, H.; Tran, T. T.; Aharonovich, I.; Takeuchi, S., Coupling Quantum Emitters in 2D Materials with Tapered Fibers. *ACS Photonics* **2017,** *4* (4), 761-767.

232. Jungwirth, N. R.; Fuchs, G. D., Optical Absorption and Emission Mechanisms of Single Defects in Hexagonal Boron Nitride. *Phys. Rev. Lett.* **2017,** *119* (5), 057401.

233. Sontheimer, B.; Braun, M.; Nikolay, N.; Sadzak, N.; Aharonovich, I.; Benson, O., Photodynamics of quantum emitters in hexagonal boron nitride revealed by low-temperature spectroscopy. *Phys. Rev. B* **2017,** *96* (12), 121202.

234. Becker, J. N.; Gorlitz, J.; Arend, C.; Markham, M.; Becher, C., Ultrafast all-optical coherent control of single silicon vacancy colour centres in diamond. *Nat. Commun.* **2016,** *7*, 13512.

235. Taminiau, T. H.; Stefani, F. D.; Segerink, F. B.; Van Hulst, N. F., Optical antennas direct single-molecule emission. *Nat. Photon.* **2008,** *2* (4), 234-237.

236. Grandi, S.; Major, K. D.; Polisseni, C.; Boissier, S.; Clark, A. S.; Hinds, E. A., Quantum dynamics of a driven two-level molecule with variable dephasing. *Phys. Rev. A* **2016,** *94* (6).

237. Faez, S.; Türschmann, P.; Haakh, H. R.; Götzinger, S.; Sandoghdar, V., Coherent Interaction of Light and Single Molecules in a Dielectric Nanoguide. *Phys. Rev. Lett.* **2014,** *113* (21), 213601.

238. Englund, D.; Majumdar, A.; Faraon, A.; Toishi, M.; Stoltz, N.; Petroff, P.; Vuckovic, J., Resonant excitation of a quantum dot strongly coupled to a photonic crystal nanocavity. *Phys. Rev. Lett.* **2010,** *104* (7), 073904.

239. Faraon, A.; Fushman, I.; Englund, D.; Stoltz, N.; Petroff, P.; Vuckovic, J., Coherent generation of non-classical light on a chip via photon-induced tunnelling and blockade. *Nat. Phys.* **2008,** *4* (11), 859-863.

240. Bourrellier, R.; Meuret, S.; Tararan, A.; Stéphan, O.; Kociak, M.; Tizei, L. H. G.; Zobelli, A., Bright UV Single Photon Emission at Point Defects in h-BN. *Nano Lett.* **2016,** *16* (7), 4317-4321.

241. Rabeau, J. R.; Stacey, A.; Rabeau, A.; Prawer, S.; Jelezko, F.; Mirza, I.; Wrachtrup, J., Single Nitrogen Vacancy Centers in Chemical Vapor Deposited Diamond Nanocrystals. *Nano Lett.* **2007,** *7* (11), 3433-3437.

242. Sipahigil, A.; Jahnke, K. D.; Rogers, L. J.; Teraji, T.; Isoya, J.; Zibrov, A. S.; Jelezko, F.; Lukin, M. D., Indistinguishable Photons from Separated Silicon-Vacancy Centers in Diamond. *Phys. Rev. Lett.* **2014,** *113* (11), 113602.

243. Robledo, L.; Bernien, H.; van Weperen, I.; Hanson, R., Control and Coherence of the Optical Transition of Single Nitrogen Vacancy Centers in Diamond. *Phys. Rev. Lett.* **2010,** *105* (17).

244. Yin, J.; Li, J.; Hang, Y.; Yu, J.; Tai, G.; Li, X.; Zhang, Z.; Guo, W., Boron Nitride Nanostructures: Fabrication, Functionalization and Applications. *Small* **2016,** *12* (22), 2942-2968.

245. Li, L. H.; Chen, Y., Atomically Thin Boron Nitride: Unique Properties and Applications. *Adv. Funct. Mater.* **2016,** *26* (16), 2594-2608.

246. Acosta, V. M.; Santori, C.; Faraon, A.; Huang, Z.; Fu, K. M. C.; Stacey, A.; Simpson, D. A.; Ganesan, K.; Tomljenovic-Hanic, S.; Greentree, A. D.; Prawer, S.; Beausoleil, R. G., Dynamic Stabilization of the Optical Resonances of Single Nitrogen-Vacancy Centers in Diamond. *Phys. Rev. Lett.* **2012,** *108* (20), 206401.

247. Zhao, H. Q.; Fujiwara, M.; Okano, M.; Takeuchi, S., Observation of 1.2-GHz linewidth of zero-phonon-line in photoluminescence spectra of nitrogen vacancy centers in nanodiamonds using a Fabry-Perot interferometer. *Opt. Express* **2013,** *21* (24), 29679-86.

248. Tamarat, P.; Gaebel, T.; Rabeau, J. R.; Khan, M.; Greentree, A. D.; Wilson, H.; Hollenberg, L. C. L.; Prawer, S.; Hemmer, P.; Jelezko, F.; Wrachtrup, J., Stark Shift Control of Single Optical Centers in Diamond. *Phys. Rev. Lett.* **2006,** *97* (8), 083002.

249. Kumar, S.; Brotóns-Gisbert, M.; Al-Khuzheyri, R.; Branny, A.; Ballesteros-Garcia, G.; Sánchez-Royo, J. F.; Gerardot, B. D., Resonant laser spectroscopy of localized excitons in monolayer WSe2. *Optica* **2016,** *3* (8), 882-886.

250. Naguib, M.; Mashtalir, O.; Carle, J.; Presser, V.; Lu, J.; Hultman, L.; Gogotsi, Y.; Barsoum, M. W., Two-Dimensional Transition Metal Carbides. *ACS Nano* **2012,** *6* (2), 1322-1331.

251. Fiori, G.; Bonaccorso, F.; Iannaccone, G.; Palacios, T.; Neumaier, D.; Seabaugh, A.; Banerjee, S. K.; Colombo, L., Electronics based on two-dimensional materials. *Nature Nanotech.* **2014,** *9* (10), 768-779.

252. Yang, J.; Wang, Z.; Wang, F.; Xu, R.; Tao, J.; Zhang, S.; Qin, Q.; Luther-Davies, B.; Jagadish, C.; Yu, Z.; Lu, Y., Atomically thin optical lenses and gratings. *Light Sci Appl* **2016,** *5*, e16046.

253. Chen, W.-F.; Muckerman, J. T.; Fujita, E., Recent developments in transition metal carbides and nitrides as hydrogen evolution electrocatalysts. *Chemical Communications* **2013,** *49* (79), 8896-8909.

254. Liu, X.; Galfsky, T.; Sun, Z.; Xia, F.; Lin, E.-c.; Lee, Y.-H.; Kéna-Cohen, S.; Menon, V. M., Strong light–matter coupling in two-dimensional atomic crystals. *Nat. Photonics* **2015,** *9* (1), 30-34.

255. Sie, E. J.; McIver, J. W.; Lee, Y.-H.; Fu, L.; Kong, J.; Gedik, N., Valley-selective optical Stark effect in monolayer WS2. *Nature Mater.* **2015,** *14* (3), 290-294.

256. Eda, G.; Yamaguchi, H.; Voiry, D.; Fujita, T.; Chen, M.; Chhowalla, M., Photoluminescence from Chemically Exfoliated MoS2. *Nano Lett.* **2011,** *11* (12), 5111-5116.

257. Roy, T.; Tosun, M.; Kang, J. S.; Sachid, A. B.; Desai, S. B.; Hettick, M.; Hu, C. C.; Javey, A., Field-Effect Transistors Built from All Two-Dimensional Material Components. *ACS Nano* **2014,** *8* (6), 6259-6264.

258. Caldwell, J. D.; Kretinin, A. V.; Chen, Y.; Giannini, V.; Fogler, M. M.; Francescato, Y.; Ellis, C. T.; Tischler, J. G.; Woods, C. R.; Giles, A. J.; Hong, M.; Watanabe, K.; Taniguchi, T.; Maier, S. A.; Novoselov, K. S., Sub-diffractional volume-confined polaritons in the natural hyperbolic material hexagonal boron nitride. *Nat Commun* **2014,** *5*.

259. Cassabois, G.; Valvin, P.; Gil, B., Hexagonal boron nitride is an indirect bandgap semiconductor. *Nat. Photonics* **2016,** *advance online publication*.

260. Wong, D.; Velasco Jr, J.; Ju, L.; Lee, J.; Kahn, S.; Tsai, H.-Z.; Germany, C.; Taniguchi, T.; Watanabe, K.; Zettl, A.; Wang, F.; Crommie, M. F., Characterization and manipulation of individual defects in insulating hexagonal boron nitride using scanning tunnelling microscopy. *Nat Nano* **2015,** *10* (11), 949-953.

261. Tran, T. T.; Bray, K.; Ford, M. J.; Toth, M.; Aharonovich, I., Quantum emission from hexagonal boron nitride monolayers. *Nature Nanotechnology* **2016,** *11*, 37-41.

262. Jungwirth, N. R.; Calderon, B.; Ji, Y.; Spencer, M. G.; Flatte, M. E.; Fuchs, G. D., Temperature Dependence of Wavelength Selectable Zero-Phonon Emission from Single Defects in Hexagonal Boron Nitride. *arXiv:1605.04445* **2016**.

263. Petravic, M.; Peter, R.; Kavre, I.; Li, L. H.; Chen, Y.; Fan, L.-J.; Yang, Y.-W., Decoration of nitrogen vacancies by oxygen atoms in boron nitride nanotubes. *Phys. Chem. Chem. Phys.* **2010,** *12* (47), 15349-15353.

264. Tran, T. T.; ElBadawi, C.; Totonjian, D.; Gross, G.; Moon, H.; Englund, D.; Ford, M. J.; Aharonovich, I.; Toth, M., Robust multicolor single photon emission from point defects in hexagonal boron nitride. *arXiv:1603.09608* **2016**.

265. Pezzagna, S.; Naydenov, B.; Jelezko, F.; Wrachtrup, J.; Meijer, J., Creation efficiency of nitrogen-vacancy centres in diamond. *New J. Phys.* **2010,** *12*, 065017.

266. Bao, W.; Borys, N. J.; Ko, C.; Suh, J.; Fan, W.; Thron, A.; Zhang, Y.; Buyanin, A.; Zhang, J.; Cabrini, S.; Ashby, P. D.; Weber-Bargioni, A.; Tongay, S.; Aloni, S.; Ogletree, D. F.; Wu, J.; Salmeron, M. B.; Schuck, P. J., Visualizing nanoscale excitonic relaxation properties of disordered edges and grain boundaries in monolayer molybdenum disulfide. *Nat Commun* **2015,** *6*.

267. Staudacher, T.; Ziem, F.; Häussler, L.; Stöhr, R.; Steinert, S.; Reinhard, F.; Scharpf, J.; Denisenko, A.; Wrachtrup, J., Enhancing the spin properties of shallow implanted nitrogen vacancy centers in diamond by epitaxial overgrowth. *Appl. Phys. Lett.* **2012,** *101* (21), 212401.

268. Aharonovich, I.; Lee, J. C.; Magyar, A. P.; Buckley, B. B.; Yale, C. G.; Awschalom, D. D.; Hu, E. L., Homoepitaxial Growth of Single Crystal Diamond Membranes for Quantum Information Processing. *Adv. Mater.* **2012,** *24*, OP54-OP59.

269. Santori, C.; Barclay, P. E.; Fu, K.-M. C.; Beausoleil, R. G., Vertical distribution of nitrogen-vacancy centers in diamond formed by ion implantation and annealing. *Phys. Rev. B* **2009,** *79* (12), 125313.

270. Li, X.; Wu, X.; Zeng, X. C.; Yang, J., Band-Gap Engineering via Tailored Line Defects in Boron-Nitride Nanoribbons, Sheets, and Nanotubes. *ACS Nano* **2012,** *6* (5), 4104-4112.

271. Buividas, R.; Aharonovich, I.; Seniutinas, G.; Wang, X. W.; Rapp, L.; Rode, A. V.; Taniguchi, T.; Juodkazis, S., Photoluminescence from voids created by femtosecond-laser pulses inside cubic-BN. *Opt. Lett.* **2015,** *40* (24), 5711-5713.

272. Tadas, K.; Gintas, Š.; Saulius, J., Surface-texturing of sapphire by femtosecond laser pulses for photonic applications. *Journal of Physics D: Applied Physics* **2010,** *43* (14), 145501.

273. Benson, O., Assembly of hybrid photonic architectures from nanophotonic constituents. *Nature* **2011,** *480* (7376), 193-199.

274. Tame, M. S.; McEnery, K. R.; Ozdemir, S. K.; Lee, J.; Maier, S. A.; Kim, M. S., Quantum plasmonics. *nature Physics* **2013,** *9* (6), 329-340.

275. Koenderink, A. F.; Alù, A.; Polman, A., Nanophotonics: Shrinking light-based technology. *Science* **2015,** *348* (6234), 516-521.
276. Schuller, J. A.; Barnard, E. S.; Cai, W.; Jun, Y. C.; White, J. S.; Brongersma, M. L., Plasmonics for extreme light concentration and manipulation. *Nat. Mater.* **2010,** *9* (3), 193-204.
277. Akselrod, G. M.; Argyropoulos, C.; Hoang, T. B.; Ciracì, C.; Fang, C.; Huang, J.; Smith, D. R.; Mikkelsen, M. H., Probing the mechanisms of large Purcell enhancement in plasmonic nanoantennas. *Nat Photon* **2014,** *8* (11), 835-840.
278. Schietinger, S.; Barth, M.; Alchele, T.; Benson, O., Plasmon-Enhanced Single Photon Emission from a Nanoassembled Metal-Diamond Hybrid Structure at Room Temperature. *Nano Lett.* **2009,** *9* (4), 1694-1698.
279. Choy, J. T.; Hausmann, B. J. M.; Babinec, T. M.; Bulu, I.; Khan, M.; Maletinsky, P.; Yacoby, A.; Loncar, M., Enhanced single-photon emission from a diamond-silver aperture. *Nat Photon* **2011,** *5* (12), 738-743.
280. Zakharko, Y.; Graf, A.; Zaumseil, J., Plasmonic Crystals for Strong Light–Matter Coupling in Carbon Nanotubes. *Nano Lett.* **2016,** *16* (10), 6504-6510.
281. Hoang, T. B.; Akselrod, G. M.; Mikkelsen, M. H., Ultrafast Room-Temperature Single Photon Emission from Quantum Dots Coupled to Plasmonic Nanocavities. *Nano Lett.* **2016,** *16* (1), 270-275.
282. Demory, B.; Hill, T. A.; Teng, C.-H.; Zhang, L.; Deng, H.; Ku, P.-C., Plasmonic Enhancement of Single Photon Emission from a Site-Controlled Quantum Dot. *ACS Photonics* **2015,** *2* (8), 1065-1070.
283. Russell, K. J.; Liu, T.-L.; Cui, S.; Hu, E. L., Large spontaneous emission enhancement in plasmonic nanocavities. *Nat. Photon.* **2012,** *6* (7), 459-462.
284. Jungwirth, N. R.; Calderon, B.; Ji, Y.; Spencer, M. G.; Flatté, M. E.; Fuchs, G. D., Temperature Dependence of Wavelength Selectable Zero-Phonon Emission from Single Defects in Hexagonal Boron Nitride. *Nano Lett.* **2016,** *16* (10), 6052-6057.

285. Yang, A.; Hoang, T. B.; Dridi, M.; Deeb, C.; Mikkelsen, M. H.; Schatz, G. C.; Odom, T. W., Real-time tunable lasing from plasmonic nanocavity arrays. *Nature Communications* **2015,** *6*, 6939.

286. Zhou, W.; Dridi, M.; Suh, J. Y.; Kim, C. H.; Co, D. T.; Wasielewski, M. R.; Schatz, G. C.; Odom, T. W., Lasing action in strongly coupled plasmonic nanocavity arrays. *Nat Nano* **2013,** *8* (7), 506-511.

287. Henzie, J.; Lee, M. H.; Odom, T. W., Multiscale patterning of plasmonic metamaterials. *Nat Nano* **2007,** *2* (9), 549-554.

288. Boulesbaa, A.; Babicheva, V. E.; Wang, K.; Kravchenko, I. I.; Lin, M.-W.; Mahjouri-Samani, M.; Jacobs, C. B.; Puretzky, A. A.; Xiao, K.; Ivanov, I.; Rouleau, C. M.; Geohegan, D. B., Ultrafast Dynamics of Metal Plasmons Induced by 2D Semiconductor Excitons in Hybrid Nanostructure Arrays. *ACS Photonics* **2016**.

289. Johnson, P. B.; Christy, R. W., Optical Constants of the Noble Metals. *Physical Review B* **1972,** *6* (12), 4370-4379.

290. Zhou, W.; Dridi, M.; Suh, J. Y.; Kim, C. H.; Co, D. T.; Wasielewski, M. R.; Schatz, G. C.; Odom, T. W., Lasing action in strongly coupled plasmonic nanocavity arrays. *Nat. Nanotechnol.* **2013,** *8* (7), 506-11.

291. Xu, Z.-Q.; Zhang, Y.; Lin, S.; Zheng, C.; Zhong, Y. L.; Xia, X.; Li, Z.; Sophia, P. J.; Fuhrer, M. S.; Cheng, Y.-B.; Bao, Q., Synthesis and Transfer of Large-Area Monolayer WS2 Crystals: Moving Toward the Recyclable Use of Sapphire Substrates. *ACS Nano* **2015,** *9* (6), 6178-6187.

292. Beveratos, A.; Brouri, R.; Gacoin, T.; Poizat, J.-P.; Grangier, P., Nonclassical radiation from diamond nanocrystals. *Phys. Rev. A* **2001,** *64* (6), 061802.

293. Zhao, W.; Ribeiro, R. M.; Eda, G., Electronic structure and optical signatures of semiconducting transition metal dichalcogenide nanosheets. *Acc. Chem. Res.* **2015,** *48* (1), 91-9.

294. Chhowalla, M.; Shin, H. S.; Eda, G.; Li, L. J.; Loh, K. P.; Zhang, H., The chemistry of two-dimensional layered transition metal dichalcogenide nanosheets. *Nature Chemistry* **2013,** *5* (4), 263-75.

295. Kumar, S.; Kaczmarczyk, A.; Gerardot, B. D., Strain-Induced Spatial and Spectral Isolation of Quantum Emitters in Mono- and Bilayer WSe2. *Nano Lett.* **2015,** *15* (11), 7567-7573.

296. Berkdemir, A.; Gutiérrez, H. R.; Botello-Méndez, A. R.; Perea-López, N.; Elías, A. L.; Chia, C.-I.; Wang, B.; Crespi, V. H.; López-Urías, F.; Charlier, J.-C.; Terrones, H.; Terrones, M., Identification of individual and few layers of WS2 using Raman Spectroscopy. *Scientific reports* **2013,** *3*.

297. Rong, Y.; He, K.; Pacios, M.; Robertson, A. W.; Bhaskaran, H.; Warner, J. H., Controlled Preferential Oxidation of Grain Boundaries in Monolayer Tungsten Disulfide for Direct Optical Imaging. *ACS Nano* **2015,** *9* (4), 3695-3703.

298. Yamamoto, M.; Dutta, S.; Aikawa, S.; Nakaharai, S.; Wakabayashi, K.; Fuhrer, M. S.; Ueno, K.; Tsukagoshi, K., Self-limiting layer-by-layer oxidation of atomically thin WSe2. *Nano Lett.* **2015,** *15* (3), 2067-73.

299. Fu, C. C.; Lee, H. Y.; Chen, K.; Lim, T. S.; Wu, H. Y.; Lin, P. K.; Wei, P. K.; Tsao, P. H.; Chang, H. C.; Fann, W., Characterization and application of single fluorescent nanodiamonds as cellular biomarkers. *Proc. Natl. Acad. Sci.* **2007,** *104* (3), 727-32.

300. Brouri, R.; Beveratos, A.; Poizat, J.-P.; Grangier, P., Photon antibunching in the fluorescence of individual color centers in diamond. *Opt. Lett.* **2000,** *25* (17), 1294-1296.

301. Watanabe, H.; Fujikata, K.; Oaki, Y.; Imai, H., Band-gap expansion of tungsten oxide quantum dots synthesized in sub-nano porous silica. *Chemical Communications* **2013,** *49* (76), 8477-8479.

302. Deb, S. K., Optical and photoelectric properties and colour centres in thin films of tungsten oxide. *Philosophical Magazine* **1973,** *27* (4), 801-822.

303. Choi, S.; Johnson, B. C.; Castelletto, S.; Ton-That, C.; Phillips, M. R.; Aharonovich, I., Single photon emission from ZnO nanoparticles. *Appl. Phys. Lett.* **2014,** *104* (26), -.

304. Jungwirth, N. R.; Pai, Y. Y.; Chang, H. S.; MacQuarrie, E. R.; Nguyen, K. X.; Fuchs, G. D., A single-molecule approach to ZnO defect studies: Single photons and single defects. *J. Appl. Phys.* **2014,** *116* (4), -.

305. Tawfik, S. A.; Ali, S.; Fronzi, M.; Kianinia, M.; Tran, T. T.; Stampfl, C.; Aharonovich, I.; Toth, M.; Ford, M. J., First-principles investigation of quantum emission from hBN defects. *Nanoscale* **2017,** *9* (36), 13575-13582.

306. Wu, F.; Andrew, G.; Sundararaman, R.; Rocca, D.; Ping, Y., First-principles Engineering of Charged Defects for Two-dimensional Quantum Technologies. *arXiv preprint arXiv:1710.00257* **2017**.

307. Abdi, M.; Chou, J.-P.; Gali, A.; Plenio, M. B., Color centers in hexagonal boron nitride monolayers: A group theory and\textit {ab initio} analysis. *arXiv preprint arXiv:1709.05414* **2017**.

308. Koperski, M.; Nogajewski, K.; Potemski, M., Single Photon Emitters in Boron Nitride: More Than a Supplementary Material. *arXiv preprint arXiv:1708.03612* **2017**.

309. Vogl, T.; Lu, Y.; Koy Lam, P., Room temperature single photon source using fiber-integrated hexagonal boron nitride. *J. Phys. D: Appl. Phys.* **2017,** *50* (29), 295101.

310. Schell, A. W.; Tran, T. T.; Takashima, H.; Takeuchi, S.; Aharonovich, I., Non-linear excitation of quantum emitters in hexagonal boron nitride multiplayers. *APL Photonics* **2016,** *1* (9), 091302.

311. Kianinia, M.; Bradac, C.; Wang, F.; Sontheimer, B.; Tran, T. T.; Nguyen, M.; Kim, S.; Xu, Z.-Q.; Jin, D.; Schell, A. W., Super-resolution imaging of quantum emitters in layered materials. *arXiv preprint arXiv:1709.08683* **2017**.

Appendix

This section describes the procedure to perform normalization, background-correction, and jitter-convoluted fitting function on the second-order autocorrelation function.

Normalization

First, we start with normalization of the $g^{(2)}(\tau')$ function. The $g^{(2)}(\tau')$ relates to the photo-coincidence counts, $C(\tau')$, by the following equation:

$$g^{(2)}(\tau') = \frac{C(\tau')}{I_1 I_2 \, T \, w}$$

where I_1 and I_2 are the average count rates recorded from APD 1 and APD 2, respectively. T and w are the total integration time and the bin width, respectively.

Alternatively, there is another approach in the literature for the normalization of the autocorrelation function, that is to normalize the $C(\tau')$ with regard to the $C(\tau')$ at infinity since $g^{(2)}(\infty) = 1$ by definition, i.e. where there is no longer a correlation between the two photons in comparison.

It must be noted that this normalization procedure does not take into account the background fluorescence contribution.

Background contribution

To account for the background contribution in the autocorrelation measurement, one has to measure the count rate from the background only, B, and the total count rate, S + B, where S represents the count rate of the emitter's emission only. The background-corrected $g^{(2)}(\tau')$ then becomes:

$$g^2_{corr}(\tau') = \frac{(g^2(\tau) - (1 - \rho^2))}{\rho^2}$$

where $\rho = S/(S+B)$ is the emitter's signal to total signal ratio.

In the first approach, the background only, B, is measured a few micron away from the emitter while the total signal, S+B, is measured in the middle of the emitter. In the second approach, the background only, B, is obtained at the emitter by rotating the excitation polarization such that the count rate is minimized. To ensure that the collected light is purely from the background, an autocorrelation measurement is recorded to see if the photon statistic is Poissonian.

It should be noted that this procedure renders the background-corrected data $g^{(2)}(\tau')$, not its fitting function.

Jitter-convoluted fitting function

The non-zero dip from the autocorrelation function can arise even when background-correction procedure is performed. This imperfection is due to the instrument response function (IRF) of the system that makes the clocking process a Gaussian distribution rather than a perfect delta function. The Gaussian IRF can be expressed as follows:

$$J(\tau - \tau') = \frac{1}{\sigma\sqrt{2\pi}} e^{\frac{-(\tau-\tau')^2}{2\sigma^2}}$$

where $J(\tau - \tau')$ is the IRF, and σ is the standard deviation.

For a three-level system, the fitting function of $g^{(2)}(\tau')$ reads:

$$g^{(2)}(\tau') = 1 - (1 + a)e^{-\tau'/\tau_1} + ae^{-\tau'/\tau_2}$$

where a is the bunching factor, while τ_1 and τ_2 are the antibunching and bunching time, respectively.

In order to describe the effect of IRF impinging on the fitting function, we need to convolute the fitting function with the IRF according to the following equation:

$$g^{(2)}_{meas}(\tau) = \int_{-\infty}^{+\infty} g^{(2)}(\tau')\, J(\tau - \tau') d\tau'$$

where $g^{(2)}_{meas}(\tau)$ is the Gaussian-convoluted three-level model fitting function.

Once the data is fit with the $g^{(2)}_{meas}(\tau)$, the fitting coefficients a, τ_1 and τ_2 are extracted, and used to plot the original three-level model fitting function, $g^{(2)}(\tau')$. The $g^{(2)}(0)$ value obtained from this curve is jitter-free.